Université catholique de Louvain

Institute of Mechanics, Materials and Civil Engineering

November 2020

Assessment of mechanical properties of neutron irradiated tungsten and its alloys

Doctoral thesis

Chao Yin

Members of the examining board:

Prof. Thomas Pardoen, promoter	UCLouvain, Belgium
Prof. Roumen Petrov, co-promoter	UGent, Belgium
Dr. Dmitry Terentyev, mentor	SCK CEN, Belgium
Prof. Laurent Delannay, president	UCLouvain, Belgium
Prof. Pascal Jacques	UCLouvain, Belgium
Prof. Marc Geers	TU/e, Netherlands
Dr. Gerald Pintsuk	FZJ, Germany

The research was performed at:

UCLouvain
Institute of Mechanics, Materials
and Civil Engineering
Av. Georges Lemaître 4,
1348 Louvain-la-Neuve, Belgium

SCK CEN
The Belgium Nuclear Research Centre
Institute for Nuclear Materials Science (NMS)
Expert group on Structural Materials (SMA)
Boeretang 200,
2400 Mol, Belgium

UGent
Ghent University
Department of Electrical Energy, Metals,
Mechanical Constructions & Systems
Technologiepark Zwijnaarde 131,
9052 Ghent, Belgium

The work was supported by:

EUROfusion
Boltzmannstr. 2
85748 Garching, Germany

SCK CEN Academy
for Nuclear Science and Technology
Boeretang 200,
2400 Mol, Belgium

e-mail: chaoyin@sckcen.be

Acknowledgments

After four years of hard-working in my doctoral research, I would like to express my deepest gratitude to my mentors, Dr. Dmitry Terentyev and Dr. Andrei Goussarov, and my promotors, Prof. Thomas Pardoen and Prof. Roumen Petrov, for their guidance and support during my doctoral study in Belgian Nuclear Research Centre (SCK CEN). I especially acknowledge Dr. Dmitry Terentyev for his great effort to help me construct my research skills and build up the connection with experts in fusion society.

This doctoral thesis cannot be accomplished without the help of my colleagues and friends in SCK CEN: Jan Knaeps, Geert Berkmans, Kris Kaers, Roel Vanuytven, Dr. Jelle Van Eyken, Dr. Giovanni Bonny, Dr. Aleksandr Zinovev, Dr. Alexander Bakaev, Dr. Nicolas Castin, Dr. Wouter Van Renterghem, and Dr. Marlies Lambrecht. Thank you for your generous support.

Thanks to the SCK CEN Academy and Eurofusion program for financial support for the research and technical meetings. Through these technical meetings, I met a lot of new friends and earned scientific knowledge.

I would also like to show my gratitude to Min Lu, Meng Li, Wei Ren, Chih-Cheng Chang, Han-Hung Hsu, Zhongzhu Li, Xiang Li, and Hongshan Zhu. We all are students far away from home. Without you guys, I cannot imagine how homesick I will become.

I also want to give my gratefulness to my dear, Dan Chen. Although long distances separate us, she still supported and encouraged me throughout my years in Belgium. Moreover, I would like to express thanks to my best friends Sumit Srivastava, Saeid Babaei, and Rosa Fucci. Thank you for your company; we spent countless nice dinners and fantastic trips together. It is hard to imagine that we have known each other for four years already. I still remember the day we arrived in Mol, Belgium; we were such a group of naïve rookies. Finally, I have many thanks to my parents, Shiung-Lung Yin and Hsiu-Chin Hsu, and my younger sister, Chieh Yin, to believe me and support me in finishing my doctoral degree.

Mol, October 2020

Chao Yin

Abstract

Tungsten (W) is the main candidate material for plasma-facing components (PFCs) armor in nuclear fusion reactors. In the magnetic confinement reactor called “Tokamak”, the confined hot plasma is directed by the magnetic field to the divertor component in order to remove the impurities and He ash. In addition, the fast neutrons generated from D-T reactions irradiate the surrounding components in the reactor’s vacuum chamber. As a result, the divertor component receives a high heat flux and a high neutron flux at the same time. In order to assess and design a divertor with the ability to endure such a harsh environment, the investigation of mechanical degradation after high-temperature neutron irradiation is required.

Twelve W grades are investigated, including Plansee (Austria) ITER specification W and recrystallized W, A.L.M.T. (Japan) ITER specification W, AT&M (China) ITER specification W, A.L.M.T. (Japan) K doped W, A.L.M.T. (Japan) K doped W - 3 wt% Re alloy, KIT (Germany) K doped heavily deformed tungsten, fine grain pure W from IPP (Czech Rep.) produced by spark plasma sintering, two products strengthened by 1 wt% TiC and 2 wt% Y_2O_3 particles from KIT (Germany) produced by powder injection molding, rolled W strengthened by 0.5 wt% ZrC from ISSP (China), and single crystal W produced by MaTeck (Germany). The neutron irradiation is performed in the Belgian materials testing reactor (BR2) in Mol, Belgium. The highest irradiation temperature and irradiation dose are designed to be 1200 ^{o}C and ~1 dpa, which are close to the expected normal operation temperature and highest dose of the divertor in the first nuclear phase of ITER.

The results consist of three parts and can be summarized as follows:

(i) Development of miniaturized mechanical testing methods:

In order to reduce the complicated logistics of post-irradiation examination (PIE) driven by the need of the usage of a hot cell facility, small sample testing technics (SSTT) with novel improvements in the term of the methodology is introduced. The miniaturized three-point bending test method developed in this Ph.D. work can be implemented to determine the ductile to brittle transition temperature (DBTT) and as a piece of complementary information to determine the DBTT transition curve from the fracture toughness test. Another newly developed mechanical testing method is the single specimen interrupted tensile test. This novel tensile testing method identifies the yield strength at various temperatures by finding the stress at half the maximum load rate (HLR) and minimizes the number of specimens required for the

DBTT identification. Finally, in order to improve the accuracy of irradiation hardening evaluation for single crystal W, a simple unbiased hardness value H_0 is proposed. This efficient method can extract the hardness of neutron irradiated single crystal, for which the specific crystallographic orientation of the sample is a priori unknown.

(ii) DBTT of non-irradiated W:

Based on the results of the three-point bending and tensile tests assisted with the microstructural investigation by analysis of electron backscattered diffraction (EBSD), the controlling factors of DBTT for rolled/forged W and particle reinforced W are identified. Firstly, the grain orientation with respect to the tensile stress orientation and grain aspect ratio has a strong effect on the DBTT for rolled/forged W with elongated grains. For example, the one with elongated grains parallel to the tensile stress direction has a lower DBTT. In the case of Plansee ITER specification W, the difference in DBTT for two perpendicular orientations is around 250 °C since it has carrot-like grains (high grain aspect ratio). Secondly, the introduction of strengthening particles in W without the rolling/forging process has a limited effect on the reduction of DBTT. The rolling/forging process is essential to produce a low DBTT W product since it can increase the density of low-angle grain boundaries, which has a strong and positive effect on the reduction of the DBTT.

(iii) Neutron irradiation hardening in W:

The first results of fracture toughness of W after irradiated at 600 °C are reported in this work. The irradiation embrittlement (i.e., DBTT shift) is evaluated by the developed fitting method for the DBTT transition curve. The results indicate that the DBTT shifts to a temperature higher than 600 °C for AT&M ITER specification W irradiated at 600 °C to 0.67 dpa. In addition to the fracture toughness analysis, the analysis from the microindentations and EBSD measurements shows that an increase of grain boundary density does not always have a positive effect on the resistance of irradiation hardening for W products irradiated at 600 °C to 1 dpa. Furthermore, the results of microindentation indicate that the maximum irradiation hardening for polycrystalline W happens at an irradiation temperature of ~1000 °C for a dose of ~1 dpa, and a reduction of the irradiation hardening is observed for W irradiated at 1200 °C to ~1 dpa. However, this reduction of the hardening effect at an irradiation temperature of 1200 °C does not happen for W strengthened by TiC, which is unexpected and requires further investigation. For single crystal W, the maximum irradiation-induced hardening realizes around 800 °C, and above this temperature, the reduction of the hardening takes place.

Table of Contents

Acknowledgments ..... **i**
Abstract ..... **ii**
List of Abbreviations ..... **ix**
List of publications ..... **xii**
Publications summarized in this thesis xii
Other publications xiii
Chapter 1 Introduction **1**
1.1. New fire 1
1.2. Tokamak 2
1.3. Tungsten as plasma facing material with structural function 4
1.3.1. Improvement of tungsten ductility 6
1.3.2. Neutron irradiation effects on mechanical properties 9
1.3.3. Determination of ductile to brittle transition temperature 13
1.4. Objectives and expected Impact 15
1.5. References 17
Chapter 2 Overview of experimental methodology **24**
2.1. Materials 24
2.2. Mechanical test 28
2.2.1. Tensile test (Chapter 3 and 6) 28
2.2.2. Fracture toughness test (Chapter 4 and 7) 30
2.2.3. Three-point bending test (Chapter 4 and 5) 32
2.2.4. Microindentation (Chapter 8 and 9) 33
2.2.5. Post-irradiation examination (Chapter 6 to 9) 34
2.3. Scanning Electron Microscopy 35
2.3.1. Electron backscattered diffraction 35
2.3.2. Energy dispersive spectroscopy 38
2.4. Neutron irradiation 40

2.4.1. Tensile specimens (Chapter 6) 41
2.4.2. Fracture toughness specimens (Chapter 7) 42
2.4.3. Microindentation specimens (Chapter 8 and 9) 42
2.5. Reference 43
Chapter 3 Tensile properties of baseline and advanced tungsten grades ..45
3.1 Materials 45
3.2. Result 47
3.2.1. Strength and ductility 47
3.2.2. Delamination fracture 49
3.2.3. Transgranular and intergranular fracture 49
3.3. Discussion 53
3.3.1. Mechanical properties 53
3.3.2. Analysis of stress-strain response 54
3.3.3. Baseline W 56
3.3.4 Advanced W 56
3.4. Summary 59
3.5 Reference 61
Chapter 4 Ductile to brittle transition in ITER specification tungsten assessed by combined fracture toughness and bending tests analysis 62
4.1. Methodology and experimental details 62
4.1.1. Materials and microstructural analysis 62
4.1.2. Fitting method 65
4.2. Results 66
4.2.1. Three-points bending tests 66
4.2.2. Fracture toughness tests 67
4.2.3. Fracture surface 69
4.2.4. Texture 71
4.3. Discussion 73
4.3.1. Methodology to construct K_{Jc}(T) curve by single temperature measurement 73
4.3.2. Linking microstructure and fracture mechanism 77

4.4. Summary 81
4.5 Reference 83
Chapter 5 Ductile to Brittle Transition Temperature of advanced tungsten alloys for nuclear fusion applications deduced by miniaturized three-point bending tests 85
5.1. Experimental details 85
5.1.1. Materials 85
5.1.2. Microstructural investigation and fitting method 88
5.2. Results 89
5.2.1. Grain boundary density 89
5.2.2. Three-point bending tests 91
5.3. Discussion 94
5.3.1. Dependence of DBTT on grain orientation 94
5.3.2. DBTT and grain boundary density 98
5.3.3. Pros and cons of miniaturized three-point bending tests 100
5.4. Summary 102
5.5. References 104
Chapter 6 Impact of neutron irradiation on the strength and ductility of pure and ZrC reinforced tungsten grades 107
6.1. Experimental 107
6.1.1. Materials 107
6.1.2. Interrupted tensile tests 108
6.2. Results and discussion 115
6.2.1. Strength and ductility of non-irradiated materials 115
6.2.2. Interrupted tensile testing of non-irradiated specimens 116
6.2.3. Standard and interrupted tensile testing of irradiated samples 120
6.3. Summary 127
6.4. References 128

Chapter 7 Effect of high temperature neutron irradiation on fracture toughness of ITER-specification tungsten 130
7.1. Materials 130
7.2. Results and discussion 131
7.2.1. Fracture toughness and fracture surface 131
7.2.2. Estimation of the transition curve 135
7.3. Summary 138
7.4. Reference 139
Chapter 8 High temperature neutron irradiation hardening in baseline and advanced tungsten grades assessed by hardness measurements 140
8.1. Experimental procedures 140
8.1.1. Materials 140
8.1.2. Microstructure 140
8.1.3. Yield strength estimation from Vickers hardness 142
8.2. Results and Discussion 144
8.2.1. Microstructure 144
8.2.2. Vickers hardness and irradiation hardening 149
8.2.3. Estimation of irradiation hardening on tensile yield strength 154
8.3. Summary 157
8.4. Reference 158
Chapter 9 Anisotropy in the hardness of single crystal tungsten before and after neutron irradiation 160
9.1. Materials and microindentation measurement 160
9.2. Results and discussion 162
9.2.1. Anisotropy in single crystal tungsten 162
9.2.2. Effect of neutron irradiation 168
9.3. Summary 172
9.4. References 173
Chapter 10 Summary and Conclusions 175
10.1. Mechanical testing methods 176

10.2. Mechanical properties of non-irradiated tungsten alloys.....178
10.3. Mechanical properties of irradiated tungsten alloys 180
10.4. Conclusion 183
10.5. Perspectives.....184

List of Abbreviations

ΔDBTT	Shift of ductile to brittle transition temperature
0.2% YS	0.2% yield strength
AES	Auger electron spectroscopy
A_{ideal}	Ideal projected area
ALK	Potassium doped pure tungsten
ALKR	Potassium doped tungsten-3 wt% rhenium alloy
A_{true}	True projected area
ATW	ITER specification tungsten, AT&M
AT&M	Advanced Technology & Materials Co., Ltd
BSE	Backscattered electron
B-type	Brittle type
BR2	Belgian Material Test Reactor
CFETR	China Fusion Engineering Test Reactor
CRSS	Critical resolved shear stress
CS	Central solenoid
CSL	Coincidence site lattices
D10	Equivalent 10% diameter
D50	Equivalent median diameter
D90	Equivalent 90% diameter
DBTT	Ductile to brittle transition temperature
DCT	Disk-shaped compact tension
DEMO	Demonstration fusion power plant
DEMO-S	Russian DEMO
D-type	Ductile type
EBSD	Electron backscattered diffraction
EDM	Electrical discharge machining
EDS	Energy dispersive x-ray spectroscopy
ELM	Edge-localized mode
EN-type	Early necking type
EU DEMO	European DEMO
FG	Fine grain tungsten
FS	Flexural strain
Fstrain	True fracture strain
Fstrength	True fracture strength
FZJ	Forschungszentrum Jülich
GB	Grain boundary
HAGB	High angle grain boundary
HDK	Heavily deformed potassium doped pure tungsten

HFIR	High Flux Isotope Reactor
HFR	High Flux Reactor
H_{ideal}	Ideal hardness
HMLR	Strength at half maximum loading rate
H_{true}	True hardness
HV	Vickers hardness
IGA	ITER specification tungsten, A.L.M.T.
IGP	ITER specification tungsten, Plansee
IPF	Inverse pole figure
IPP	Institute of Plasma Physics
ISSP	Institute of Solid State Physics
IT	Interrupted uniaxial tensile tests
JA DEMO	Japanese DEMO
JET	Joint European Torus
JMTR	Japan Materials Testing Reactor
JOYO	Japanese experimental fast reactor
K-DEMO	Korean DEMO
KIT	Karlsruhe Institute of Technology
LD	Longitudinal direction
LAGB	Low angle grain boundary
LEFM	Linear elastic fracture mechanics
MLR	Maximum loading rate
MTR	Material test reactors
ND	Normal direction
OKMC	Object kinetic Monte Carlo
PAS	Positron annihilation spectroscopy
PF coils	Poloidal field coils
PFCs	Plasma facing components
PFUs	Plasma facing units
PIE	Post-irradiation examination
PIM	Powder injection molding
Q_{DBT}	Activation energy for the ductile to brittle transition
RD	Rolling direction
SCK CEN	Belgian nuclear research centre
SE	Secondary electron
SEM	Scanning electron microscopy
SIA	Self-interstitial atom
SPS	Spark plasma sintering
SSTT	Small specimen testing techniques
ST	Standard uniaxial tensile test
TD	Transverse direction
T_0	Transition temperature

TEM	Transmission electron microscopy
TF coils	Toroidal field coils
TFTR	Tokamak Fusion Test Reactor
T_{irr}	Irradiation temperature
T_m	Melting temperature
TMT	Thermo mechanical treatment
T_{test}	Test temperature
UTS	Ultimate tensile strength
UYS	Upper yield strength
W(100)	Single crystal tungsten
W0.5ZrC	0.5 wt% ZrC reinforced tungsten
W1TiC	1 wt% TiC reinforced tungsten
W2YO	2 wt% Y_2O_3 reinforced tungsten
W-RX	Recrystallized IGP
YS	Yield strength

List of publications

Publications summarized in this thesis

- **Chao Yin**, Giovanni Bonny, Dmitry Terentyev, “Anisotropy in the hardness of single crystal tungsten before and after neutron irradiation”, Journal of Nuclear Materials, submitted in Sep. 2020
- **Chao Yin**, Dmitry Terentyev, Andrii Dubinko, Tao Zhang, Marius Wirtz, Steffen Antusch, Roumen H. Petrov, Thomas Pardoen, “Impact of neutron irradiation on hardening of baseline and advanced tungsten grades and its link to initial microstructure”, Journal of Nuclear Materials, submitted in Sep. 2020
- **Chao Yin**, Dmitry Terentyev, Tao Zhang, Shuhei Nogami, Steffen Antusch, Chih-Cheng Chang, Roumen H. Petrov, Thomas Pardoen, “Ductile to Brittle Transition Temperature of advanced tungsten alloys for nuclear fusion applications deduced by miniaturized three-point bending tests”, International Journal of Refractory Metals and Hard Materials, submitted in Sep. 2020
- **Chao Yin**, Dmitry Terentyev, Tao Zhang, Roumen H. Petrov, Thomas Pardoen, “Impact of neutron irradiation on tensile properties of pure and ZrC reinforced tungsten grades”, Journal of Nuclear Materials 537, 152226, 2020
- **Chao Yin**, Dmitry Terentyev, Steven Van Dyck, Alexey Stankovskiy, Roumen H. Petrov, Thomas Pardoen, “Effect of high temperature neutron irradiation on fracture toughness of ITER-specification tungsten”, Physica Scripta, Volume 2020, Number T171, 2020
- **Chao Yin**, Dmitry Terentyev, Thomas Pardoen, Roumen Petrov, Zhenfeng Tong, “Ductile to brittle transition in ITER specification tungsten assessed by combined fracture toughness and bending tests analysis”, Materials Science and Engineering: A 750, 2019
- **Chao Yin**, Dmitry Terentyev, Thomas Pardoen, Anastasiia Bakaeva, Roumen Petrov, et al., “Tensile properties of baseline and advanced tungsten grades for fusion applications”, International Journal of Refractory Metals and Hard Materials 75, pp. 153-162, 2018

Other publications

- Dmitry Terentyev, **Chao Yin**, Andrii Dubinko, Chih-Cheng Chang, Jeong-Ha You, "Neutron irradiation hardening across ITER divertor tungsten armour", International Journal of Refractory Metals and Hard Materials, submitted in Oct. 2020
- Wouter Van Renterghem, Dmitry Terentyev, Shanmugam Balaji, Christopher David, Andrii Dubinko, **Chao Yin**, Tao Zhang, "Microstructural evolution in tungsten strengthened by ZrC under ion irradiation at 600°C", Journal of Nuclear Materials, submitted in Sep. 2020
- Andrii Dubinko, **Chao Yin**, Dmitry Terentyev, Aleksandr Zinovev, Michael Rieth, Steffen Antusch, Monika Vilémová, Jiří Matějíček, Tao Zhang, "Plastic deformation in advanced tungsten-based alloys for fusion applications studied by mechanical testing and TEM", International Journal of Refractory Metals and Hard Materials, accepted in Oct 2020
- Giovanni Bonny, Timofii Khvan, Anastasiia Bakaeva, **Chao Yin**, Andrii Dubinko, Celine Cabet, Marie Loyer-Prost, Nicolas Castin, Alexander Bakaev, Dmitry Terentyev, "Effect of statistically stored dislocations in tungsten on the irradiation induced nano-hardening analyzed by different methods", Journal of Nuclear Materials 543, 152543, 2021
- Jiri Matejicek, Jakub Veverka, **Chao Yin**, Monika Vilemova, Dmitry Terentyev, Marius Wirtz, Mauricio Gago, Andrii Dubinko, Hynek Hadraba, "Spark Plasma Sintered Tungsten – Mechanical Properties, Irradiation Effects and Thermal Shock Performance", Journal of Nuclear Materials 542, 152518, 2020
- Giovanni Bonny, Milan J. Konstantinovic, Anastasiia Bakaeva, **Chao Yin**, Nicolas Castin, Konstantina Mergia, Vassilis Chatzikos, et al., "Trends in vacancy distribution and hardness of high temperature neutron irradiated single crystal tungsten", Acta Materialia 198, pp. 1-9, 2020
- Dmitry Terentyev, Monika Vilémová, **Chao Yin**, Jakub Veverka, Andrii Dubinko, Jiří Matějíček, "Assessment of mechanical properties of SPS-produced tungsten including effect of neutron

irradiation", International Journal of Refractory Metals and Hard Materials 89, 105207, 2020

- Alexander Bakaev, Aleksandr Zinovev, Dmitry Terentyev, Giovanni Bonny, **Chao Yin**, Nicolas Castin, Yuri A. Mastrikov, and Evgeny E. Zhurkin, "Interaction of carbon with microstructural defects in a W-Re matrix: An ab initio assessment", Journal of Applied Physics 126, Issue 7, 2019
- Peter Rindt, Jaume Mata Gonzalez, Peter Hoogerhuis, Patrick van den Bosch, Marc van Maris, Dmitry Terentyev, **Chao Yin**, et al., "Using 3D-printed tungsten to optimize liquid metal divertor targets for flow and thermal stresses", Nuclear Fusion 59, 2019

Chapter 1
Introduction

1.1. New fire

The use of fire was a huge leap for humankind two million years ago. The event symbolizes a milestone that humans control chemical energy. After that, for thousands of years, human civilization depended on fire to produce tools, cook their food, and defend themselves. Without fire, humans would still struggle to survive, and the industrial revolution would never have happened. Beside chemical energy, the “new fire,” which powers our solar system, is nuclear energy. For example, the sun is driven by nuclear fusion, and part of the geothermal energy is provided by radioactive decay inside the planet. The combination of solar and geothermal energy dominates the climate and tectonic activities, which shape our planet. After two centuries of the bumming process of science and technology, starting from the first industrial revolution, the discovery and application of nuclear energy for peaceful applications is another ground-breaking event for human civilization.

Nuclear energy can provide low carbon emission electricity to the industrialized world and a stable source of heat and electricity for deep space missions. There are two ways to harvest nuclear energy: nuclear fission and nuclear fusion. The nuclear fission reactor is a well-developed technology and has powered the world for more than a half-century. However, the public concern of spent fuel for its long-term storage and proliferation has limited the speed of implementation and development of the new nuclear fission reactor. Different from nuclear fission, the waste product of nuclear fusion is not long-term radioactive nuclear waste and does not have military applications. Moreover, the energy per nucleon produced by nuclear fusion is higher than nuclear fission. Therefore, nuclear fusion is a promising energy source, which can convince the public to accept nuclear energy. Although nuclear fusion has these advantages, the technical and scientific challenges of nuclear fusion result in slow progress of development. Fortunately, the global demands for clean energy have catalyzed the development. Additionally, with the support of new technology and international cooperation, fusion energy might become commercialized in the mid of the 21st century.

As we know, until now, nuclear fusion in nature only happens in the core of the sun, where extremely high pressure and high temperatures are realized,

allowing the fusion reaction to overcome the Coulomb barrier. In order to achieve nuclear fusion on earth, even higher temperatures will be required since the sun-level high pressure is impossible to achieve. The fuel, hydrogen isotopes, will become plasma at this extremely high temperature. To contain this hot plasma, since the 1950s, many types of conceptual reactors have been proposed and attempted to make controlled nuclear fusion become a reality. Magnetic confinement realized in a toroidal chamber, known as "Tokamak", has the most advanced development among these concepts and might be the first type of the fusion reactor to be commercialized.

1.2. Tokamak

The Tokamak, standing from Russian "toroidal chamber with magnetic coils", is a type of reactor based on the idea of magnetic confinement. In the 1950s, Soviet physicists Igor Tamm and Andrei Sakharov introduced the concept of Tokamak inspired after Oleg Lavrentiev. Soon the first working Tokamak "T-1" started its operation in 1958. The ultimate goal is to confine hot plasma in order to reach a temperature higher than several 100 million Kelvin such that the nuclear fusion reaction will self-sustain. The major components of the Tokamak for a nuclear fusion power plant are central solenoid (CS), poloidal field coils (PF coils), toroidal field coils (TF coils), a vacuum vessel, divertor cassettes, and blanket segments, as shown in **Figure 1.1**.

The major task for the CS is to initiate the plasma, to induce and maintain the plasma current during operation. Thus, CS is the strongest magnet system in a Tokamak. Moreover, the CS assists the PF coils in controlling the shape of plasma. The confinement of the plasma is achieved by the magnetic field rotational transform, which results from the combination of the toroidal magnetic field and the poloidal magnetic field generated from the TF coils and the plasma current. The result of rotational transform is a helical magnetic field, which makes the average drift of the charged particles of plasma to be zero, and thus the charged particles are confined in the vacuum vessel. Although plasma can self-heating by Ohmic heating from the plasma current, the heating efficiency decreased as the plasma temperature gets higher. Thus, external heating methods like neutral beam injection and radio frequency heating are required in order to reach the target temperature for the optimized fusion reaction rate. Since the plasma current is induced by the CS, which acts as a transformer, the plasma current is not continuously maintained but in pulsed mode during operation.

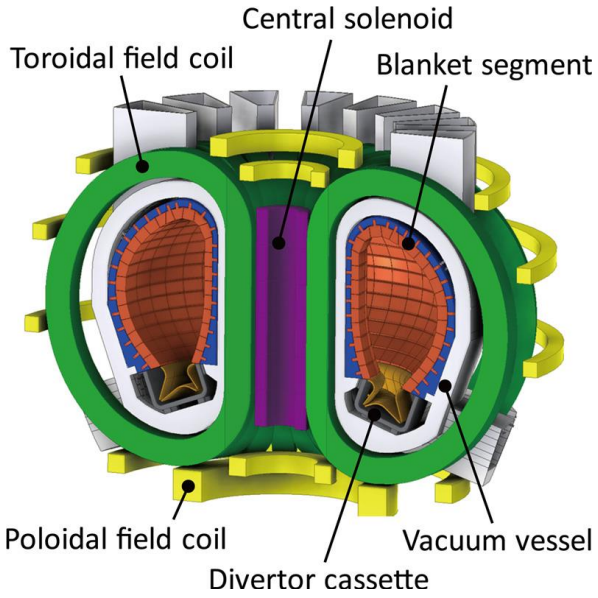

Figure 1.1. Scheme of a Tokamak for nuclear fusion power plant [1]

Currently, the target fuel type for a Tokamak is deuterium (D) and tritium (T); both are isotopes of hydrogen (H). D is abundant in the ocean. But T requires nuclear reactions to generate, and it normally can be collected in the heavy water nuclear reactor. The D-T reaction is shown as follow,

$$ {}_{1}^{2}D + {}_{1}^{3}T \rightarrow {}_{2}^{4}He(3.5\ MeV) + {}_{0}^{1}n(14.1\ MeV)\ . \qquad \textbf{(1.1)} $$

The result of the D-T reaction is helium (He) and a fast neutron. The helium will ionize and is confined with the other charged particles. However, since the neutron is a neutral particle, the neutrons are not confined and will bombard the surrounding reactor components. The components, which receive the highest neutron dose, are divertor cassettes and blanket segments. The divertor cassettes are part of the reactor exhaust system, where the impurities and the fusion product (He) are guided to the divertor by the magnetic field and are then extracted by a cryopump. Thus, the divertor will receive periodic high heat flux and fast neutron bombardment during operation. Besides neutron irradiation damages, the interaction of the neutron and the materials of the components will also create heat. This heating effect will be significant for future fusion power plants since 80% of the fusion energy is carried by the neutrons. Both divertor cassette and blanket segment have a water or gas cooling system to extract this heat. In the case of electricity generation, the heated coolant will then go through the heat exchanger to create steam, and the steam will drive the turbine of the

generator. Another purpose of the blanket segment is to self-sustain the supply of T by breeding it, since T cannot be found in nature. The reaction for breeding T is shown as follow,

$$ {}^{1}_{0}n + {}^{6}_{3}Li \rightarrow {}^{3}_{1}T + {}^{4}_{2}He \ , \tag{1.2} $$

$$ {}^{1}_{0}n + {}^{7}_{3}Li \rightarrow {}^{3}_{1}T + {}^{4}_{2}He + {}^{1}_{0}n \ . \tag{1.3} $$

Lithium (Li) is also abundant on earth. Therefore, with an almost unlimited supply of D and Li, the Tokamak driven by D-T reaction can power our civilization for thousands of years.

Most of the existed Tokamak only focus on plasma science and engineering since the instability of the plasma is one of the major challenges for magnetic confinement. Until now, only two Tokamaks, Joint European Torus (JET) and Tokamak Fusion Test Reactor (TFTR), operate with D-T fuel and go to the nuclear phase. Operated with fuel of 50% D and 50% T, their maximum achieved Q ratio, which is the ratio between fusion power and total power input, is more than 0.64 for JET [2] and 0.27 for TFTR [3]. In order to conquer the challenge of nuclear fusion, 35 countries have worked together to construct the international Tokamak named “ITER” based on years of experience from previous and current Tokamak operations. ITER will be the largest Tokamak ever build with a fusion power of 500 MW, and its target Q ratio will be larger than 10 [4]. Moreover, the concept of the blanket module for T breeding will be tested during its operation [5]. ITER will be the stepping stone towards a demonstration fusion power plant (DEMO), which is the last step before the commercialized fusion power plant. Several DEMO designs have been proposed by different countries or political unions: for example, the European DEMO (EU DEMO) [6], the China Fusion Engineering Test Reactor (CFETR) [7], the Korean DEMO (K-DEMO) [8], the Japanese DEMO (JA DEMO) [9], the Indian DEMO [10], the Russian DEMO (DEMO-S) [11].

1.3. Tungsten as plasma facing material with structural function

As demonstrated in **Figure 1.2** [12], the divertor cassette assembly contains three parts: inner vertical target, dome, and outer vertical target (from left to right). These targets consist of groups of plasma facing units (PFUs), which are assembled with tungsten monoblocks and CuCrZr cooling tubes. As discussed in section 1.2, the divertor and blanket are designed to receive intense neutron bombardment at the phase of nuclear fusion reactions. The divertor will also need to handle a periodic high heat flux, which amounts up

to 20 MW/m^2 in steady-state operation [13]. The temperature gradient in the divertor monoblock from the plasma facing side to the heat sink side is about 1500 ^oC, where the plasma facing side is at a temperature of 2000 ^oC [14]. In H-mode operation, the instability called edge-localized mode (ELM) might occur [15, 16]. In this event, the ELM releases a high energy (more than 1 MJ/m^2) in microseconds on the first wall armor of plasma-facing components (PFCs), especially on the divertor. With this extreme high power, cracking or melting will occur on the surface of the divertor [17]. In order to meet these high heat flux conditions, high melting point materials are preferred for the construction of divertor and first wall armor.

Among all metals, tungsten has the highest melting point. Moreover, it also has other attractive properties, i.e., low erosion rate, low fuel retention, high thermal conductivity, etc., which makes tungsten the main candidate material for PFCs of ITER and EU DEMO [18-20]. However, tungsten has a well-known mechanical weak spot: high ductile to brittle transition temperature (DBTT). Ductile to brittle transition is a phenomenon when the fracture behavior of the material transitions from ductile to brittle at a certain temperature, which is defined as DBTT. The DBTT of tungsten will even increase to higher temperature after neutron irradiation during fusion reactions because of the irradiation introduced defects. Moreover, during long-term operation at a temperature higher than 1200 ^oC, recrystallization will happen, which decreases the strength of tungsten [21, 22]. Combined with the periodic thermal loads from the high heat flux during normal operation, the divertor based on the tungsten monoblock design will experience thermo-mechanical fatigue, which will result in crack nucleation and propagation [22, 23]. Thus, in order to ensure the safety and structural integrity of the divertor, various methods have been implemented to improve low temperature mechanical performance of tungsten and its alloys.

Currently, various commercial ITER specification [24] pure tungsten grades, provided by different companies, i.e., Plansee in Austria, AT&M in China, or ALMT in Japan, are available on the market. These pure tungsten grades are manufactured by mechanical processes, like rolling or forging, after sintering through the powder metallurgical process to improve mechanical properties at low temperature [25]. Moreover, in order to improve thermal stability at high temperature and low temperature mechanical performance, different particle and alloying elements are introduced to reinforce tungsten grades. For example, tungsten grade reinforced with ZrC [26, 27], TiC [28], Y_2O_3 [29], La_2O_3 [30], etc, and tungsten alloys with potassium (K) and rhenium (Re) [31, 32]. Tungsten composites with tungsten fibers also have the potential to compete with tungsten alloys since composite materials have a unique toughening mechanism, which can enhance toughness at low temperature

[33]. Novel manufacturing processes, coupled with the mentioned advanced grade tungsten alloys, are also developed to ease the manufacturing process. For instance, 3D printing, spark plasma sintering (SPS), powder injection molding (PIM) [34], etc. These novel manufacturing processes have the potential to provide divertor components in the future.

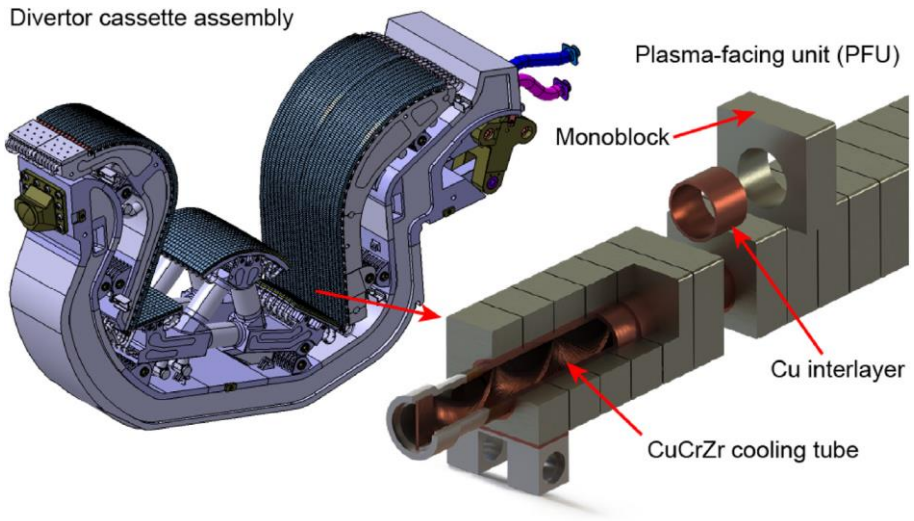

Figure 1.2. CAD model of a single cassette of the ITER tungsten divertor [12]

1.3.1. Improvement of tungsten ductility

The ductile to brittle transition temperature is one of the most common characteristics of materials applied to describe the properties of the materials as well as to choose the desirable operation temperature range. In that respect, the development of advanced tungsten grades is largely focused on the possible means of reducing DBTT.

Principally, there are three ways to reduce the DBTT of tungsten: via mechanical (or thermo-mechanical) processing (i.e., rolling or forging) [25], solid solution alloying with Re [35], strengthening grain boundaries (GB) by chemical alloying [26, 36]. As the tungsten is plastically deformed by rolling or forging, the dislocation density will increase and form a network of low angle grain boundaries (LAGB). Since the plastic deformation is controlled by the movement of dislocations, tungsten with high dislocation density and LAGB density act as a source of edge or mixed dislocations [37], which can exhibit some ductility below the temperature for the activation of screw

dislocation motion. Alternatively, in single crystals or recrystallized polycrystallines, the DBTT is defined by the activation of the slip of screw dislocations [38]. The alloying of tungsten with Re, as reported by Romaner, et al. [35], modifies the core of the 1/2<111> screw dislocation from a symmetric to an asymmetric structure, which assists the nucleation of kinks on the dislocation line, thereby allowing the dislocation to displace at a lower shear stress as well as to emit kinks in different planes. As a result, the ductility of tungsten at low temperature is enhanced since a higher number of slip planes are available, and the critical stress for plastic deformation is reduced.

Upon severe mechanical loading in the region close to DBTT, a fracture usually initiates near GB. The GB is the weakest link of metals in general and tungsten in particular because of the segregation of impurities, like oxygen and nitrogen, whose presence reduces their cohesive strength. Thus, at sufficiently low temperatures, tungsten might exhibit an intergranular brittle fracture before the applied load reaches the critical stress for plastic deformation. In order to prevent such failure to happen, the amount of the impurities or the density of the impurities on GBs should be reduced. The impurities can be removed by introducing secondary particles, which can form chemical compounds with the impurities [26]. The reduction of the density of the impurities can be achieved by reducing the grain size of tungsten [36]. Smaller grains have a larger surface-to-volume fraction, and thus the density of the impurities per GB surface unit will be reduced given a fixed concentration of impurities in the material.

As mentioned above, the reduction of DBTT is one of the main goals for the development of fabrication routes of commercially pure tungsten and advanced tungsten grades. The possible impact factors on the DBTT of rolled pure tungsten have been summarized by Bonnekoh, et al. [25], as shown in **Table 1.1**. Although these parameters for DBTT reduction for pure tungsten have been studied, further clarification of these parameters on the fracture mechanisms after neutron irradiation is necessary to provide feedback for the engineering of the next generation of tungsten grades with improved low temperature mechanical properties and resistance to irradiation damage.

Table 1.1. Summary of possible impact factors on the DBTT of pure tungsten [25]

Parameter		Explanation	Impact on DBTT
Lattice defect (introduced by rolling/forging)	Vacancies	Only affect the climb of edge dislocations	No impact
	Dislocations	Dislocation mobility reduced by dislocation hardening [39]	Increase DBTT
		LAGB [37] and debris loops act as a dislocation source	Decrease DBTT
	Grain boundaries	Dislocation pile-up at GB, plastic zone confinement [40]	Increase DBTT
		GB ledges act as a dislocation source [41]	Decrease DBTT
Crystallographic texture		Refer to study of single crystals tungsten [38]	Weak impact
Plane strain or plane stress fracture (sample thickness)		Only impact on the fracture toughness, but not on the DBTT [42]	No impact
Foreign atoms (impurities)	Located at dislocation	With higher dislocation density, the density of impurity reduced.	Decrease DBTT
	Located at GB	With higher GB area, the density of impurity reduced. Thus, GB is strengthened [36]	Decrease DBTT
Geometrical arrangement of low/high fracture toughness areas		Low fracture toughness: GB and sinter pores	High impact
		High fracture toughness: grain	

1.3.2. Neutron irradiation effects on mechanical properties

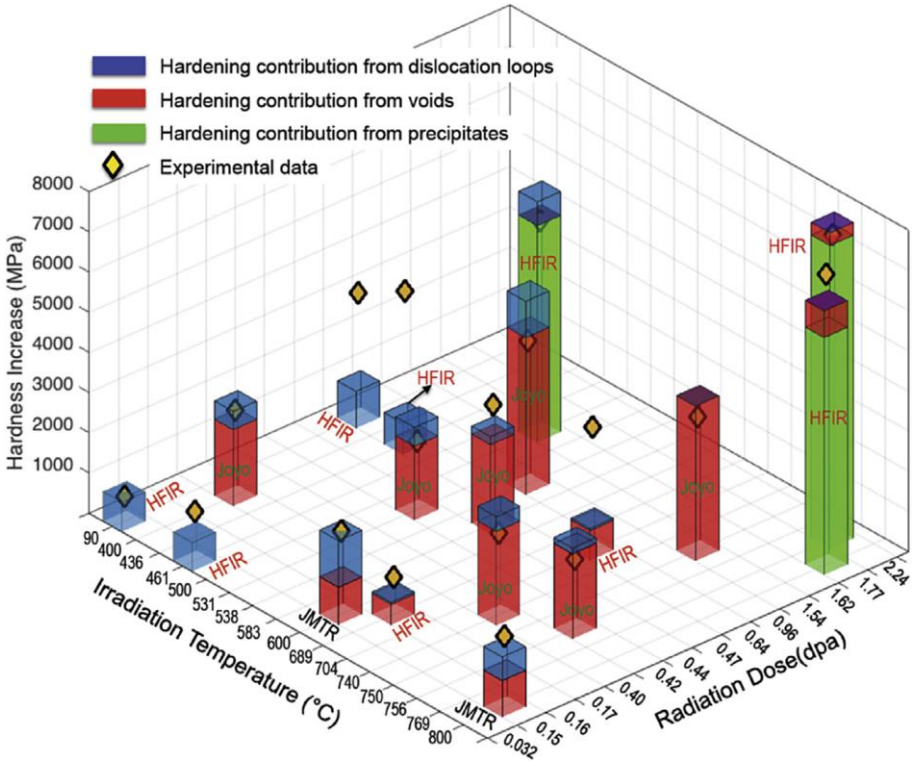

Figure 1.3. Neutron irradiation induced defects and their contribution to the hardening effect after various irradiation conditions and damage [43]. The neutron irradiation experiments were performed in three different reactors: Japanese experimental fast reactor (JOYO), Japan Materials Testing Reactor (JMTR), and High Flux Isotope Reactor (HFIR).

In essence, the neutron irradiation is expressed in two reactions of a neutron with the atomic lattice of a metal. In-elastic scattering leads to transmutation reactions (Re and Os are introduced in W), and elastic scattering causes the formation of collision cascades, which result in the formation of stable lattice defects (Frenk pairs). Further diffusion, recombination of adjective and mutual interaction alike defects cause the formation of the microstructure, which is detectable by conventional means like transmission electron microscopy (TEM). Hasegawa, et al. and Hu, et al. summarized the different type of defects, such as precipitates (σ phase: ReW or χ phase: Re3W), dislocation loops, and voids, whose presence varies with the irradiation

temperatures and neutron fluence [43, 44]. As the irradiation temperature and dose increase, the irradiation induced microstructure transforms from being dominated by dislocation loops to voids dominant or large precipitates dominant depending on the thermal neutron flux (i.e., depending on the neutron spectrum of the reactor). The appearance of Re by alloying or transmutation is found to suppress the formation of the voids [44]. Thus, the microstructure containing a high density of precipitates exhibits smaller voids (smaller in size and density).

The above listed lattice defects and precipitates will suppress plastic deformation, thereby increasing the stress required to initiate plastic yield, which is called the irradiation hardening phenomenon. The contribution of the different types of defects to the irradiation hardening have been summarized by Hu, et al. [43], as shown in **Figure 1.3**. A precipitate has the highest contribution to irradiation hardening, followed by voids and dislocation loops. The population of transmuted elements varies with the neutron spectrum, where a higher thermal neutron flux generates more transmution elements [45]. Different from the fission reactor delivering a mixed spectrum, the fast neutrons with 14 MeV energy are the majority in the fusion reactor. Thus, the concentration of Re and Os transmution metallic elements will be lower than the one introduced by the fission test reactor. [45]. This means that, in the fusion reactor, the contribution of precipitates to irradiation hardening is expected to be smaller. However, at considerable irradiation doses (above 1 dpa) He bubbles will contribute to additional hardening [46]. Most of the studies related to the assessment of mechanical properties of tungsten after neutron irradiation were focused on modeling and hardness measurements [43, 44, 47-54]. Fukuda et al. have reported the irradiation hardening induced by neutron irradiated in various test reactors (JOYO and JMTR) for advanced tungsten grades [51]. Their results show that the ultra-fine grain structure and the addition of strengthening particles will enhance the resistance to irradiation hardening because of the large density of sinks for irradiation defect. However, since these hardness tests were performed at room temperature, it is hard to transfer these experimental data to predict the actual change of the yield stress and tensile strength at elevated temperature.

The studies of high temperature mechanical tests for neutron irradiated tungsten are rather scarce. Only a few studies, performed in the 1970s and very recent years, reported the change of tensile and bending properties of tungsten. In the 1970s, Alexandrov, et al. [55] reported that the DBTT increased by ~200 ^{o}C and the ultimate tensile strength (UTS) doubled after neutron irradiation at 100 ^{o}C with a neutron dose of 4.2 x 10^{19} n/cm^2 (~0.05 dpa) for a sintered pure tungsten. The tensile properties of sintered pure

tungsten irradiated at a higher temperature (371 – 380 °C) and a higher dose of 0.5-0.9 x 10^{22} n/cm^2 (0.5-0.9 dpa) were reported by Steichen [56], and the result showed that the increase of the strength was also around a factor two and the DBTT increased by ~350 °C. In the 1990s, Gorynin et al. [57] assessed the neutron irradiation effect on tensile properties of tungsten at a dose up to 2.2 x 10^{22} n/cm^2 (> 2.5 dpa) in the BOR-60 fast reactor, and they indicated that tungsten irradiated at a temperature between 250 to 550 °C experienced brittle intergranular fracture while being tested at 550°C i.e., the irradiation a converted ductile material into a brittle one.

In recent years, more studies have been published. Habainy et al. [58] reported the result of three point bending tests for tungsten irradiated at a spallation neutron source. They observed the reduction of fracture strength and brittle fracture for irradiated specimens at test temperatures up to 500 °C for doses ranging from 1.3 to 3.5 dpa, where the DBTT of non-irradiated specimens was ~350 °C. Garrison, et al. [59] and Katoh, et al. [60] reported the mechanical properties after the irradiation at the HFIR reactor using single crystal tungsten irradiated at 90 – 830 °C up to 1.8 dpa. The results showed that the tensile strength of specimens tested in the <110> direction experienced less irradiation embrittlement than the one tested in the <100> direction. The tensile behaviors of these irradiated single crystal tungsten specimens are summarized in **Figure 1.4** [60], where the modulus of toughness (the integration of the area beneath the engineering stress-strain curve) reduced and the DBTT increased with increasing neutron dose, climbing above 500 °C at a dose exceeding 0.5 dpa. Moreover, they reported the variation of tensile fracture stress or UTS versus irradiation dose, where single crystal tungsten had the highest fracture stress or UTS at 0.02 dpa regardless of the testing orientation [59, 60]. Four point bending tests performed using single crystal tungsten irradiated in the High Flux Reactor (HFR, Petten, Netherland) were reported by Abernethy, et al. [61]. The results showed that the DBTT increased up to ~600 °C after irradiation at 900 °C to a dose of 1.7 dpa. The DBTT was assessed using the bending specimens with a sharp pre-crack along the (100)<001> crack system. Besides the irradiation campaigns on single crystal tungsten, the tensile properties of tungsten alloyed with Re or doped with K, and irradiated in HFIR at 600 and 800 °C to a dose up to 0.74 dpa, were presented by Miyazawa, et al. [62]. They indicated that tungsten alloys doped with K had better resistance to irradiation degradation at ~800 °C to ~0.7 dpa, where the K-doped tungsten alloys had a DBTT lower than 500 °C compared to DBTT of 700 °C for non-doped tungsten alloys.

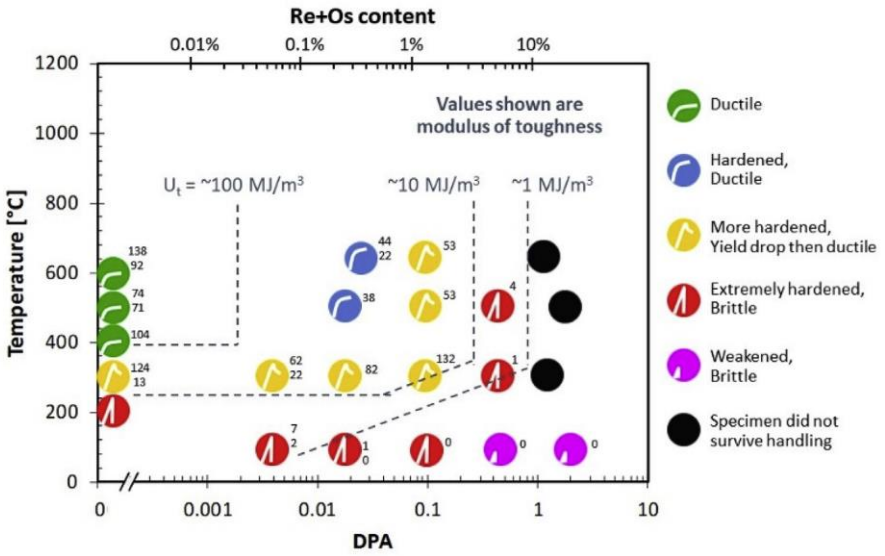

Figure 1.4. Tensile behavior of irradiated single crystal tungsten [60]. The vertical axis is the irradiation/test temperature. The color code shows the effect of irradiation.

In summary, neutron irradiation taking place in the temperature range of 400 – 800 °C with a dose varying between 0.5 and 2 dpa results in an increase of DBTT of tungsten to a temperature of around 500 to 600 °C, depending on the irradiation temperature and fluence. However, the irradiation temperature in a fusion environment is higher, which can reach up to 1200 °C (surface of tungsten during the steady-state operation in ITER) or even higher during off-normal operation, as discussed in the previous section. Therefore, the research to fill the gap in knowledge of the effect of neutron irradiation on mechanical properties of commercial/advanced tungsten grades in the high temperature range is critical for the design and safety studies of plasma facing components under prolonged operational conditions [63]. The following high priority engineering mechanical properties are required: (i) stress-strain curves, preferably with the extraction of true stress after the necking (if any); (ii) fracture toughness; (iii) hardness data as important complimentary data that allows connecting the irradiation hardening with earlier works.

1.3.3. Determination of ductile to brittle transition temperature

Conventionally, the DBTT is identified by the Charpy test [64]. It has a simple test set-up, which consists of a hammer and a specimen platform. During the test, the hammer will be dropped from a certain height and breaks the Charpy single notched specimen. The tests are performed at a range of temperatures close to DBTT, and the modulus of toughness of the specimen, which is the energy absorbed by the specimen during the impact of the hammer, is recorded at various temperatures. The DBTT can then be identified from the increase of modulus of toughness in a certain temperature range.

Besides the Charpy test, the DBTT range can also be determined by the Master Curve approach, which presents the variation of the fracture toughness over a certain temperature range, as illustrated in **Figure 1.5** [65]. The weakest link theory and Weibull statistics are the foundation of the Master Curve approach, which is presented in the ASTM standard 1921 [66, 67]. The Master Curve approach in the standard has a fixed shape and a constant Weibull modulus of 4. Moreover, the definition of the transition temperature (T_0), which can be considered as DBTT, is the temperature at which the fracture toughness reaches 100 $\mathrm{MPa}\sqrt{\mathrm{m}}$ for 25 mm thick steel specimen. Different from ferritic/martensitic steel, tungsten has a lower fracture toughness in the lower shelf [65, 68-74] and in the transition temperature region. In addition, the fracture strength distribution varies for some brittle materials, which the Weibull distribution cannot describe perfectly [75-79]. Weibull statistics also require a sufficient number of specimens to perform the test in order to get the Weibull modulus [80], which is a shape parameter of the probability density function. However, the number of specimens, which can be exposed to neutron irradiation, is usually limited by the cost and precious space in the reactor (which is usually a multi-purpose facility and therefore competing commercial programs such as isotope production are always present). A common method to counter the limitation on the number of available test specimens, which is also implemented by the ASTM standard, is to take the Weibull modulus as constant based on sound assumptions. But this method can only be implemented to materials with a narrow transition temperature range since the Weibull modulus is a function of temperature [81]. Therefore, the application of other distribution functions, i.e., normal distribution, instead of the Weibull distribution, will be more appropriate for brittle materials [75, 77].

Other mechanical test methods can also identify DBTT besides the above-discussed master curve approach. A method to determine the DBTT by three-

point bending test, executed on a flat bar specimen without a notch, have been reported by Lawrence Livermore national laboratory [82]. Instead of fracture toughness, they determined the DBTT based on the flexural strain and defined the DBTT as the temperature, where the flexural strain reaches 5%. Other researchers have implemented this approach for tungsten-based materials [83, 84].

As mentioned already, neutron irradiation experiments impose high cost and time-consuming operation in hot cells. Thus, alternative options like ion irradiation [85-87] and/or small specimen testing techniques (SSTT) [88, 89] are proposed. The validity of small specimen testing procedures can significantly reduce the cost and time required for the mechanical characterization. The SSTT developed for neutron irradiation can also benefit ion irradiation experiments since the depth of ion irradiation damage is within the micrometer range. Therefore, SSTT will be a crucial task to accelerate the development of neutron resistant materials for the applications in ITER/DEMO PFCs.

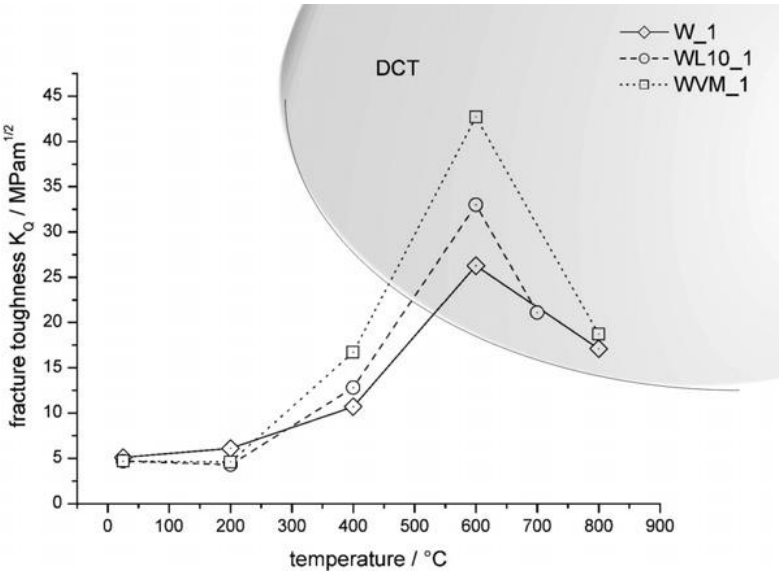

Figure 1.5. Fracture toughness of disk-shaped compact tension (DCT) specimens of as-sintered tungsten alloys in the DBTT region. The grey area indicates the region where linear elastic fracture mechanics (LEFM) is no longer valid since plastic deformation is observed [65].

1.4. Objectives and expected Impact

Following the concise literature summary presented above, this thesis aims to address the following scientific and engineering problems/questions related to the assessment of mechanical properties and irradiation effects on the mechanical properties of baseline ITER tungsten grades and advanced tungsten grades:

1. Investigation of the tensile mechanical properties of a series of advanced W-based alloys before neutron irradiation. Analysis of the fracture mechanism by investigating the fracture surface. Determination of the DBTT of these alloys compared to baseline ITER specification pure tungsten.
2. Execution of irradiation campaigns on a series of baseline and advanced tungsten alloys to explore the effect of neutron irradiation at medium and high temperature on the mechanical properties using conventional destructive and non-destructive tests. The ultimate goal of those tests is the estimation of the DBTT shift after neutron irradiation.
3. Implementation of the miniaturization testing and validation of its applicability for the samples exposed to neutron irradiation.

The realization of the above listed objectives will help to advance the current state of the art and to assess the following important aspects related to the materials for PFC for the nuclear phase of operation:

1. Various methods have been applied to tungsten alloys for improving its low temperature mechanical properties. Comparative analysis of microstructure, DBTT, and tensile properties of advanced tungsten alloys will help to identify the possible parameters that are crucial for DBTT reduction before and after neutron irradiation.
2. During steady state operation, the divertor faces high heat flux and fast neutron irradiation, which results in irradiation degradation at high temperature. Therefore, new data on neutron irradiation effects on mechanical properties of tungsten alloys, especially after irradiation at high temperature, will be established in order to assist the structural and nuclear safety analysis.
3. Mechanical tests applied to neutron irradiated materials are time-consuming and expensive. In order to reduce the cost and to improve reactor space usage, small specimen testing techniques (SSTT) are

essential. Furthermore, the improvement of the testing method to provide sufficient information for a valid conclusion is required to compensate for the limited number of test specimens. Given that up to now, the SST is mostly focused on steels, the contribution to the development SSTT for tungsten is important for the assessment of neutron irradiation effects on future fusion neutron sources such IFMIF and DONES.

1.5. References

[1] Y. Someya, K. Tobita, R. Hiwatari, Y. Sakamoto, J.S.D.T. for Fusion, Fusion DEMO reactor design based on nuclear analysis, Fusion Eng Des 136 (2018) 1306-1312.
[2] M. Keilhacker, A. Gibson, C. Gormezano, P. Lomas, P. Thomas, M. Watkins, P. Andrew, B. Balet, D. Borba, C. Challis, High fusion performance from deuterium-tritium plasmas in JET, Nuclear Fusion 39(2) (1999) 209.
[3] K. McGuire, H. Adler, P. Alling, C. Ancher, H. Anderson, J. Anderson, J. Anderson, V. Arunasalam, G. Ascione, D. Ashcroft, Review of deuterium–tritium results from the Tokamak Fusion Test Reactor, Physics of Plasmas 2(6) (1995) 2176-2188.
[4] M. Shimada, D. Campbell, V. Mukhovatov, M. Fujiwara, N. Kirneva, K. Lackner, M. Nagami, V. Pustovitov, N. Uckan, J. Wesley, Progress in the ITER physics basis-Chapter 1: overview and summary, Nuclear Fusion 47 (2007) S1-S17.
[5] L. Giancarli, M. Abdou, D. Campbell, V. Chuyanov, M. Ahn, M. Enoeda, C. Pan, Y. Poitevin, E.R. Kumar, I. Ricapito, Overview of the ITER TBM Program, Fusion Eng Des 87(5-6) (2012) 395-402.
[6] G. Federici, R. Kemp, D. Ward, C. Bachmann, T. Franke, S. Gonzalez, C. Lowry, M. Gadomska, J. Harman, B. Meszaros, Overview of EU DEMO design and R&D activities, Fusion Eng Des 89(7-8) (2014) 882-889.
[7] G. Zhuang, G. Li, J. Li, Y. Wan, Y. Liu, X. Wang, Y. Song, V. Chan, Q. Yang, B. Wan, Progress of the CFETR design, Nuclear Fusion 59(11) (2019) 112010.
[8] K. Kim, K. Im, H. Kim, S. Oh, J. Park, S. Kwon, Y. Lee, J. Yeom, C. Lee, G. Lee, Design concept of K-DEMO for near-term implementation, Nuclear Fusion 55(5) (2015) 053027.
[9] K. Tobita, R. Hiwatari, Y. Sakamoto, Y. Someya, N. Asakura, H. Utoh, Y. Miyoshi, S. Tokunaga, Y. Homma, S. Kakudate, Japan's efforts to develop the concept of JA DEMO during the past decade, Fusion Science and Technology 75(5) (2019) 372-383.
[10] R. Srinivasan, S. Deshpande, Strategy for the Indian DEMO design, Fusion Eng Des 83(7-9) (2008) 889-892.
[11] B. Kolbasov, V. Belyakov, E. Bondarchuk, A. Borisov, I. Kirillov, V. Leonov, G. Shatalov, Y.A. Sokolov, Y.S. Strebkov, N. Vasiliev, Russian concept for a DEMO-S demonstration fusion power reactor, Fusion Eng Des 83(7-9) (2008) 870-876.
[12] R. Pitts, S. Bardin, B. Bazylev, M. van den Berg, P. Bunting, S. Carpentier-Chouchana, J. Coenen, Y. Corre, R. Dejarnac, F. Escourbiac, Physics conclusions in support of ITER W divertor monoblock shaping, Nuclear Materials and Energy 12 (2017) 60-74.

[13] G. Federici, W. Biel, M. Gilbert, R. Kemp, N. Taylor, R. Wenninger, European DEMO design strategy and consequences for materials, Nuclear Fusion 57(9) (2017) 092002.
[14] S. Panayotis, T. Hirai, V. Barabash, C. Amzallag, F. Escourbiac, A. Durocher, V. Komarov, J. Martinez, M. Merola, Fracture modes of ITER tungsten divertor monoblock under stationary thermal loads, Fusion Eng Des 125 (2017) 256-262.
[15] A. Loarte, G. Saibene, R. Sartori, D. Campbell, M. Becoulet, L. Horton, T. Eich, A. Herrmann, G. Matthews, N. Asakura, Characteristics of type I ELM energy and particle losses in existing devices and their extrapolation to ITER, Plasma Physics and Controlled Fusion 45(9) (2003) 1549.
[16] A.W. Leonard, Edge-localized-modes in tokamaks, Physics of Plasmas 21(9) (2014) 090501.
[17] K. Wittlich, T. Hirai, J. Compan, N. Klimov, J. Linke, A. Loarte, M. Merola, G. Pintsuk, V. Podkovyrov, L. Singheiser, Damage structure in divertor armor materials exposed to multiple ITER relevant ELM loads, Fusion Eng Des 84(7-11) (2009) 1982-1986.
[18] J. You, E. Visca, T. Barrett, B. Böswirth, F. Crescenzi, F. Domptail, M. Fursdon, F. Gallay, B. Ghidersa, H. Greuner, European divertor target concepts for DEMO: Design rationales and high heat flux performance, Nuclear Materials and Energy 16 (2018) 1-11.
[19] T.R. Barrett, G. Ellwood, G. Pérez, M. Kovari, M. Fursdon, F. Domptail, S. Kirk, S. McIntosh, S. Roberts, S. Zheng, Progress in the engineering design and assessment of the European DEMO first wall and divertor plasma facing components, Fusion Eng. Des. 109-111 (2016) 917-924.
[20] R. Pitts, X. Bonnin, F. Escourbiac, H. Frerichs, J. Gunn, T. Hirai, A. Kukushkin, E. Kaveeva, M. Miller, D. Moulton, Physics basis for the first ITER tungsten divertor, Nuclear Materials and Energy 20 (2019) 1-25.
[21] K. Tsuchida, T. Miyazawa, A. Hasegawa, S. Nogami, M. Fukuda, Recrystallization behavior of hot-rolled pure tungsten and its alloy plates during high-temperature annealing, Nuclear Materials and Energy 15 (2018) 158-163.
[22] G. Pintsuk, S. Antusch, T. Weingaertner, M. Wirtz, Recrystallization and composition dependent thermal fatigue response of different tungsten grades, Int. J. Refract. Met. Hard Mater. 72 (2018) 97-103.
[23] M. Li, J.-H. You, Interpretation of the deep cracking phenomenon of tungsten monoblock targets observed in high-heat-flux fatigue tests at 20 MW/m2, Fusion Eng. Des. 101 (2015) 1-8.
[24] T. Hirai, S. Panayotis, V. Barabash, C. Amzallag, F. Escourbiac, A. Durocher, M. Merola, J. Linke, T. Loewenhoff, G. Pintsuk, Use of tungsten material for the ITER divertor, Nuclear Materials and Energy 9 (2016) 616-622.

[25] C. Bonnekoh, A. Hoffmann, J. Reiser, The brittle-to-ductile transition in cold rolled tungsten: On the decrease of the brittle-to-ductile transition by 600 K to− 65 C, International Journal of Refractory Metals and Hard Materials 71 (2018) 181-189.
[26] Z.M. Xie, R. Liu, S. Miao, X.D. Yang, T. Zhang, X.P. Wang, Q.F. Fang, C.S. Liu, G.N. Luo, Y.Y. Lian, X. Liu, Extraordinary high ductility/strength of the interface designed bulk W-ZrC alloy plate at relatively low temperature, Scientific Reports 5 (2015) 1-11.
[27] H. Deng, Z. Xie, Y. Wang, R. Liu, T. Zhang, T. Hao, X. Wang, Q. Fang, C. Liu, Mechanical properties and thermal stability of pure W and W-0.5 wt% ZrC alloy manufactured with the same technology, Materials Science and Engineering: A 715 (2018) 117-125.
[28] S. Lang, Q. Yan, N. Sun, X. Zhang, L. Deng, Y. Wang, C. Ge, Microstructure, basic thermal–mechanical and Charpy impact properties of W-0.1 wt.% TiC alloy via chemical method, Journal of Alloys and Compounds 660 (2016) 184-192.
[29] M. Battabyal, R. Schäublin, P. Spätig, N. Baluc, W–2 wt.% Y2O3 composite: Microstructure and mechanical properties, Materials Science and Engineering: A 538 (2012) 53-57.
[30] Y. Chen, Y. Wu, F. Yu, J. Chen, Microstructure and mechanical properties of tungsten composites co-strengthened by dispersed TiC and La2O3 particles, International Journal of Refractory Metals and Hard Materials 26(6) (2008) 525-529.
[31] P. Lied, C. Bonnekoh, W. Pantleon, M. Stricker, A. Hoffmann, J. Reiser, Comparison of K-doped and pure cold-rolled tungsten sheets: As-rolled condition and recrystallization behaviour after isochronal annealing at different temperatures, Int. J. Refract. Met. Hard Mater. 85 (2019) 105047.
[32] M. Fukuda, S. Nogami, K. Yabuuchi, A. Hasegawa, T. Muroga, Anisotropy in the mechanical properties of potassium and rhenium doped tungsten alloy plates for fusion reactor applications, Fusion Science and Technology 68(3) (2015) 690-693.
[33] J. Coenen, Y. Mao, J. Almanstötter, A. Calvo, S. Sistla, H. Gietl, B. Jasper, J. Riesch, M. Rieth, G. Pintsuk, Advanced materials for a damage resilient divertor concept for DEMO: Powder-metallurgical tungsten-fibre reinforced tungsten, Fusion Eng Des 124 (2017) 964-968.
[34] S. Antusch, D.E. Armstrong, T.B. Britton, L. Commin, J.S.-L. Gibson, H. Greuner, J. Hoffmann, W. Knabl, G. Pintsuk, M. Rieth, Mechanical and microstructural investigations of tungsten and doped tungsten materials produced via powder injection molding, Nuclear Materials and Energy 3 (2015) 22-31.
[35] L. Romaner, C. Ambrosch-Draxl, R. Pippan, Effect of rhenium on the dislocation core structure in tungsten, Phys. Rev. Lett. 104(19) (2010) 195503.

[36] Q. Wei, H. Zhang, B. Schuster, K. Ramesh, R. Valiev, L. Kecskes, R. Dowding, L. Magness, K. Cho, Microstructure and mechanical properties of super-strong nanocrystalline tungsten processed by high-pressure torsion, Acta materialia 54(15) (2006) 4079-4089.
[37] D. Hull, D.J. Bacon, Introduction to dislocations, Butterworth-Heinemann2001.
[38] P. Gumbsch, J. Riedle, A. Hartmaier, H.F. Fischmeister, Controlling factors for the brittle-to-ductile transition in tungsten single crystals, Science 282(5392) (1998) 1293-1295.
[39] P. Gumbsch, Brittle fracture and the brittle-to-ductile transition of tungsten, J Nucl Mater 323(2-3) (2003) 304-312.
[40] X. Zeng, A. Hartmaier, Modeling size effects on fracture toughness by dislocation dynamics, Acta materialia 58(1) (2010) 301-310.
[41] L. Murr, Dislocation ledge sources: dispelling the myth of Frank–Read source importance, Metallurgical and Materials Transactions A 47(12) (2016) 5811-5826.
[42] B. Neale, An assessment of fracture toughness in the ductile to brittle transition regime using the Euro fracture toughness dataset, Engineering fracture mechanics 69(4) (2002) 497-509.
[43] X. Hu, T. Koyanagi, M. Fukuda, N.K. Kumar, L.L. Snead, B.D. Wirth, Y. Katoh, Irradiation hardening of pure tungsten exposed to neutron irradiation, J Nucl Mater 480 (2016) 235-243.
[44] A. Hasegawa, M. Fukuda, S. Nogami, K. Yabuuchi, Neutron irradiation effects on tungsten materials, Fusion Eng Des 89(7-8) (2014) 1568-1572.
[45] M.E. Sawan, Transmutation of tungsten in fusion and fission nuclear environments, Fusion Science and Technology 66(1) (2014) 272-277.
[46] M. Cui, T. Shen, L. Pang, Y. Zhu, P. Jin, C. Liu, X. Fang, Z. Wang, He ion implantation induced He bubbles and hardness in tungsten, Nuclear Materials and Energy 15 (2018) 232-236.
[47] C.-H. Huang, M.R. Gilbert, J. Marian, Simulating irradiation hardening in tungsten under fast neutron irradiation including Re production by transmutation, J Nucl Mater 499 (2018) 204-215.
[48] Q. Zhao, Z. Zhang, M. Huang, X. Ouyang, Effects of transmutation elements in tungsten, Computational Materials Science 162 (2019) 133-139.
[49] A. Hasegawa, T. Tanno, S. Nogami, M. Satou, Property change mechanism in tungsten under neutron irradiation in various reactors, J Nucl Mater 417(1-3) (2011) 491-494.
[50] A. Hasegawa, M. Fukuda, T. Tanno, S. Nogami, Neutron irradiation behavior of tungsten, Materials transactions (2013) MG201208.
[51] M. Fukuda, A. Hasegawa, T. Tanno, S. Nogami, H. Kurishita, Property change of advanced tungsten alloys due to neutron irradiation, J Nucl Mater 442(1-3) (2013) S273-S276.

[52] M. Fukuda, N.K. Kumar, T. Koyanagi, L.M. Garrison, L.L. Snead, Y. Katoh, A. Hasegawa, Neutron energy spectrum influence on irradiation hardening and microstructural development of tungsten, J Nucl Mater 479 (2016) 249-254.
[53] A. Hasegawa, M. Fukuda, K. Yabuuchi, S. Nogami, Neutron irradiation effects on the microstructural development of tungsten and tungsten alloys, J Nucl Mater 471 (2016) 175-183.
[54] Y. Katoh, L. Snead, L. Garrison, X. Hu, T. Koyanagi, C. Parish, P. Edmondson, M. Fukuda, T. Hwang, T. Tanaka, Response of unalloyed tungsten to mixed spectrum neutrons, J Nucl Mater 520 (2019) 193-207.
[55] I. Alexandrov, I.V. Gorynin, Metallovedenie 22 (1979) 35.
[56] J.M. Steichen, Tensile Properties of Neutron-Irradiated Tzm and Tungsten, J Nucl Mater 60(1) (1976) 13-19.
[57] I.V. Gorynin, V.A. Ignatov, V.V. Rybin, S.A. Fabritsiev, V.A. Kazakov, V.P. Chakin, V.A. Tsykanov, V.R. Barabash, Y.G. Prokofyev, Effects of Neutron-Irradiation on Properties of Refractory-Metals, J Nucl Mater 191 (1992) 421-425.
[58] J. Habainy, Y. Dai, Y. Lee, S. Iyengar, Mechanical properties of tungsten irradiated with high-energy protons and spallation neutrons, J. Nucl. Mater. 514 (2019) 189-195.
[59] L.M. Garrison, Y. Katoh, N.A.P. Kiran Kumar, Mechanical properties of single-crystal tungsten irradiated in a mixed spectrum fission reactor, J. Nucl. Mater. 518 (2019) 208-225.
[60] Y. Katoh, L. Snead, L. Garrison, X. Hu, T. Koyanagi, C. Parish, P. Edmondson, M. Fukuda, T. Hwang, T. Tanaka, Response of unalloyed tungsten to mixed spectrum neutrons, J Nucl Mater (2019).
[61] R. Abernethy, J.-L. Gibson, A. Giannattasio, J. Murphy, O. Wouters, S. Bradnam, L. Packer, M. Gilbert, M. Klimenkov, M. Rieth, Effects of neutron irradiation on the brittle to ductile transition in single crystal tungsten, J Nucl Mater 527 (2019) 151799.
[62] T. Miyazawa, L.M. Garrison, J.W. Geringer, M. Fukuda, Y. Katoh, T. Hinoki, A. Hasegawa, Neutron irradiation effects on the mechanical properties of powder metallurgical processed tungsten alloys, J Nucl Mater 529 (2020) 151910.
[63] M.Y. Li, J.H. You, Interpretation of the deep cracking phenomenon of tungsten monoblock targets observed in high-heat-flux fatigue tests at 20 MW/m^2, Fusion Eng Des 101 (2015) 1-8.
[64] ASTM, Standard test methods for notched bar impact testing of metallic materials, E23-07a, ASTM international, Pennsylvania, PA, USA, 2007.
[65] M. Faleschini, H. Kreuzer, D. Kiener, R. Pippan, Fracture toughness investigations of tungsten alloys and SPD tungsten alloys, J Nucl Mater 367 (2007) 800-805.

[66] F.W. Zok, On weakest link theory and Weibull statistics, Journal of the American Ceramic Society 100(4) (2017) 1265-1268.
[67] ASTM, Standard test method for determination of reference temperature, T0, for ferritic steels in the transition range, E1921-16, ASTM international, Pennsylvania, PA, USA, 2016.
[68] R. Margevicius, J. Riedle, P. Gumbsch, Fracture toughness of polycrystalline tungsten under mode I and mixed mode I/II loading, Materials Science & Engineering: A 270(2) (1999) 197-209.
[69] D. Rupp, S.M. Weygand, Experimental investigation of the fracture toughness of polycrystalline tungsten in the brittle and semi-brittle regime, J Nucl Mater 386-88 (2009) 591-593.
[70] D. Rupp, S. Weygand, Anisotropic fracture behaviour and brittle-to-ductile transition of polycrystalline tungsten, Philosophical Magazine 90(30) (2010) 4055-4069.
[71] E. Gaganidze, D. Rupp, J. Aktaa, Fracture behaviour of polycrystalline tungsten, J Nucl Mater 446(1-3) (2014) 240-245.
[72] B. Gludovatz, S. Wurster, A. Hoffmann, R. Pippan, Fracture toughness of polycrystalline tungsten alloys, Int J Refract Met H 28(6) (2010) 674-678.
[73] S. Wurster, B. Gludovatz, R. Pippan, High temperature fracture experiments on tungsten-rhenium alloys, Int J Refract Met H 28(6) (2010) 692-697.
[74] J. Ast, M. Göken, K. Durst, Size-dependent fracture toughness of tungsten, Acta Materialia 138 (2017) 198-211.
[75] C. Lu, R. Danzer, F.D. Fischer, Fracture statistics of brittle materials: Weibull or normal distribution, Physical Review E 65(6) (2002) 067102.
[76] R. Danzer, P. Supancic, J. Pascual, T. Lube, Fracture statistics of ceramics–Weibull statistics and deviations from Weibull statistics, Engineering Fracture Mechanics 74(18) (2007) 2919-2932.
[77] R. Doremus, Fracture statistics: A comparison of the normal, Weibull, and Type I extreme value distributions, Journal of applied physics 54(1) (1983) 193-198.
[78] Z. Bertalan, A. Shekhawat, J.P. Sethna, S. Zapperi, Fracture strength: Stress concentration, extreme value statistics, and the fate of the Weibull distribution, Physical Review Applied 2(3) (2014) 034008.
[79] Z. Baant, Y. Xi, S. Reid, Statistical size effect in quasi-brittle structures: I. Is Weibull theory applicable?, Journal of Engineering Mechanics ASCE 117 (1991) 2609-2622.
[80] D. Wu, Y. Li, J. Zhang, L. Chang, D. Wu, Z. Fang, Y. Shi, Effects of the number of testing specimens and the estimation methods on the Weibull parameters of solid catalysts, Chemical engineering science 56(24) (2001) 7035-7044.

[81] C. Seal, A. Sherry, Weibull distribution of brittle failures in the transition region, Procedia Structural Integrity 2 (2016) 1668-1675.
[82] D.H. Lassila, F. Magness, D. Freeman, Ductile-Brittle Transition Temperature testing of tungsten using the three-point bend test, Lawrence Livermore National Lab., CA (United States), 1991.
[83] Z.M. Xie, R. Liu, S. Miao, X.D. Yang, T. Zhang, X.P. Wang, Q.F. Fang, C.S. Liu, G.N. Luo, Y.Y. Lian, X. Liu, Extraordinary high ductility/strength of the interface designed bulk W-ZrC alloy plate at relatively low temperature, Sci Rep-Uk 5 (2015).
[84] V. Krsjak, S. Wei, S. Antusch, Y. Dai, Mechanical properties of tungsten in the transition temperature range, J Nucl Mater 450(1-3) (2014) 81-87.
[85] F. F., Y. X., K. Arakawa, S.P. Fitzgerald, P.D. Edmonds, S.G. Roberts, High temperature annealing of ion irradiated tungsten, Acta Materialia 90 (2015) 380-393.
[86] J. Gibson, D. Armstrong, S. Roberts, The micro-mechanical properties of ion irradiated tungsten, Phys Scripta T159 (2014).
[87] D.E.J. Armstrong, X. Yi, E.A. Marquis, S.G. Roberts, Hardening of self ion implanted tungsten and tungsten 5-wt% rhenium, J Nucl Mater 432(1-3) (2013) 428-436.
[88] B.J. Kim, R. Kasada, A. Kimura, H. Tanigawa, Evaluation of grain boundary embrittlement of phosphorus added F82H steel by SSTT, J Nucl Mater 421(1-3) (2012) 153-159.
[89] N. Igata, K. Miyahara, C. Tada, D. Blasl, G. Lucas, Phenomenological Studies of the Effects of Miniaturization and Irradiation on the Mechanical-Properties of Stainless-Steels, Radiat Eff Defect S 101(1-4) (1987) 131-146.

Chapter 2
Overview of experimental methodology

2.1. Materials

Twelve different types of tungsten grades are investigated in this thesis:

- **Four commercial ITER grade pure tungsten:**

  These tungsten grades are ITER specification Plansee (IGP), 1600°C/one-hour recrystallized IGP (W-RX), ITER specification A.L.M.T. (IGA), and ITER specification AT&M (ATW). IGP, IGA, and ATW are produced by Plansee, Austria, A.L.M.T, Japan, and AT&M, China, respectively. The tensile specimens of IGP and ATW are cut from a rod with a 35 mm x 35 mm cross section and a 13 mm thick plate by electrical discharge machining (EDM) in the Belgian nuclear research centre (SCK CEN), respectively. W-RX samples are cut from the IGP product and annealed at Forschungszentrum Jülich (FZJ), Germany. FZJ also supplies the tensile and disk specimens of IGA and disk specimens of IGP.

- **Two pure tungsten grades:**

  The specimens of fine grain tungsten (FG) produced by spark plasma sintering (SPS) are provided by the Institute of Plasma Physics (IPP), Czech Republic. And the single crystal tungsten (W(100)) is produced by MaTeck (Germany) in the form of a cylindrical rod with an axial direction of <100>.

- **Three potassium doped tungsten alloys:**

  They are potassium doped pure tungsten (ALK), potassium doped tungsten alloyed with 3 wt% of rhenium (ALKR), and heavily deformed potassium doped pure tungsten (HDK). ALK and ALKR are manufactured by A.L.M.T., and their specimens are provided by Tohoku University. The specimens of HDK are cut from a 1 mm thick heavily rolled plate, as developed and provided by Karlsruhe Institute of Technology (KIT), Germany.

- **Three particle reinforced tungsten grades:**

  They are reinforced with 1 wt% TiC (W1TiC), 2 wt% Y_2O_3 (W2YO), and 0.5 wt% ZrC (W0.5ZrC). W1TiC and W2YO are produced with powder

injection molding (PIM), and their specimens are provided by Karlsruhe Institute of Technology, Germany. The Institute of Solid State Physics, China provides the raw material of W0.5ZrC, which is rolled into an 8 mm thick plate and treated with thermo mechanical treatment (TMT). The specimens of W0.5ZrC are manufactured by EDM cutting in SCK CEN.

The inverse pole figure maps of polycrystalline tungsten grades are shown in **Figure 2.1**. And their composition, grain properties, and manufacturing process are summarized in **Table 2.1**. The methodology for microstructural analysis is discussed in **Chapter 2.3**. The strengthening particle size of W1TiC, W2YO, and W0.5ZrC are shown in **Table 2.2**. The particle identification and analysis procedure for the particle can be found in **Chapter 8.1**. The equivalent median diameter (D50), equivalent 10% diameter (D10), and equivalent 90% diameter (D90) of grains or particles indicate that there are 50%, 10%, and 90% (in area fraction) of the grains or particles smaller than this diameter, respectively.

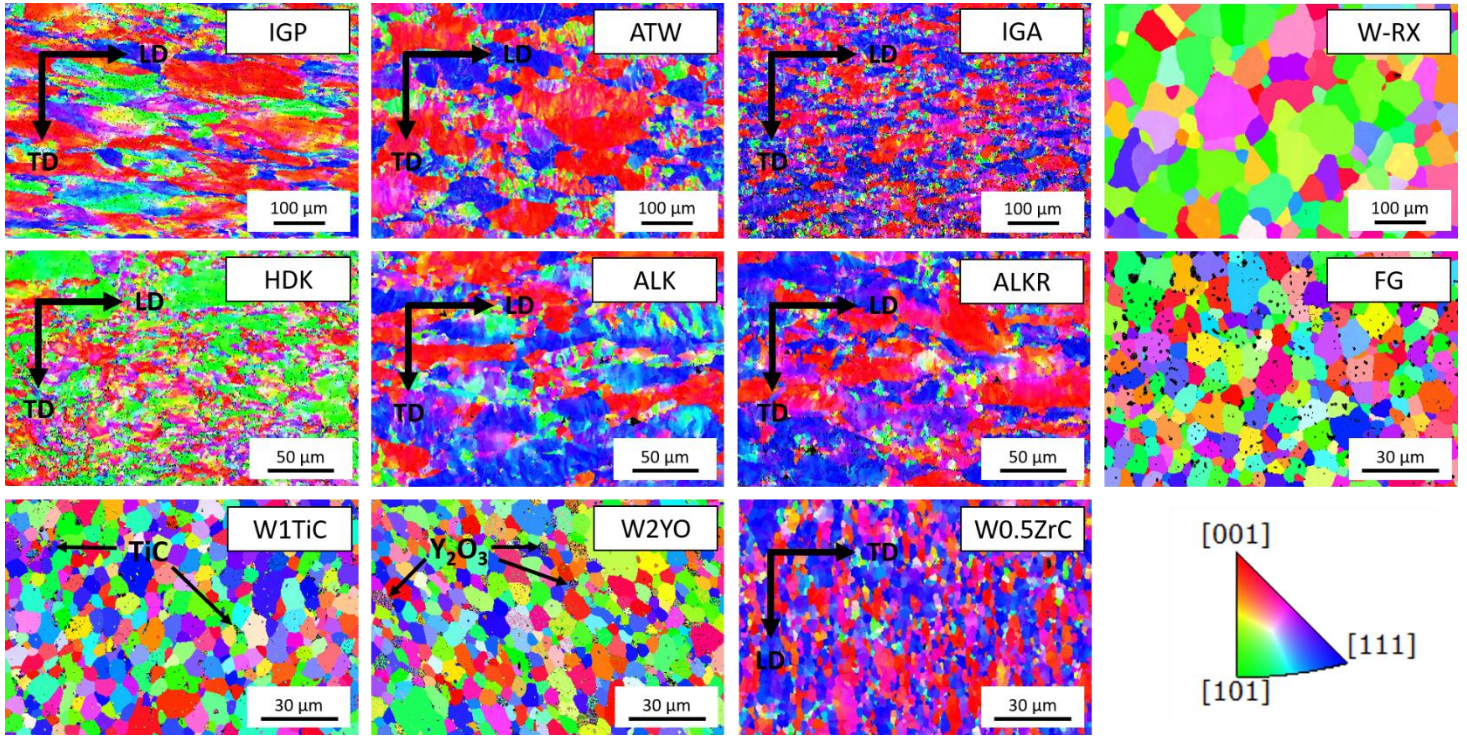
IGP
LD
TD
100 µm
ATW
LD
TD
100 µm
IGA
LD
TD
100 µm
W-RX
100 µm
HDK
LD
TD
50 µm
ALK
LD
TD
50 µm
ALKR
LD
TD
50 µm
FG
30 µm
W1TiC
TiC
30 µm
W2YO
Y_2O_3
30 µm
W0.5ZrC
TD
LD
30 µm
[001]
[111]
[101]

Figure 2.1. Inverse pole figure maps of polycrystalline tungsten grades

Table 2.1. Composition, grain shape morphology, and manufacturing process of tungsten products. (The composition is provided by the manufacturer)

Materials	Composition (by weight)	Grain size (μm)			Grain shape	Manufacturing process
		D10	D50	D90		
IGP	Pure W	15.7	87.4	151.5	Carrot-like	Double hammering
IGA	Pure W	5.9	19.5	41.0	Pancake-like	Rolling
ATW	Pure W	21.2	60.3	139.7	Pancake-like	Rolling
W-RX	Pure W	31.7	60.4	108.4	Equiaxial	IGP annealed 1600 ^{o}C/1 hr
FG	Pure W	4.7	9.4	15.6	Equiaxial	SPS
HDK	W + 60 ppm K	3.5	26.5	111.1	Pancake-like	Heavily deformed (Rolling)
ALK	W + 30 ppm K	7.8	37.0	108.9	Pancake-like	Rolling
ALKR	W + 3% Re + 28 ppm K	7.0	32.7	60.8	Pancake-like	Rolling
W1TiC	W + 1% TiC	4.0	7.8	12.1	Equiaxial	PIM
W2YO	W + 2% Y_2O_3	4.1	7.3	11.8	Equiaxial	PIM
W0.5ZrC	W + 0.5% ZrC	2.6	6.7	14.2	Pancake-like	Rolling + TMT

Table 2.2. Size of strengthening particles

Materials	Particle	Particle size (μm)		
		D10	D50	D90
W1TiC	Ti rich	0.42	0.92	1.60
W2YO	Y rich	0.63	1.15	1.98
W0.5ZrC	Zr rich	0.20	0.42	0.83

2.2. Mechanical test

2.2.1. Tensile test (Chapter 3 and 6)

Uniaxial tensile tests were performed on small dog-bone shaped specimens, as shown in **Figure 2.2**. The overall length of the specimens is 16 mm with a gauge length of 5.2 mm and an effective cross section of 2.4 mm2 (1.6 mm x 1.5 mm) or 2.88 mm2 (1.6 mm x 1.8 mm). The gauge length to width ratio of was 3.25, which is close to the ASTM standard value (being 4). The thickness of the specimen will not influence the mechanical properties if the grain size is smaller than ≈1/10 of the specimen thickness such that each cross-section slab is being a representative volume element [1, 2]. According to the EBSD analysis, all selected products in this thesis have a grain size smaller than 100 µm. Thus, the cross-section contains at least hundreds of grains making the response of the material to be representative. Moreover, for the IGP product, it has been confirmed by the tensile tests that the mechanical response is equivalent (within the error of the measurement) for both 2.4 and 2.88 mm^2 cross-section, within the bounds of the test temperatures. In addition, according to the work by Zhao, et al. [3], the effect of thickness on R.A.% is negligible when the thickness of specimen is larger than 1 mm.

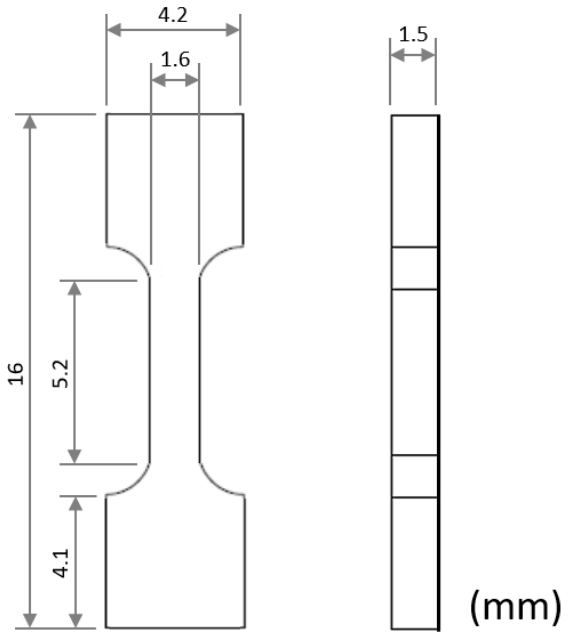

Figure 2.2. Sketch of small dog-bone shaped specimens

Given that the commercial products are characterized by a certain texture, two sets of samples with longitudinal (L) and transverse (T) orientation were investigated for IGP, ATW, IGA, and W0.5ZrC, as shown schematically in **Figure 2.3**. For all the studied materials, the samples were cut by electric discharge machine using the wire of 20-50 µm and no special treatment was applied to the surface.

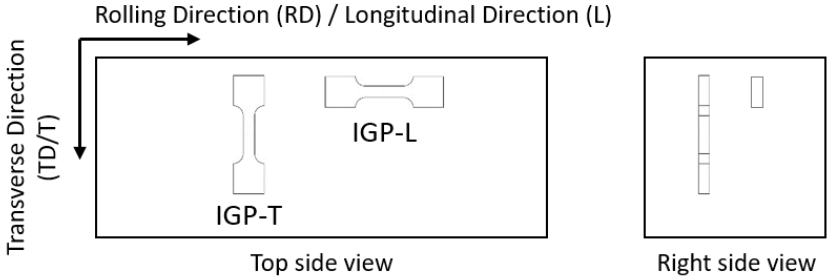

Figure 2.3. The studied sample orientations for tensile specimens. The IGP material is taken as an example.

The tests were conducted within the temperature range from 150 to 600 °C to comply with the critical need to clarify the onset of ductility in W for the water-cooled design of DEMO Diverter. The tests were performed using a 100 kN load cell. To ensure the correct alignment of the specimen, a preloading force equal to 100 N or 200 N was applied. The selection of preloading force was determined on the basis of the yield strength of the studied materials: the higher the yield strength the higher preloading force is. The tests were performed at a constant displacement rate of 0.2 mm/min, corresponding to the strain rate of 6.41×10^{-4} s^{-1}. In order to reduce the uncertainty of the cross-head displacement, the employed test bench was calibrated and qualified according to the industrial ASTM standard prior to start the measurements. The precis true strain will not be discussed in this work because small size testing techniques (SSTT) requires advanced methodology to measure strain (or even its distribution in the gauge section) [3, 4].

The load is measured by the strain gauge load cell and the displacement is measured by the actuator, which corresponds to the displacement of the crosshead. In order to compensate the machine compliance contribution to the total displacement, the elastic displacement component of each data

point from the raw data (u_{tot}) is replaced by the value calculated using the elastic modulus E taken from the literature [5, 6] for pure tungsten and Fe-Cr alloy; and for the particle reinforced tungsten, E was calculated based on Halpin-Tsai equation, which describes the change of elastic modulus after introducing additional particles into matrix [7]. The equation to account for machine compliance is described as,

$$u = u_{tot} - \frac{F}{K} + \frac{F \cdot L}{E \cdot S} \quad \textbf{(2.1)}$$

where u is the displacement of the test specimen associated with the gauge length L, F is the load, K is the elastic slope of the raw load-total displacement curve, and S is the area of cross section in the gauge zone. The data corrected for machine compliance are used for the calculation of engineering stress – engineering strain curve and true stress – true strain response of the standard tensile tests.

The notation of utilized mechanical property measurements can be described as follows. The yield strength (YS) is measured at 0.2% of plastic deformation followed after the linear elastic deformation. The ultimate tensile strength (UTS) is the highest engineering stress measured, and the sample elongation at UTS point is defined as the uniform elongation. Fracture strength (Fstrength) is the true stress at the point of the fracture. Fracture strain (Fstrain) is the true strain at the point of the fracture, which is determined by the cross-area of the gauge before test and the smallest cross-area of gauge of the fractured sample.

2.2.2. Fracture toughness test (Chapter 4 and 7)

The disk-shaped compact tension (DCT) specimens are machined with T-L orientation according to the ASTM E399 [8], as shown in **Figure 2.4**. The DCT specimens were cut by electrical discharge machining (EDM) from the block materials (IGP was provided as rod with a 35 mm side square cross-section, ATW as a 13 mm thick plate). The dimension ratio of the DCT specimens follows the ASTM standard. However, fatigue pre-cracking is not performed on the DCT specimens. Instead of fatigue pre-crack, an EDM cut notch with root radius around 50 to 90 µm is introduced into each DCT specimen. The sketch of the DCT specimen and the dimensions of the specimen are shown in **Figure 2.4** and **Table 2.3**.

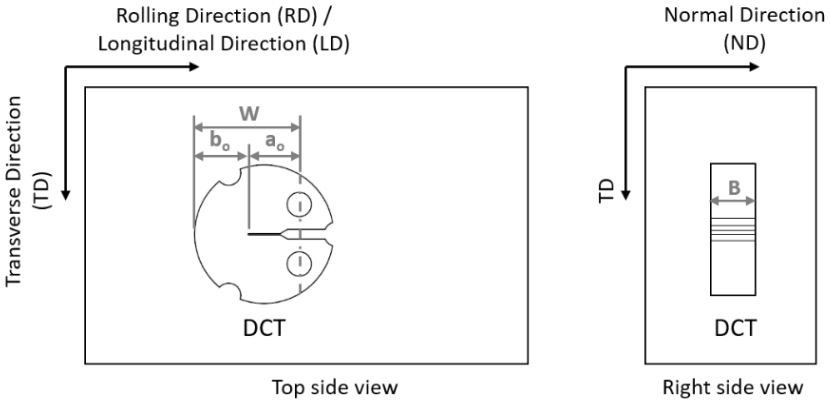

Figure 2.4. Cutting scheme showing how test samples were fabricated given the longitudinal direction of the W products. The samples were cut by electric discharge machining.

Table 2.3. Dimensions of DCT specimen

	W	a_o	b_o	B
Dimension	~8.5 mm	~4.2 mm	~4.3 mm	~4 mm

The fracture toughness is calculated according to ASTM E1921 [9] and referring to ASTM E1820 [10]. The determination of fracture toughness in ASTM E1921 [9] is different from the one in ASTM E399 [8] where the later considers a linear elastic behavior only. As a result, the fracture toughness value determined in ASTM E399 [8] is lower than the one determined in ASTM E1921 [9] when a specimen shows a non-linear load displacement response. The stress intensity factor rate during the elastic region is 0.43 ± 0.08 $\mathrm{MPa}\sqrt{\mathrm{m}}/s$. The qualification of the fracture toughness K_{Jc} is based on the ASTM E1820 J_c criterion [10]: K_{Jc} can be defined if B and $b_o \geq 100 J_{Qc}/\sigma_Y$, where J_{Qc} is the J-integral value without qualification and $\sigma_Y = (\sigma_{TS} + \sigma_{YS})/2$, where σ_{TS} is the ultimate tensile strength and σ_{YS} is the 0.2% offset yield strength. The fracture toughness K_{Jc} that does not meet the J_c criterion will be replaced by the highest K_{Jc} value at the same temperature that meets the criterion. This procedure is adopted from the ASTM E1921 [9] in order to determine the K_{Jc}– temperature curve within the transition temperature range rather than to find the upper shelf fracture toughness. **Equation 2.2** is used for the determination of the fracture toughness K_{Jc}:

$$K_{Jc} = \sqrt{J_c \frac{E}{1-\nu^2}} \ , \tag{2.2}$$

where $J_c = J_e + J_p$, with J_e the elastic part of the J-integral, which can be deduced from **equation 2.3** and J_p the plastic part of J-integral and can be calculated using **equation 2.4**. J_e is expressed as

$$J_e = \frac{(1-\nu^2)K_e^2}{E} \ , \tag{2.3}$$

in which ν is the Poisson ratio, *E* is the elastic modulus, and K_e is the linear elastic fracture toughness defined as the linear elastic equivalent stress intensity factor when the force equal to the fracture load *P*, as shown in **Figure 2.5**. In the other hand, J_p is expressed as

$$J_p = \frac{\eta A_p}{B b_o} \ , \tag{2.4}$$

where A_p is the work of plastic deformation, as shown in **Figure 2.4**, $B \times b_o$ is the cross section of the ligament, and the parameter η is equal to $2 + 0.522\frac{b_o}{W}$.

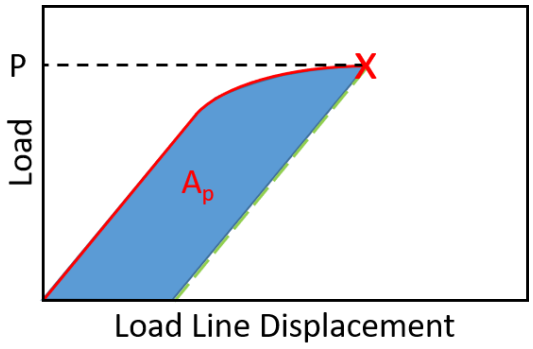

Figure 2.5. Schematics of the mechanical load vs. load line displacement curve; *P* is the load when cleavage or any unstable cracking occur.

2.2.3. Three-point bending test (Chapter 4 and 5)

Miniaturized bending specimens are implemented with the three-point bending test configuration. The specimens are manufactured by electrical discharge machining (EDM) from the block materials. The length of each specimen is 12 mm, and both of its width and height are equal to 1 mm. As

shown in **Figure 2.6a**, two orientations are investigated in this study: T-L and L-T, as defined in the ASTM standard E399: the long dimensions of the T-L specimen and L-T specimen are parallel to the TD and LD directions, respectively. The three-point bending tests are performed on a universal testing machine equipped with a furnace in air. And the test temperature is ranging from -196 °C to 600 °C. Moreover, the load and displacement are measured with a strain gauge based load cell and an position encoder for the actuator, respectively. The test is performed at a constant displacement rate with a cross-head speed of 0.723 mm/min equivalent to the (flexural) strain rate of 10^{-3} s^{-1} along the tension side of the specimen. The design of the test set-up follows the ASTM standard E290 [11] where the three pins for testing have a diameter of 2.5 mm, and the span of the lower pins is equal to 8.5 mm. The scheme of the test set-up with specimen orientation is shown in **Figure 2.6b** where the X-direction is TD and Y-direction is LD for T-L specimens, and vice versa for the L-T specimens.

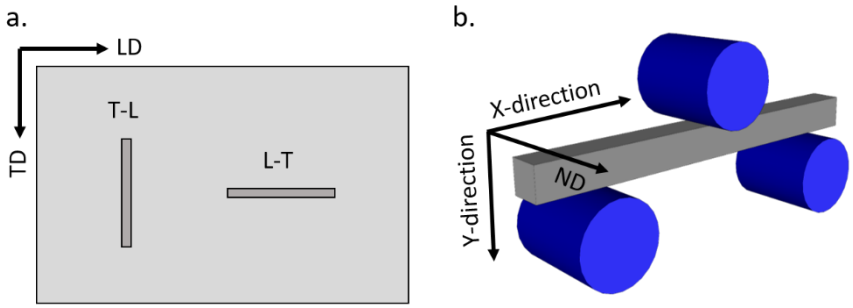

Figure 2.6. (a) Specimen orientation; (b) Test set-up of the three-point bending test.

The flexural strain (FS) is determined as,

$$FS\% = \frac{6Dd}{L^2}, \tag{2.5}$$

where D is the maximum deflection of the specimen, d is the thickness, and L is the span of the lower pins.

2.2.4. Microindentation (Chapter 8 and 9)

The specimens for micro-hardness tests are disks with ~12 mm in diameter and 0.5 mm in thickness. The final surface for indentation is polished with P2000 SiC paper or higher grades. The micro-hardness test is performed by

Vickers indentation under a force of 200 gf at room temperature. Both the time to reach the maximum force and the hold time are equal to 10 seconds. ASTM standard E384 is referred for the calculation of Vickers hardness (HV, measured in GPa). In order to generate the statistically reliable data, up to nine indents are applied to each studied specimen in different areas around the center of the disk. The hardness tests are performed on the plane orthogonal to the normal direction (ND) for W0.5ZrC and on the plane orthogonal to the longitudinal direction (LD) for IGP and IGA. Such a choice is made because the plane of IGP and IGA (orthogonal to LD) will correspond to the side of the plasma facing unit facing the plasma beam in the Tokamak. This orientation is chosen to prevent the flaking (due to crack deflection) and the detachment of some tungsten grains into the plasma, which can contaminate the plasma. Differently from IGP and IGA, the preferential plasma facing plane for W0.5ZrC has not been selected yet. Moreover, the grain size of W0.5ZrC is much smaller than that of the two commercial tungsten grades, and thus the anisotropy of hardness (depending on the indented plane) is much smaller. Therefore, the plane orthogonal to ND is selected for W0.5ZrC to perform the hardness test in this work since manufacturing the samples is easier for this orientation.

2.2.5. Post-irradiation examination (Chapter 6 to 9)

For radiation protection purpose, the researchers should not physically contact the irradiated specimens. The PIE can only be performed in a protective facility designed for radioactive materials, which calls “Hot Cell”. A hot cell is constructed with thick lead plates and concrete walls, which isolate the irradiated specimens and thus protect the workers from the irradiation. Each hot cell has at least one protective lead window so that researchers can observe the irradiated specimens during operation. The irradiated specimens cannot be tested right after neutron irradiation because of its high radioactivity. Before performing PIE, the irradiated specimens are stored in the special storage facility of Belgian Material Test Reactor (BR2) to cool-down (in terms of radioactivity) for a few months. As the activity reduces to an acceptable level for transportation, the specimens are transported by a lead shielded capsule to the hot cell facility for mechanical tests and microstructural analysis. The universal testing machine, hardness testing platform, and scanning electron microscope for PIE are also located in the hot cells. Therefore, the experiments can only be remotely performed by remote manipulators (two robotic arms) and controlling panel.

2.3. Scanning Electron Microscopy

Scanning electron microscopy (SEM) is implemented to investigate the microstructure of the tested materials. The principle of SEM is using the electromagnetic field to accelerate, control, and focus electron beam to scan the surface of the specimen. After interacting with the primary electron beam, the material in a certain interaction volume emits various types of electrons and signals for detection, such as auger electrons, secondary electrons (SE), backscattered electrons (BSE), X-rays. With the proper use of these signals, the microstructure, including chemical composition and crystallography, of the material can be characterized. One of the most used signals is SE. The SE efficiency depends on the relative distance and angle of the scanning spot and detector. Thus, it is widely implemented for topography analysis, like fracture surface analysis in this thesis. Besides topography analysis based on SE, the qualitative analysis of the composition distribution can be achieved by the BSE since the BSE is sensitive to the atomic number of the element. Other techniques that are implemented in this thesis will be discussed in the following section.

2.3.1. Electron backscattered diffraction

Electron backscattered diffraction (EBSD) is a kind of technique for crystallographic analysis. A typical set-up is illustrated in **Figure 2.7a**, where the sample is titled to 70°, and the diffraction of the electron creates a Kikuchi pattern (**Figure 2.7b**), which is recorded by the phosphor in front of the specimen. The diffraction condition for a given Bragg angle θ is described by Bragg's Law, as shown in **equation 2.6**.

$$n\lambda = 2d\,sin\,\theta, \tag{2.6}$$

where n is an integer, λ is the wavelength of the primary beam, and d is the distance between two parallel atomic-scale crystal lattice planes.

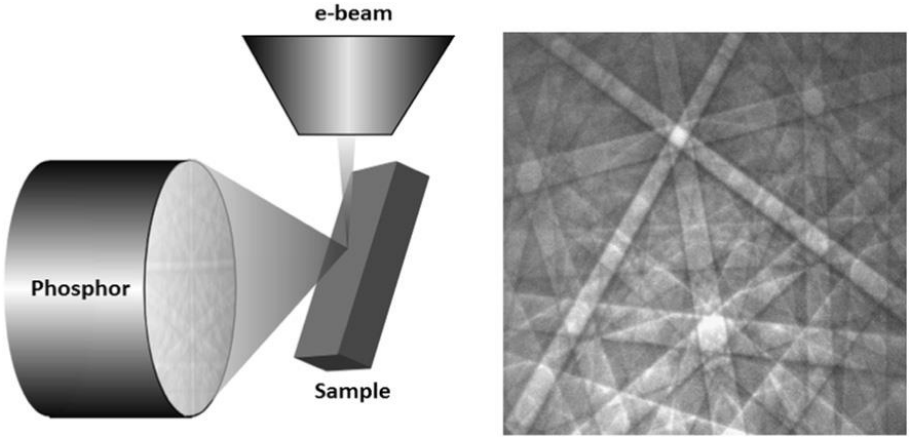

Figure 2.7. (a) Scheme of EBSD set-up (b) Kikuchi pattern [12]

The Kikuchi pattern contains the crystallographic information, which can be automatically processed by the EBSD software. The bands are identified by an image processing technique called Hough transform. The bandwidths and the angles between bands correspond to the interplanar distances and angles of the crystal lattice, respectively. During the EBSD mapping, this crystallographic information is recorded for each pixel as the electron beam scans through a well-polished specimen surface. In this thesis, the specimen surface for EBSD analysis is electropolished. The electrolyte for electropolishing is 1.5 wt% NaOH solution, and the parameters are 25 V with a flow rate of 18 L/min in the mask area of 2 cm2 for 1 minute at room temperature. All the EBSD measurements performed in this thesis are based on the Bruker QUANTAX EBSD system. After the EBSD measurement, the recorded crystallographic information is processed into various of map and figure to present the crystallographic texture and the feature of grains (shown in **Figure 2.8**) by the analysis software, i.e., MTEX (MATLAB based program), Bruker Quantax, EDAX-TSL OIM.

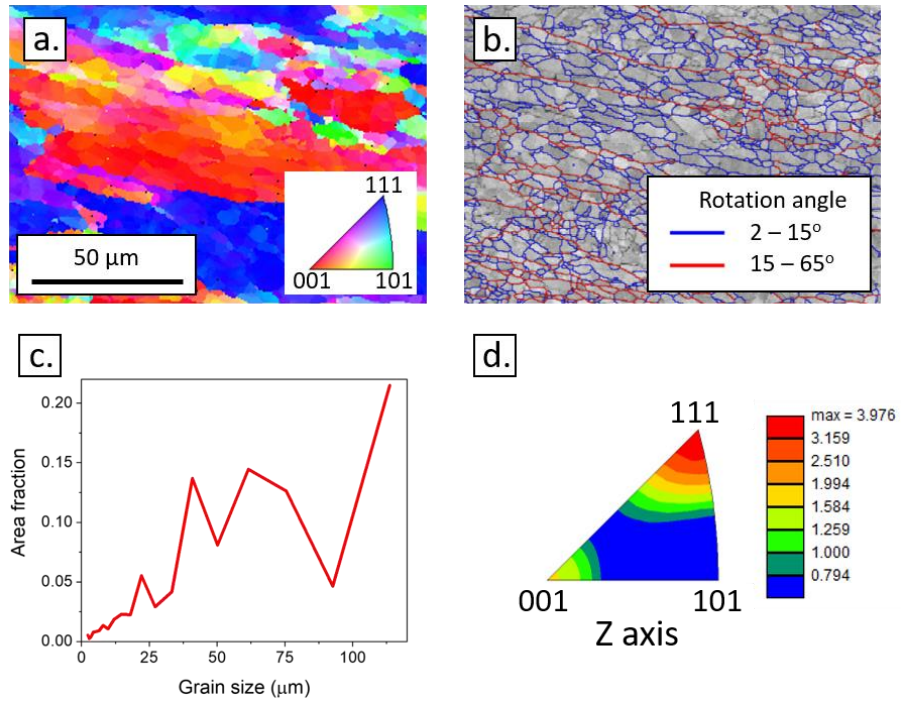

Figure 2.8. (a) Inverse pole figure (IPF) map, (b) image quality (IQ) map with indication of grain boundaries, (c) grain size distribution, (d) IPF in respect to the Z axis of the specimen.

The details of the parameters applied in the EBSD analysis are listed as follows.

- **Chapter 3 and 6:**
  The inverse pole figure (IPF) maps were plotted by Bruker Quantax analysis software, and the grain size is analyzed and calculated by MTEX.

- **Chapter 4:**
  The measurements are performed based on the Bruker QUANTAX EBSD system, and EDAX-TSL OIM analysis software is used to calculate low angle grain boundary density (with a step size of 2.74 µm) and to plot the IPF after the EBSD measurements. The grain size is calculated by MTEX.

- **Chapter 5:**
  The EBSD analysis is performed using an EDAX-TSL OIM analysis software. The grain boundary analysis is based on the scan with a step size of ~0.54 µm over an area of about 270 x 200 μm^2 on the plane

normal to ND. Low angle grain boundaries (LAGB) and high angle grain boundaries (HAGB) are defined as the boundaries with a misorientation angle from 2 to 15° and larger than 15°, respectively. The coincidence site lattices (CSL) boundaries are determined by the Brandon's criterion $\Delta\theta_{max} = \theta\Sigma^{-n}$, where $\Delta\theta_{max}$ is the maximum permissible deviation from coincidence, θ is a constant equal to 15°, n is a constant equal to 0.5, and the boundary fraction is from Σ3 to Σ27. The grain boundary density for each type of grain boundary is defined as the total length of each type of boundary per unit area.

- **Chapter 8:**
  The grain size, grain orientation, and grain boundary misorientation angles are identified by analyzing the EBSD data using EDAX-TSL OIM analysis software.

2.3.2. Energy dispersive spectroscopy

The element identification and analysis in this thesis are achieved by energy dispersive spectroscopy (EDS) based on the analysis of X-rays energy. The X-rays generated by electron interaction with the matter is categorized into two groups: continuum X-rays and characteristic X-rays. An example of these X-rays is shown in **Figure 2.9**. The continuum X-rays is the results of the interaction between primary beam electrons and the nucleus of the atoms. And the characteristic X-rays is generated as an inner shell hole (created by the high energy incident electron) is filled by an outer shell electron. Since the energy difference between shells is related to the atomic number, these characteristic X-rays can serve to identify the chemical elements and their population.

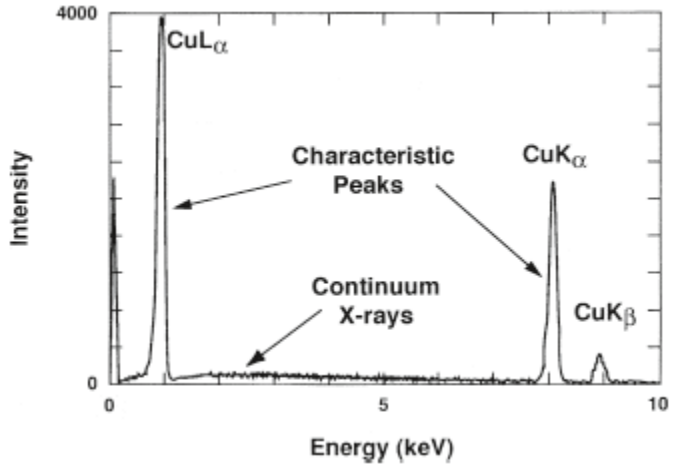

Figure 2.9. Continuum X-rays and characteristic X-rays. Here, copper (Cu) is considered as an example. [13]

2.4. Neutron irradiation

Neutron irradiation was performed in the Belgian Material Test Reactor BR2. The specially developed irradiation device (rig) was used to deliver fusion-relevant irradiation conditions. In particular, the rig was actively cooled with helium gas and the temperature on the samples was measured at several positions of the rig. The rig itself is made of a 1.5 mm thick stainless steel pressurized pipe, which is plugged to an out of pile equipment controlling temperature by adjusting the gas pressure. The temperature is monitored with four thermocouples located in different parts of the rig.

The rig was designed to deliver ~50% of the volume with active temperature control (i.e. central part of the rig) while outer regions would exhibit a temperature gradient due to the reduction of the neutron flux. The temperature at the ends of the rig was 550 °C. Such design not just allows for extremely accurate temperature control in the central part (±3 °C) but also exhibits reasonable temperature oscillations in the outer parts. For the samples studied in this thesis, the temperature fluctuation was ±20 °C. The example of the irradiation temperature profile during one cycle (28 days) on the tensile specimens located in the T-controlled and outer regions is provided in **Figure 2.10**. The central part of the rig exhibits a flat temperature profile set to be 800 °C. To avoid "cold start", the rig was equipped with an electrical heater, which enables the heating of the samples up to 800 °C before the irradiation starts. In addition to the thermocouple data, the reactor power is added to the figure. Due to the parallel irradiation experiment, the reactor power was reduced by ~10%, and one can see that this power reduction did not have any impact on the stability of the irradiation temperature, practically.

The rig was placed directly inside the fuel element in the position close to the central channel of the reactor such that in a mid-plane the fast neutron (E > 0.1 MeV) flux is equal to 7×10^{14} n/cm^2/s at a nominal power of 60 MW. The irradiation dose was calculated by MCNPX 2.7.0 [14]. The dpa cross sections for W have been prepared from the JENDL4 file (MT444) for the threshold displacement energy of 55 eV, following the recommendation of IAEA [15]. The transmutation of Re and Os was calculated based on the ALEPH code developed by SCK CEN and available nuclear databases [16-20]. Note that the established levels of Re and Os are much lower than what was typically reported in other irradiation studies performed e.g. at the HFIR reactor, which has a similar neutron spectrum. In the current experiment, the strong reduction of the transmutation rate could result from (i) absorption of thermal neutrons by thick stainless steel pressurized pipe; and (ii) by achieving high ratio of fast-to-thermal neutron flux thanks to the deployment

of the rig directly inside the fuel element, thus screening from other thermal neutrons.

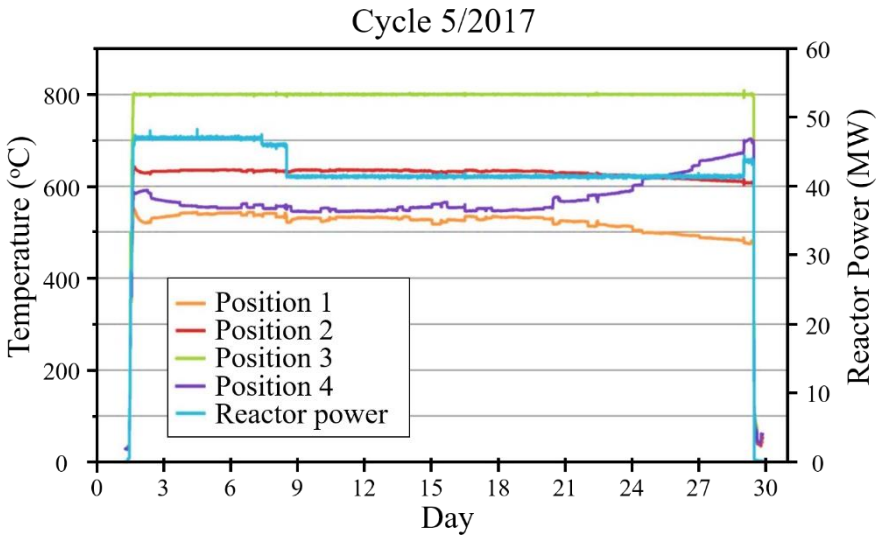

Figure 2.10. Evolution of the temperature on the samples located in the T-controlled zone (in green), the temperature on the samples located between T-controlled zone and outer parts of the rig (in red), the temperature on the samples located in the outer parts of the rig (light brown, dark blue), power reactor (in light blue).

2.4.1. Tensile specimens (Chapter 6)

The samples were fixed inside the graphite matrix, which was machined to accommodate the samples, heater, and feedthrough for thermocouples. In order to avoid carbon contamination, the samples were wrapped in the 25 µm tungsten foil. The graphite matrix consists of 26-unit sample holders (13 and 14 holders were located exactly in the mid-flux position). Each unit of graphite holder has a height of 27 mm and could accommodate either 8 tensile test specimens or 4 fracture toughness specimens (of KLST type). The samples studied here were extracted from the unit holders 5, 7, 8, which have a mean irradiation temperature of 610 °C, 725 °C, and 760 °C, respectively. The irradiation was performed for 6 cycles in order to accumulate 1.25 dpa (in W) in the central part of the rig. The irradiation dose of 1.075, 1.2 and 1.225 dpa was imposed, respectively, in the holders 5, 7, and 8. The

transmutation of tungsten resulted in the production of 1.5 at% Re and 0.2 at% Os on the samples irradiated up to 1.225 dpa. The samples at lower irradiated doses exhibit lower concentrations of Re and Os.

2.4.2. Fracture toughness specimens (Chapter 7)

The samples were encapsulated in a steel tube with 1.5 mm wall thickness filled with He. The gap between the samples and the pressure tube was adjusted to achieve 600 ^{o}C during the irradiation following the thermal and neutronic calculations. Following finite element analysis of thermal flow, a variation of about 25 ^{o}C could occur due to the burn out of the fuel element within a reactor cycle. The irradiation dose found to be 0.08 dpa, 0.44 dpa, and 0.67 dpa. The upper limit of the summed concentration (at%) of Re and Os together is 0.61 at%, 0.97 at%, and 1.40 at% for 0.08 dpa, 0.44 dpa, and 0.67 dpa, respectively. The fraction of Os is about 10 % of the totally produced Re and Os. The transmutation rate is related to the axial position of the specimen in the channel and radiation postion of the channel in the reactor because the neutron spectrum varies with the location. As a result, the transmutation rate is different for specimen irradiated at different doses and in different channels.

2.4.3. Microindentation specimens (Chapter 8 and 9)

The specimens are placed in the steel capsule filled with inert gas to prevent oxidation. The position of the specimens inside the capsule is secured by centering ceramic guiding rods in order to maintain the dedicated gap between the stack of specimens and capsule wall to achieve the required irradiation temperature.

Polycrystalline tungsten grades

The irradiation doses and temperatures were revealed to be 0.95 dpa at 600 ^{o}C, 1.00 dpa at 1000 ^{o}C, and 1.13 dpa at 1200 ^{o}C. The summed concentration of transmuted Re and Os for 0.95 dpa, 1.00 dpa, and 1.13 dpa is 1.80 at%, 1.96 at%, and 2.13 at%, respectively.

Single crystal tungsten

The irradiation doses and temperatures were revealed to be 1.05 dpa at 600 ^{o}C, 800 ^{o}C, 900 ^{o}C, and 1200 ^{o}C. The summed concentration of transmuted Re and Os at 1.05 dpa is 1.9-2.2 at% and 0.19-0.25 at%, respectively

2.5. Reference

[1] P. Jung, A. Hishinuma, G. Lucas, H. Ullmaier, Recommendation of miniaturized techniques for mechanical testing of fusion materials in an intense neutron source, J Nucl Mater 232(2-3) (1996) 186-205.
[2] A. Kohyama, K. Hamada, H. Matsui, Specimen size effects on tensile properties of neutron-irradiated steels, J Nucl Mater 179 (1991) 417-420.
[3] Y. Zhao, Y. Guo, Q. Wei, T. Topping, A. Dangelewicz, Y. Zhu, T. Langdon, E. Lavernia, Influence of specimen dimensions and strain measurement methods on tensile stress–strain curves, Materials Science and Engineering: A 525(1-2) (2009) 68-77.
[4] Y. Zhao, Y. Guo, Q. Wei, A. Dangelewicz, C. Xu, Y. Zhu, T. Langdon, Y. Zhou, E. Lavernia, Influence of specimen dimensions on the tensile behavior of ultrafine-grained Cu, Scripta Materialia 59(6) (2008) 627-630.
[5] B. Drapkin, The variation in young's modulus of Fe-Cr, Fe-Mo, and Fe-W alloys, Strength of Materials 5(4) (1973) 475-476.
[6] R. Lowrie, A. Gonas, Single-Crystal Elastic Properties of Tungsten from 24° to 1800° C, J. Appl. Phys. 38(11) (1967) 4505-4509.
[7] Z. Yuan, F. Li, P. Zhang, B. Chen, F. Xue, Mechanical properties study of particles reinforced aluminum matrix composites by micro-indentation experiments, Chinese Journal of Aeronautics 27(2) (2014) 397-406.
[8] ASTM, Standard test method for linear-elastic plane strain fracture toughness KIC of metallic materials, E 399-12, ASTM international, Pennsylvania, PA, USA, 2012.
[9] ASTM, Standard test method for determination of reference temperature, T0, for ferritic steels in the transition range, E1921-16, ASTM international, Pennsylvania, PA, USA, 2016.
[10] ASTM, Standard test method for measurement of fracture toughness, E1820-15a, ASTM International, 2015.
[11] ASTM, Standard Test Methods for Bend Testing of Material for Ductility, E290-14, ASTM international, Pennsylvania, PA, USA, 2014.
[12] D. Fullwood, B. Adams, J. Basinger, T. Ruggles, A. Khosravani, C. Sorensen, J. Kacher, Microstructure detail extraction via EBSD: an overview, Strain And Dislocation Gradients From Diffraction: Spatially-resolved Local Structure And Defects, World Scientific2014, pp. 405-437.
[13] J.I. Goldstein, D.E. Newbury, P. Echlin, D.C. Joy, C.E. Lyman, E. Lifshin, L. Sawyer, J.R. Michael, Generation of X-Rays in the SEM Specimen, Scanning Electron Microscopy and X-Ray Microanalysis, Springer2003, pp. 271-296.
[14] D. Pelowitz, J. Durkee, J. Elson, M. Fensin, M. James, R. Johns, G. McKinney, S. Mashnik, L. Waters, T. Wilcox, MCNPX 2.7. 0 Extensions, Los Alamos National Laboratory, 2011.

[15] S.L. Dudarev, DPA definition and estimates. <https://www-amdis.iaea.org/CRP/IrradiatedTungsten/RCM2/RCM2Presentation-DudarevDPA-2015-09-10.pdf>, 2015).
[16] A. Stankovskiy, G. Van den Eynde, L. Fiorito, ALEPH V.2.7, A Monte Carlo Burn-Up Code, SCK•CEN, 2018.
[17] JEFF Scientific Working group, The joint evaluated fission and fusion nuclear data library, JEFF-3.3, Nuclear Energry Agency, 2017.
[18] D.A. Brown, M. Chadwick, R. Capote, A. Kahler, A. Trkov, M. Herman, A. Sonzogni, Y. Danon, A. Carlson, M. Dunn, ENDF/B-VIII. 0: the 8th major release of the nuclear reaction data library with CIELO-project cross sections, new standards and thermal scattering data, Nuclear Data Sheets 148 (2018) 1-142.
[19] A.Y. Konobeyev, U. Fischer, Y.A. Korovin, S. Simakov, Evaluation of effective threshold displacement energies and other data required for the calculation of advanced atomic displacement cross-sections, Nuclear Energy and Technology 3(3) (2017) 169-175.
[20] M. Norgett, M. Robinson, I. Torrens, A proposed method of calculating displacement dose rates, Nuclear engineering and design 33(1) (1975) 50-54.

Chapter 3
Tensile properties of baseline and advanced tungsten grades

3.1 Materials

Six types of materials were studied in this work. The W grades were selected in accordance with the most recent advances in the development of W for DEMO applications. Two commercial grades were produced in Europe and China: Plansee ITER specification W (IGP) and AT&M ITER specification W (ATW), respectively. Four R&D grades were developed, respectively, by Karlsruhe Institute of Technology at Germany (two particle reinforced tungsten products), by Institute of Plasma Physics at Czech Republic, and Institute of Solid State Physics at China: W-1 wt% TiC (W1TiC), W-2 wt% Y_2O_3 (W2YO), Fine Grain W (FG), and W-0.5 wt% ZrC (W0.5ZrC). The main elements of the chemical composition of those grades are reported in **Table 3.1**.

Three grades (IGP, ATW, and W0.5ZrC) were produced by powder metallurgy and normalized by forging or rolling. The double-hammering was applied for IGP, and rolling for ATW and W0.5ZrC grades. The manufacturing process of W0.5ZrC, which is developed by Chinese Academy of Sciences, also introduced thermo mechanical treatment (TMT) to reduce the grains size [1]. The two particle reinforced tungsten products (W1TiC and W2YO) were manufactured by powder injection molding (PIM). Finally, the FG products were manufactured by spark plasma sintering (SPS) processing.

To provide a quick glance at the variety of the microstructure, we performed SEM-EBSD analysis. The maps, which was mapped by Bruker Quantax software, reported in **Figure 3.1** indicate the morphology and size of grains (reported in **Table 3.1**; analyzed and calculated by MTEX). IGP and ATW show strong texture with elongated grains parallel to the rolling direction. As a result, IGP has carrot-like grains, and ATW has plate-like grains. W0.5ZrC also shows crystallographic texture but with the nearly equiaxed grains, which is apparently the result of TMT. Since normalization forging or rolling was not applied to the advanced grades, they all have equiaxed grains. Among the selected R&D materials, W0.5ZrC has the smallest grains. The commercial IGP and ATW grades have comparable grain size.

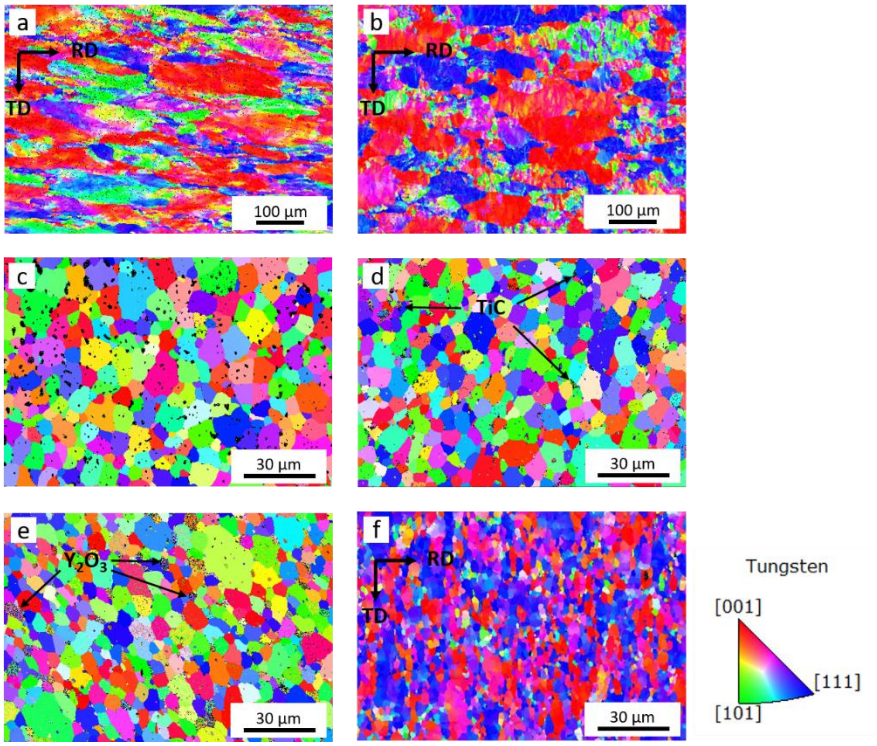

Figure 3.1. Normal direction (ND) Inverse pole figure (IPF) of baseline and advanced W; (a) IGP; (b) ATW; (c) FG; (d) W1TiC; (e) W2YO; and (f) W0.5ZrC

Table 3.1. The composition and grain size of tested materials observed from ND; the equivalent median diameter is defined as the equivalent diameter of grains that have 50% cumulative area fraction

Materials	IGP	ATW	FG	W1TiC	W2YO	W0.5ZrC
Composition (wt%)	Pure W > 99.97%	Pure W > 99.94%	Pure W > 99.7%	99% W + 1% TiC	98% W + 2% Y_2O_3	99.5% W + 0.5% ZrC
Equivalent Median Diameter (µm)	87.44	60.28	9.36	7.76	7.32	6.66

3.2. Result

3.2.1. Strength and ductility

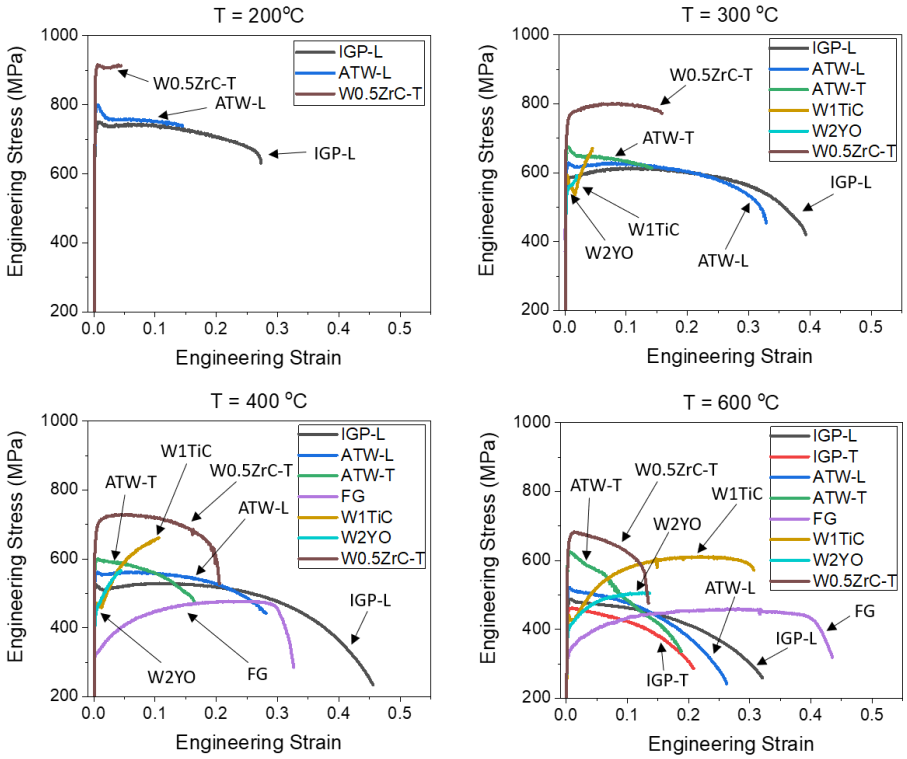

Figure 3.2. Stress-strain curve of baseline and advanced W

As shown in **Figure 3.2** and **Figure 3.3c**, the uniform elongation of W1TiC, W2YO and FG increases with raising the temperature and W1TiC shows quite large value at 600 °C. Although FG also has a considerable uniform elongation, its UTS is lower as compared to other tested materials, and increasing the temperature does not lead to any substantial improvement. The uniform elongation of FG is practically independent of test temperature.

The stress-strain diagram for W0.5ZrC differs from all other tested materials. Even though this material has extraordinary ductility below 300°C, the uniform elongation at 400°C and above is reduced drastically appearing the early necking deformation. However, this material preserves high YS and UTS in the whole studied temperature range.

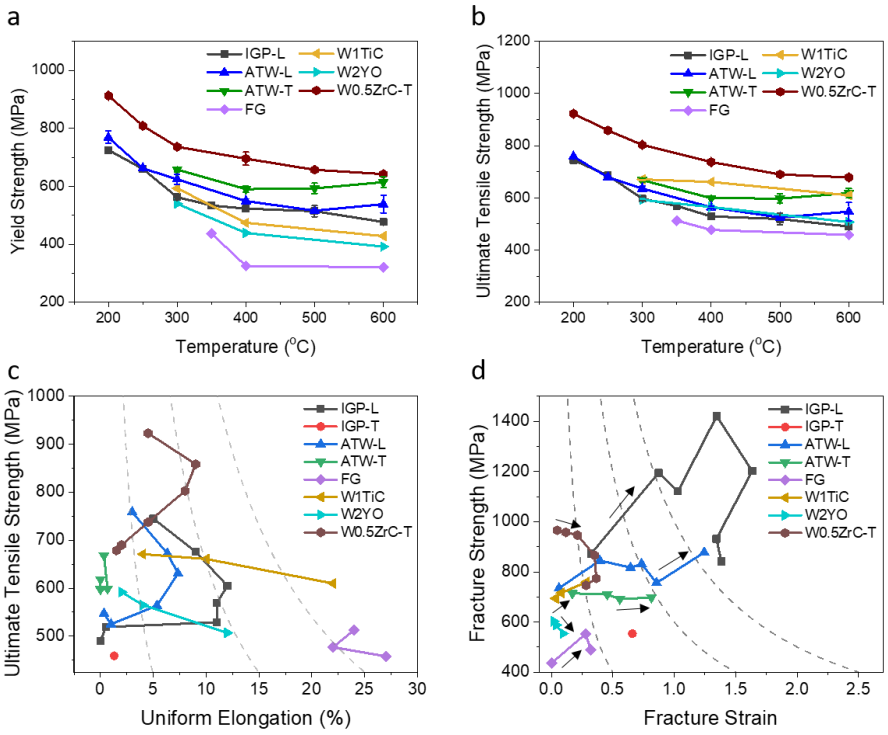

Figure 3.3. Comparison of the mechanical properties of baseline and advanced W as a function of test temperature; (a) YS; (b) UTS; (c) UTS vs. uniform elongation; (d) Fracture strength vs. fracture strain, the arrows indicate the trend of increasing/reducing the test temperature.

All the tested materials exhibit similar trends, namely both YS and UTS are reduced with increasing the test temperature (see **Figure 3.3a** and **b**). Depending on the particular grade, the reduction follows either an exponential or linear trend line.

W0.5ZrC shows the highest YS and UTS among all other advanced W grades in the whole temperature range. Comparison of IGP and ATW products (i.e. baseline commercial materials) reveals that AT&M grade has a higher YS and UTS. Moreover, as it will follow, the texture, grain orientation and shape, will also affect the strength of materials, for example, baseline W ATW-T had higher strength than ATW-L at all tested temperatures.

In order to compare the ductility and strength of the materials, UTS and uniform elongation were plotted in the same diagram (see **Figure 3.3c**). A combination of high strength and large uniform elongation indicates a

material with high toughness and better fatigue resistance, which can also be quantified by calculating the product of both these values (see iso-values). The UTS variation on that figure could also serve as representation of the impact of testing temperature, since the UTS is inversely proportional to the test temperature for these materials. For commercial tungsten, both IGP and ATW grades show similar results, but IGP-L appears to have a larger uniform elongation, which indicates that IGP-L has a better ductility in terms of resistance to plastic localization.

The fracture properties quantified by the FStrength and by the Fstrain are plotted in **Figure 3.3d**. As one can see, the baseline W indicates a better fracture resistance compared to advanced W. The IGP-L has the highest FStrength and the largest Fstrain among the other grades. Even though the FStrength of IGP-L dropped strongly at 600°C, the FStrength is still higher compared to the results obtained for other grades. The FStrength of ATW, for both L and T orientations, remains nearly constant over the whole temperature range, without dropping below 700 MPa. On the other hand, the FStrength and Fstrain measured for the advanced W appear to be rather low suggesting poor fracture resistance, at least in the range of tested temperature.

3.2.2. Delamination fracture

Microstructure analysis by SEM shows partial delamination of the fracture surface of IGP-L and ATW-L samples (tested at 300°C) where the crack initiated on the down-left corner and upper two corners, respectively (see **Figure 3.4**). The fracture surface of the IGP sample, tested at 400 °C and above for L-orientation, and tested at 600 °C for T-orientation, contains the delaminated fibers that are parallel with the RD. These features are apparently being related to the elongated grains that can be seen on EBSD maps. On the other hand, the delamination of ATW-L and –T oriented samples occurs along the TD-RD plane (see **Figure 3.4**) and the grains show plastic deformation with elongated grains and dimples (see **Figure 3.5**) at the test temperature exceeding 400 °C.

3.2.3. Transgranular and intergranular fracture

At 300 °C, the majority of the fracture surface of IGP-L and ATW-L appears to have features of the transgranular fracture (see **Figure 3.5**). It indicates that both materials display strong adhesion between grains. For the T-orientated

samples of both baseline W products, the fracture surface indicates the presence of both intergranular and transgranular fracture with a fraction close to 50/50. At 400 °C, the IGP-T sample still shows both brittle fracture features. The fracture surface of IGP grade displayed in **Figure 3.5** corresponds to the stress-strain curve in **Figure 3.2**, which proves that the IGP-T fractures in brittle manner up to 400 °C.

The grades appearing the best mechanical properties have flatter (as compared to the delaminated samples) fracture surface covered with micro-dimples, which might be initial pores or left-out of particles, except for the W0.5ZrC grade (see **Figure 3.4** and **3.7**). The delamination fracture surface is observed only on the W0.5Zsample tested at 300 °C. The FG, W1TiC, and W2YO materials exhibit intergranular fracture at 300 °C. However, the fracture surface of the FG and W1TiC also contains a small fraction of transgranular fracture. At 400 °C, a part of the fracture surface of the FG exhibits dimples and a signature of the grain deformation hence it starts to show large elongation. These dimples indicate point to the ductile fracture mechanism operating via nucleation, growth and coalescence of voids. On the other hand, the fracture surface of the W1TiC and W2YO grades, tested at 400 °C, remains the same as at 300 °C. Finally, at the highest test temperature i.e. 600 °C, the evidence of brittle fracture is no longer observed. In the FG grade, only dimples are observed on the fracture surface. The fracture surface of the W1TiC and W2YO grades contains the trace of the deformation of grains, as well as the typical patterns of both intergranular and transgranular fracture modes are observed.

The fracture surface of W0.5ZrC differs from all other products. At 300 °C and 400 °C, the surface contains several types of fracture patterns, including intergranular fracture, transgranular cleavage, dimples, deformation of grains, and delamination; however, dimples, deformation of grains, and delamination are only observed at the edges where the cracks initiated. Moreover, the percentage of intergranular fracture at 300 °C is higher than the one at 400 °C; intergranular fracture almost disappears on the fracture surface at 400 °C. With increasing the test temperature to 600 °C, the majority of the fracture changes and it contains dimples and delamination pattern.

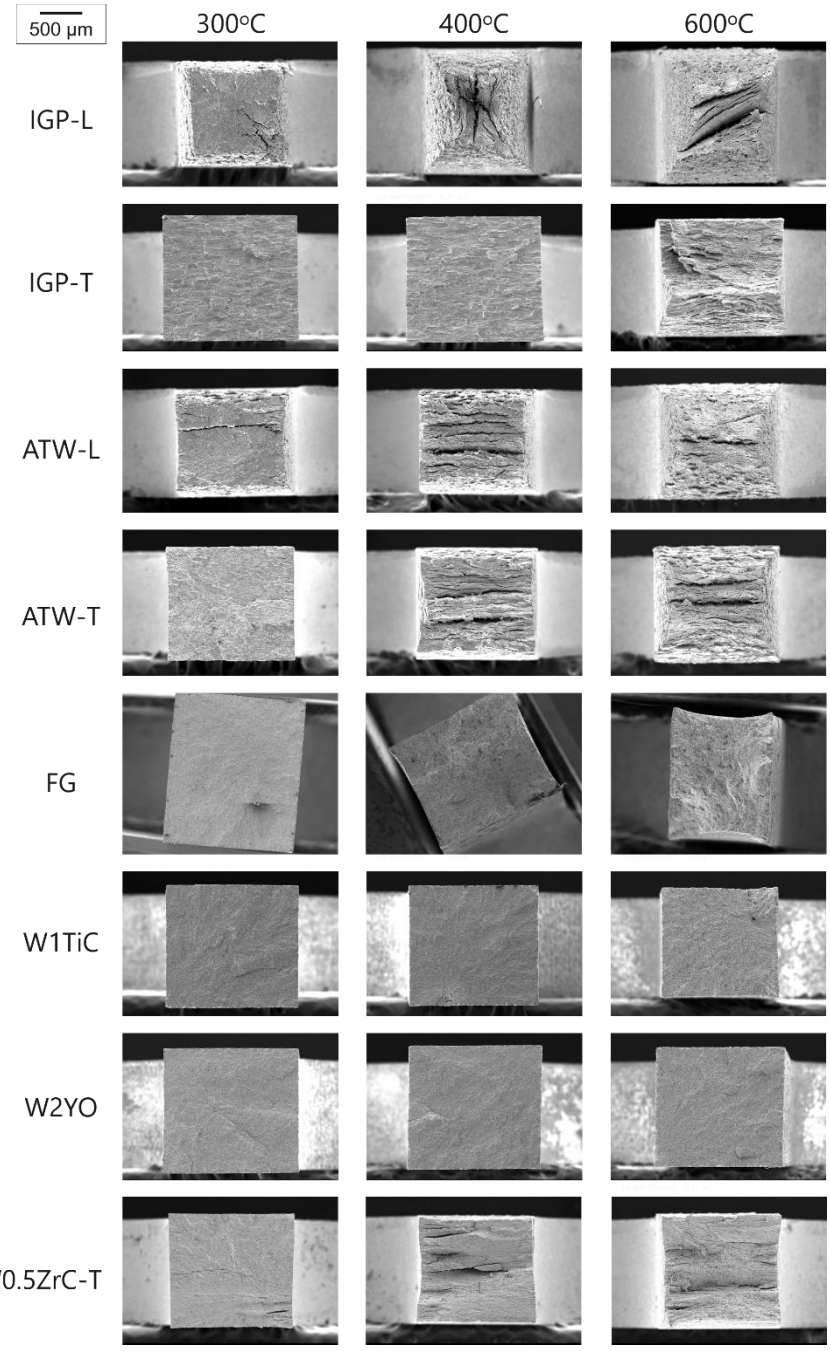

Figure 3.4. Macroscopic appearance of fracture surface, as observed by SEM. The length scale bar, to be applied for all the micrographs, is depicted in the upper left corner.

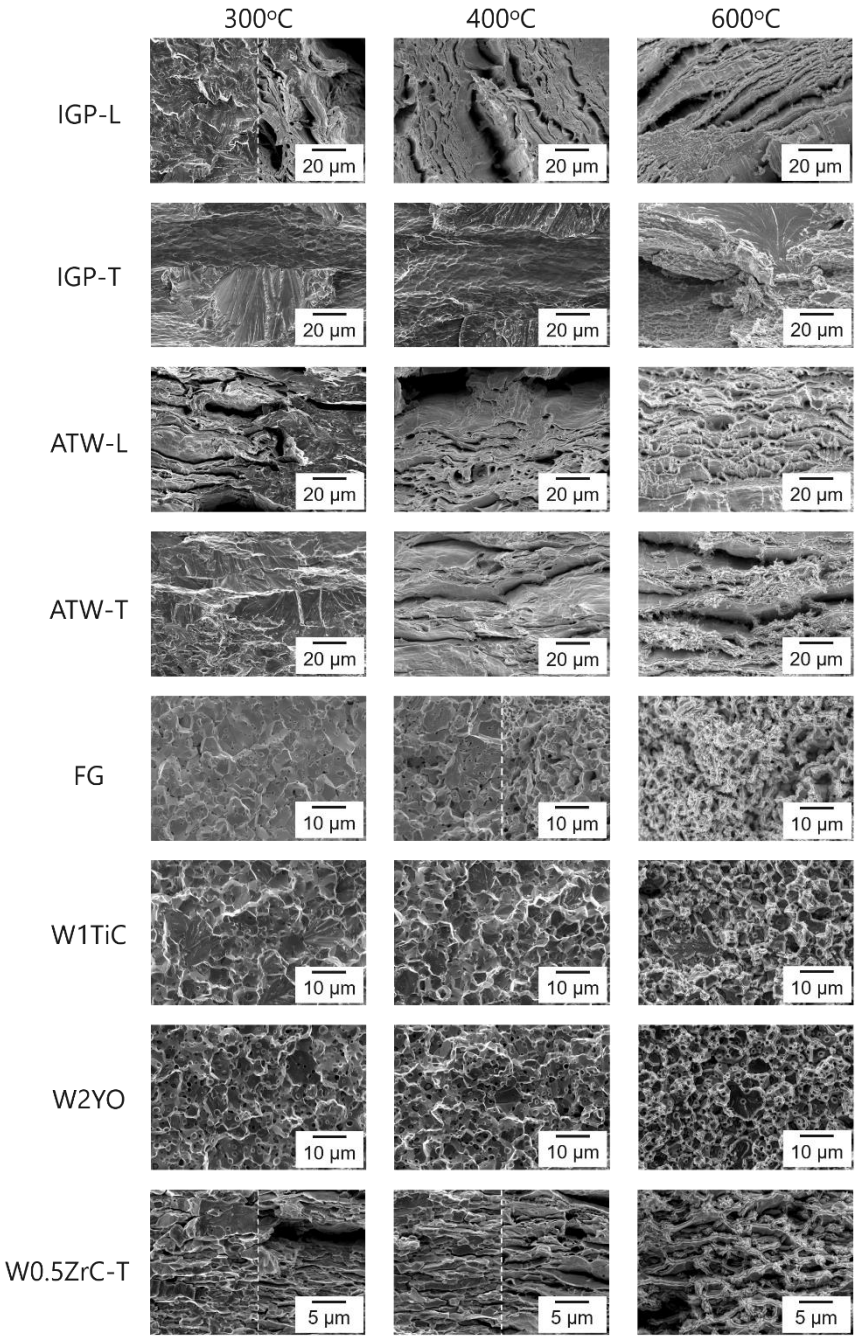

Figure 3.5. High magnification of fracture surface, as observed by SEM

3.3. Discussion

3.3.1. Mechanical properties

The product of UTS and uniform elongation reflects the amount of energy that can be accumulated in the material prior to the necking or plastic flow localization. The resistance to the occurrence of the plastic flow localization is directly connected to the strain hardening capacity. Materials with the large capacity exhibit longer uniform deformation as well as an elevation of the strength compared to the initial yield stress. The improved uniform deformation and high strength is also important for the good performance under fatigue condition. Thus, the material with the large uniform elongation and high strength is preferred for the application in the diverter PFC to sustain the thermal fatigue under the plasma discharge, to be coupled with the necessity to operate above the DBTT. The latter increases with the accumulation of the neutron irradiation dose. To this end, if one concerns with the structural integrity of PFC, the optimized operational temperature range with acceptable mechanical properties is defined by the DBTT and upper temperature above which the early necking onsets.

As shown in **Figure 3.3c**, each test material has a different suitable working temperature window. For example, W0.5ZrC can be applied for the components working at low temperature, baseline W can operate in the medium temperature range, and W1TiC or FG can be used for the high-temperature components.

A product of FStrength and FStrain can be used to qualitatively indicate the material with the high resistance to fracture and crack propagation, hence high fracture toughness. A high toughness material can sustain high stresses and can experience significant plastic deformation before the fracture. However, the FStrength × FStrain value can only be used as an indicator since the actual fracture toughness will be proportional to the product of FStrength × FStrain × X_0, where X_0 is a characteristic microstructural length scale [2]. For instance, it can be the spacing between the particles that promote stress concentration accumulation and subsequent void damage prior to the development of the crack. Following the results of the microstructural analysis (see **Figure 3.5**), the average dimple distance observed in the baseline W products (around 4-6 μm at 600 ^{o}C) is larger than that in the advanced W materials (around 3-4 μm at 600 ^{o}C). Moreover, the average dimple spacing measured in the ATW-L (6.49 μm at 600 ^{o}C) is larger than in the IGP-L sample (4.90 μm at 600 ^{o}C). Thus, if one considers FStrength × FStrain × X_0 value as a measure of the fracture resistance, the baseline W product performs better than the advanced W materials. In particular, among

the tested baseline W samples, the IGP-L sample has the best fracture resistance. It would be important to confirm this by the fracture toughness measurements.

3.3.2. Analysis of stress-strain response

Three types of the stress-strain deformation patterns were identified, namely: brittle (B), ductile (D), and early necking type (EN). B-type deformation corresponds to the fracture during the load in the elastic mode or just right after the yield point. D-type of deformation is the textbook curve of a ductile metallic material, which has a yield point, work hardening stage, ultimate tensile strength, and fracture limit. EN-type deformation refers to the case when necking occurs right after the yield point but it is accompanied with considerable total post-necking elongation.

The materials, which have early necking at 600 ^{o}C, were produced by rolling or forging process, which implies texture, presence of elongated grains. This was less apparent for W0.5ZrC due to the post-heat treatment but still present in some extend. According to our understanding, the main deformation mode in those materials is the in-grain plastic deformation; this kind of deformation by dislocation multiplication and glide is essentially limited by the small grain size. The inter-grain deformation occurs by the formation of dislocation pile-ups in front of GBs, they absorb by GBs and the newly formed dislocations move along the GBs. Note that transmission of dislocation slip between grains in the materials with strong texture and chaotic grain misorientation should be strongly suppressed. In such a picture, the GB triple junctions will act stress-concentrators where the nano-voids should nucleate and then coalescence. In turn, the nucleation and stress-driven coalescence of these voids would result in the reduction of the actual cross-section area of the sample being loaded under constant deformation rate. This would promote the formation of the necking region, and then the main plastic deformation would be concentration in the neck making the reduction of the ligaments even faster [3]. The reason why such flow softening behavior is promoted by increasing temperature is apparently due to the fact that thermal activation assists coalescence of voids in the temperature range where the transmission of plasticity between grain boundaries is still suppressed.

Table 3.2 summarizes the pattern of the stress-strain responses registered for the tested conditions. One can see that all tested materials can be sub-divided into two groups for which the trend, as the test temperature increases, is B-D-EN or B-EN. The materials of the former group are IGP-L, ATW-L, W0.5ZrC, FG, W1TiC, and W2YO. On the other hand, IGP-T and ATW-

T belong to the second group. This classification can also be observed from the plot showing the UTS and uniform elongation, presented in **Figure 3.6**. As soon as the material operates above its DBTT, the uniform elongation increases with raising the test temperature and reaches its largest value at around DBTT+100 °C. However, as temperature reaches around DBTT+200 °C the uniform elongation starts to decrease. Clarification of this trend for the FG, W1TiC, W2YO materials requires additional tests at a higher temperature.

Table 3.2. Summary of classification of stress-strain curve

	200 °C	**300 °C**	**400 °C**	**600 °C**
IGP-L	D	D	D	EN
IGP-T	B	B	B	EN
ATW-L	D	D	D	EN
ATW-T	B	B/EN	EN	EN
FG	B	B	D	D
W1TiC	B	D	D	D
W2YO	B	B/D	D	D
W0.5ZrC-T	D	D	D	EN

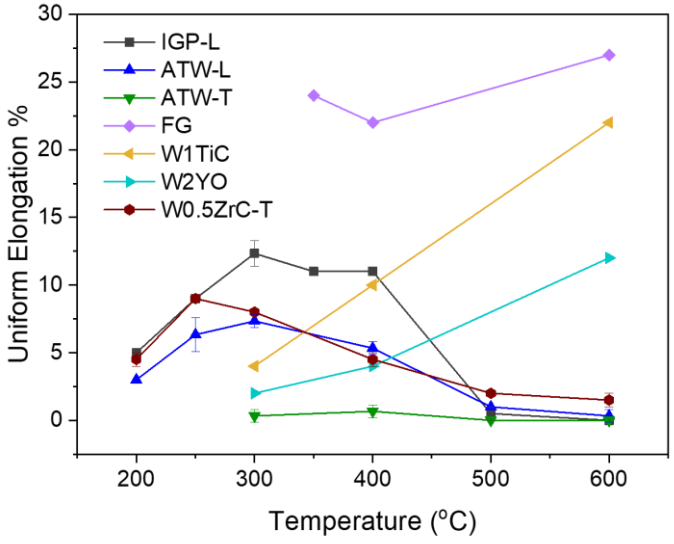

Figure 3.6. The variation of uniform elongation with temperature

3.3.3. Baseline W

The results of the tensile tests for the commercial grades show that these materials exhibit early necking with increasing the test temperature irrespective of the load orientation. Below, we reconcile our explanation for the early necking in the L- and T-orientation of baseline W. In the case of L-orientation, the micro-cracks nucleate on the rough high angle grain boundaries, which oppose the transmission of piled dislocations into neighboring grains. Upon continuously applied load, the nucleated micro-crack begins to propagate until they get arrested by the elongated grain boundary interfaces. This results in the crack deflection and promotes intergranular fracture pattern [4, 5]. Sustaining this deformation process requires input energy, and therefore material keeps undergoing macroscopic plastic deformation without significant loss of the engineering flow stress. As a result, a series of micro-cracks nucleate until they coalesce into a larger crack which defines the formation of the localized necking region. The numerous micro-cracks can be seen as delaminated grains all over the fracture surface, while few macro-cracks propagated across the whole fracture surface. Thus, the formation of numerous micro-cracks and their deflection by the elongated grains apparently delays the formation of the localized stress concentration resulting in the local necking region and eventual fracture. Macroscopically, such deformation results in the large post-necking elongation.

In the case of T-orientation, the grain interior available for the pile-up accumulation is smaller. As soon as the resolved shear stress is high enough to activate dislocation glide, the pile-ups will establish stress concentration near grain boundaries; this phenomenon will generate micro-cracks in a similar way as for the deformation mechanism of the samples with L-orientation. But since the elongated grains are parallel to the direction of crack propagation, the crack deflection distance is much smaller. Thus, the propagation of such micro-cracks should be much faster as compared to the situation in the L-orientation load. Correspondingly, the strain localization happens shortly after the yield point, and total elongation is also reduced, as compared to the results obtained for the L-orientation sample.

3.3.4 Advanced W

It is well known that the strength of the materials is defined by the properties of the weakest links available. Usually, it is grain boundary interface which

causes the accumulation of stress concentration by the dislocation pile-up formation. Thus pile-ups can dissolve by transmission through or absorption by grain boundaries. In the latter case, the absorbed bulk dislocations are converted into grain boundary dislocations (which produce grain boundary sliding, respectively). Segregation of impurities to grain boundary interfaces can further suppress plasticity by obstructing movement of grain boundary dislocations. Thus, the grain boundary accumulated a large fraction of interstitial impurities (like carbon, nitrogen or oxygen) tend to be prone to an intergranular fracture failure. However, as indicated by Gludovatz et al. [6], the impurities on grain boundaries have limited influence on fracture behavior at a test temperature below DBTT. Thus, the fracture behavior can be used as an indication of the purity/cleanness of grain boundaries from interstitial impurities, based on tests done above DBTT.

The fracture surface of the FG grade contains a high fraction of transgranular fracture is observed. It indicates that most of the grain boundaries are free from impurities. Moreover, FG grade had the highest DBTT among the lab grades studied here. The limited porosity found in the FG material, as observed on the EBSD maps, might be the reason of the high DBTT measured from the tests, since large number of micro-voids should act as nuclei for stress concentration regions. As a result, the FG samples fractured without any plastic deformation below 400^{o}C. However, the porosity can be considerably reduced by advanced heat treatment and improved sintering procedure, as preliminary tests have already shown.

The fracture surface of the W1TiC and W2YO grades showed the presence of the micrometer size particles, located on the grain boundaries, which is in line with results of Antusch et al. [7]. The particles on grain boundaries also will introduce suppression of the grain-boundary plastic deformation provoking stress concentration. Thus, these materials exhibit a relatively small total elongation below 400 ^{o}C. However, the TiC particles strengthen the grain boundaries and therefore shift the temperature for the onset of the early necking deformation [8-10]. The microstructural analysis has shown that the W1TiC grade had a higher grain boundary coherency compared to W2YO, which is in line with the higher fraction of transgranular fracture observed in W1TiC material. Therefore, at elevated temperature, large uniform elongation was recorded in the W1TiC samples.

In the microstructure of non-deformed materials, we did not observe pores except in the FG grade. The original work describing the development of W1TiC and W2YO grades indicates that Ti and Y elements, detected by the Auger electron spectroscopy (AES), are present in the pores of the fracture surface [7]. Thus, the pores on the fracture surface of W1TiC and W2YO

observed here might be the left-out of the carbide or oxide particles. Also, in the fractured grains of W0.5ZrC at 300 °C and 400 °C, micro-pores are observed (see **Figure 3.5**), these pores might be the left-outs of ZrC particles, nearly distributed in the W grains as mentioned in the original work [1].

In the original work of W0.5ZrC [1], it is noted that Zr acts as an oxygen gatherer, which "cleans" the grain boundaries. In other words, the grain boundary coherency of W0.5ZrC is improved. As observed from the fracture surface of W0.5ZrC, the majority of the fracture grains showed transgranular feature, which also support the conclusion on low impurity concentration at grain boundaries. This improved grain boundary coherency should reduce the resistance (as compared to other grades) for the permeation/absorption of dislocations through/by grain boundaries. That is probably why rather low work hardening is observed for the W0.5ZrC 400 °C. Yet thanks to nano-sized ZrC, the achieved grain refinement apparently enables both high yield strength and low DBTT at the same time. The limited size of ZrC particles ensures stability and fine structure of grain boundary interfaces and at the same time does not suppress the inter-granular plasticity. W0.5ZrC also shows early necking at 600 °C but with smaller post-necking elongation. In the following, we construct our explanation. The grains of W0.5ZrC are less elongated and nearly equiaxed. Therefore, the transmission of dislocation slip between grains is only weakly suppressed; the transmission of dislocation slip couples with the coherency grain boundaries results in larger uniform elongation compared with commercial W at 600 °C. However, the coalescence of voids is promoted by the increasing temperature; and these voids reduce the actual cross-section. Thus, the result is early necking.

Relatively high DBTT of FG, W1TiC, and W2YO materials, as compared to the fine-grain W0.5ZrC grade, should probably be attributed to the mis-ordered structure of grain boundary interfaces, porosity, and presence of large-size particles at the grain boundary interfaces (in PIM-produced grades). However, as FG operates above DBTT, thanks to the presence of initially low dislocation density and refined grain interfaces (both invoked by the high temperature sintering), the large uniform elongation and work hardening capacity are ensured by the multiplication of dislocations and transgranular slip [11]. On the other hand, we suspect that the transgranular slip is reduced in the PIM-based W grades because of the high density of precipitates, which increase the flow stress but suppress the plasticity in the grain boundary region.

3.4. Summary

In this chapter, two commercially available W grades and several lab-scale recently developed grades were tested in the temperature range 150-600°C using miniaturized tensile sample geometry. The main purpose of the work was to reveal the threshold temperature for ductile plastic deformation as well as to clarify the features of the fracture mechanisms in the ductile regime. Based on the obtained results and discussions it is possible to state the following:

I. Commercial IGP and ATW products, tested in L direction, have considerable uniform elongation in the temperature range 300-400 °C, which depends on the texture and initial microstructure. Although W0.5ZrC also has large uniform elongation at 250 °C and 300 °C, the uniform elongation gradually reduces with increasing temperature. Important to note that IGP, tested in L direction, has the highest fracture resistance out of all tested materials. While, the W0.5ZrC has the lowest DBTT (around 100 °C), as indicates in the original work [1], and still sustains rather high yield strength at 600 °C.

II. The lab-scale FG, W1TiC, W2YO grades exhibit relatively high DBTT, above 300 °C, however, these materials show large uniform elongation and capacity for work hardening up to 600 °C, and likely even higher.

III. Overall, each tested material exhibits brittle-ductile-early necking deformation behavior as the test temperature rises. The ductile behavior and capacity for work hardening are preserved over a limited temperature range, which is extends by about 300 degrees above the DBTT, as was revealed for the IGP-L, ATW-L and W0.5ZrC. Clarification of the value for this temperature range for the FG, W1TiC, W2YO grades requires additional tests at a higher temperature.

IV. The presence of texture in the commercial grades has an impact on the above discussed Brittle/Ductile/Early Necking trend. In particular, for both IGP and ATW grades tested in T-orientation, the observation indicates the direct transition from brittle to early necking deformation pattern without attaining the ductile deformation with somewhat considerable uniform elongation.

V. The fracture surface analysis indicates that the commercial grades tend to delaminate at high temperature. On the other hand, the fracture surface of the lab-scale grades mainly consists of trans/inter-granular fracture. Worth to note that W0.5ZrC revealed all types of fracture,

where the fraction of each type of pattern depends on the test temperature.

3.5 Reference

[1] Z.M. Xie, R. Liu, S. Miao, X.D. Yang, T. Zhang, X.P. Wang, Q.F. Fang, C.S. Liu, G.N. Luo, Y.Y. Lian, X. Liu, Extraordinary high ductility/strength of the interface designed bulk W-ZrC alloy plate at relatively low temperature, Sci Rep-Uk 5 (2015).
[2] T. Pardoen, J. Hutchinson, Micromechanics-based model for trends in toughness of ductile metals, Acta Materialia 51(1) (2003) 133-148.
[3] D. Lassance, D. Fabregue, F. Delannay, T. Pardoen, Micromechanics of room and high temperature fracture in 6xxx Al alloys, Progress in Materials Science 52(1) (2007) 62-129.
[4] D. Rupp, R. Mönig, P. Gruber, S. Weygand, Fracture toughness and microstructural characterization of polycrystalline rolled tungsten, International Journal of Refractory Metals and Hard Materials 28(6) (2010) 669-673.
[5] E. Gaganidze, D. Rupp, J. Aktaa, Fracture behaviour of polycrystalline tungsten, J Nucl Mater 446(1) (2014) 240-245.
[6] B. Gludovatz, S. Wurster, T. Weingärtner, A. Hoffmann, R. Pippan, Influence of impurities on the fracture behaviour of tungsten, Philosophical Magazine 91(22) (2011) 3006-3020.
[7] S. Antusch, D.E. Armstrong, T.B. Britton, L. Commin, J.S.-L. Gibson, H. Greuner, J. Hoffmann, W. Knabl, G. Pintsuk, M. Rieth, Mechanical and microstructural investigations of tungsten and doped tungsten materials produced via powder injection molding, Nuclear Materials and Energy 3 (2015) 22-31.
[8] H. Kurishita, Y. Amano, S. Kobayashi, K. Nakai, H. Arakawa, Y. Hiraoka, T. Takida, K. Takebe, H. Matsui, Development of ultra-fine grained W–TiC and their mechanical properties for fusion applications, J Nucl Mater 367 (2007) 1453-1457.
[9] M. Kajioka, T. Sakamoto, K. Nakai, S. Kobayashi, H. Kurishita, S. Matsuo, H. Arakawa, Effects of plastic working and MA atmosphere on microstructures of recrystallized W–1.1% TiC, J Nucl Mater 417(1) (2011) 512-515.
[10] H. Kurishita, S. Matsuo, H. Arakawa, M. Narui, M. Yamazaki, T. Sakamoto, S. Kobayashi, K. Nakai, T. Takida, K. Takebe, High temperature tensile properties and their application to toughness enhancement in ultra-fine grained W-(0-1.5) wt% TiC, J Nucl Mater 386 (2009) 579-582.
[11] A.F. Liu, Mechanics and mechanisms of fracture: an introduction, ASM International2005.

Chapter 4
Ductile to brittle transition in ITER specification tungsten assessed by combined fracture toughness and bending tests analysis

4.1. Methodology and experimental details

4.1.1. Materials and microstructural analysis

The microstructure and fracture surface of the specimens are analyzed using a JEOL JSM6610 scanning electron microscope. The surface fraction of the different fracture patterns are quantified by ImageJ image analysis software. Electron backscattered diffraction (EBSD) is used to analyze the morphology and orientation of the grains. The measurements are performed based on the Bruker QUANTAX EBSD system, and OIM TSL analysis software is used to calculate low angle grain boundary density (with a step size of 2.74 μm) and to plot the inverse pole figure (IPF) after the EBSD measurements.

Two grades of commercially pure tungsten (W) processed according to the ITER specification [1] were studied. These grades will be referred to as IGP and ATW, being manufactured by Plansee (Austria) and AT&M (China), respectively. Both materials were produced by powder metallurgy methods. The mechanical treatments are different: double hammering was applied to IGP W and rolling was applied to CEFTR W. Their composition (provided by the manufacturer) and grain size are shown in **Table 4.1**; the grain characteristics are calculated by the MTEX Matlab code.

Table 4.1. Composition and grain characteristics (normal to normal direction) of the W materials; the equivalent median diameter is defined as the equivalent diameter of grains that have 50% cumulative area fraction; the median aspect ratio is defined as the ratio between the long side and the short side of an equivalent ellipse, which has the best match with the grain shape.

Materials	**IGP**						**ATW**					
Composition	Pure W (>99.97 wt%)						Pure W (>99.94 wt%)					
Major impurities (maximum concentration, x 10^{-3} wt%)	C	O	N	Fe	Ni	Si	C	O	N	Fe	Ni	Si
	3	2	0.5	3	2	2	10	10	10	10	10	10
Plane normal to (the directions are shown in **Figure 4.2**)	Normal direction			Transverse direction			Normal direction			Transverse direction		
Equivalent median diameter (μm)	78.6			43.6			58			37.6		
Median aspect ratio	9.79			10.75			2.42			7.43		
Low angle grain boundaries (LANGs) density (m^{-1})	2.17 x 10^5			2.01 x 10^5			2.20 x 10^5			2.03 x 10^5		

The microstructure of the two W materials can be analyzed based on the map of inverse pole figures (**Figure 4.1**), where the color mapping is related to the orientation of grains. Because of the hot rolling (ATW) and hot forging/hammering (IGP), the microstructure consists of essentially elongated grains whose axis coincides with the longitudinal direction. The grains are elongated, and therefore the measured median diameter represents only the effective size, while the apparent size is essentially different. The main differences between these materials are (1) the grain shape aspect ratio in TD-LD plane (plane normal to ND), see **Table 4.1**; and (2) the texture, see **Figure 4.1c** and d. The impact due to these differences will be discussed further after presentation and analysis of the failure process. The microstructure of IGP and ATW material have been investigated by TEM revealing that both materials have similar dislocation density, which is around 4.5×10^{12} m^{-2} [2].

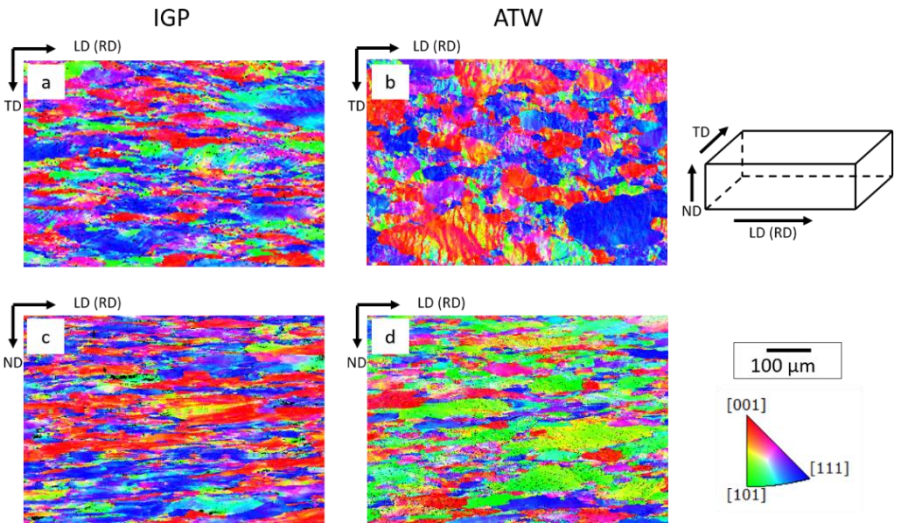

Figure 4.1. Map of inverse pole figure of IGP and ATW; (a) and (b) are normal to normal direction (ND); (c) and (d) are normal to transverse direction (TD).

4.1.2. Fitting method

In order to fit the dependence of K_{Jc} and flexural strain (FS) on test temperature, we use the mean values of the experimental results instead of the median values of the Weibull distribution. This choice is motivated by the limited number of tests performed at each temperature (1 to 6 samples were tested at each temperature). Later on, it will be shown that the two W materials exhibit different transition temperatures, and in the case of IGP that the flexural strain shows a plateau as the temperature reaches 525 °C. On the other hand, the saturation of the flexural strain for ATW is not attained yet at the highest flexural strain capacity of the test stage, which is around 20%. Because of this, two functions are exploited to fit the FS experimental results: (i) an exponential function (**equation 4.1**) for ATW and (ii) a Boltzmann sigmoidal function (**equation 4.2**) for IGP. The experimental results of fracture toughness for both materials is fitted using a Boltzmann sigmoidal function (**equation 4.3**).

$$FS\% = FS_{base} + B \cdot exp(C \cdot T) \quad (4.1)$$

$$FS\% = FS_{base} + \frac{FS_{top} - FS_{base}}{1 + exp\left(C\left(T_{half} - T\right)\right)} \quad (4.2)$$

$$K_{Jc} = K_{base} + \frac{K_{top} - K_{base}}{1 + exp\left(C\left(T_{half} - T\right)\right)} \quad (4.3)$$

where FS_{base} and K_{base} are constants that define the lowest values of FS and fracture toughness, FS_{top} and K_{top} are constants that define the highest values i.e. the values obtained at 600 °C, *B* and *C* are deduced from the fitting procedure, the constant *C* will be referred to as the slope parameter, and T_{half} is the temperature of the inflection point (the temperature that the second derivative of the curve is equal to zero).

4.2. Results

4.2.1. Three-points bending tests

Figure 4.2a presents the results of the three-point bending tests. The flexural strain increases exponentially with increasing temperature for both materials. As proposed by Lassila et al. [3], DBTT is in the range where the flexural bending strain reaches 5%. This temperature will be referred to as $T_{5\%}$. This definition is different from the method used to find the DBTT through the fracture toughness tests, where the DBTT is considered to be the temperature at which linear elastic fracture mechanics (LEFM) is no longer valid [4, 5] or the temperature corresponding to the maximum value of fracture toughness [6-8].

According to the results of 3PB tests, the transition is around 300°C for the ATW and around 400°C for the IGP material. In the IGP grade, the Boltzmann sigmoidal function fits well the experimental results, while in the case of ATW material the exponential function closely captures the experimental trend. The best fit parameters are collected in **Table 4.2**. Both fits have a R^2 value higher than 0.95, which indicates the good quality of the fit. According to the fitted curves, $T_{5\%}$ of IGP T-L is 389 +16/-19 °C and , $T_{5\%}$ of ATW T-L is 305 ± 12 °C, which makes a difference of 85 °C.

Table 4.2. Parameters obtained from the best fit of the FS-Temperature curves.

Materials	Parameters					R^2
	FS_{base}	FS_{top}	B	C	T_{half}	
IGP T-L	0 ± 1.613	16.951 ± 3.649	-	0.023 ± 0.012	426.383 ± 25.208	0.958
ATW T-L	0 ± 1.923	-	0.017 ± 0.038	0.019 ± 0.006	-	0.967

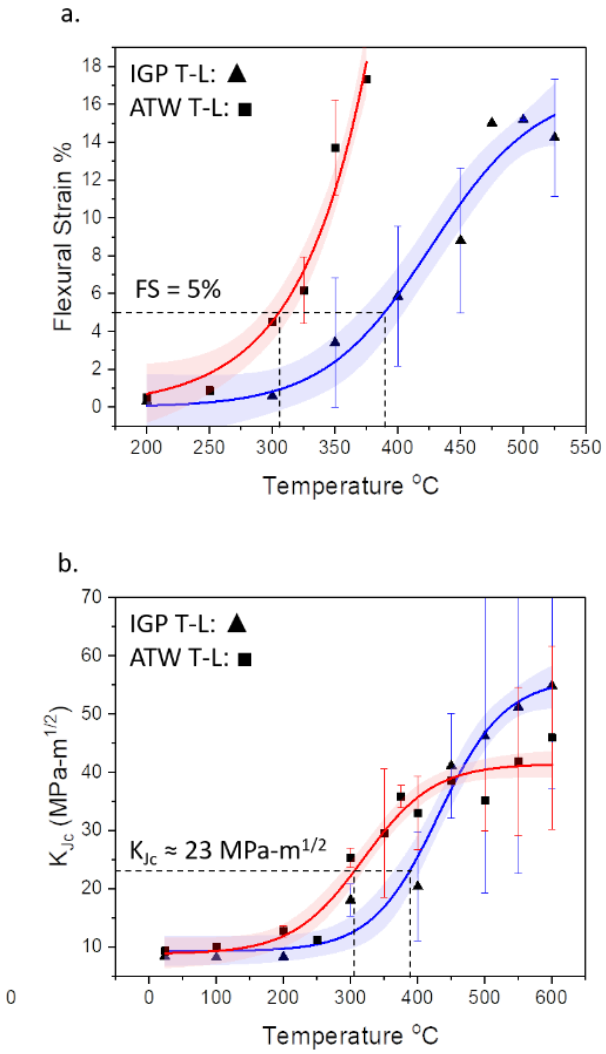

Figure 4.2. (a) Variation of FS as a function of Temperature and (b) variation of K_{Jc} as a function of Temperature curve for IGP T-L (triangles) and ATW T-L (squares) grades. The error bars in both figures represent one standard deviation of the experimental data. The pink and blue bands show the 68% confidence bands.

4.2.2. Fracture toughness tests

The fracture toughness measured for both materials and presented in **Figure 4.2b** is found to increase according to the Boltzmann sigma type function

with temperature for IGP and for ATW material. The parameters obtained by applying the fitting procedure are presented in **Table 4.3**. Just as in the case of flexural strain, the confidence factor R^2 exceeds 95%, hence we consider the fitting procedure to be reliable.

Table 4.3. The parameters of the fitted K_{Jc}-Temperature curve.

Materials	Parameters					R^2
	K_{base}	K_{top}	B	C	T_{half}	
IGP T-L	9.292 ± 2.352	55.994 ± 5.034	-	0.020 ± 0.008	431.040 ± 17.991	0.974
ATW T-L	8.822 ± 2.613	41.442 ± 2.293	-	0.019 ± 0.006	318.966 ± 18.789	0.950

The rate at which the fracture toughness increases with temperature levels off at 400 °C for ATW and at around 500 °C for the IGP material. Earlier studies on similar textured commercially pure W grades found the maximum of the fracture toughness in the temperature range of 600-800 °C [7, 9]. The standard deviation on the mean value also increases with the test temperature. Statistical aspects become very important on the determination of K_{Jc} at high temperature.

Using the coefficients reported in **Table 4.3**, the fracture toughness of IGP and ATW at $T_{5\%}$ is found to be 23.3 ± 3.8 $\mathrm{MPa}\sqrt{\mathrm{m}}$ and 23.0 ± 2.3 $\mathrm{MPa}\sqrt{\mathrm{m}}$, respectively, hence, equal to one another. K_{top} is determined at the highest test temperature. The value of K_{base} should be close to the value predicted by the Griffith criterion considering a fully brittle material at 0 K. The surface energy G required to form the new open surfaces at fracture is around 3 J/m^2 [10]. Therefore, the fracture toughness K_e should be equal to 1.6 $\mathrm{MPa}\sqrt{\mathrm{m}}$ for the "ideal" fully brittle tungsten. However, the experimental results, obtained at low temperature, do not match with the result coming from the Griffith limit because some degree of micro-plastic deformation still occurs at the crack tip of tungsten [11]. Hammering and/or rolling during the manufacture process indeed increases the fracture toughness of tungsten [6, 11-16]. As a result, the obtained K_{base} is found to be 9 ± 2.7 $\mathrm{MPa}\sqrt{\mathrm{m}}$ for technical grade tungsten and also is in line with other experimental data obtained earlier [7, 9, 17-19].

4.2.3. Fracture surface

To substantiate the results of mechanical testing and the approach of Lassila [3] regarding the determination of the transition temperature, we performed a detailed investigation of the fracture surface. Scanning electron microscopy analysis was performed on the materials deformed at low temperature (in the 100% cleavage region), near the transition temperature and at the upper studied temperature. **Figure 4.3** shows the fracture surface of both materials as obtained using the 3PB samples, which were tested near the $T_{5\%}$ temperature. Both intergranular and transgranular brittle fracture are observed on the fracture surface. However, the transgranular brittle fracture pattern of ATW T-L is higher than the one of IGP T-L i.e. approximately 30% and 50% of the pattern correspond to the transgranular brittle fracture for IGP T-L and ATW T-L, respectively.

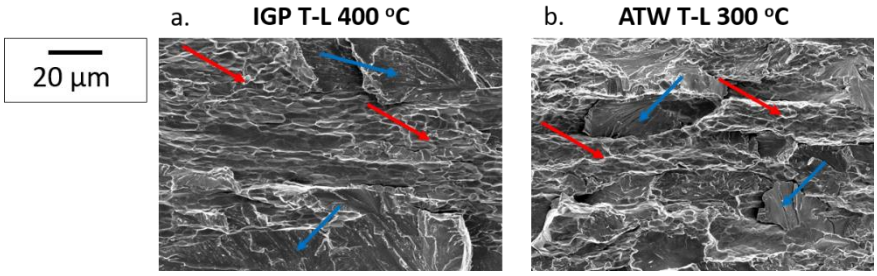

Figure 4.3. The fracture surface of 3PB specimens obtained for (a) IGP at 400 °C and (b) ATW at 300 °C, which is near $T_{5\%}$ as determined from mechanical tests. The red arrow indicates intergranular fracture failure; the blue arrow indicates transgranular brittle fracture.

The evolution of the DCT fracture surfaces of the IGP grade tested at 23, 400 and 600 °C are shown in **Figure 4.4**. As the test temperature increases to 400 °C (i.e. close to $T_{5\%}$ of this material), the fraction of transgranular brittle fracture pattern increases from 10% to 20%. At 600 °C, oxidation happens and the delamination is clearly observed, which implies a ductile deformation behavior. However, the stability of the crack propagation process cannot be determined by characterization of the fracture surface. Further investigation of crack propagation, e.g. by means of video registration, is required.

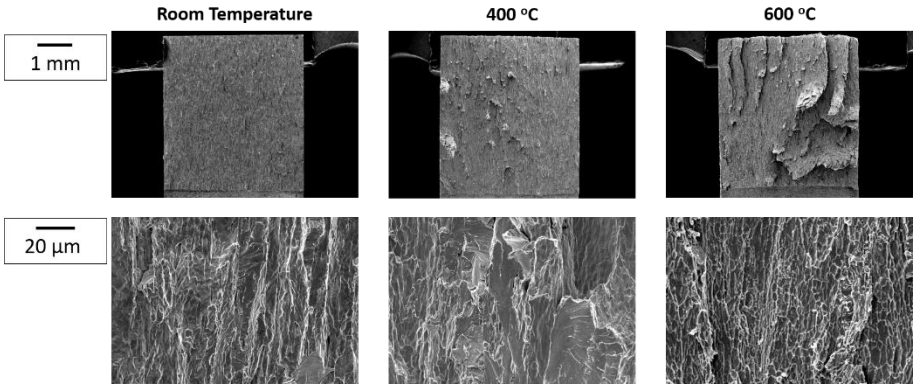

Figure 4.4. Fracture surface of the DCT specimens of IGP material obtained at 22, 400 and 600°C.

The fracture surfaces of the ATW grade tested at 23, 300 and 600 °C are shown in **Figure 4.5**. The comparison between **Figure 4.5** and **6**, shown that the evolution of the fracture surface pattern is different in the case of ATW. At 300 °C (close to $T_{5\%}$) both trans- and intergranular brittle fracture is observed (transgranular brittle fracture is around 30%). The pattern at 300 °C is different from the one at 23 °C, which shows high fraction of transgranular brittle fracture (60%). Whereas at 600 °C, no delamination is observed but just a mixture of transgranular brittle fracture (30%) and intergranular brittle fracture with oxides is presented.

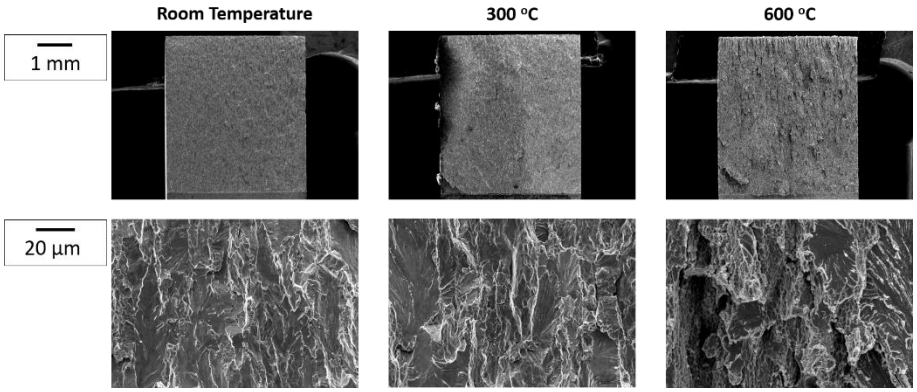

Figure 4.5. Fracture surface of DCT specimens of ATW material tested at 22, 300 and 600°C.

4.2.4. Texture

A deeper analysis of the crystallographic texture is performed as a starting point to explain the differences in the DBTT of IGP and ATW grades. The inverse pole figure (IPF) indicates the intensity associated to crystallographic directions, which align toward the specific specimen orientation. The corresponding distribution of crystallographic planes normal to different crystallographic directions indicated on the IPF can also be identified.

As shown in **Figure 4.6**, both materials exhibit a preferential texture on the fracture plane normal to TD. IGP appears to have high intensity of $\{001\}$ and $\{111\}$ crystallographic planes and high intensity of $\langle 101 \rangle$ crystallographic direction, as shown in **Figure 4.6a** and **8b**. Moreover, the IPF of IGP exhibits medium intensity of $\langle 001 \rangle$ crystallographic direction. Differently from the IGP, the ATW material exhibits medium intensity of $\{001\}$ and $\{101\}$ crystallographic planes and high intensity of $\langle 101 \rangle$ crystallographic direction, as shown in **Figure 4.6c** and **8d**. The quantized intensity of crystallographic planes and crystallographic directions, which are analyzed by the crystal direction function of OIM TSL analysis software, are shown in **Table 4.4**. This information will be used later in the discussion of the results.

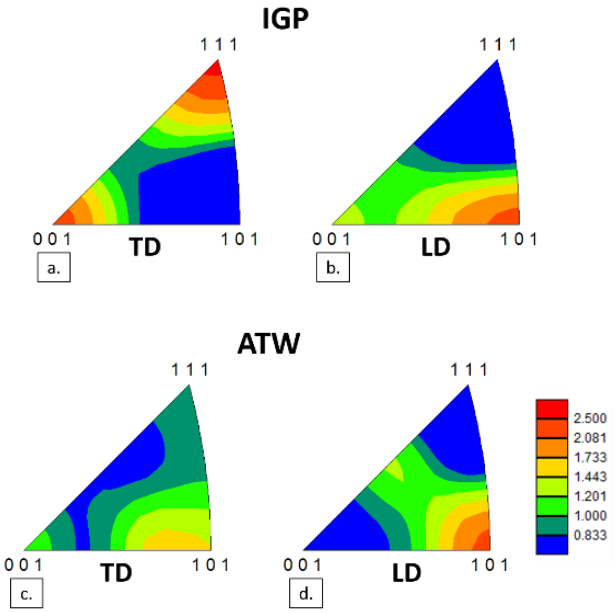

Figure 4.6. Inverse pole figure for (a, b) IGP and (c, d) ATW materials

Table 4.4. Fraction of crystallographic planes normal to TD and fraction of crystallographic directions parallel to LD (with the ± 15^{o} of angular range from the reference crystallographic planes or reference crystallographic directions)

	Fraction of planes normal to TD			Fraction of directions parallel to LD		
	$\{001\}$	$\{101\}$	$\{111\}$	$\langle 100 \rangle$	$\langle 101 \rangle$	$\langle 111 \rangle$
IGP	0.174	0.046	0.269	0.118	0.326	0.019
ATW	0.090	0.276	0.118	0.065	0.316	0.047

4.3. Discussion

4.3.1. Methodology to construct K_{Jc}(T) curve by single temperature measurement

The purpose of this section is to summarize the results and to discuss how small specimen test configurations can be used to explore the transition temperature range in order to guide the standardized fracture toughness testing.

At first, the relationship between the fracture toughness K_{Jc} and flexural strain of the two tested materials is shown in **Figure 4.7a**. One can see that the fracture toughness K_{Jc} of both materials is almost identical in the range of the low flexural strain (up to ~5%). This can be explained by the grain properties. As shown in **Table 4.1**, the two tested materials have similar aspect ratio and similar density of low angle grain boundaries (LAGB) over the fracture plane (ND-LD plane). As indicated in the literature, the aspect ratio [17] and dislocation sources e.g. LAGB [6, 8, 12] do have an impact on the fracture toughness below the DBTT. Similarity of the microstructure of the two grades is likely the reason why the fracture toughness vs. FS of both materials at low temperature (i.e. below $T_{5\%}$) is almost the same. At higher values of FS, the fracture toughness curve begin to deviate, which implies that the two materials show different sensitivity to strain state in the upper shelf regime.

Secondly, the slope parameter C (see **equations 4.1 - 4.3**, **Tables 4.2, 4.3**) was obtained from both 3PB and DCT tests. An easy way to compare the slope parameters obtained from the two types of tests is to plot the natural logarithm vs. test temperature as presented in **Figure 4.7b**. The values of $Ln(K_B)$, $Ln(FS\%_E)$ and $Ln(FS\%_B)$ are derived from the equations used to fit K_{Jc} curves, and these values read:

$$LN(K_B) = ln\left(\frac{K_{Jc}-K_{base}}{K_{top}-K_{Jc}}\right) + CT_{half} = CT \qquad (4.4)$$

$$LN(FS\%_E) = ln\left(\frac{FS\%}{B}\right) = CT \qquad (4.5)$$

$$LN(FS\%_B) = ln\left(\frac{FS\%-FS_{base}}{FS_{top}-FS\%}\right) + CT_{half} = CT \qquad (4.6)$$

where the constants B, C, K_{base}, and K_{top} are taken from **Table 4.2** and **4.3**.

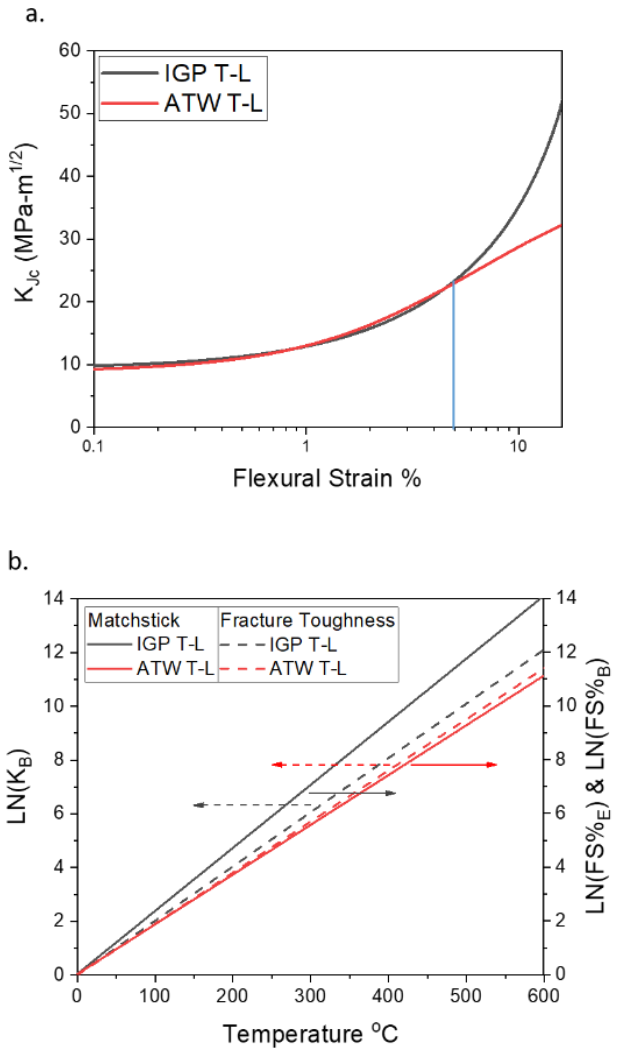

Figure 4.7. (a) Variation of K_{Jc} as a function of flexural strain; (b) variation of natural logarithm of Exponential and Boltzmann sigma parameters as a function of temperature for both tested materials.

Ln(KB), Ln(FS%E) and Ln(FS%B) are plotted in **Figure 4.7b**, and the figure clearly demonstrates the parameter C for ATW T-L agrees much better than that for the IGP T-L. The deviation of the slope parameter from the two types of tests for IGP T-L can be explained by a relatively large dispersion of the fracture toughness values measured at high test temperature, as shown in **Figure 4.2b**. In order to quantify the accuracy of the agreement of slope

parameters of IGP T-L and to account for the relative error (calculated as propagated error of the slopes from the both tests), we propose to compare the convergence criterion $f = |1 - C_{FT}/C_{FS}|$ with this error (C_{FT} is the slope parameter of fracture toughness test, and C_{FS} is the slope parameter of three-points bending test). Following the rule of error propagation, the resulting error equals to $C_{FT}\sqrt{(\sigma_{FT}/C_{FT})^2 + (\sigma_{FS}/C_{FS})^2}/C_{FS}$ where σ_{FT} and σ_{FS} are the uncertainty of C_{FT} and C_{FS}, respectively, as shown in **Table 4.2** and **4.3**. If the propagated error is larger than the convergence criterion f, the two slope parameters can be considered as agreed. The propagated error and f of IGP T-L are found to be 0.57 and 0.13, respectively. Hence, the slope parameters for the flexural strain obtained from the miniaturized 3PB tests are very close to the slope parameters measured for the fracture toughness using standardized DCT geometry. Because of this, the flexural strain measurements can be proposed as a complimentary method to define the transition temperature range and therefore to guide and minimize the number of fracture toughness tests to determine DBTT.

The complementary approach can be implemented in the following way. Since the slope parameters of both 3PB and DCT fracture toughness test are similar, and given that K_{base} is known, it should be possible to deduce the K_{Jc}-Temperature curve by performing a set of fracture toughness tests at a single temperature. Of course, this curve can be determined only in the transition temperature range and will not cover the temperature range where ductile tearing is observed. a

We now assess our approach on the example of the ATW material, whose fracture toughness is best fitted by the Boltzmann sigmoidal function (**equation 4.3**). The function requires four parameters: the slope parameter *C*, K_{base}, K_{top}, and T_{half}. The slope parameter *C* is taken from the 3PB tests (**Table 4.2**). As shown in **Table 4.3**, K_{base} for both materials is around 9 $\mathrm{MPa}\sqrt{\mathrm{m}}$. In order to assess the influence of this parameter on the prediction of the K_{Jc}-Temperature curve, it is varied in the range of 5-10 $\mathrm{MPa}\sqrt{\mathrm{m}}$. K_{top} and T_{half} are calculated from the following equations:

$$K_{top} = \frac{K_{Jc1} - \alpha K_{Jc2}}{1 - \alpha} \tag{4.7}$$

$$T_{half} = T_2 + \frac{ln\left(\frac{K_{top} - K_{Jc2}}{K_{Jc2} - K_{base}}\right)}{C} \tag{4.8}$$

where K_{Jc1} is the fracture toughness at temperature equal to $T_{5\%}$, which is equal to 23 $\mathrm{MPa}\sqrt{\mathrm{m}}$, the constant α is equal to $exp\left[CT_2 - CT_1 +\right.$

$\ln\left(\frac{K_{Jc1}-K_{base}}{K_{Jc2}-K_{base}}\right)\Big]$, and K_{Jc2} has to be obtained by the fracture toughness tests at T_2. The temperature T_2 can be selected according to the transition temperature range determined from 3PB tests.

For instance, if T_2 is taken equal to 550 °C, the constructed functions for both ATW and IGP materials are shown in **Figure 4.8**. The predicted curves of both materials match reasonably well the experimental points in the transition temperature range. The variation of K_{base} does not have a strong influence on the K_{Jc} curve in the transition temperature range. As a result, the shift of the DBTT after irradiation can be determined using the same methodology in two steps. In step 1, a set of 3PB tests is performed to identify the transition temperature range, slope parameter *C*, $T_{5\%}$ and T_2. In step 2, a set of fracture toughness tests is performed at T_2 to deduce K_{top} and T_{half}. The selection of T_2 is very important since it must be higher than the DBTT but still comply with the criteria of validity of K_{Jc} according to ASTM E1820. Moreover, the fracture toughness has a larger spread at high temperature. Therefore, a sufficient number of specimens (at least 3 specimens) is required to reliably determine a K_{Jc2} value.

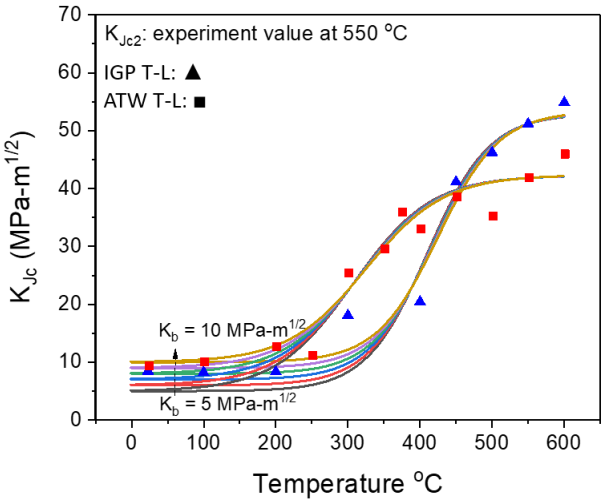

Figure 4.8. Boltmann sigma curve single temperature fitting approach

The main objective of this approach is to reduce the number of test specimens required to assess the DBTT shift after neutron irradiation. With this respect, three important warnings regarding the proposed approach

should be mentioned:

(i) the application of the equivalent slope *C* for non-irradiated and irradiated materials implies that the ductile-to-brittle transition is controlled by the same type of thermally activated mechanisms (e.g. activation of screw dislocation movement). Should the irradiation change the main mechanism of the plastic deformation, the *C* parameter must be redefined, which can be done by 3PB tests. In this case, the assessment of the microstructure becomes important and extra information to substantiate the mechanical testing procedure is required.

(ii) the assumption that K_{base} for irradiated materials is the same as that for non-irradiated material remains valid as long as the grain microstructure and texture is not altered by the irradiation. In the case of irradiation at high temperature, removal of texture and some partial recrystallization may happen in addition to the formation of neutron irradiation defects. In this situation, the ambient microstructure (i.e. grain size, grain shape, dislocation density) before and after irradiation will no longer be the same and hence K_{base} can differ as well. However, a moderate variation of K_{base} (i.e. 5-10 $\mathrm{MPa}\sqrt{\mathrm{m}}$;) does not lead to the strong impact of the transition temperature, as shown above.

(iii) besides the shift of DBTT after neutron irradiation, the upper shelf of the fracture toughness is also known to decrease. Therefore, the approach requires further validation whether the K_{Jc} value at $T_{5\%}$ for neutron irradiated material is equal to 23 $\mathrm{MPa}\sqrt{\mathrm{m}}$.

4.3.2. Linking microstructure and fracture mechanism

The results of the mechanical tests show a difference of 85 °C in the DBTT (determined by $T_{5\%}$) and in the fracture behavior between IGP and ATW grades. As summarized by Bonnekoh, et al. [20, 21], the DBTT can be influenced by aspect ratio of the grains, impurities, lattice defects, and crystallographic texture (the degrees of impact decreases respectively). Since the density of LAGB, initial density of dislocations and grain size aspect ratio of both materials on fracture plane (ND-LD plane) are similar, the difference in the DBTT could originate from impurities and crystallographic texture.

Because of the difference in the manufacturing process, the microstructure

of the IGP and ATW materials differs as well, as shown in Fig.1. The grains of IGP exhibit a carrot-like shape, while the ATW T-L grains have pancake-like shape. Following the literature [4-6, 12, 13, 22, 23], the fracture toughness and the DBTT depend on the crystallographic plane and direction along which the crack(s) propagate. For example, the activation energy for the ductile to brittle transition (Q_{DBT}) in the case of $\{001\}\langle 100\rangle$ crack system (where $\{001\}$ is the fracture plane and $\langle 100\rangle$ is the crack propagation direction) is higher than for the $\{110\}\langle 1\bar{1}0\rangle$ crack system [5, 6, 12]. Moreover, from the results of P. Gumbsch, et al. [6], the crystallographic direction, in which the crack propagates, has stronger influence on the DBTT than the crystallographic plane that is parallel to the crack surface. The effect of texture on DBTT can be observed from IGP materials, which has high fraction of $\{001\}$ planes (higher DBTT than $\{110\}$ planes if the crack propagation direction is $\langle 100\rangle$ [6]) along the fracture plane and a high fraction of $\langle 100\rangle$ directions (higher DBTT than $\langle 110\rangle$ directions [6]) along LD (crack propagation direction), as indicated from **Table 4.4**. And these high fraction of $\{001\}$ planes and of $\langle 100\rangle$ directions can be the reason why the IGP has higher DBTT than ATW. Thus, the difference in the texture of IGP and ATW provides an explanation of the reasons for the difference in the DBTT and in the fracture surface pattern.

Besides crystallographic texture, one should keep in mind that the two materials have slightly different chemical composition. However, at temperature significantly below the DBTT (for instance, room temperature), the effect of impurities on the fracture behavior can be ignored [24]. Therefore, the main factor that influences the fracture behavior is likely the orientation and morphology of grains, which is known to play a key role [17, 18, 25, 26]. As indicated by Prakash et al. [26], the intergranular failure will occur in the fracture process zone if the kink angle between grain boundary and crack propagation direction (see **Figure 4.9a**) is smaller than a threshold angle (the threshold angle is around 50^{o} and will be smaller if the cohesive strength of grain boundary is higher); in other words, the grain will have transgranular brittle failure if the kink angle is larger than the threshold angle.

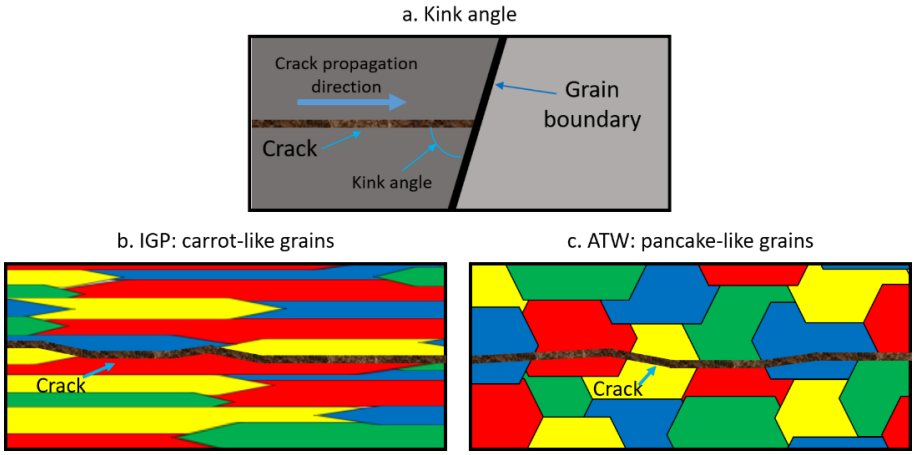

Figure 4.9. (a) Kink angle between grain boundary and crack propagation direction; (b) IGP and (c) ATW are the scheme of crack propagation route in TD-LD plane at low temperature

In the ND-LD plane, the fracture surface of IGP T-L exhibits a very high fraction of intergranular fracture (around 90%) because the material has carrot-like grains (high aspect ratio, as shown in **Table 4.1**) along the crack propagation direction; as a result, the kink angle is very small, as shown schematically in **Figure 4.9b**. Unlike IGP T-L, ATW T-L samples have pancake shaped grains (low aspect ratio, as shown in **Table 4.1**), which are oriented normal to the fracture surface. Consequently, the kink angle is higher in most of the cases, as shown in **Figure 4.9c**. And in agreement with this, the fracture surface of ATW T-L shows higher fraction of transgranular brittle fracture (around 60%) and the measured fracture toughness value of ATW T-L is slightly higher than the one of IGP T-L at room temperature.

As the test temperature increases, the effect of impurities (which can strengthen or weaken the grain boundary cohesion) may become important [27]. Therefore, impurities might be the reason why the fracture behavior of both materials changes. Impurities, segregating to the grain boundaries, can reduce the cohesive strength between sub-grains and/or grains. For IGP, at temperature near $T_{5\%}$, the fracture surface has both intergranular and transgranular brittle fracture patterns since the purity of the material is higher and the grains with $\langle 100 \rangle$ directions parallel to LD (the fraction is around 11%, as shown in **Table 4.4**) start to act as a competitive weakest links because of the high Q_{DBT} [5]. As a result, the fraction of intergranular fracture is reduced to ~10% in IGP T-L near the DBTT. But, for ATW, the impurity concentration is higher, and therefore, the transgranular brittle fracture is

reduced from 60% to 30%.

At temperature exceeding the DBTT, both $\{hkl\}\langle 100\rangle$ and$\{hkl\}\langle 110\rangle$ crack system become ductile (the Q_{DBT} is related to the activation energy for the dislocation slip [12]). Thus, ductile fracture features, i.e. delamination, become evident in the IGP as a result of the plastic deformation and dislocation slip. On the other hand, in the ATW, some grains still demonstrate cleavage fracture. Therefore, the fracture surface exhibits partial transgranular brittle fracture (around 30% of the fracture area). Keeping in mind that the difference between the texture of IGP T-L and ATW T-L is not just confined with the texture components that had been mentioned above, the detail of other texture components will require further investigation.

4.4. Summary

The fracture toughness and maximum flexural strain have been assessed for two commercial tungsten grades produced by European and Chinese companies. The grades are produced to comply with ITER specifications and the mechanical tests were performed for the T-L orientation, which is relevant for plasma facing components, accounting for the texture of the materials. On the basis of the obtained results by performing the mechanical tests and microstructural analysis, we come to the following conclusions:

I. The fracture toughness and three point bending tests were performed in the temperature range of RT-600°C, where the transition from ductile to brittle behavior is expected. The temperature dependence of the K_{Jc} and flexural strain follow very similar variation, which suggests that the three point bending tests can be used to explore the temperature bounds of the ductile to brittle transition range with high confidence.

II. The dependence of the fracture surface on temperature (K_{Jc}-T curve) in the transition temperature range can be derived by combination of the three point bending tests and single temperature fracture toughness test. Such approach can be used to assess the DBTT of the neutron irradiated material which is already well pre-characterized in the non-irradiated conditions. If proved to be valid, the approach will enable to reduce the number of samples and tests to construct K_{Jc}-T curve. In this work, we have simulated the construction of the K_{Jc}-T curve for two commercial tungsten grades, which has been shown to be rather accurate if one overlays the experimental fracture toughness data obtained in the whole transition temperature range. The next step is to demonstrate the robustness of this approach and to perform heat treatments and proton irradiation (generating 1 mm uniform damage) on non-irradiated materials to change its DBTT that should be captured by 3PB tests.

III. Considering that the temperature at which the material deforms up to 5% of flexural strain can be taken as the DBTT (criterion induced in [3]), the fracture toughness at $T_{5\%}$ was calculated for the two grades by interpolating the experimental data and was found to be same for both being equal to 23 $\mathrm{MPa}\sqrt{\mathrm{m}}$. The fracture surfaces of the bending samples and disk compact tension samples were compared at $T_{5\%}$ for both materials, and a good correspondence of the microstructural features and morphology observed in the two kinds of samples is found. These findings substantiate further the applicability of the miniaturized

three point bending tests to assess the transition temperature range in forged fine-structured tungsten.

IV. The transition temperature $T_{5\%}$ of the IGP and ATW materials is found to be, respectively, 389 +16/-19 ^{o}C and 305 ± 12 ^{o}C. The difference in the transition temperature, fracture behavior, and fracture toughness measured for the two materials is discussed on the basis of the microstructure assessed by electron back-scattering diffraction and by fracture surface analysis through scanning electron microscopy.

4.5 Reference

[1] T. Hirai, S. Panayotis, V. Barabash, Et.al., Use of tungsten material for the ITER divertor, Nuclear Materials and Energy 9 (2016) 1-7.
[2] A. Dubinko, C. Yin, D. Terentyev, A. Zinovev, M. Rieth, S. Antusch, M. Vilémová, J. Matějíček, T. Zhang, Plastic deformation in advanced tungsten-based alloys for fusion applications studied by mechanical testing and TEM, International Journal of Refractory Metals and Hard Materials (2020) 105409
[3] D.H. Lassila, F. Magness, D. Freeman, Ductile-Brittle Transition Temperature testing of tungsten using the three-point bend test, Lawrence Livermore National Lab., CA (United States), 1991.
[4] J. Ast, J. Schwiedrzik, J. Wehrs, D. Frey, M.N. Polyakov, J. Michler, X. Maeder, The brittle-ductile transition of tungsten single crystals at the micro-scale, Materials & Design 152 (2018) 168-180.
[5] A. Giannattasio, S.G. Roberts, Strain-rate dependence of the brittle-to-ductile transition temperature in tungsten, Philosophical Magazine 87(17) (2007) 2589-2598.
[6] P. Gumbsch, J. Riedle, A. Hartmaier, H.F. Fischmeister, Controlling factors for the brittle-to-ductile transition in tungsten single crystals, Science 282(5392) (1998) 1293-1295.
[7] D. Rupp, S.M. Weygand, Loading rate dependence of the fracture toughness of polycrystalline tungsten, J Nucl Mater 417(1-3) (2011) 477-480.
[8] P. Gumbsch, Brittle fracture and the brittle-to-ductile transition of tungsten, J Nucl Mater 323(2-3) (2003) 304-312.
[9] M. Faleschini, H. Kreuzer, D. Kiener, R. Pippan, Fracture toughness investigations of tungsten alloys and SPD tungsten alloys, J Nucl Mater 367 (2007) 800-805.
[10] W. Tyson, W.J.S.S. Miller, Surface free energies of solid metals: Estimation from liquid surface tension measurements, Surface Science 62(1) (1977) 267-276.
[11] B. Gludovatz, S. Wurster, A. Hoffmann, R. Pippan, Fracture toughness of polycrystalline tungsten alloys, Int J Refract Met H 28(6) (2010) 674-678.
[12] J. Reiser, J. Hoffmann, U. Jäntsch, M. Klimenkov, S. Bonk, C. Bonnekoh, M. Rieth, A. Hoffmann, T. Mrotzek, Ductilisation of tungsten (W): On the shift of the brittle-to-ductile transition (BDT) to lower temperatures through cold rolling, International Journal of Refractory Metals and Hard Materials 54 (2016) 351-369.
[13] V. Nikolić, S. Wurster, D. Firneis, R. Pippan, Fracture toughness evaluation of UFG tungsten foil, International Journal of Refractory Metals and Hard Materials 76 (2018) 214-225.

[14] S. Wurster, B. Gludovatz, R. Pippan, High temperature fracture experiments on tungsten-rhenium alloys, Int J Refract Met H 28(6) (2010) 692-697.
[15] V. Nikolic, S. Wurster, D. Firneis, R. Pippan, Improved fracture behavior and microstructural characterization of thin tungsten foils, Nuclear Materials and Energy 9 (2016) 181-188.
[16] Z.S. Levin, A. Srivastava, D.C. Foley, K.T. Hartwig, Fracture in Annealed and Severely Deformed Tungsten, Materials Science & Engineering: A (2018).
[17] M. Mahler, E. Gaganidze, J. Aktaa, Simulation of anisotropic fracture behaviour of polycrystalline round blank tungsten using cohesive zone model, J Nucl Mater 502 (2018) 213-219.
[18] D. Rupp, S.M. Weygand, Experimental investigation of the fracture toughness of polycrystalline tungsten in the brittle and semi-brittle regime, J Nucl Mater 386-88 (2009) 591-593.
[19] D. Rupp, S. Weygand, Anisotropic fracture behaviour and brittle-to-ductile transition of polycrystalline tungsten, Philosophical Magazine 90(30) (2010) 4055-4069.
[20] C. Bonnekoh, A. Hoffmann, J. Reiser, The brittle-to-ductile transition in cold rolled tungsten: On the decrease of the brittle-to-ductile transition by 600 K to− 65° C, International Journal of Refractory Metals Hard Materials 71 (2018) 181-189.
[21] C. Bonnekoh, U. Jäntsch, J. Hoffmann, H. Leiste, A. Hartmaier, D. Weygand, A. Hoffmann, J. Reiser, The brittle-to-ductile transition in cold rolled tungsten plates: Impact of crystallographic texture, grain size and dislocation density on the transition temperature, International Journal of Refractory Metals Hard Materials 78 (2019) 146-163.
[22] C. Bohnert, N. Schmitt, S. Weygand, O. Kraft, R. Schwaiger, Fracture toughness characterization of single-crystalline tungsten using notched micro-cantilever specimens, International Journal of Plasticity 81 (2016) 1-17.
[23] J. Ast, M. Göken, K. Durst, Size-dependent fracture toughness of tungsten, Acta Materialia 138 (2017) 198-211.
[24] B. Gludovatz, S. Wurster, T. Weingärtner, A. Hoffmann, R. Pippan, Influence of impurities on the fracture behaviour of tungsten, Philosophical Magazine 91(22) (2011) 3006-3020.
[25] E. Gaganidze, D. Rupp, J. Aktaa, Fracture behaviour of polycrystalline tungsten, J Nucl Mater 446(1-3) (2014) 240-245.
[26] C. Prakash, H. Lee, M. Alucozai, V. Tomar, An analysis of the influence of grain boundary strength on microstructure dependent fracture in polycrystalline tungsten, International Journal of Fracture 199(1) (2016) 1-20.
[27] J. Morniroli, M. Gantois, M. Lahaye, Brittle fracture of polycrystalline tungsten, Journal of Materials Science 20(1) (1985) 199-206.

Chapter 5
Ductile to Brittle Transition Temperature of advanced tungsten alloys for nuclear fusion applications deduced by miniaturized three-point bending tests

5.1. Experimental details

5.1.1. Materials

Nine different types of tungsten grades are investigated in this study:

- There are two commercial ITER grade pure tungstens, which are named IGP and ATW produced by Plansee, Austria, and AT&M, China, respectively. Respectively, IGP and ATW has carrot-like grains and pancake-like grains because of the different processes after powder metallurgy sintering, where IGP is double hammered into a rod with a 35 mm x 35 mm cross section, and ATW is rolled into 13 mm thick plate.
- Another pure tungsten grade is made of a fine grain tungsten (FG) produced by spark plasma sintering (SPS) is provided by the Institute of Plasma Physics, Czech Republic.
- Beside pure tungsten, there are three kinds of potassium doped tungsten alloys with pancake-like grains: potassium doped pure tungsten (ALK), potassium doped tungsten alloyed with 3 wt% of rhenium (ALKR), and heavily deformed potassium doped pure tungsten (HDK). ALK and ALKR, which are manufactured by A.L.M.T., are rolled into 7 mm sheet [1]. HDK is heavily deformed by rolling into 1 mm sheet, as developed by Karlsruhe Institute of Technology, Germany.
- Finally, three kinds of particle reinforced tungsten are also studied, they are reinforced with 1 wt% TiC (W1TiC), 2 wt% Y_2O_3 (W2YO), and 0.5 wt% ZrC (W0.5ZrC). W1TiC and W2YO are produced with powder injection molding (PIM) and provided by Karlsruhe Institute of Technology, Germany. Because the rolling or forging is not applied during the PIM process, W1TiC and W2YO have equiaxed grains.

Institute of Solid State Physics, China provides the W0.5ZrC, which is rolled and treated with thermal mechanical treatment (TMT) in order to get semi-equiaxed grains.

The tungsten grades are categorized according to their manufacturing process or composition into three groups, which are commercial pure tungsten grades (IGP and ATW), advanced grades (HDK, ALK, ALKR, FG), and particle reinforced grades (W1TiC, W2YO, W0.5ZrC). The inverse pole figures of these tungsten grades are shown in **Figure 5.1** with the indication of longitudinal direction (LD) and transverse direction (TD). **Table 5.1** provides the composition, and median equivalent diameter (D50), 10% equivalent diameter (D10), and 90% equivalent diameter (D90) of the grains, which are defined as the equivalent grain sizes that are larger than 50%, 10%, and 90% of the total grains, respectively.

Table 5.1. Chemical composition and grain size of different tungsten grades. The compositions of the commercial grades are provided by the manufacturer.

Materials	Major composition (by weight)	D10 (µm)	D50 (µm)	D90 (µm)
IGP	Pure W (> 99.97 %)	15.74	87.44[2]	151.51
ATW	Pure W (> 99.94 %)	21.16	60.28[2]	139.73
HDK	Pure W + 60 ppm of K[3]	3.47	26.52	111.05
ALK	Pure W + 30 ppm of K[4]	7.73	37.04	108.92
ALKR	97 % W + 3 % Re + 28 ppm of K[4]	6.98	32.65	60.77
FG	Pure W (> 99.7 %)[5]	4.74	9.36[2]	15.64
W1TiC	99 % W + 1 % TiC[6]	4.06	7.76[2]	12.06
W2YO	98 % W + 2 % Y_2O_3[6]	4.09	7.32[2]	11.76
W0.5ZrC	99.5 % W + 0.5 % ZrC[7]	2.55	6.66[2]	14.15

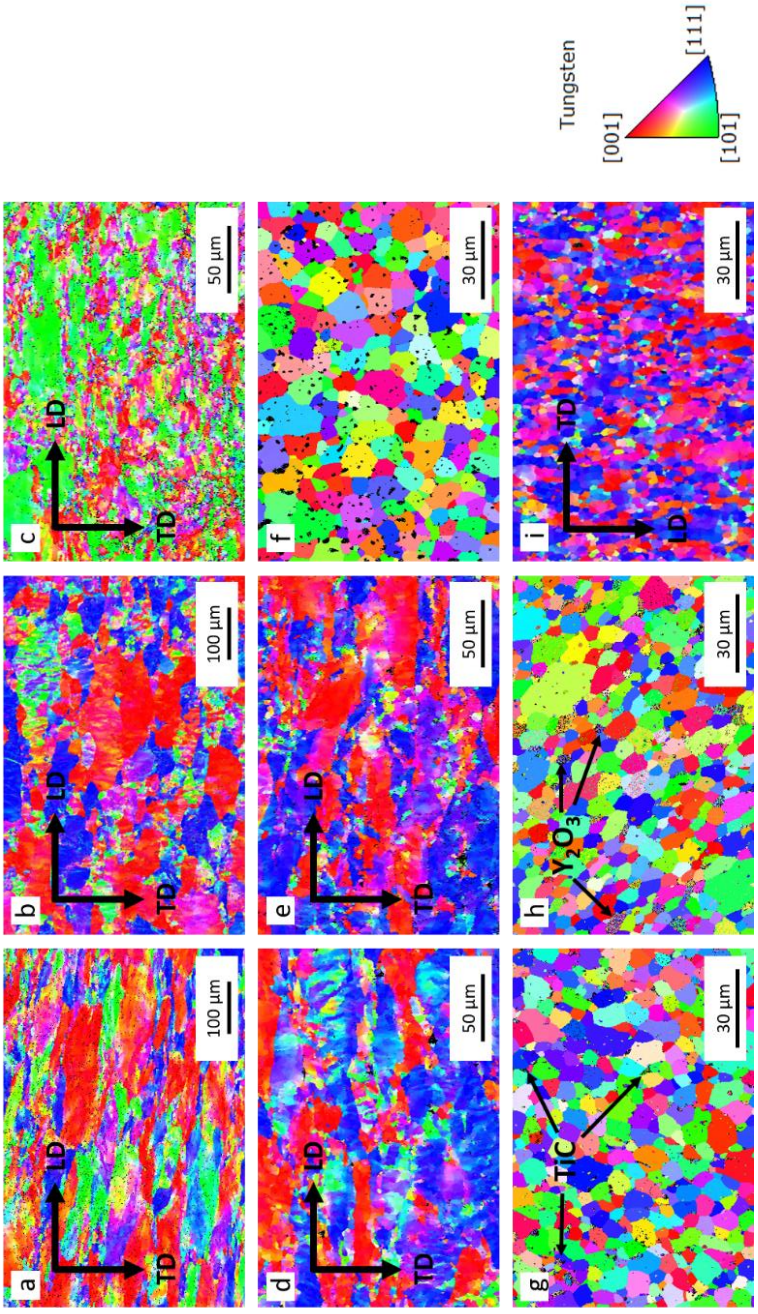

Figure 5.1. Inverse pole figure of different tungsten grades: (a) IGP; (b) ATW; (c) HDK; (d) ALK; (e) ALKR; (f) FG; (g) W1TiC; (h) W2YO; (i) W0.5ZrC. The figure for IGP, ATW, FG, W1TiC, W2YO, W0.5ZrC has been reported in our previous work [2].

5.1.2. Microstructural investigation and fitting method

The electron back-scatter diffraction (EBSD) analysis is performed using an OIM analysis software. The grain boundary analysis is based on the scan with a step size of ~0.54 µm in an area around 270 x 200 µm^2 on the plane normal to ND. Low angle grain boundaries (LAGB) and high angle grain boundaries (HAGB) are defined as the boundaries with a misorientation angle from 2 to 15° and larger than 15°, respectively. The coincidence site lattices (CSL) boundaries are determined by the Brandon's criterion $\Delta\theta_{max} = \theta\Sigma^{-n}$, where $\Delta\theta_{max}$ is the maximum permissible deviation from coincidence, θ is a constant equal to 15°, n is a constant equal to 0.5, and the boundary fraction is from Σ3 to Σ27. The grain boundary density for each type of grain boundary is defined as the total length of each type of boundary per unit area.

By performing the tests in the ductile to brittle transition region, the flexural strain increases from zero to above 10% within a relatively narrow temperature interval. Hence, one can extract the DBTT by fitting the obtained values and setting a threshold for the flexural strain above which the material could be considered as ductile. The fitting method is a modified version of the one used in our previous work [8]. Here, the upper shift of the flexural strain (FS_{top}) is defined as 10%, and the lower base of the flexural strain (FS_{base}) is defined as 0%. Therefore, a flexural strain higher than the defined upper shift will be reported as having a value of 10%. And the equation for fitting the flexural stain transition curve reads as follow:

$$FS(T) = \frac{10\%}{1+exp\left(C\left(T_{half}-T\right)\right)} \quad \textbf{(5.1)}$$

where C is the slope of the transition curve; T is the test temperature. T_{half}, which is also defined as the DBTT in this study (following the criterion proposed by [9]), is the temperature corresponding to flexural strain equal to 5%.

5.2. Results

5.2.1. Grain boundary density

The grain boundary density and fraction of HAGB, LAGB, and CSL are shown in **Figure 5.2**. The mechanically processed tungsten grades (i.e., IGP, ATW, HDK, ALK, ALKR, and W0.5ZrC) exhibit a much larger density of LAGB than the grades (i.e., FG, W1TiC, and W2YO) manufactured by the advanced processes. The deformation process during rolling or hammering introduces dislocations and LAGB (which can be seen as an array of dislocations). The degree of deformation influences the amount of dislocations and LAGB. As a result, HDK has the highest LAGB density because it is heavily deformed during the manufacturing process. Moreover, with the presence of the potassium bubbles, which will suppress the migration of grain and dislocation boundaries [3], the removal of LAGB during high temperature mechanical process and heat treatment will be suppressed, which results in a smaller grain size. This can also explain why the HAGB and LAGB density of HDK, ALK, and ALKR are higher than the one of IGP and ATW. The HAGB density of W0.5ZrC, W1TiC, W2YO, and FG are also high since they involve a small grain size, especially for W0.5ZrC, which has the highest HAGB density and the smallest grain size because of the TMT [7]. CSL boundary has a lower boundary energy compared to other HAGB and therefore has better resistance to crack propagation (i.e. higher cohesion bonding and lower capacity to suppress plastic slip). Although the absolute CSL density varies in the studied tungsten grades (i.e. W0.5ZrC and HDK have high CSL density), the ratio of CSL boundaries to HAGB fraction is similar for all the tungsten grades, being around 0.11 to 0.15. Given that the fraction of CSL boundaries is very small compared to LAGB and/or HAGB, we include CSL boundaries into a population of HAGB in further discussion.

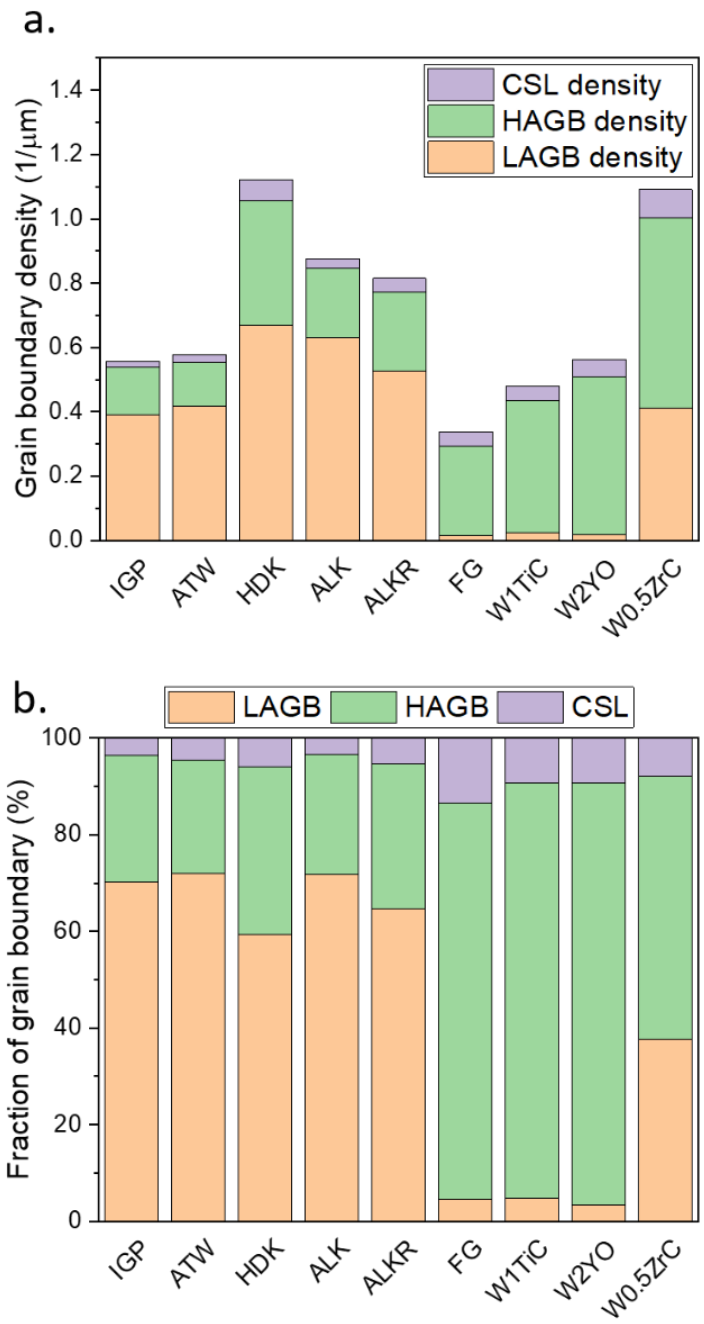

Figure 5.2. (a) Grain boundary density and (b) fraction of grain boundary of different tungsten grades

5.2.2. Three-point bending tests

The variation of flexural strain as a function of temperature and the fitted curves are shown in **Figure 5.3**. The fitting parameters are gathered in **Table 5.2**. The orientation of the specimens strongly affects the DBTT, with L-T specimen exhibits lower DBTT than T-L ones, as shown in **Figure 5.3a** and **c**. Compared to the commercial grades IGP and ATW in **Figure 5.3a**, the potassium doped tungsten has lower DBTT, especially ALKR L-T, with a DBTT below 0 °C, as shown in **Figure 5.3b**. The addition of Re is indeed known to enhance the mobility of ½<111> screw dislocations (due to modification of its core structure) and thereby to reduce the DBTT of W-Re alloys [10]. Moreover, the grain size in the potassium doped tungsten grades is smaller than in the commercial pure grades. Smaller grain size will result in a higher density of dislocation sources, which also contributes to the improvement of low temperature ductility [11, 12]. As a result, the toughness and strength of such materials should be higher together with the reduced DBTT compared to tungsten with a larger grain size.

Tungsten grades manufactured without mechanical treatment like rolling or forging have a higher DBTT. Moreover, the temperature span of the transition of W1TiC, W2YO, and FG are different from other tungsten grades, where W1TiC and W2YO have a wider temperature span, and FG has a very sharp transition. The sharp transition of FG results in missing data points in the transition region and therefore has a very large standard error for the fitting parameters. This sharp transition of FG has also been observed in fracture toughness tests [13].

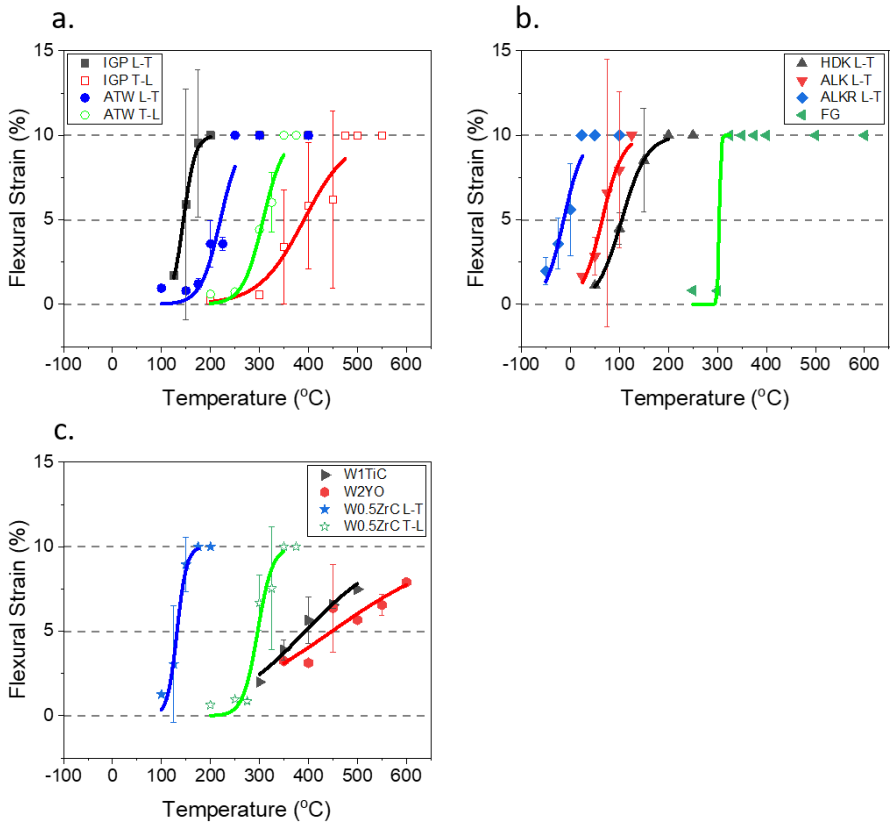

Figure 5.3. The flexural strain of different tungsten alloys as a function of temperature. (a) Commercial tungsten grades; (b) Advanced tungsten grades; (c) Particle reinforced tungsten grades. The data of IGP T-L and ATW T-L can be referred to our previous work [8].

Table 5.2. Fitting parameters for the flexural strain transition curve of various tungsten grades

Materials	T_{half}	C
IGP L-T	145 ± 1	0.085 ± 0.007
IGP T-L	391 ± 13	0.022 ± 0.006
ATW L-T	220 ± 9	0.050 ± 0.021
ATW T-L	307 ± 6	0.048 ± 0.014
HDK L-T	105 ± 2	0.039 ± 0.002
ALK L-T	65 ± 3	0.048 ± 0.007
ALKR L-T	-14 ± 7	0.051 ± 0.018
FG	304 ± 17141	0.645 ± 2925.228
W1TiC	394 ± 8	0.012 ± 0.002
W2YO	448 ± 20	0.008 ± 0.002
W0.5ZrC L-T	132 ± 3	0.103 ± 0.025
W0.5ZrC T-L	296 ± 5	0.067 ± 0.020

5.3. Discussion

5.3.1. Dependence of DBTT on grain orientation

Early studies conducted by Reiser et al. [14] have shown that for the heavily deformed W plate (HDK, here) the DBTT in the rolling and transversal direction differs by 100 ^{o}C. At the same time, Shen et al. [15] reported the difference of DBTT in rolling and transversal direction to be about 50 ^{o}C for the commercial rolled W (ATW, here) based on tensile tests, which is in a reasonable agreement with the result obtained here (~100 ^{o}C). As was recently studied by Oude Vrielink et al. [16], the dependence of the DBTT on the loading direction can be understood by introducing the cleavage criterion based on the maximum principal stress at grain level (given the grain size distribution and crystallographic texture). However, the modeled DBTT difference between the transversal and rolling direction (predicted based on the crystallography texture and the grain distribution of ATW material) was found to be only 16°C, which is much lower compared to the experimental data. The explanation for this difference comes from the fact that different fracture mechanisms (or their mixture) might operate in the different loading directions of rolled/forged tungsten. Moreover, the shape of the elongated grains and their orientation will also influence the DBTT since the anisotropy in the fracture toughness increases with increasing aspect ratio [11]. This is confirmed in **Figure 5.4** showing that the DBTT difference increases monotonically with the aspect ratio. The IGP has the highest DBTT difference between L-T and T-L orientation, equal to ~250 ^{o}C, and with an aspect ratio of 9.79 [8], followed by W0.5ZrC (DBTT difference of ~160 ^{o}C and aspect ratio of 3.12), and finally ATW (DBTT different of ~90 ^{o}C and aspect ratio of 2.42 [8]).

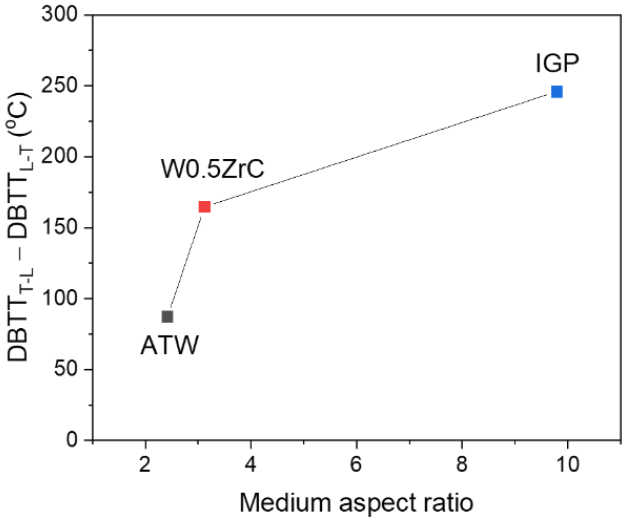

Figure 5.4. Anisotropy of DBTT (quantified as the difference of DBTT between T-L and L-T orientation) as a function of median aspect ratio. The median aspect ratio of IGP and ATW are taken from [8].

The possible explanations for the effect of grain shape on the DBTT are presented in the following. First, the correspondence between the elongated grains and the crack propagation plane are different for T-L and L-T orientations, as shown in **Figure 5.5a**. For example, the orientation of the elongated grains of IGP T-L samples is along the crack propagation plane. As a result, the crack propagation between elongated grain boundaries will not be deviated/deflected by the grains [8], and that is why IGP has the largest DBTT difference from T-L and L-T orientation. Second, since the mean free path for dislocation glide varies with the relative angle between the major axis of elongated grains (including subgrains) and the loading direction, the mean free path for dislocation glide in grains or subgrains of T-L orientation is shorter than the one of L-T orientation. Hence, for the T-L orientation, dislocation pile-ups on GBs form at lower values of strain, creating stress concentration and leading to earlier micro-crack nucleation, globally resulting in a lower toughness [11]. Thus, the DBTT of a T-L orientated sample is higher than the L-T. Third, the density of grain boundary triple junctions close to the fracture plane of L-T orientation is different from the one of T-L orientation. As presented in **Figure 5.5a**, section A and section B correspond to the area around the fracture plane for L-T and T-L orientations, respectively. Section A has a larger number of grain boundary triple junctions (indicated

as yellow dots) than section B. Upon application of a tensile load to the sample, the stress distributed on each triple junction of the L-T sample is lower than the one of T-L sample. As a result, the fracture strength (the quotient of load at fracture to the actual fracture cross-section area) of the L-T sample will be higher than the T-L sample. This simple picture is supported by the tensile test results from our earlier studies [2, 17], as shown in **Figure 5.5b**. The fracture strength of the tensile sample tested in LD (IGP-L, ATW-L, and W0.5ZrC-L) is regularly higher than the one tested in TD (IGP-T, ATW-T, and W0.5ZrC-T). The fracture plane of LD-loaded and TD-loaded tensile samples is the same as the fracture plane of L-T and T-L bending samples, respectively. The difference of yield strength and ultimate tensile strength for LD and TD loads is small at a test temperature of 600 ^{o}C since the plastic deformation at the temperature of 600 ^{o}C is mainly governed by the gliding of screw dislocations, and the screw dislocations in tungsten are fully activated at this temperature. Since the yield strength and ultimate tensile strength are almost the same for both L-T and T-L fracture plane, the one with higher fracture strength, which is L-T orientation, exhibits lower DBTT.

Another important assumption utilized in the model of Oude Vrielink et al. [16] is that the evolution of plastic deformation (i.e., strain to fracture) is mainly driven by the activation of screw dislocations, which might not necessarily be true in the case of heavily deformed material, where a high density of LAGB with mixed dislocations is present. The activation of the plastic slip by mixed and edge dislocations nucleated from the LAGB may also contribute to the macroscopic plastic deformation, and therefore the criterion for the DBTT can be fulfilled below the temperature of the screw dislocation activation.

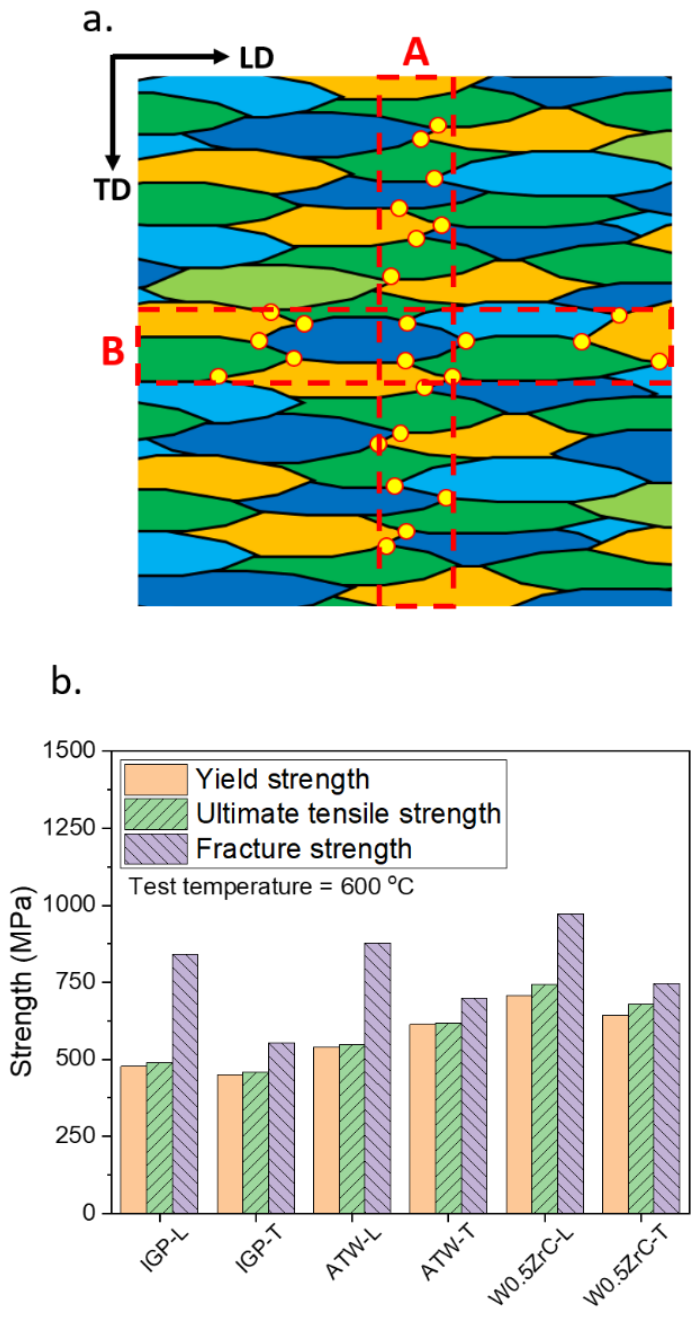

Figure 5.5. (a) Grain boundary triple junctions of tungsten with elongated grains; (b) Yield strength, Ultimate tensile strength, and fracture strength of the tensile sample made of IGP, ATW, and W0.5ZrC tested along LD and TD orientation [2, 17].

5.3.2. DBTT and grain boundary density

The relationship between DBTT and total HAGB density, which is the sum of CSL density and HAGB density, does not lead to a clear trend, as shown in **Figure 5.6a**. The possible reason is that the presence of HAGB might not be the main factor that affects the DBTT. However, a better trend can be observed if one separates tungsten grades into two groups: the first group is the commercial tungsten grades and advance tungsten grades, and the second group is particle reinforced tungsten grades. The two groups now show that the DBTT reduces with increasing total HAGB density. Besides the effect of alloying elements and strengthening particles, this phenomenon can be related to an increase of dislocation sources as the grains are smaller in size [11, 12]. Moreover, a higher total HAGB density can reduce the density/size of the clusters of impurities segregating to grain boundaries, and thus the strength of the grain boundary increases [18].

However, when discussing the effect of grain boundary on DBTT, the HAGB density is not the only controlling factor. As shown in **Figure 5.6b**, the DBTT has a strong and clear relationship to the LAGB density, where higher LAGB density results to lower DBTT. As summarized by Bonnekoh, et al. [19], LAGB can act as dislocation source and thus reduce the DBTT. Moreover, the triple junctions of the LAGB or HAGB can act as a source of stress-concentration and crack nucleation. Although the material with high LAGB and HAGB density will have a larger number of stress-concentration sources, the average stress per source is reduced. As a result, the failure of the material is delayed to higher level strains and stresses, which means that the material has a higher toughness. The LAGB are introduced by the mechanical process like rolling or forging during manufacture. Therefore, the mechanically processed tungsten grades like potassium doped tungsten grades, commercial tungsten grades, and W0.5ZrC have lower DBTT than FG, W1TiC, and W2YO, which are produced by advanced manufacturing processes.

Although the DBTT shows a strong dependence on LAGB density, further theoretical and experimental investigation of the role played by LAGB in the overall macroscopic deformation of polycrystalline tungsten is required. At least two aspects of the plastic deformation mechanisms are to be addressed: (i) accumulation of dislocation pile-ups in front of LAGB and transmission of the dislocation slip between LAGB; and (ii) conservative grain boundary slip by displacement of the misfit dislocations available at LAGB. Clarification of these mechanisms in tungsten will help to envisage the impact of neutron irradiation on DBTT and thus to make the next step with respect to the development of the materials with controlled DBTT in the fusion operational environment.

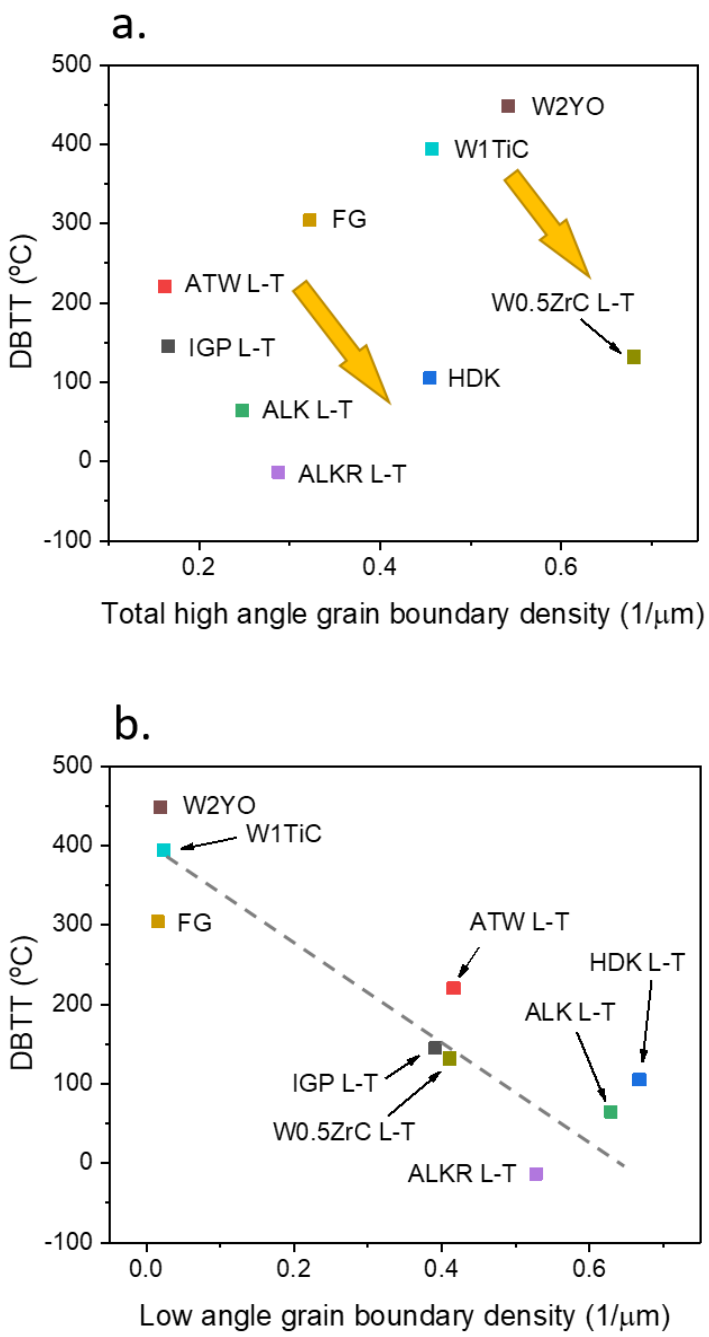

Figure 5.6. Relationship between DBTT and grain boundary density. (a) Total HAGB; (b) LAGB.

5.3.3. Pros and cons of miniaturized three-point bending tests

Prior to summarize the conclusions, the advantages and caveats of the sub-miniaturized 3PB testing techniques are discussed. Conducting mechanical testing on the neutron irradiated samples of standardized dimensions is associated with high cost and complicated logistics driven by the need of usage of hot cell (underpressurized chamber protecting operator from the ionizing irradiation emitted by the neutron irradiation samples) equipment. The neutron irradiation itself is also costly due to the large infrastructure required for the operation of material test reactors (MTR). The irradiation volume primarily defines the cost because usage of neutrons for other competing purposes (e.g. medical isotope production, silicon doping, etc.) Therefore, small size testing techniques (SSTT) [20, 21] and surrogate irradiation sources, like high energy proton or heavy ion irradiation, which can generate similar irradiation damage pattern as neutron irradiation, are introduced [22-24]. They cannot substitute neutron irradiation for the qualification of mechanical properties to be accepted by regulatory bodies, but the application of surrogate irradiation can certainly move forward the screening and down selection of the advanced materials compared to the baseline ones (for which the effect of neutron irradiation is already assessed), thereby optimizing (reducing the cost of) the test matrix to be executed on MTRs. Our earlier work presents an example, how sub-miniaturized testing was demonstrated to be capable to deduce the DBTT region in adequate agreement with the results obtained using fracture toughness samples of standardized geometry [8]. Thereby, the presented method utilizing the miniaturized three-point bending test is categorized as one belonging to the SSTT portfolio.

Since the geometry of the miniaturized three-point bending specimen is not complicated to machine, small in volume (i.e. factor 27 volume gain compared to the conventionally accepted KLST sample [25]), and rectangular in shape, it is very efficient to be used for so called “piggy-back” irradiation, when the sample load unit has limited space available. Given the limited dimensions of the sample, the gradient of the heat release and transmutation reactions (materials like tungsten can impose self-shielding effect such that transmutation at the edge of the sample is higher than in its center) under high flux neutron irradiation is also limited compared to standardized samples. Finally, a major advantage of the application of sub-miniaturized samples is their immediate readiness of the microstructural or chemical studies after the destructive mechanical testing. The application of scanning electron microscopy, focus ion beam milling, or thermal desorption spectroscopy usually is performed in glove boxed (rarely instruments are placed in hot cells) where the ALARA (as low as possible activation) principle

defines the permission on usage of the sample, and typically the maximum dose rate on sample contact is limited to 2-5 μSv/hour. In the case of the samples studied in this work, half broken 3PB samples would have a dose rate below 2 μSv/hour after receiving about 1 dpa in fission spectrum reactors (like BR2, HFIR, HFR). Hence, the samples can be immediately passed to advanced post-irradiation examination (PIE) without any extra processing. Naturally, the nuclear waste produced by the testing campaign utilizing sub-miniaturized samples is essentially reduced.

Besides the above listed advantages, the concern about the representation of the mechanical properties by the miniaturized 3PB samples compared to standardized samples should not be ignored. Indeed, in the case of sub-miniaturized samples only a small volume of the material undergoes large tensile stress and strain, which is not uniform, in addition. Given that the loaded volume is limited, a special attention needs to be paid to the sample surface preparation. The statistics of the measurements will depend on the surface roughness (the smoother – the better) and if the irradiation experiment does not allow to preserve the original surface roughness (e.g. irradiation in corrosive environment) the eventual post irradiation testing may generate invalid results. The extraction of engineering properties such as yield stress, work hardening rate, and ultimate tensile stress requires rigorous post-processing using finite element method. The validation of such procedures (i.e. extracting true stress – true strain by matching FEM with experimental load – displacement curves) requires additional tests involving tensile samples in reference and equivalent neutron irradiated state. This work is currently ongoing in support of SSTT preparation for DONES-IFMIF [26]. However, given the limited volume in which the accumulation of stress/strain is established, one may also consider the application of surrogate irradiation sources like heavy ion irradiation to damage the region mostly exposed to the tensile deformation. The application of high energy protons (exceeding several MeV) would generate the uniform damage across a thickness of ~1 mm, hence enabling to perform fully valid mechanical testing.

To sum up, the main drawbacks of the sub-miniaturized 3PB testing are: high precision sample preparation and surface roughness, lack of standardized procedure to extract major tensile properties, relatively high number of samples required to establish statistically significant result.

The main advantages are: high efficiency for occupation of the irradiation volume, simple handling for tests in hot cells, immediate (or short-term cooling time) readiness for advanced PIE; low waste.

5.4. Summary

A parametric set of miniaturized three-point bending mechanical tests is performed on various tungsten grades (in non-irradiated state) selected for the screening of their neutron irradiation. The final goal beyond this research is to validate the improvement of these tungsten grades regarding the resistance to irradiation degradation. The DBTT is determined based on the flexural bending strain criterion as applied earlier in [9, 27], which is proven to be adequate when compared with conventional fracture toughness test methods. SEM-EBSD technique is applied to support a detailed grain boundary structural analysis in order to understand and establish a relationship between the obtained DBTT and grain boundary distribution and morphology. The deduced DBTT values of the different tungsten grades are summarized in **Figure 5.7**. Overall, the DBTT varies from -25 °C up to +450 °C, depending on the grade. The hot rolled W-3%Re material in L-T orientation has the lowest DBTT of -25 °C, which is believed to be a synergistic effect of a high density of low angle grain boundaries and addition of Re. Re-free hot rolled and heavily deformed K-doped tungsten products have the DBTT below 100 °C. The main findings can be summarized as follows:

I. For the textured materials, the DBTT is orientation dependent, where L-T has a lower DBTT than T-L for the forged or rolled tungsten grades. The DBTT difference between L-T and T-L is ranging from ~90 to ~250 °C, which depends on the grain aspect ratio of the tungsten grades. The orientation dependence of the condition to start plastic deformation might have strong implications after neutron irradiation during the tokamak operation, as the grains with T-L orientation will be subject to primary loading due to the plasma heat exposure.

II. The presence of LAGB has a strong effect on the reduction of the DBTT. For all grades, the DBTT varies inversely with the LAGB density. The availability of LAGB favours plastic deformation i.e., activation of the edge and mixed dislocations located at the LAGB interfaces, which enables the plastic deformation at temperatures below the one required to activate screw dislocations. On the other hand, the presence of a high density of LAGB naturally reduces the spacing between grain boundary triple junctions, which are generally considered as sources for stress-concentration and crack nucleation. Correspondingly, the stress at which micro cracks begin to nucleate and then proceed to coalesce is delayed, effectively resulting in the higher fracture stress.

III. The mechanical (or even thermo-mechanical) processing during the manufacture (and post fabrication stress-relief) is critical for producing a material with high strength and high ductility simultaneously. Given the relationship between DBTT and the availability of LAGB, as shown here, an important step for reducing the DBTT is by rolling or forging, which could be enhanced by Re alloying. Particle reinforcement does not have such a strong positive effect on the DBTT reduction. Coupling the particle reinforcement and thermo-mechanical treatment (e.g., W-0.5ZrC) provides a considerable reduction of DBTT (down to ~150^{o}C) and resistance to high temperature recrystallization. The PIM processing (with or without strengthening particles), which does not involve any rolling or forging, leads to a relatively high DBTT even though the grain size is rather small. The high DBTT of these materials could be explained by the lack of sources for low-temperature plastic deformation.

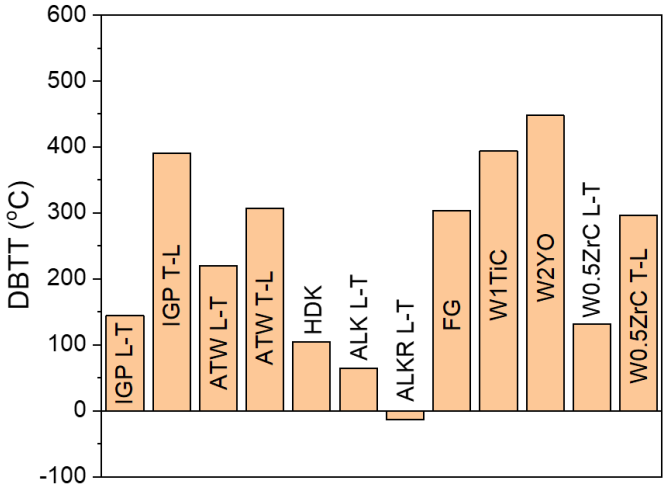

Figure 5.7. DBTT of different tungsten grades

5.5. References

[1] S. Nogami, A. Hasegawa, M. Fukuda, S. Watanabe, J. Reiser, M. Rieth, Tungsten modified by potassium doping and rhenium addition for fusion reactor applications, Fusion Eng. Des. 152 (2020) 111445.
[2] C. Yin, D. Terentyev, T. Pardoen, A. Bakaeva, R. Petrov, S. Antusch, M. Rieth, M. Vilemova, J. Matejicek, T. Zhang, Tensile properties of baseline and advanced tungsten grades for fusion applications, Int. J. Refract. Met. Hard Mater. 75 (2018) 153-162.
[3] P. Lied, C. Bonnekoh, W. Pantleon, M. Stricker, A. Hoffmann, J. Reiser, Comparison of K-doped and pure cold-rolled tungsten sheets: As-rolled condition and recrystallization behaviour after isochronal annealing at different temperatures, Int. J. Refract. Met. Hard Mater. 85 (2019) 105047.
[4] M. Fukuda, S. Nogami, K. Yabuuchi, A. Hasegawa, T. Muroga, Anisotropy in the mechanical properties of potassium and rhenium doped tungsten alloy plates for fusion reactor applications, Fusion Science and Technology 68(3) (2015) 690-693.
[5] L. Tanure, A. Bakaeva, L. Lapeire, D. Terentyev, M. Vilémová, J. Matějíček, K. Verbeken, Nano-hardness, EBSD analysis and mechanical behavior of ultra-fine grain tungsten for fusion applications as plasma facing material, Surf. Coat. Technol. 355 (2018) 252-258.
[6] S. Antusch, D.E. Armstrong, T.B. Britton, L. Commin, J.S.-L. Gibson, H. Greuner, J. Hoffmann, W. Knabl, G. Pintsuk, M. Rieth, Mechanical and microstructural investigations of tungsten and doped tungsten materials produced via powder injection molding, Nuclear Materials and Energy 3 (2015) 22-31.
[7] Z.M. Xie, R. Liu, S. Miao, X.D. Yang, T. Zhang, X.P. Wang, Q.F. Fang, C.S. Liu, G.N. Luo, Y.Y. Lian, X. Liu, Extraordinary high ductility/strength of the interface designed bulk W-ZrC alloy plate at relatively low temperature, Scientific Reports 5 (2015) 1-11.
[8] C. Yin, D. Terentyev, T. Pardoen, R. Petrov, Z. Tong, Ductile to brittle transition in ITER specification tungsten assessed by combined fracture toughness and bending tests analysis, Materials Science and Engineering: A 750 (2019) 20-30.
[9] D.H. Lassila, F. Magness, D. Freeman, Ductile-Brittle Transition Temperature Testing of Tungsten Using the Three-Point Bend Test, Report Lawrence Livermore National Laboratory UCRL-ID-108258 (1991).
[10] L. Romaner, C. Ambrosch-Draxl, R. Pippan, Effect of rhenium on the dislocation core structure in tungsten, Phys. Rev. Lett. 104(19) (2010) 195503.
[11] J. Reiser, A. Hartmaier, Elucidating the dual role of grain boundaries as dislocation sources and obstacles and its impact on toughness and brittle-to-ductile transition, Scientific reports 10(1) (2020) 1-18.

[12] C. Bonnekoh, U. Jäntsch, J. Hoffmann, H. Leiste, A. Hartmaier, D. Weygand, A. Hoffmann, J. Reiser, The brittle-to-ductile transition in cold rolled tungsten plates: impact of crystallographic texture, grain size and dislocation density on the transition temperature, Int. J. Refract. Met. Hard Mater. 78 (2019) 146-163.
[13] D. Terentyev, M. Vilémová, C. Yin, J. Veverka, A. Dubinko, J. Matějíček, Assessment of mechanical properties of SPS-produced tungsten including effect of neutron irradiation, Int. J. Refract. Met. Hard Mater. 89 (2020) 105207.
[14] J. Reiser, S. Wurster, J. Hoffmann, S. Bonk, C. Bonnekoh, D. Kiener, R. Pippan, A. Hoffmann, M. Rieth, Ductilisation of tungsten (W) through cold-rolling: R-curve behaviour, Int J Refract Met H 58 (2016) 22-33.
[15] T.L. Shen, Y. Dai, Y. Lee, Microstructure and tensile properties of tungsten at elevated temperatures, Journal of Nuclear Materials 468 (2016) 348-354.
[16] M.O. Vrielink, J. van Dommelen, M.G. Geers, Numerical investigation of the brittle-to-ductile transition temperature of rolled high-purity tungsten, Mech. Mater. (2020) 103394.
[17] C. Yin, D. Terentyev, T. Zhang, R.H. Petrov, T. Pardoen, Impact of neutron irradiation on the strength and ductility of pure and ZrC reinforced tungsten grades, J. Nucl. Mater. (2020) 152226.
[18] Q. Wei, H. Zhang, B. Schuster, K. Ramesh, R. Valiev, L. Kecskes, R. Dowding, L. Magness, K. Cho, Microstructure and mechanical properties of super-strong nanocrystalline tungsten processed by high-pressure torsion, Acta materialia 54(15) (2006) 4079-4089.
[19] C. Bonnekoh, A. Hoffmann, J. Reiser, The brittle-to-ductile transition in cold rolled tungsten: On the decrease of the brittle-to-ductile transition by 600 K to− 65 C, International Journal of Refractory Metals and Hard Materials 71 (2018) 181-189.
[20] B.J. Kim, R. Kasada, A. Kimura, H. Tanigawa, Evaluation of grain boundary embrittlement of phosphorus added F82H steel by SSTT, J Nucl Mater 421(1-3) (2012) 153-159.
[21] N. Igata, K. Miyahara, C. Tada, D. Blasl, G. Lucas, Phenomenological Studies of the Effects of Miniaturization and Irradiation on the Mechanical-Properties of Stainless-Steels, Radiat Eff Defect S 101(1-4) (1987) 131-146.
[22] F. F., Y. X., K. Arakawa, S.P. Fitzgerald, P.D. Edmonds, S.G. Roberts, High temperature annealing of ion irradiated tungsten, Acta Materialia 90 (2015) 380-393.
[23] J. Gibson, D. Armstrong, S. Roberts, The micro-mechanical properties of ion irradiated tungsten, Phys Scripta T159 (2014).

[24] D.E.J. Armstrong, X. Yi, E.A. Marquis, S.G. Roberts, Hardening of self ion implanted tungsten and tungsten 5-wt% rhenium, J Nucl Mater 432(1-3) (2013) 428-436.
[25] E. Gaganidze, D. Rupp, J. Aktaa, Fracture behaviour of polycrystalline tungsten, J Nucl Mater 446(1-3) (2014) 240-245.
[26] F. Arbeiter, E. Diegele, U. Fischer, A. Garcia, A. Ibarra, J. Molla, F. Mota, A. Moslang, Y.F. Qiu, M. Serrano, F. Schwab, Planned material irradiation capabilities of IFMIF-DONES, Nuclear Materials and Energy 16 (2018) 245-248.
[27] C. Yin, D. Terentyev, T. Pardoen, R. Petrov, Z.F. Tong, Ductile to brittle transition in ITER specification tungsten assessed by combined fracture toughness and bending tests analysis, Mat Sci Eng a-Struct 750 (2019) 20-30.

Chapter 6
Impact of neutron irradiation on the strength and ductility of pure and ZrC reinforced tungsten grades

6.1. Experimental

The experimental section consists of two parts, namely: a brief description of the test materials (detailed information could be found in earlier works [1, 2]), and tensile test procedures. The latter contains a description of the standard and interrupted uniaxial tensile tests which we applied here to deduce the yield strength to generate the maximum amount of information with one specimen. The procedure does not follow the currently available standards and therefore we provide a detailed description in Annex A together with examples of the application of this original test procedure on tungsten and ferritic martensitic steel.

6.1.1. Materials

One commercial tungsten product fabricated according to ITER specification (referred to as ATW, which is the abbreviation of AT&M tungsten) is compared to one lab-scale tungsten product (referred to as W0.5ZrC, with the zirconium-carbide strengthening applied in this product). ATW is a rolled pure tungsten plate of 13 mm thickness produced by AT&M China with a median equivalent grain size of ~60 μm [1]. W0.5ZrC is a rolled tungsten (formed as a plate of 8 mm thickness) reinforced with 0.5 wt% of ZrC produced by the Institute of Solid State Physics, Chinese Academy of Science with a median equivalent grain size of ~7 μm [1]. The median equivalent grain size is defined as the equivalent diameter of grains corresponding to 50% cumulative area fraction. Although both products are rolled after sintering, W0.5ZrC was processed following a thermo mechanical treatment (TMT) to reduce grain size and have nearly equiaxed grains [1, 3]. The uniaxial tensile specimens are machined along the rolling direction (RD) also called longitudinal direction (LD). Therefore, the specimens are named with the indication of sampling direction: ATW-L and W0.5ZrC-L. The inverse pole figure of both products and specimen dimensions are shown in **Figure 6.1** where TD is the abbreviation of transverse direction. For a comprehensive analysis of the interrupted test

method proposed in this study, RAFM steel (referred to as Eurofer97) of Eurofer97 specification [2] is used to conduct tests in the non-irradiated condition. The chemical composition and production route is within the specification of the Eurofer97 steel.

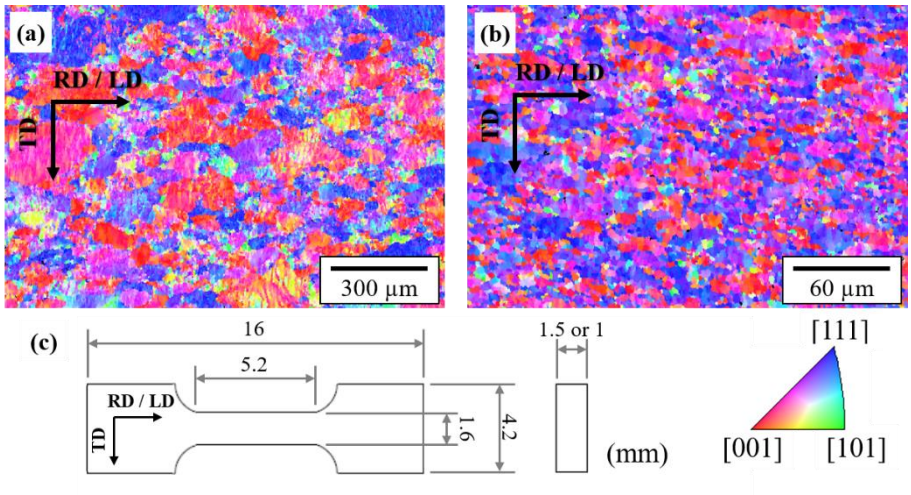

Figure 6.1. Normal direction inverse pole figure of (a) ATW and (b) W0.5ZrC. (c) Schematic of the tensile specimen with dimensions [1] (the thicknesses of specimen for tungsten and Eurofer97 are 1.5 mm and 1 mm, respectively).

6.1.2. Interrupted tensile tests

Interrupted uniaxial tensile tests (IT) were implemented to identify the yield strength at various temperatures with a single specimen. This is an original side development of this research. Interrupted tensile tests are performed in a static tensile mode with a constant crosshead speed of 0.2 mm/min at various temperatures in air.

The development of the interrupted uniaxial tensile test method is driven by the need to determine the temperature dependence of the yield strength using a limited number of specimens available for the tests. The idea of the interrupted tensile test is based on the assumption of a power law relationship between the flow stress and strain. As shown in **Figure 6.2**, The true stress-strain response can be defined into two regimes. One is the elastic regime (red line) and the other one corresponds to the plastic regime (blue line). In the elastic regime, the true stress σ is proportional to the elastic

strain ε_e with the theoretical elastic modulus E:

$$\sigma = E\varepsilon_e \qquad (\sigma < \sigma_E) \quad . \tag{6.1}$$

When σ exceeds the elastic limit σ_E, plastic deformation starts and the strength increases, equal to σ. A typical hardening law in metals is given by Ludwik's equation:

$$\sigma \equiv \sigma_p = K(\varepsilon - \varepsilon_e)^n + E\varepsilon_E \qquad (\sigma \geq \sigma_E) \tag{6.2}$$

where K is a strength coefficient, ε is the true total strain, ε_e is the elastic strain, n is the strain hardening exponent, and ε_E is the strain at the elastic limit.

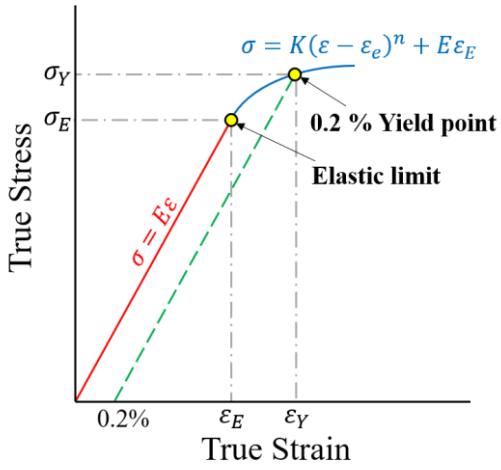

Figure 6.2. True stress-strain curve at early yielding

The hardening rate σ' is defined as the derivative of σ with respect to ε. When σ is larger than the elastic limit σ_E, the relation between σ' and ε is given for the Ludwik's equation, as

$$\frac{d\sigma}{d\varepsilon} = \sigma' = \frac{nKE}{E(\varepsilon - \varepsilon_e)^{1-n} + nK} \quad . \tag{6.3}$$

Since the plastic strain ε_p is equal to $\varepsilon - \varepsilon_e$,

$$\frac{d\sigma}{d\varepsilon} = \sigma' = \frac{nKE}{E(\varepsilon_p)^{1-n} + nK} \quad . \tag{6.4}$$

The hardening rate ratio R_S between $\dot{\sigma}$ and E is defined as,

$$R_S = \frac{\sigma'}{E} = \frac{n}{\frac{E}{K}(\varepsilon_p)^{1-n}+n} \quad . \tag{6.5}$$

At the 0.2% yield point, where $\varepsilon_p = 0.2\%$, R_S is given by,

$$R_{S,0.2\%} = \frac{\sigma'}{E} = \frac{n}{\frac{E}{K}(0.2\%)^{1-n}+n} \quad . \tag{6.6}$$

Equation 6.6 is implemented as the criterion for the interruption based on the change of the loading rate is proposed and applied to tungsten and steel products. Both products are used to show the conservatism of the proposed approach for materials, which exhibits either a standard stress-strain response or a yield drop (i.e. presence of upper yield strength (UYS)).

Practically, the loading rate is calculated and plotted on the operational screen on the fly during the tensile test. The operator follows the loading rate and stops the pulling displacement once the loading rate reduces to a value lower than half of the maximum loading rate. A typical variation of the load and of its rate with time is shown in **Figure 6.3**. In order to reduce the noise of the raw *P-t* curve, the experimental data are smoothened using a polynomial function,

$$F = \sum_{x=0}^{9} a_x t^x \tag{6.7}$$

where F is the load, x is an integer, a_x is a constant, and t is the time. The derivative of the polynomial curve is taken with respect to t. The smoothing process is operated using the Origin analysis software, which only provides one-term to ten-term polynomial. Thus, in order to get the best fit from the software, a ten-term polynomial is implemented. The first derivative of $F(t)$ is the loading rate. The stress at the maximum loading rate (MLR) is defined as σ_E. The stress when the loading rate reduces to half of MLR is defined as the strength at half maximum loading rate (HMLR).

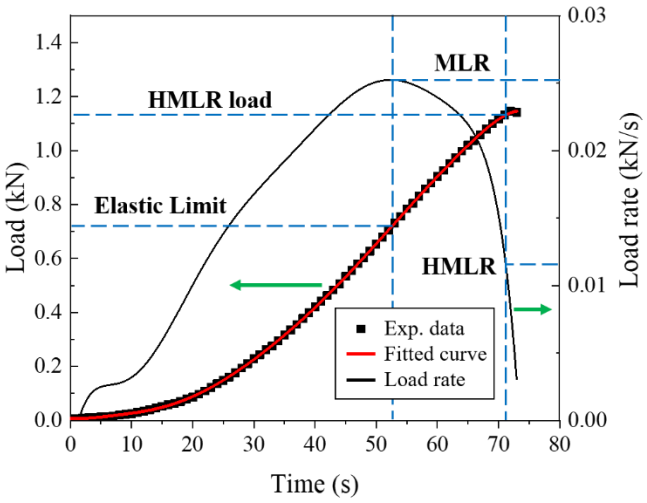

Figure 6.3. Variation of the load and loading rate as a function of time for a single temperature test

In order to evaluate the applicability of the HMLR approach, an analysis of the hardening rate ratio is proposed. The analysis is based on the true stress and true strain before UYS for W0.5ZrC-L and ATW-L and for strain smaller than 1% for Eurofer97 from **Figure 6.7**. The loading rate ratio (R_L) is the ratio between loading rate (F') and the maximum loading rate (MRL), which can relate to the raw elastic slope:

$$R_L = \frac{F'}{MRL} \quad . \tag{6.8}$$

Both R_L and R_S are unitless. **Figure 6.4a** shows the R_L and R_S at 0.2% YS, noted as $R_{L,0.2\%}$ and $R_{S,0.2\%}$, respectively. The largest $R_{L,0.2\%}$ is around 0.5 and $R_{S,0.2\%}$ is not larger than 0.1. Therefore, HMLR ($R_{HMLR} = 0.5$) is a conservative approach to estimate the 0.2% YS because the HMLR will be lower than or similar to 0.2% YS, as shown in **Figure 6.6**. HMLR will also be lower than the UYS since the stress rate ratio of UYS, $R_{L,UYS}$, is 0.

The value of $R_{L,0.2\%}$ is much higher than $R_{S,0.2\%}$ because $R_{L,0.2\%}$ includes the machine compliance where the elastic slope is much smaller than the theoretical elastic slope from $R_{S,0.2\%}$. R_S increases with higher elastic modulus and strength coefficient but is not sensitive to the variation of strain hardening exponent when 0.1 < n < 0.4, as shown in **Figure 6.4b**. Therefore, $R_{S0.2\%}$ is equal to $R_{L0.2\%}$ when the elastic modulus takes into account of machine compliance effects. Moreover, the HMLR is not sensitive to the different type of metals but might need to redefine the value of

R_{HMLR} for the different testing machine since the machine compliance varies.

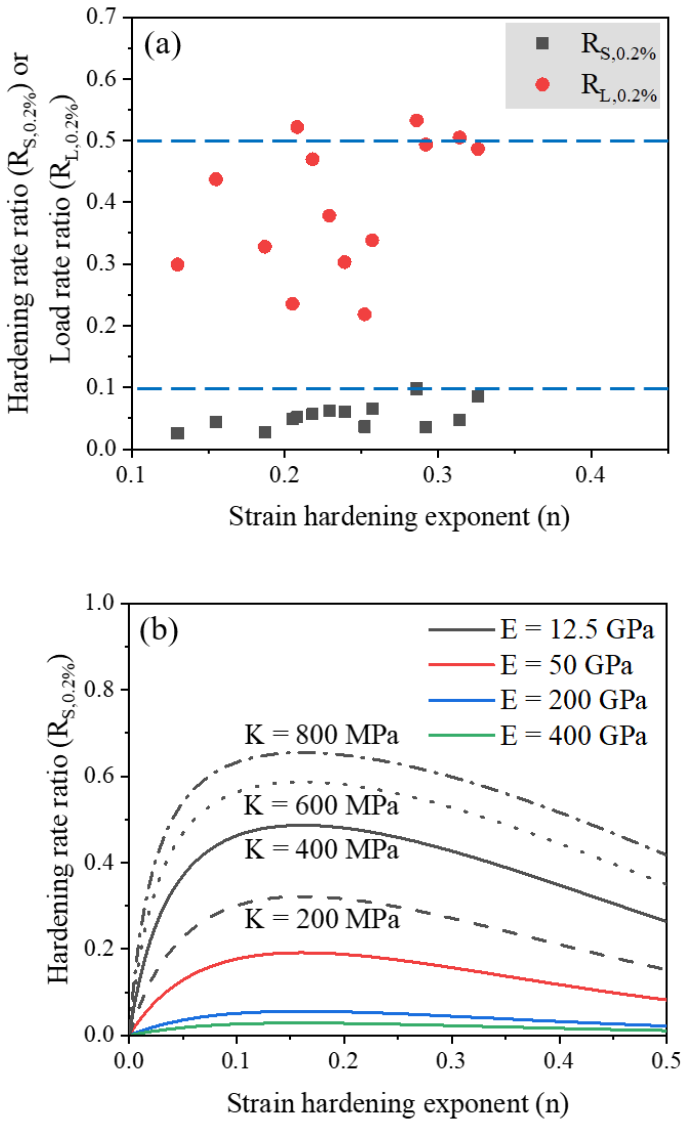

Figure 6.4. Experimental results (a) and theoretical calculation (b) of hardening rate ratio and loading rate ratio at 0.2% yield strength of W0.5ZrC-L, ATW-L, and Eurofer97. In (b), solid lines have a K equal to 400 MPa and black lines have a E equal to 12.5 GPa. (The analyzed data includes ATW-L, which is the material "CEFTR-L" from our previous work [1].)

In order to implement the above interrupted tensile test procedure at different temperatures, the heating scheme shown in **Figure 6.5** is applied. At first, the specimen is heated up to the highest temperature envisaged for the test campaign (around 600 °C in this study for the irradiated samples). After the first test is performed, the temperature is reduced to the second target temperature to perform another interrupted tensile test and the following steps repeat the same procedure until the test at the lowest target temperature is completed. In order to get the full stress-strain curve of the material at the target temperature, the specimen is heated up again to the target temperature and a standard static tensile test is resumed with the same constant cross-head speed until final fracture. The temperature at each step is maintained for 30 minutes to achieve a homogenous temperature distribution in the specimen and pulling rod before testing.

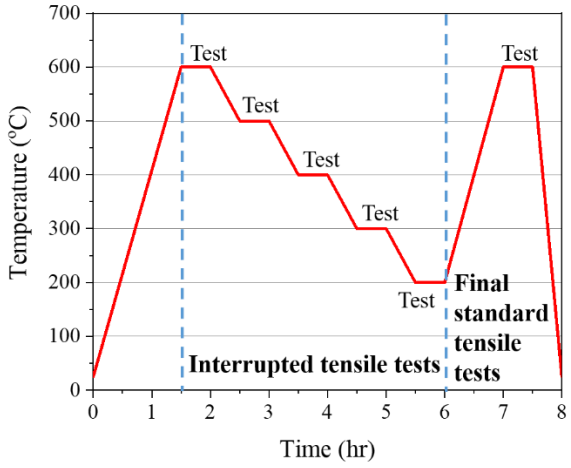

Figure 6.5. Temperature scheme for the heating process to perform multiple numbers of interrupted tensile tests.

To validate the proposed approach, we present the results obtained using both standard and interrupted uniaxial tensile tests for the tungsten products under interest and the Eurofer97 steel. The comparison of the yield stress values extracted from the standard uniaxial tensile tests is provided in **Figure 6.6**. The strength corresponding to the HMLR criterion applied to standard tensile tests has a value close to the 0.2% yield strength (0.2% YS) and UYS at various temperatures for non-irradiated W0.5ZrC-L, ATW-L, and Eurofer97. Moreover, HMLR, 0.2% YS, and UYS show similar trends, increasing with decreasing test temperature. The UYS of both tungsten grades and 0.2% YS

of ATW-L at 150 °C cannot be found on the plot because the samples fracture before reaching UYS or 0.2% YS, as shown in **Figure 6.7a** and **b**. A detailed discussion about these results and about the applicability of the interrupted tensile test method in the case of multiple-temperature testing, which involves accumulation of the strain, is provided in Section 6.2.2.

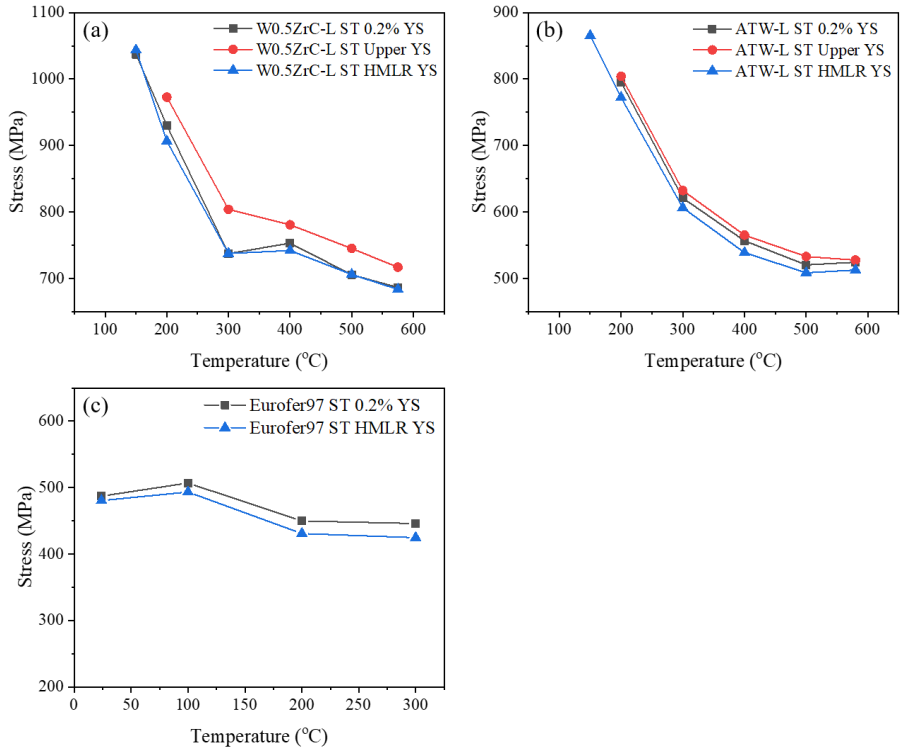

Figure 6.6. Comparison of upper yield strength, 0.2% yield strength, and HMLR from the standard uniaxial tensile tests (ST) of W0.5ZrC-L (a), ATW-L (b), and Eurofer97 (c) at various temperatures (The data for ATW-L is from our previous work, which can be referred as CEFTR-L [1].)

6.2. Results and discussion

6.2.1. Strength and ductility of non-irradiated materials

In order to demonstrate the applicability of the interrupted tensile test procedure, the strength and ductility values of the non-irradiated materials are determined first by standard uniaxial tensile testing. These data are also used for the analysis of HMLR in Chapter 2.

The stress-strain curves extracted from the standard uniaxial tensile tests performed at different temperatures (relevant for this study) are shown in **Figure 6.7**. Both tungsten products W0.5ZrC-L and ATW-L exhibit an upper yield point at all test temperatures. The Eurofer97 steel does not exhibit the yield drop phenomenon, as shown in **Figure 6.7c**. In W0.5ZrC-L and ATW-L materials, a small degree of plastic deformation is attained before reaching the upper yield strength (UYS). This unrecoverable microstrain, a concept introduced in the 1960s [4, 5], is defined as the deformation attained when the stress exceeds σ_E but being lower than UYS. As indicated in the literature [6], the yield drop in tungsten depends on crystallographic orientation. Only the tensile loading along the [110] crystallographic direction involves a yield drop. Moreover, the tensile strength along the [110] crystallographic direction is lower than the one in the [100] direction [6, 7]. Both W0.5ZrC-L and ATW-L are deformed during the rolling process. As a result, all the dislocations are free from the interstitial atoms like carbon or nitrogen, which pin these dislocations before deformation. Moreover, more dislocations are emitted after deformation. However, during heat treatment, stress release or tempering, some of the free dislocations are again pinned by the interstitial atoms, which diffuse to dislocations to reduce Gibbs free energy at high temperature. When a tensile test is performed the unpinned dislocations start gliding as the stress reaches the critical resolved shear stress (CRSS) but still within the microstrain region [4, 8]. The mobile dislocation density increases as the pinned dislocations start to be released from the interstitial atoms with increasing stress [5]. Therefore, the larger microstrain before peak found in tungsten might be caused by the combination of strain hardening from unpinned dislocation, release of pinned dislocation, and crystallographic dependence of tensile properties. Because of the larger microstrain before peak, 0.2% yield strength (0.2% YS) can be found before the upper yield strength for both tungsten products.

As shown in **Figure 6.7a** and **b**, both non-irradiated W0.5ZrC-L and ATW-L exhibit only very small plastic deformation at temperature lower than 200 °C. However, since the small degree of deformation of W0.5ZrC-L is larger than the one of ATW-L, the lower boundary of the DBTT range, which was

evaluated by tensile property, of W0.5ZrC-L should be lower than 150 °C, presumably around 100 °C (which is the DBTT reported from a previous study [3]). As a result, the lower boundary of the DBTT range of W0.5ZrC-L might be 50 °C lower than the one for ATW-L, which is around 150 °C (shown in **Figure 6.7b**).

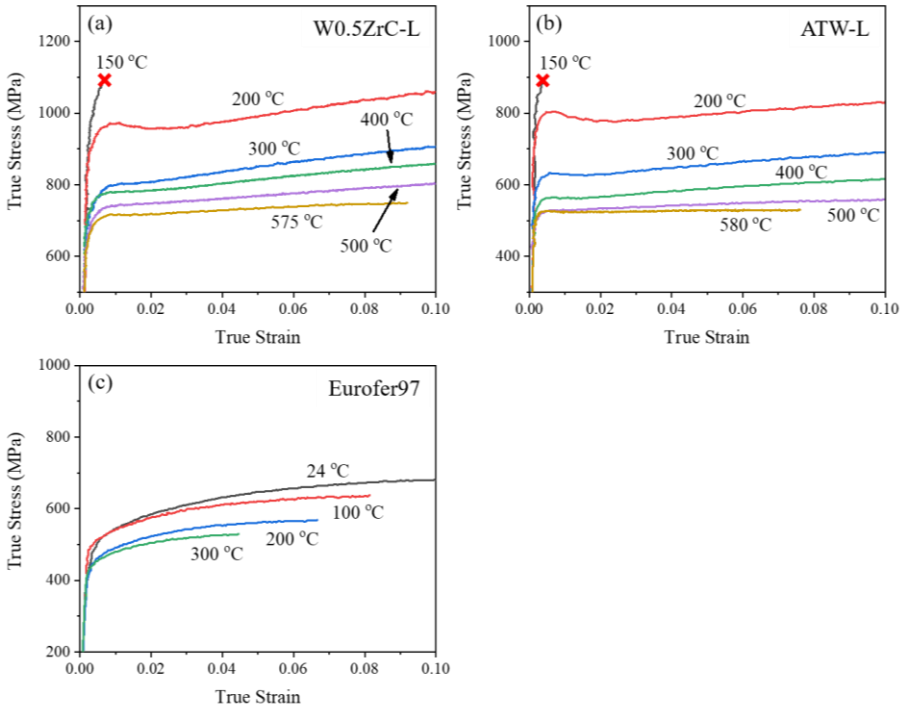

Figure 6.7. True stress-strain curves of W0.5ZrC-L (a), ATW-L (b), and Eurofer97 (c). The curves here only show data before the ultimate tensile strength. The red cross represents the fracture point. (The data for ATW-L is from our previous work, which can be referred as CEFTR-L [1].)

6.2.2. Interrupted tensile testing of non-irradiated specimens

An Interrupted Tensile test (IT) is similar to a usual uniaxial tensile test but with loading few cycles of loading/unloading applied at various temperatures. The purpose of the IT is to estimate, from a single specimen, the 0.2% YS or UYS at different temperatures in order to find the variation of the 0.2% YS or of the UYS as a function of temperature. However, in order to identify the yield strength, which indicates the onset of overall plastic deformation, an IT will involve a small plastic strain increment and thus minute amounts of strain

hardening after each step. As a result, the strength of the material will slightly increase after each step.

Figure 6.8 shows the variation of ΔHMLR and Δ0.2% YS of W0.5ZrC-L, ATW-L, and Eurofer97 as a function of temperature. The quantities ΔHMLR and Δ0.2% YS are defined as the change of strength (HMLR or 0.2% YS) at each test temperature with respect to the strength (HMLR or 0.2% YS) at the highest test temperature, in the following way,

$$\Delta HMLR(T) = HMLR(T) - HMLR_{HT} \quad \textbf{(6.9)}$$

$$\Delta 0.2\%YS(T) = 0.2\%YS(T) - 0.2\%YS_{HT} \quad \textbf{(6.10)}$$

where $HMLR(T)$ and $0.2\%YS(T)$ is the HMLR and the 0.2%YS at the test temperature T, respectively; the $HMLR_{HT}$ and $0.2\%YS_{HT}$ is the HMLR and the 0.2% YS at the highest test temperature HT, respectively.

Figure 6.8 shows that the ΔHMLR extracted from the interrupted tensile tests is regularly higher than the Δ0.2% YS from the standard tests. In the case of ATW product, the mean difference is less than 15 MPa. However, the values of ΔHMLR of W0.5ZrC-L and Eurofer97 are higher than Δ0.2 % YS by ~50-100 MPa, and the difference increases with the number of tests (i.e. when approaching lower temperatures). This can be explained by the strain hardening developed within the microstrain regime at each strain achieved before the test is interrupted. Note that Eurofer97 has the highest strain hardening exponent n (0.21 to 0.33, depending on temperature), W0.5ZrC-L has the second highest n (0.16 to 0.29), and ATW-L has the lowest n (0.1 to 0.25). Moreover, the magnitude of the plastic strain accumulated after each step will also slightly affect the strain hardening. The plastic strain after each test step is shown in **Table 6.1**. Therefore, the material with a higher n and a higher accumulated plastic strain will acquire higher strength step after step. This phenomenon might limit the applicability of IT for materials without a yield drop. Indeed, materials with no softening stage do not exhibit a UYS, which is the basis for indicating the onset of plastic strain after each test step through $R_{L,UYS} = 0$.

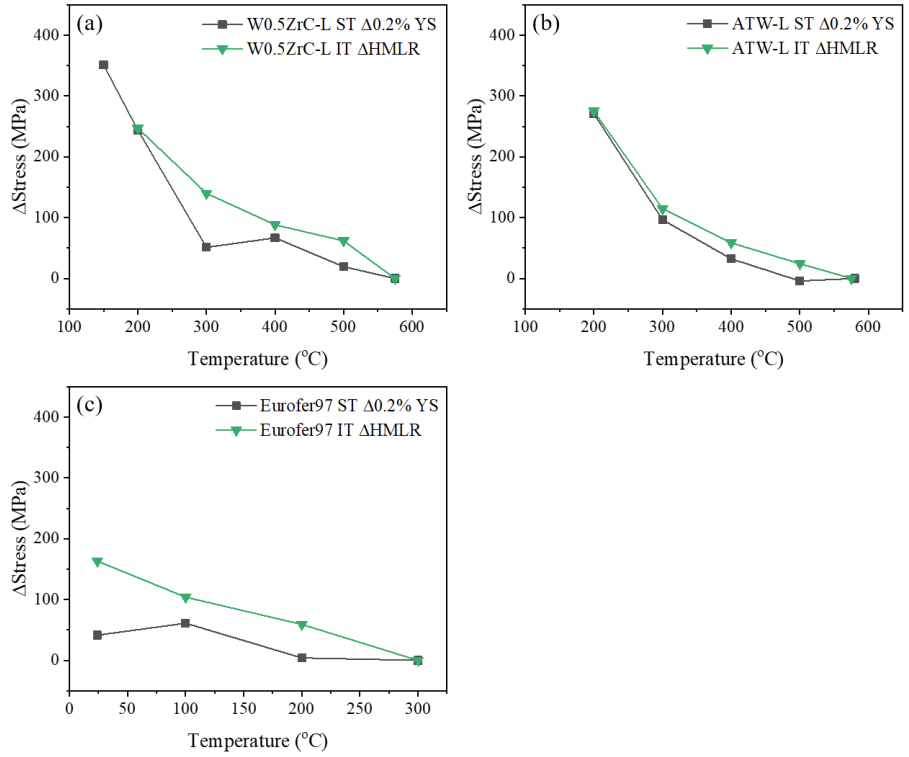

Figure 6.8. ΔHMLR from interrupted tensile tests (IT) and Δ0.2% YS from standard tensile tests (ST) of W0.5ZrC-L (a), ATW-L (b), and Eurofer97 (c) as a function of temperature (The data for ATW-L ST is from our previous work, which can be referred as CEFTR-L [1].)

Table 6.1. Plastic strain increment corresponding to each loading step of various test temperatures (T_{test}).

Step #	Plastic Strain (%)					Total Accumulated Plastic Strain[a] (%)
	1	2	3	4	5	
W0.5ZrC-L (T_{test}, °C)	0.50 (575)	0.42 (500)	0.43 (400)	0.33 (300)	0.51 (200)	2.19
ATW-L (T_{test}, °C)	0.21 (575)	0.46 (500)	0.35 (400)	0.30 (300)	0.62 (200)	1.94
Eurofer97 (T_{test}, °C)	1.53 (300)	0.37 (200)	0.54 (100)	0.54 (24)	-	2.98

[a] The total plastic strain represents the accumulated plastic strain after all test steps from the interrupted tensile test method are finished.

However, if a material exhibits a yield drop, the test will stop before reaching UYS. In other words, the plastic strain after each loading step is smaller than the strain corresponding to UYS. Thus, some of the pinned dislocations are still immobilized at the end of the loading step. Since the pinned dislocations are not all free from interstitial atoms, the yield drop will still happen during each loading step. As a result, the HMLR of an interrupted tensile test will be similar to the UYS of a standard tensile test, as shown in **Figure 6.9a** and **b**. The HMLR of the first interrupted step is lower than the yield stress derived from the standard test. However, the difference remains well within the spread of 0.2% YS, caused by the natural variation of local microstructure in the material block. Nevertheless, the trend in the HMLR vs. 0.2% YS as a function of temperature for both W0.5ZrC-L and ATW-L is well captured by an interrupted tensile test procedure when comparing with standard non-interrupted tests, as shown in **Figure 6.9c**.

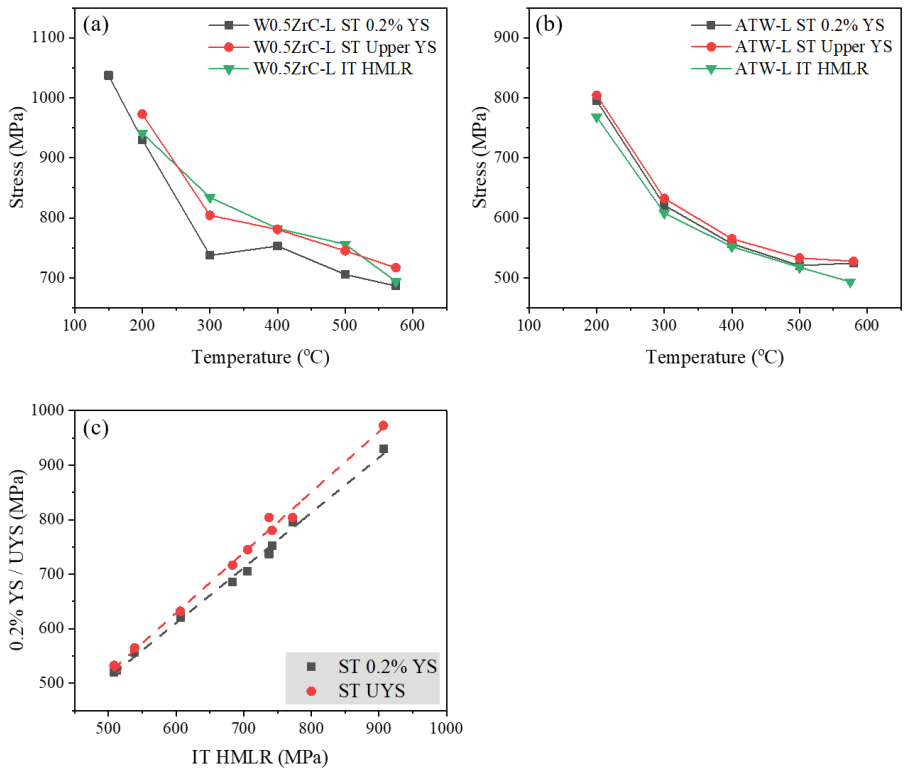

Figure 6.9. Comparison of 0.2% YS and UYS from standard tensile tests (ST) with HMLR from interrupted tensile tests (IT). W0.5ZrC-L (a), ATW-L (b). (c) Correlation of IT HMLR with ST 0.2% YS and ST UYS for W0.5ZrC-L and ATW-L. (The data for ATW-L ST is from our previous work, which can be referred as CEFTR-L [1].)

6.2.3. Standard and interrupted tensile testing of irradiated samples

Regardless of the irradiation dose and irradiation temperature (T_{irr}), the total elongation of both tungsten grades is reduced and the tensile strength is increased by neutron irradiation, as shown in **Figure 6.10** (detail tensile properties are shown in **Table 6.2**). At high temperature (560 – 580 ^{o}C), the irradiated W0.5ZrC-L shows plastic deformation with almost no strain hardening after UYS for all doses. Unlike W0.5ZrC-L, the irradiated ATW-L does not exhibit an UYS but it has a larger strain hardening ability before the deformation reaches ~2.5%. However, as the test temperature drops to 500 ^{o}C, the plastic deformation limit of irradiated ATW-L is much smaller compared to the plastic deformation limit of irradiated W0.5ZrC-L, which is around 10%. At temperature below 400 ^{o}C, no macrostrain (large elongation) is observed in both W0.5ZrC-L and ATW-L. Moreover, all irradiated W0.5ZrC-L specimens show various degrees of yield drop at test temperatures higher than 500 ^{o}C. Neutron irradiation also affects the elongation: the total elongation of all irradiated W0.5ZrC-L decreases with increasing irradiation dose and irradiation temperature, as shown in **Figure 6.10a**.

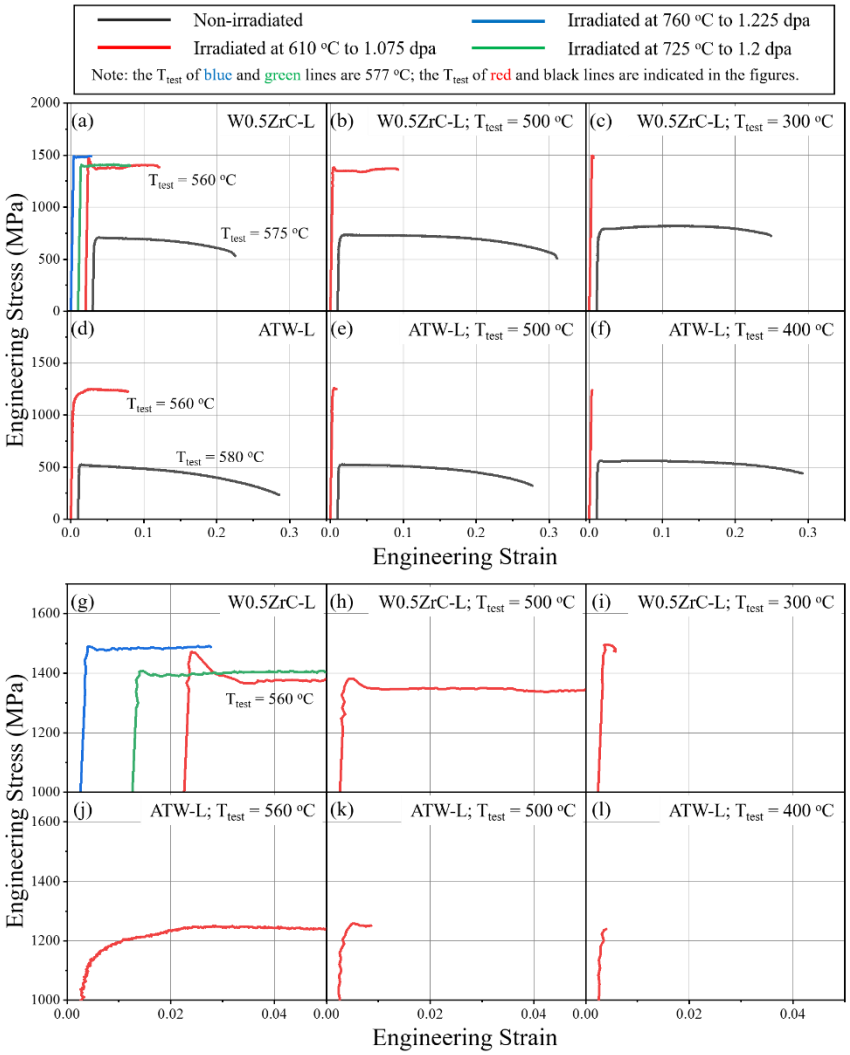

Figure 6.10. Engineering stress-strain curves from standard uniaxial tensile tests (ST) of non-irradiated and irradiated samples from W0.5ZrC-L (a, b, c) and ATW-L (d, e, f); partial magnification of near yielding region for W0.5ZrC-L and ATW-L are shown in (g, h, i) and (j, k, l), respectively. (a, d, g, j) are tested at 560 – 580 °C; (b, e, h, k) are tested at 500 °C; (c, i) are tested at 300 °C; (f, l) are tested at 400 °C. The stress-strain curves are shifted with a strain of 1%. ST of W0.5ZrC-L irradiated at 760 °C 1.225 dpa of (a, g), W0.5ZrC-L irradiated at 725 °C 1.2 dpa of (a, g), W0.5ZrC-L irradiated at 610 °C 1.075 dpa of (c, i) and ATW-L irradiated at 610 °C 1.075 dpa of (f, l) are performed after interrupted tensile tests. (The data for ATW-L non-irradiated that are tested at 400 and 500 °C is from our previous work, which can be referred as CEFTR-L [1].)

Table 6.2. Tensile properties of non-irradiated and irradiated W0.5ZrC-L and ATW-L.

Materials	Dose (dpa)	T_{Test} (°C)	T_{irr} (°C)	0.2% YS (MPa)	UYS (MPa)	UTS (MPa)	Uniform elongation[a] (%)	Total elongation (%)
W0.5ZrC-L	0	300	-	737	795	823	10.1	23.8
	1.075	300	610	1493	1497	1497	0.2	0.3
	0	500	-	705	737	737	1.5	30
	1.075	500	610	1384	1388	1388	8.0	9.0
	0	575	-	686	711	711	1.4	19.4
	1.075	560	610	1456	1471	1471	7.4	9.8
	1.2	577	725	1405	1408	1411	4.6	6.8
	1.225	577	760	1487	1490	1492	2.2	2.4
ATW-L[b]	0	400	-	557	561	562	5.9	28.1
	1.075	400	610	-	-	1239	0.1	0.1
	0	500	-	520	525	525	1.6	26.6
	1.075	500	610	1265	1258	1258	0.6	0.6
	0	580	-	524	525	525	0.5	27.4
	1.075	560	610	1142	-	1250	2.6	7.6

[a] Uniform elongation is defined as the elongation at which the engineering stress starts to decrease after yield drop.

[b] The data for non-irradiated ATW-L samples tested at 400 and 500 °C is from our previous work, which can be referred as CEFTR-L [1].

The interrupted tensile test method is suitable for irradiated materials since most irradiated materials exhibit a yield drop. The total plastic strain accumulated after the interrupted tensile tests are shown in **Table 6.3**. Since irradiated W0.5ZrC-L shows a yield drop for all doses and test temperature, the strain hardening effect associated with the accumulated strain during interrupted tensile tests is not a concern. For irradiated ATW-L, as indicated in **Figure 6.10j**, a yield drop is not observed while testing at 560 °C. As mentioned before and shown in **Figure 6.8**, the plastic strain accumulated during the interrupted tensile tests for materials without yield drop needs to be carefully controlled. Therefore, for irradiated ATW-L, the interrupted tensile test for test temperature at 560 °C is not performed and the total plastic strain is maintained within 0.5% or less, as shown in **Table 6.3**. Thus, the strain hardening effect is limited in the interrupted tensile testing of irradiated ATW-L and the HMLR approach is applicable to irradiated ATW-L.

Table 6.3. Total plastic strain after interrupted tensile tests and DBTT range of non-irradiated and irradiated W0.5ZrC-L and ATW-L samples.

Materials	Dose (dpa)	Irradiation temperature (°C)	Total accumulated plastic strain (%)	DBTT range (evalued by tensile property, °C)
W0.5ZrC-L	0	-	2.19	100 – 200 [1, 3]
	1.075	610	1.04	300 – 500
	1.2	725	0.73	-
	1.225	760	0.83	-
ATW-L	0	-	1.94	150 – 200 [1]
	1.075	610	0.17	400 – 575

The 0.2% YS, UYS, and HMLR from interrupted tensile tests of all irradiated samples from both tungsten products are around 2 times higher than the HMLR from interrupted tensile tests on non-irradiated samples for both materials at various test temperature, as shown in **Figure 6.11**. Although the UYS and HMLR of all irradiated W0.5ZrC-L samples (doses around 1 dpa) scatter, they seem to have similar values (around 1400 MPa) at different temperatures. The lowest temperature at which a microstrain can be detected for W0.5ZrC-L irradiated to 1.075 dpa is 300 °C (**Figure 6.10i**), which is 100 °C lower than the one of ATW-L irradiated to 1.075 dpa (**Figure 6.10l**). Moreover, this temperature (300 °C for W0.5ZrC-L irradiated to 1.075 dpa, 400 °C for ATW-L irradiated to 1.075 dpa) is about 200 °C lower than the threshold to achieve full ductile deformation in W0.5ZrC-L and ATW-L (as shown in **Figure 6.10b** and **d**). Both microstrain and large elongation require mobile dislocation to produce plastic deformation [4, 8]. Therefore, the existence of a microstrain plasticity can be interpreted as a ductile deformation behavior. In other words, the temperature at which microstrain develops prior to UYS can be used as an indication to find the lowest temperature of DBTT range at which the material exhibits some degree of ductility. As a result, the DBTT range, which was evaluated through tensile testing, of W0.5ZrC-L is between 300 – 500 °C and the one of ATW-L is between 400 – 575 °C after being irradiated to 1.075 dpa at 610 °C. The DBTT range before and after irradiation for both materials is shown in **Table 6.3**.

The hardening effect after irradiation increases the strength of both tungsten grades and the strength increments are almost the same. This indicates that both W0.5ZrC-L and ATW-L involve a similar strain hardening mechanism. Tungsten, when irradiated by neutrons in the fission reactor, includes more transmutation elements, Re and Os, than if irradiated in a fusion reactor

because of the higher fluence of the thermal neutrons, which have a larger cross section for transmutation. As a result, the number of voids or dislocation loops for the materials irradiated in the fission reactor will be smaller since Re suppresses the formation of voids and dislocation loops [9-11].

If the concentration of Re and Os is within the solubility of tungsten, these chemical elements will remain dissolved in the matrix. The effect of Re and Os solid solution on the mechanical properties of W was studied in [12] by hardness tests performed at room temperature. The effect of Re is known to be temperature dependent and strengthening is observed at the temperatures above ~200 ^{o}C, while at lower temperatures the softening is observed (given that a certain concentation of Re is attained) [13, 14]. The temperature dependence of strengthening effect of Os is unknown but the hardness tests at room temperature show that it growth proportionally to the Os content [12]. As calculated by MCNP code, the Re and Os concentration after neutron irradiation in this study is within 1.5 at% and 0.2 at%, respectively. Based on the hardness data at elevated temperature provided in [13], the increase of the flow stress due to 1.5 at% of Re is around 3% at 400 ^{o}C and 5% at 600 ^{o}C. For 0.2 at% of Os, the estimated flow stress increase is around 1% at room temperature [12]. This is clearly a marginal increase of the flow stress compared to the experimentally measured yield stress. However, one needs to keep in mind that the diffusion and segregation of Re and Os is expected in the present experimental conditions, since the irradiation temperature exceeds the one corresponding to the long-range vacancy migration [15], being around 400°C. Thus, the estimates above based on the studies employing solid solution should be carefully analyzed.

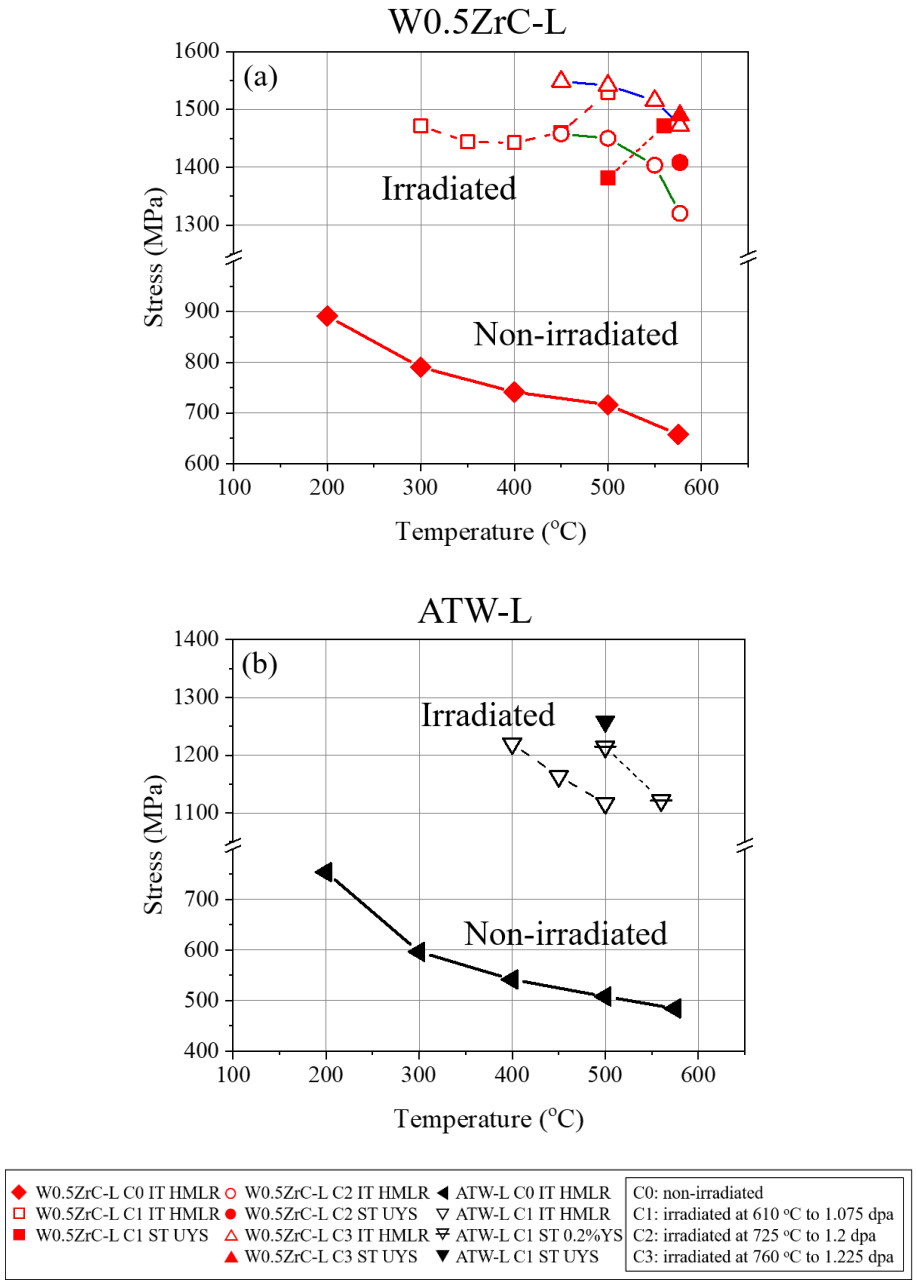

Figure 6.11. HMLR from interrupted tensile tests (IT) and 02% YS of all irradiated samples compared to HMLR from IT of non-irradiated samples from W0.5ZrC-L (a) and ATW-L (b).

After neutron irradiation in HFIR at 760 °C for 1 dpa, dislocation loops and voids were observed and precipitates of Re and Os were expected [7, 16, 17]. Although BR2 is a fission reactor, the transmutation rate is lower than in HFIR at the same neutron flux because the irradiation was performed directly inside the fuel element of BR2. Thus, the Re and Os concentration in this study is lower than the one from HFIR irradiation. Therefore, the Re/Os-based precipitates might not form (or might be lower in density and size) in the irradiated W0.5ZrC and ATW. Hence, main contribution to the strengthening of W0.5ZrC-L and ATW-L after neutron irradiation should be attributed to the dislocation pinning by dislocation loops and voids. The contribution coming from the transmuted Re and Os requires further study employing TEM and atom probe.

To summarize, because irradiation defects will act as obstacles for dislocation gliding in the metal, the critical resolved shear stress increases and the mobility of dislocation, being means of plastic deformation, reduces in the neutron irradiated material. Naturally, with the increase of the flow stress, the DBTT shifts to a higher temperature range. Because the physical nature of the irradiation hardening and DBTT increase is the same (irradiation defects), one can relate the DBTT shift with the increment of the yield strength. This relation between irradiation hardening and shift of DBTT can be perceived from the result of this study where ATW-L and W0.5ZrC-L have a similar increment of yield strength and shift of lower boundary of DBTT range (increased temperature is around 200 - 250 °C) after irradiated to 1.075 dpa at 610 °C.

Since the transmutation rate in the actual fusion reactor environment is lower than in the fission reactors, the strengthening in the plasma-facing tungsten might be lower than the one evaluated in this study at the same irradiation temperature and dose. Moreover, He bubbles are expected to be formed in the sub-surface layer of tungsten operating in a fusion reactor but not in a fission reactor [18]. Therefore, in order to transfer the information related to the neutron irradiation degradation obtained from fission reactor experiments to fusion applications, further study and justifications are required.

6.3. Summary

Standard and interrupted tensile tests of ITER specification and ZrC reinforced tungsten products have been performed at elevated temperature to assess the impact of neutron irradiation on the flow stress and ductility. Neutron irradiation was performed in BR2 material test reactor with mixed spectrum at temperature ranged from 610 to 760 °C up to a dose of ~1 dpa. The obtained results led to the following findings.

Firstly, an interrupted tensile testing approach is proposed and validated. The assumption of determining the strength at half maximum loading rate (HMLR) gives a reliable trend for the upper yield strength (UYS) as a function of temperature. The accuracy for determination of the yield stress is found satisfactory for materials exhibiting the yield drop. For materials without the yield drop, careful control of the magnitude of the plastic strain increment after each step of the interrupted tensile test is required to limit the effect of strain hardening, which results in an overestimation of the yield stress from HMLR.

Secondly, the main results of the irradiation campaign can be summarized as follows:

I. The elongation of both W0.5ZrC-L and ATW-L products is reduced after the irradiation. Both products remain ductile at the irradiation temperature. However, the DBTT range, which was evaluated through tensile testing, of W0.5ZrC (being between 300 – 500 °C) is lower than the one of ATW product (being between 400 – 575 °C). At the same time, the shift of DBTT, which is around 200 – 250 °C, is similar for both materials.

II. The hardening effect after the neutron irradiation is similar for both W0.5ZrC-L and ATW-L where the strength increases by almost a factor of two for all irradiated specimens. The irradiation hardening is primarily attributed to dislocation loops and voids, since the transmutation of Re and Os was limited benefits from the irradiation position, which is located inside the fuel element.

6.4. References

[1] C. Yin, D. Terentyev, T. Pardoen, A. Bakaeva, R. Petrov, S. Antusch, M. Rieth, M. Vilemova, J. Matejicek, T. Zhang, Tensile properties of baseline and advanced tungsten grades for fusion applications, Int. J. Refract. Met. Hard Mater. 75 (2018) 153-162.
[2] A. Puype, L. Malerba, N. De Wispelaere, R. Petrov, J. Sietsma, Effect of processing on microstructural features and mechanical properties of a reduced activation ferritic/martensitic EUROFER steel grade, J. Nucl. Mater. 494 (2017) 1-9.
[3] Z.M. Xie, R. Liu, S. Miao, X.D. Yang, T. Zhang, X.P. Wang, Q.F. Fang, C.S. Liu, G.N. Luo, Y.Y. Lian, X. Liu, Extraordinary high ductility/strength of the interface designed bulk W-ZrC alloy plate at relatively low temperature, Scientific Reports 5 (2015) 1-11.
[4] J. Meakin, Microstrain behavior of body-centered cubic metals, Can. J. Phys. 45(2) (1967) 1121-1134.
[5] R. Kossowsky, N. Brown, Microyielding in iron at low temperatures, Acta Metall. 14(2) (1966) 131-139.
[6] A. Argon, S. Maloof, Plastic deformation of tungsten single crystals at low temperatures, Acta Metall. 14(11) (1966) 1449-1462.
[7] L.M. Garrison, Y. Katoh, N.A.P. Kiran Kumar, Mechanical properties of single-crystal tungsten irradiated in a mixed spectrum fission reactor, J. Nucl. Mater. 518 (2019) 208-225.
[8] T. Malis, K. Tangri, Grain boundaries as dislocation sources in the premacroyield strain region, Acta Metall. 27(1) (1979) 25-32.
[9] M. Fukuda, N.K. Kumar, T. Koyanagi, L.M. Garrison, L.L. Snead, Y. Katoh, A. Hasegawa, Neutron energy spectrum influence on irradiation hardening and microstructural development of tungsten, J Nucl Mater 479 (2016) 249-254.
[10] A. Hasegawa, M. Fukuda, K. Yabuuchi, S. Nogami, Neutron irradiation effects on the microstructural development of tungsten and tungsten alloys, J Nucl Mater 471 (2016) 175-183.
[11] M. Klimenkov, U. Jäntsch, M. Rieth, H. Schneider, D. Armstrong, J. Gibson, S. Roberts, Effect of neutron irradiation on the microstructure of tungsten, Nuclear Materials and Energy 9 (2016) 480-483.
[12] J.-C. He, A. Hasegawa, M. Fujiwara, M. Satou, T. Shishido, K. Abe, Fabrication and characterization of W-Re-Os alloys for studying transmutation effects of W in fusion reactors, Materials Transactions 45(8) (2004) 2657-2660.
[13] E. Savitskii, M. Tylkina, S. Ipatova, E. Pavlova, Properties of tungsten-rhenium alloys, Metal Science & Heat Treatment 2(9) (1960) 483-486.

[14] M. Fukuda, S. Nogami, A. Hasegawa, H. Usami, K. Yabuuchi, T. Muroga, Tensile properties of K-doped W–3% Re, Fusion Eng. Des. 89(7-8) (2014) 1033-1036.
[15] L. Keys, J. Smith, J. Moteff, High-temperature recovery of tungsten after neutron irradiation, Phys. Rev. 176(3) (1968) 851-856.
[16] Y. Katoh, L. Snead, L. Garrison, X. Hu, T. Koyanagi, C. Parish, P. Edmondson, M. Fukuda, T. Hwang, T. Tanaka, Response of unalloyed tungsten to mixed spectrum neutrons, J. Nucl. Mater. 520 (2019) 193-207.
[17] A. Hasegawa, M. Fukuda, S. Nogami, K. Yabuuchi, Neutron irradiation effects on tungsten materials, Fusion Eng Des 89(7-8) (2014) 1568-1572.
[18] J. Marian, T.L. Hoang, Modeling fast neutron irradiation damage accumulation in tungsten, J. Nucl. Mater. 429(1-3) (2012) 293-297.

Chapter 7
Effect of high temperature neutron irradiation on fracture toughness of ITER-specification tungsten

7.1. Materials

Two ITER specification tungsten products are considered in this study: IGP (manufactured by Plansee, Austria by double hammering and supplied as rod) and ATW (manufactured by AT&M, China by rolling and supplied in a shape of plate). As a result, IGP has elongated carrot-like grains aligned in the longitudinal direction (LD) whereas ATW has flat pancake-like grains "flattened" along the rolling direction (RD) [1]. The equivalent median diameter of a grain (defined by a high angle grain boundary with a misorientation angle between grains larger than 15°), measured on the plane perpendicular to the normal direction (ND), is around 100 μm and 70 μm for IGP and ATW, respectively. Additionally, a sub-grain structure (misorientation angle between 5 to 15°) with a sub-grain size of several μm was observed in both materials. More detailed information on the microstructure and mechanical properties of these products can be found in our previous work [1].

In this chapter, we present the results of mechanical tests performed for both products at 0.08 dpa, and higher dose data are shown for ATW tungsten only. Our preliminary study had shown that the fracture toughness of the IGP irradiated to 0.44 dpa requires testing to be performed above 600 °C, which is the upper limit of this study.

7.2. Results and discussion

7.2.1. Fracture toughness and fracture surface

Figure 7.1 shows the variation of the fracture toughness with irradiation dose, together with the reference values measured at room temperature i.e. in the brittle, non-irradiated conditions. For both tested products, the measured K_{Jc} value decreases with increasing irradiation dose. At the highest dose studied here (0.67 dpa), the K_{Jc} value of ATW T-L is reduced almost down to the fracture toughness at room temperature. This indicates that the irradiation to 0.67 dpa has raised the DBTT of this product up to ~600 °C, which corresponds to an increase of 300 °C (see Ref. [1] for reference measurements). The irradiation-induced changes of microstructure in the studied samples is currently under investigation. However, as reported in the literature [2], the hardening and subsequent embrittlement induced by neutron irradiation depend not only on the fluence and irradiation temperature but also on the neutron spectrum, which defines the transmutation rate. Transmuted elements (Re and Os) are found to form secondary phases (σ phase and χ phase), while displacement damage creates voids and dislocation loops in the temperature and dose range studied here [3, 4]. The presence of precipitates, voids and dislocation loops decreases the mobility of dislocations causing hardening. As a result, the ductility and capacity to dissipate energy by plastic deformation of irradiated material is reduced such that it loses its fracture toughness i.e. becomes brittle. Moreover, the irradiation-induced defects can also act as stress concentration sites thus affecting the crack propagation not only below and but also above the DBTT region.

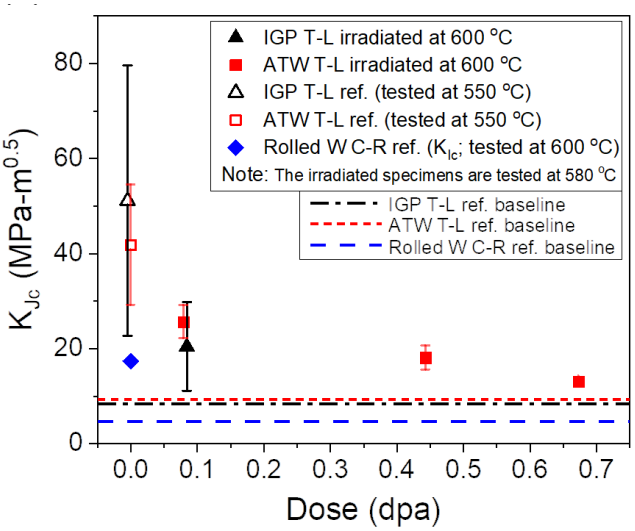

Figure 7.1. K_{Jc} as a function of irradiation dose for IGP T-L and ATW T-L (the data of reference specimens is referred to our previous work [1]; the K_{Ic} value (only considers linear elastic fracture behavior) of Rolled W C-R, which can be considered as the lower limit of the fracture toughness, is referred to Faleschini, et al [5]); the baselines are defined as the fracture toughness at room temperature; more than two specimens were tested at each test temperatures to obtain minimum statistics; the error bars represent one standard deviation of the experimental data

The amount by which K_{Jc} is reduced by the irradiation is different for the two types of tested materials. IGP T-L exhibits a larger reduction of K_{Jc} compared to the ATW T-L product. In addition, the scatter in the K_{Jc} value also decreases with increasing the irradiation dose. This is probably related to the fact the neutron irradiation induced defects, homogeneously distributed in the material, also act as stress concentrators reducing the statistical spread of the defects controlling the fracture of the non-irradiated state.

Figure 7.2 shows a collection of the fracture surface morphologies from which transgranular surface fraction has been determined. The morphology of the fracture patterns of both materials, although tested after different irradiation doses, look quite similar. At temperature below 550 °C (**Figure 7.2a, c, e, g, i, k**), the fracture surface of all specimens, no matter if they were irradiated or not, exhibit a mixture of intergranular and transgranular brittle fracture. However, oxidation start to appear at the test temperature above 550 °C (**Figure 7.2b, d, f, h, j, l**) for non-irradiated and irradiated specimens.

The surface ratio of transgranular brittle fracture mode, as calculated by ImageJ analysis of the SEM images, is given in **Figure 7.3**. For most of the inspected conditions, the fraction of transgranular brittle fracture is larger in the ATW product. Moreover, for the ATW product, the fraction of transgranular brittle fracture is seen to increase with increasing the irradiation dose, which is likely related to the suppression of dislocation-mediated plasticity inside the grains caused by the presence of the irradiation-induced defects (dislocation loops, voids and probably Re/Os precipitates). In the case of the IGP T-L product, the irradiation at 0.08 dpa does not impact the amount of transgranular brittle fracture. This difference between the fracture patterns of the IGP and ATW materials can be ascribed to the difference in the shape of grains, and mutual grain-crack orientation in the studied products [1]. IGP has carrot-like grains along the crack propagation direction and ATW has pancake-like grains perpendicular to the crack propagation plane [1]. As a result, the IGP exhibits a lower propensity for transgranular brittle fracture than the ATW product [1]. The confirmation of this hypothesis, as well as a physical explanation for the observed embrittlement, requires detailed transmission electron microscopy study as well as the measurement of the chemical composition (i.e. Re and Os) in the irradiated samples, which is currently in progress.

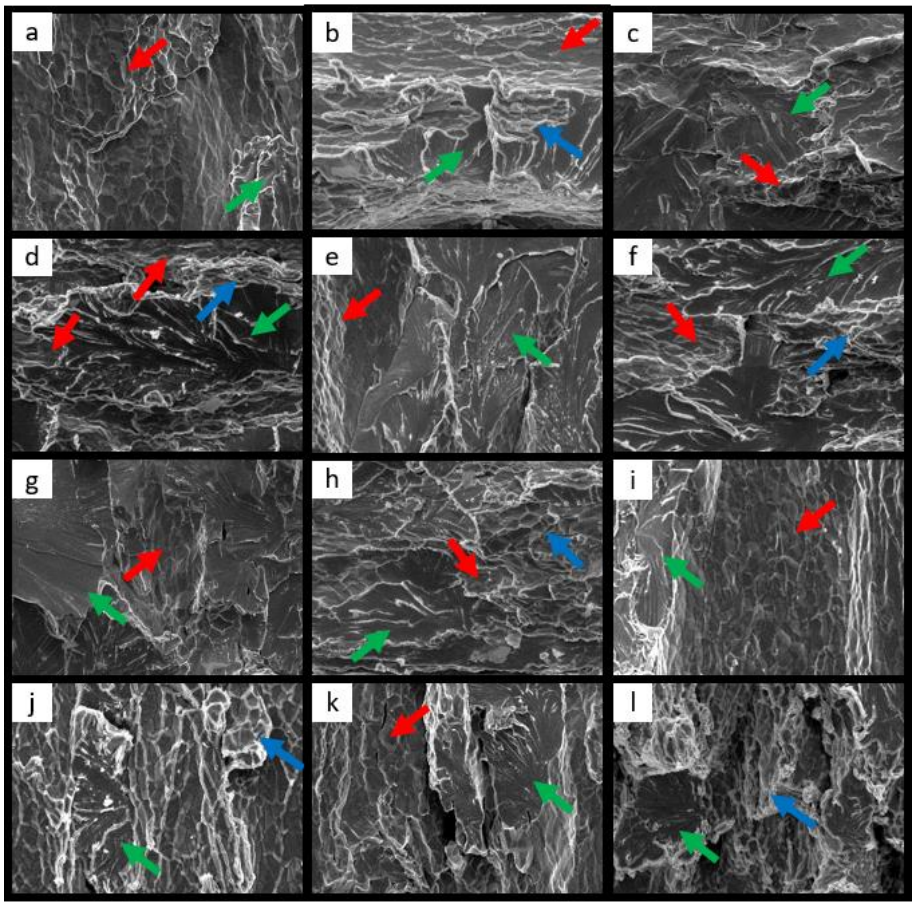

Figure 7.2. Fracture surfaces of the DCT specimens. IGP T-L 0.08 dpa tested at 500 °C (a) and 580 °C (b); ATW T-L 0.08 dpa tested at 400 °C (c) and 580 °C (d); ATW T-L 0.44 dpa tested at 500 °C (e) and 580 °C (f); ATW T-L 0.67 dpa tested at 500 °C (g) and 580 °C (h); IGP T-L reference tested at 500 °C (i) and 600 °C (j); ATW T-L reference tested at 500 °C (k) and 600 °C (l)

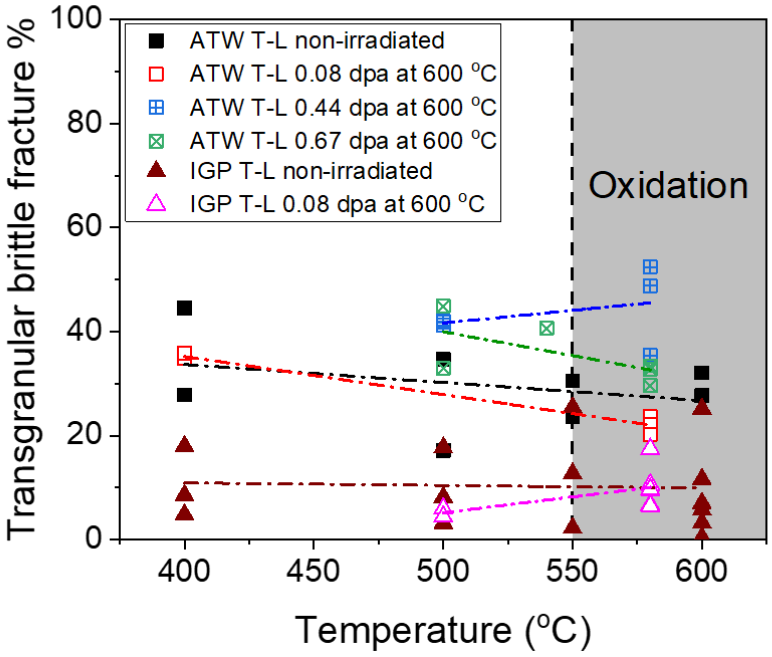

Figure 7.3. Variation of the fraction of transgranular brittle fracture as a function of test temperature: each data point in the plot represents the fraction of fracture feature corresponding to one specimen.

7.2.2. Estimation of the transition curve

A method to estimate the transition curve developed in **Chapter 4** is implemented to predict the transition curve of the irradiated IGP T-L and ATW T-L, as shown in **Figure 7.4**. And the curve parameters are shown in **Table 7.1**. However, since the upper shelf fracture toughness (K_{top}) is reduced after irradiation, the implemented method requires two data points at different temperatures to calculate K_{top} and T_{half}, which is different from the method developed from the experimental result of non-irradiated tungsten grades. Moreover, the baseline fracture toughness (K_{base}) of **equation 4.2** is fixed to a value of 7 $\mathrm{MPa}\sqrt{m}$. This fixed value of K_{base} is just an estimation for the room temperature fracture toughness after irradiation, and it should be lower than the non-irradiated tungsten grades ,which is around 9 $\mathrm{MPa}\sqrt{m}$. Moreover, the definition of DBTT, $K_{DBTT} = 23\ \mathrm{MPa}\sqrt{m}$, in **Chapter 4** cannot be used in this approach since most of the K_{top} after irradiation is lower than 23 $\mathrm{MPa}\sqrt{m}$. Alternatively, the DBTT definition of this approach

adopts the definition in **Chapter 5**, which defines the DBTT as T_{half}.

Table 7.1. Parameters for the transition curve of non-irradiated and irradiated tungsten grades. K_{top} and T_{half} are calculated from **equation 4.7** and **4.8**, respectively. However, a different definition of K_{Jc1} is applied here, where it is defined as an experimental value.

Materials	Irradiation temperature (°C)	Dose (dpa)	Parameters			
			K_{base} (MPa$\sqrt{m}$)	K_{top} (MPa$\sqrt{m}$)	C	T_{half} (°C)
IGP T-L	-	0	9.3	55.99	0.020	431
	600	0.08	7	21.54	0.020	452
ATW T-L	-	0	8.8	41.44	0.019	319
	600	0.08	7	26.45	0.019	417
		0.44	7	21.74	0.019	522
		0.67	7	13.38	0.019	423

One can see that the transition is shifted to a higher temperature with a reduction of upper shelf fracture toughness after neutron irradiation. For the transition curve of 0.08 dpa 600 °C, the upper shelf of IGP T-L is smaller than the one of ATW T-L. However, the DBTT shift of IGP T-L (~20 °C) is lower than the DBTT shift of ATW T-L (~100 °C) after irradiated to 0.08 dpa at 600 °C. At dose of 0.44 dpa, the DBTT of ATW T-L increases to an even higher temperature with a shift of ~200 °C. As irradiation dose increases to 0.67 dpa, the upper shelf has reduced to a value closed to baseline fracture toughness, as shown in **Figure 7.4b**. Since the difference between K_{top} and K_{base} is very small at 0.67 dpa, the slope parameter C of the non-irradiated ATW, which has a much higher K_{top}, might not apply. Thus, the estimation of DBTT with a temperature of 423 °C at 0.67 dpa should not be considered as a valid value and requires further investigation at higher test temperatures.

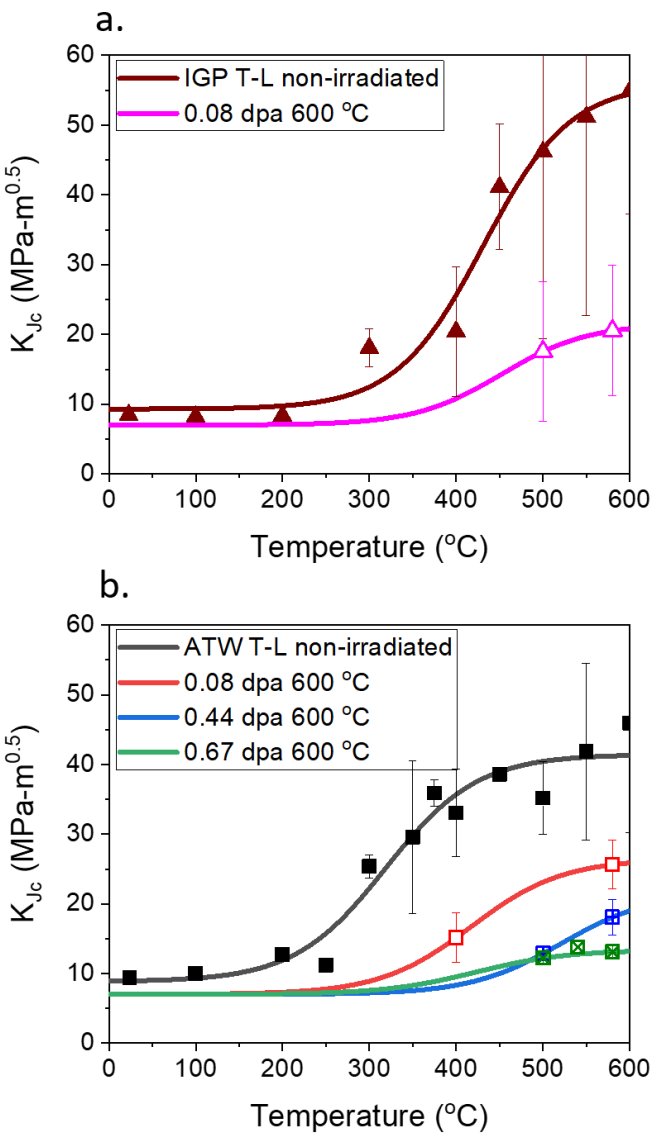

Figure 7.4. Transition curve of non-irradiated and irradiated IGP T-L (a) and ATW T-L (b)

7.3. Summary

Based on the results obtained up to now, we can draw the following conclusions:

I. K_{Jc} measured at 580 °C progressively decreases with increasing irradiation dose down to ~ 10 $\mathrm{MPa}\sqrt{m}$ i.e. approaching the room temperature fracture toughness of this material. This indicates that neutron irradiation at 600 °C, which is similar to the condition to be faced by divertor tungsten monoblock in the region close to the cooling pipe, leads to the shift of DBTT by 300 °C as the neutron fluence progressively increases i.e. the irradiation makes the material brittle under the irradiation condition. Note that the dose of 0.67 dpa is close to the design end-of-life dose for the ITER divertor components. However, the concentration of transmuted elements after irradiated in BR2 is different (approximately factor of two higher) from the one expected in fusion environment due to a higher fraction of thermal-to-fast neutrons. Understanding of the impact of enhanced transmutation due to fission environment remains a truly challenging problem for which the most natural solution is the application of fast fission spectrum (i.e. usage of CEFR or BOR60 reactors).

II. The portion of transgranular brittle fracture pattern in the ATW T-L material increases after irradiation, which can be explained by the obstruction of plastic deformation of grains due to pinning of dislocations at irradiation-induced defects. However, the same trend is not observed in the IGP T-L material.

III. The approach to estimating the transition curve of irradiated IGP T-L and ATW T-L indicates a reduction of upper shelf fracture toughness and a shift of the curve to a higher temperature. The shifts of DBTT irradiated at 600 °C are estimated to be ~20 °C for IGP T-L irradiated to 0.08 dpa, ~100 °C for ATW T-L irradiated to 0.08 dpa, and ~200 °C for ATW T-L irradiated to 0.44 dpa.

7.4. Reference

[1] C. Yin, D. Terentyev, T. Pardoen, R. Petrov, Z. Tong, Ductile to brittle transition in ITER specification tungsten assessed by combined fracture toughness and bending tests analysis, Materials Science & Engineering: A 750 (2019) 20-30.
[2] M. Fukuda, N.K. Kumar, T. Koyanagi, L.M. Garrison, L.L. Snead, Y. Katoh, A. Hasegawa, Neutron energy spectrum influence on irradiation hardening and microstructural development of tungsten, J Nucl Mater 479 (2016) 249-254.
[3] A. Hasegawa, M. Fukuda, S. Nogami, K. Yabuuchi, Neutron irradiation effects on tungsten materials, Fusion Eng Des 89(7-8) (2014) 1568-1572.
[4] A. Hasegawa, M. Fukuda, K. Yabuuchi, S. Nogami, Neutron irradiation effects on the microstructural development of tungsten and tungsten alloys, J Nucl Mater 471 (2016) 175-183.
[5] M. Faleschini, H. Kreuzer, D. Kiener, R. Pippan, Fracture toughness investigations of tungsten alloys and SPD tungsten alloys, J Nucl Mater 367 (2007) 800-805.

Chapter 8
High temperature neutron irradiation hardening in baseline and advanced tungsten grades assessed by hardness measurements

8.1. Experimental procedures

8.1.1. Materials

Six types of tungsten grades are investigated. The studied materials can be categorized into two groups: commercial pure tungsten grades (also called as ITER baseline grades) and particle reinforced grades. The three ITER baseline grades are ITER specification Plansee (henceforth referred to as IGP), 1600°C/one-hour recrystallized IGP tungsten (henceforth referred to as W-RX), and ITER specification tungsten produced by A.L.M.T. (henceforth referred to as IGA). IGP is produced by Plansee, Austria, W-RX samples are cut from IGP product and annealed at Forschungszentrum Jülich GmbH, Germany. IGA is produced by A.L.M.T, Japan (supplied by Forschungszentrum Jülich for this study). The other tungsten products are particle reinforced grades, namely: tungsten alloyed with 0.5 wt% of ZrC (henceforth W0.5ZrC), tungsten alloyed with 1 wt% of TiC (henceforth W1TiC), and tungsten alloyed with 2 wt% of Y_2O_3 (henceforth W2YO). W0.5ZrC is produced by the Institute of Solid State Physics, China, and supplied as a plate product, which is rolled and thermo-mechanically treated. Both W1TiC and W2YO are produced by PIM techniques by Karlsruhe Institute of Technology, Germany, who also supplies the samples ready for the irradiation. In results and discussion section, Table 1 summarizes the main characteristics of the six materials.

8.1.2. Microstructure

Scanning electron microscopy (SEM) equipped with the energy-dispersive X-ray spectroscopy (EDS) and electron back-scattered diffraction (EBSD) systems is employed for microstructural characterization of the studied grades. In order to perform chemical composition analysis, the samples are finally ground with P4000 SiC paper. For the EBSD analysis, electropolishing is applied to prepare the final surface just prior to taking the EBSD scan. The electrolyte for electropolishing is 1.5 wt% NaOH solution, and the parameters are 25 V with a flow rate of 18 L/min in the mask area of 2 cm^2 for 1 minute at room temperature. The grain size, grain orientation, and grain boundary

misorientation angles are identified by analyzing the EBSD data using EDAX-TSL OIM analysis software. The equivalent median diameter (D50), equivalent 10% diameter (D10), and equivalent 90% diameter (D90) of grains are identified, where D50, D10, and D90 indicate that there are 50%, 10%, and 90% (in area fraction) of the grains or particles smaller than this diameter, respectively. Therefore, the grain size distribution of each tungsten grades can be evaluated by D10 and D90. The particle identification procedure is implemented by combining back-scattered electron (BSE) signal and EDS mapping. The particle size is analyzed using the ImageJ software. As will be shown later, the hardness of the materials is linked to the size and shape of the grains. This is not surprising given that hardness is linked to the ability of the material to accommodate the change of load into elastic and plastic deformation. While, in the general case of equiaxed grains, the plastic yield stress is proportional to $D^{-1/2}$ (D is grain size) as expected from Hall-Petch relationship. Given that some of the studied products have non-equiaxed grains, we have used EBSD data to find a rigorous mathematical relationship between the grain size parameters and Vickers hardness. The basic idea is to link the Vickers hardness with the linear density of interfaces (i.e. grain boundary or precipitate interface), which are expected to obstruct plastic deformation (and therefore contribute to the hardness). The next paragraph provides a brief explanation of the quantification of the linear density of interfaces.

The elongated grain can be well approximated by an ellipsoid, as shown in **Figure 8.1**. A and B_1 are the major and minor median length (in area fraction) of the projected grain shape on a plane normal to ND. Moreover, B_2 and C are the major and minor median length of projected grains shape on a plane normal to LD. These measurements are achieved by EDAX-TSL OIM software, where the minimum pixels to define grain is 2, and the minimum misorientation angle is selected as 2° for all the grains including subgrains and as 15° for grains with high angle boundaries (HAGB). The volume (V_e), the approximated surface area (A_e) [1, 2], and the grain boundary surface area to volume ratio (S_v) of the ellipsoidal grain can be described as follow,

$$V_e = \frac{4}{3}\pi ABC, \tag{8.1}$$

$$A_e = 4\pi\left(\frac{A^pB^p+A^pC^p+B^pC^p}{3}\right)^{1/p}, \tag{8.2}$$

$$S_v = \frac{A_e}{2V_e}, \tag{8.3}$$

where p is a constant equal to 1.6075 [3], which gives a relative error of 1.061% in area. From the geometry aspect, B should be equal to both B_1 and

B_2; B is taken as the arithmetic mean value of B_1 and B_2.

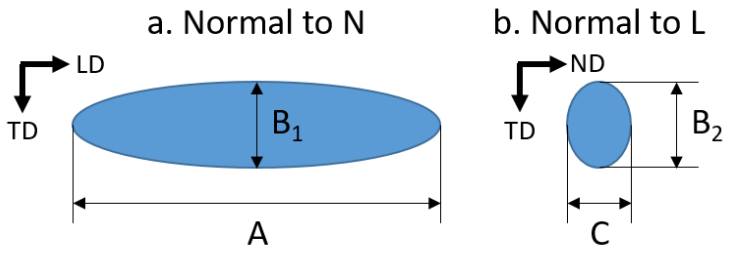

Figure 8.1. The projected shape of an ellipsoidal grain on (a) plane normal to ND and (b) plane normal to LD.

The S_v of equiaxed grains can be described as follow,

$$S_v = \frac{3}{D50}, \tag{8.4}$$

where D50 is the equivalent median diameter of the grains. The S_v of grains or sub-grains with a misorientation angle larger than 2° ($S_{v,tG}$) can be defined as the total S_v of sub-grains ($S_{v,SG}$) and grains ($S_{v,G}$) where sub-grains and grains are surrounded by low angle grain boundaries (LAGB) with misorientation between 2 to 15° and high angle grain boundaries (HAGB) with a misorientation angle larger than 15°, respectively, therefore,

$$S_{v,SG} = S_{v,tG} - S_{v,G}. \tag{8.5}$$

Contrary to grain boundaries, the strengthening particles do not share boundaries, and therefore the S_v of strengthening particles $S_{v,p}$ (i.e., valid for W1TiC, W2YO, and W0.5ZrC) is defined as:

$$S_{v,p} = \frac{6}{D50}. \tag{8.6}$$

8.1.3. Yield strength estimation from Vickers hardness

The correlation between the tensile stress and hardness value is well established for metals, where an experimentally proven ratio of the HV to true stress at 8% true strain with a value of 2.8 and 2.9 was given by Johnson [4] and Tabor [5], respectively. However, the strain hardening capacity of the metal will impact the ratio of the HV to tensile stress. This relationship

regarding HV and ultimate tensile strength (σ_{UTS}) can be described by **equation 8.7** proposed by Tabor [5]. Moreover, in order to relate HV and 0.2% yield strength ($\sigma_{y,0.2\%}$), Cahoon, et al. [6] proposed a new **equation 8.8**.

$$\frac{HV}{\sigma_{UTS}} = \frac{2.9}{(1-n)\left(\frac{12.5n}{1-n}\right)^n}, \quad \textbf{(8.7)}$$

$$\frac{HV}{\sigma_{y,0.2\%}} = \frac{3}{\left(\frac{\varepsilon_{y,0.2\%}}{0.08}\right)^n} \approx \frac{3}{(0.1)^n}, \quad \textbf{(8.8)}$$

where $\varepsilon_{y,0.2\%}$ is the true strain at $\sigma_{y,0.2\%}$, and n is the strain hardening exponent, which is determined from Hollomon's equation:

$$\sigma = K{\varepsilon_p}^n, \quad \textbf{(8.9)}$$

where σ is the true stress, ε_p is the true plastic strain, and K is the strength coefficient.

Depending on the particular microstructure and orientation of loading if texture is present, different strain hardening capacity may realise, up to the extent of the appearance of strain softening well known to exhibit after neutron irradiation [7]. In the case of commercially pure tungsten, the experiment performed up to now show that its strain hardening exponent is rather low [8-10] and in this work we assume that n of irradiated tungsten has a value of 0. According to **equation 8.8**, the ratio of HV to $\sigma_{y,0.2\%}$ for the irradiated material then has a value of 3. Therefore, the increase in the $\sigma_{y,0.2\%}$ after the irradiation ($\Delta\sigma_{y,0.2\%}$) could be be estimated as:

$$\Delta\sigma_{y,0.2\%} = \frac{\Delta HV}{3}, \quad \textbf{(8.10)}$$

where $\Delta\mathrm{HV}$ is the increase of the Vickers hardness caused by the irradiation. It is to be noted that this simplified method does not consider the non-Schmid yield behavior of tungsten, which results in tension-compression asymmetry. Moreover, the orientation of the indent on the tested surface should not be affected by plastic anisotropy since the tested tungsten grades are polycrystalline.

8.2. Results and Discussion

8.2.1. Microstructure

Figure 8.2 shows the microstructure in terms of inverse pole figures of the different tungsten materials. The thick black lines and thin black lines indicate, respectively, the HAGB (with misorientation > 15°) and LAGB (with misorientation between 2 to 15°). HAGB and LAGB can also be described as boundaries between grains and sub-grains, respectively. As shown in **Figure 8.2a** and **d**, the grains of IGP are elongated in the LD. Since the width of the grain along the ND and transverse direction (TD) is small, one can describe the shape of IGP grains as carrot-like bodies. The grain shape of W-RX is shown in **Figure 8.2g**. The elongated carrot-like grains of IGP have evolved towards equiaxed grains after recrystallization. Differently from the IGP, the grains of both IGA and W0.5ZrC exhibit a pancake-like shape with a major axis parallel to LD, as shown in **Figure 8.2b, c, e, f**. However, the grain size of W0.5ZrC is much smaller than that of IGA because of the thermo-mechanical treatment applied to W0.5ZrC [11]. The PIM manufacturing process did not include any mechanical post-treatment, and therefore W1TiC and W2YO products have equiaxed shaped grains. The strengthening particles in W1TiC, W2YO, and W0.5ZrC grades are homogeneously distributed in the matrix, as shown in **Figure 8.3**. D50, D10, and D90 of the grains and of the strengthening particles are given in **Table 8.1**.

As shown in **Table 8.2**, the median length of the major axis and minor axis of the grains and sub-grains are measured for IGP, IGA, and W0.5ZrC in the planes normal to ND and LD in order to calculate the $S_{v,G}$, and $S_{v,SG}$ based on equations (3) and (5) since they exhibit elongated grains. And the $S_{v,G}$, and $S_{v,SG}$ of W-RX, W1TiC and W2YO, which exhibit equiaxed grains, are calculated based on equations (4) and (5) where the $S_{v,G}$ and $S_{v,total}$ can be calculated from the HAGB D50 (as shown in **Table 8.1**) and D50 with the misorientation larger than 2° (W-RX: 59.25 µm; W1TiC: 5.74 µm; W2YO: 5.85 µm), respectively. Equation (6) is applied to calculate the $S_{v,p}$ of particle reinforced tungsten (W0.5ZrC, W1TiC, and W2YO). The calculated $S_{v,G}$, $S_{v,SG}$, and $S_{v,p}$ of various tungsten grades are gathered in **Figure 8.4**.

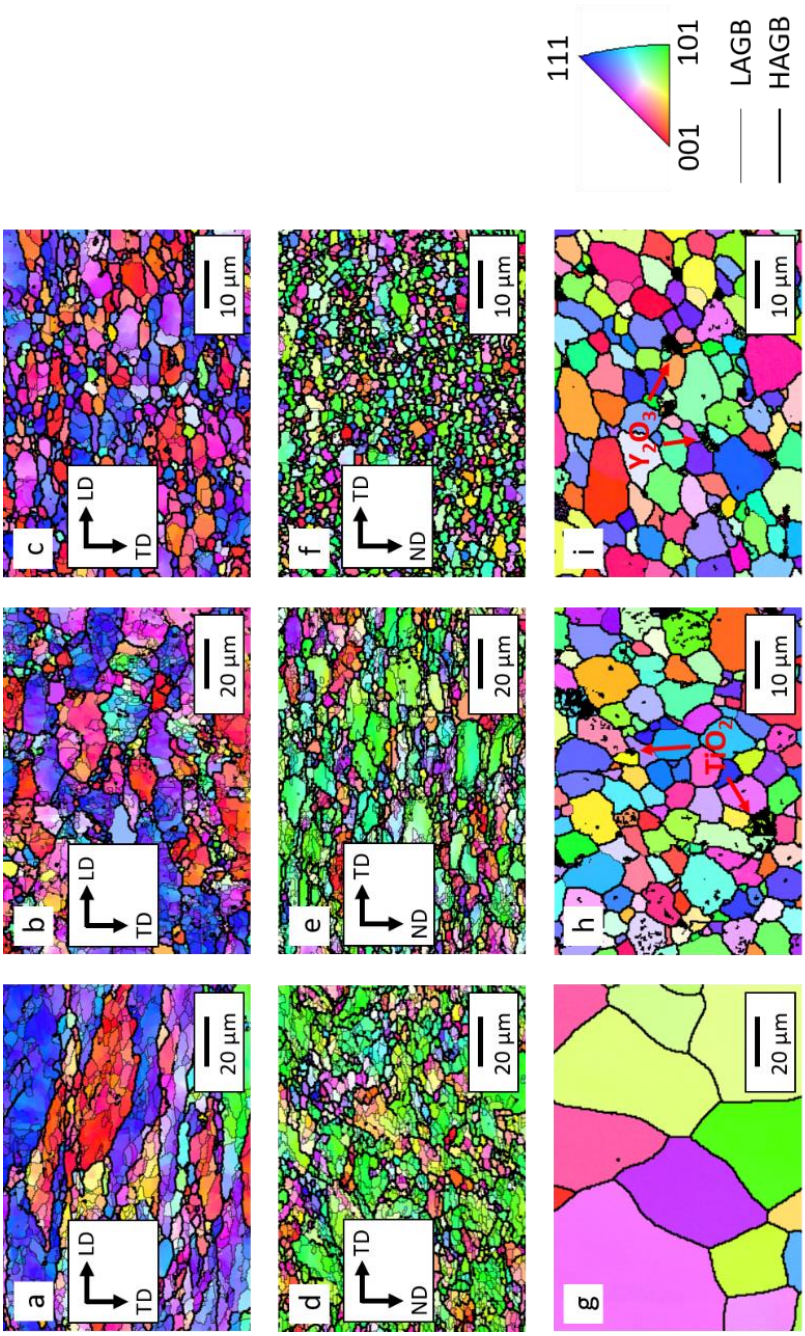

Figure 8.2. Inverse pole figure of tungsten grades showing LAGB and HAGB interfaces. (a) IGP plane normal to ND; (b) IGA plane normal to ND; (c) W0.5ZrC plane normal to ND; (d) IGP plane normal to LD; (e) IGA plane normal to LD; (f) W0.5ZrC plane normal to LD; (g) W-RX; (h) W1TiC; (i) W2YO.

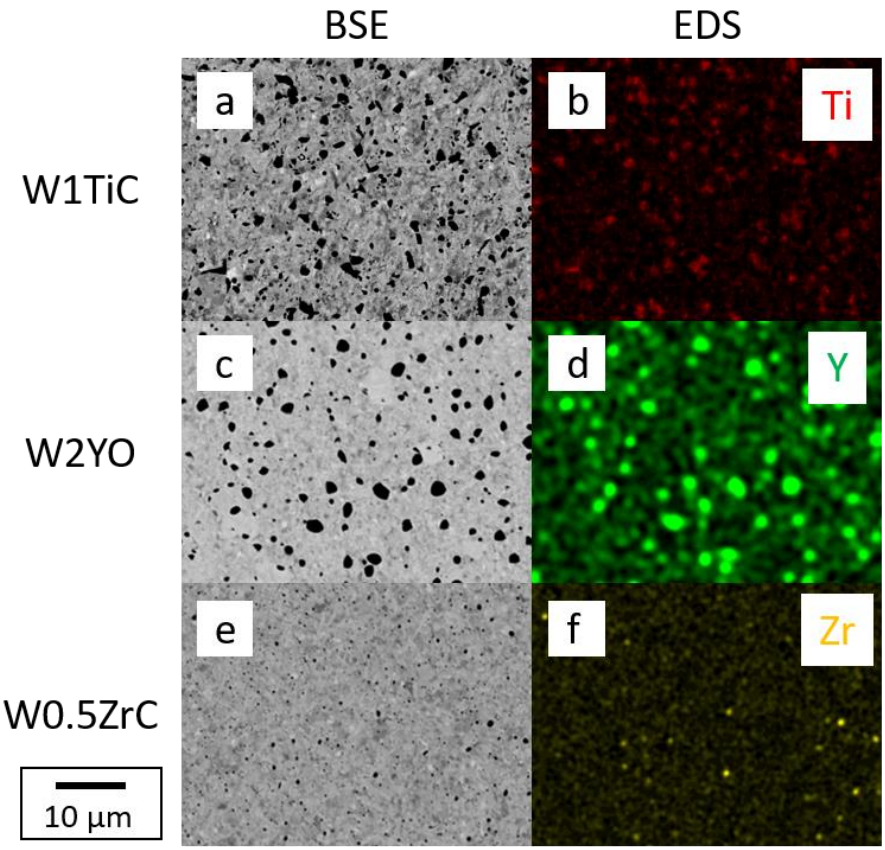

Figure 8.3. BSE image and EDS map of particle reinforced tungsten grades. (a) BSE and (b) EDS of W1TiC; (c) BSE and (d) EDS of W2YO; (e) BSE and EDS of W0.5ZrC. Red, green, and yellow colors indicate elements of Ti, Y, and Zr, respectively.

Table 8.1. Dimensions of the grains and of the strengthening particles of different tungsten grades.

Materials	Equivalent diameter (μm)						
	Plane normal to	HAGB			Particle		
		D10	D50	D90	D10	D50	D90
IGP	ND	14.46	52.66	103.87			
	LD	4.77	15.78	31.45			
IGA	ND	5.86	19.49	41.00			
	LD	4.26	9.93	19.24			
W0.5ZrC	ND	1.90	4.53	9.24	0.20	0.42	0.83
	LD	1.39	2.75	5.35			
W-RX		31.67	60.38	108.40			
W1TiC		1.76	6.03	9.75	0.42	0.92	1.60
W2YO		2.19	6.15	11.83	0.63	1.15	1.98

Table 8.2. The median length of the major and minor axes of grains of IGP, IGA, and W0.5ZrC products.

Materials	Median length (μm)							
	Grains or subgrains with misorientation > 2^o				Grains with HAGB			
	A	B_1	B_2	C	A	B_1	B_2	C
IGP	3.93	1.60	2.04	1.20	77.09	10.02	12.54	4.75
IGA	2.54	1.40	1.98	1.14	15.59	5.70	8.10	2.94
W0.5ZrC	1.73	0.94	1.42	0.75	5.06	1.72	1.85	0.97

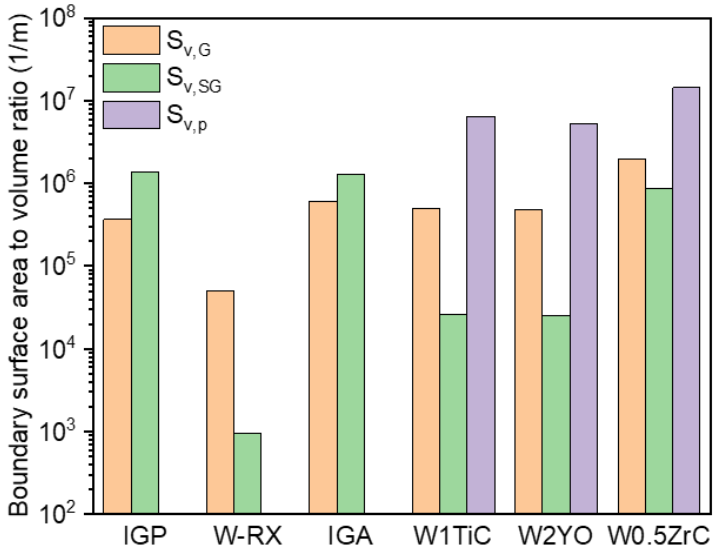

Figure 8.4. Boundary surface area to volume ratio of HAGB ($S_{v,G}$), LAGB ($S_{v,SG}$), and particle ($S_{v,p}$) of the studied tungsten grades.

Particle reinforced tungsten grades present rather high total boundary $S_{v,total}$ (the sum of $S_{v,G}$, $S_{v,SG}$, and $S_{v,p}$) apparently because of the small strengthening particles embedded in the tungsten matrix. The strengthening particles suppress grain growth (during sintering) helping to keep grain size small in comparison with the commercial tungsten grades. Especially, W0.5ZrC grade has the highest $S_{v,G}$ and $S_{v,p}$ among other tungsten grades because it has the smallest grain size and particle size, which is also reported in the earlier study [12].

The $S_{v,SG}$ (i.e., the density of low angle grain boundaries) of IGP, IGA, and W0.5ZrC grades is much larger than the one of W1TiC and W2YO materials. This is expected since W1TiC and W2YO are produced from PIM process, which is sintered at a temperature higher than 2000 °C [13] without any mechanical process like rolling or forging. As a result, the LAGB density of W1TiC and W2YO are lower than that of the rolled or hammered tungsten grades.

Respectively, the W0.5ZrC and W-RX grades exhibit the highest and lowest $S_{v,total}$ among the studied products. The low $S_{v,total}$ of W-RX is clearly an outcome of the recrystallization process, keeping in mind that before the recrystallization annealing, the IGP has very high $S_{v,SG}$, being one of the

driving forces for the recrystallization process. During the recrystallization process, the LAGB sweep across the grains and thereby getting removed. As a result, large grains with a high misorientation angle are formed.

8.2.2. Vickers hardness and irradiation hardening

The strength of materials increases with increasing boundary density. As shown in **Figure 8.5**, The hardness of non-irradiated tungsten grades is a logarithmic function of $S_{v,total}$. The boundaries act as obstacles or barriers and restrain the mobility of dislocations. Therefore, W0.5ZrC has the highest hardness because of the excessively high $S_{v,total}$.

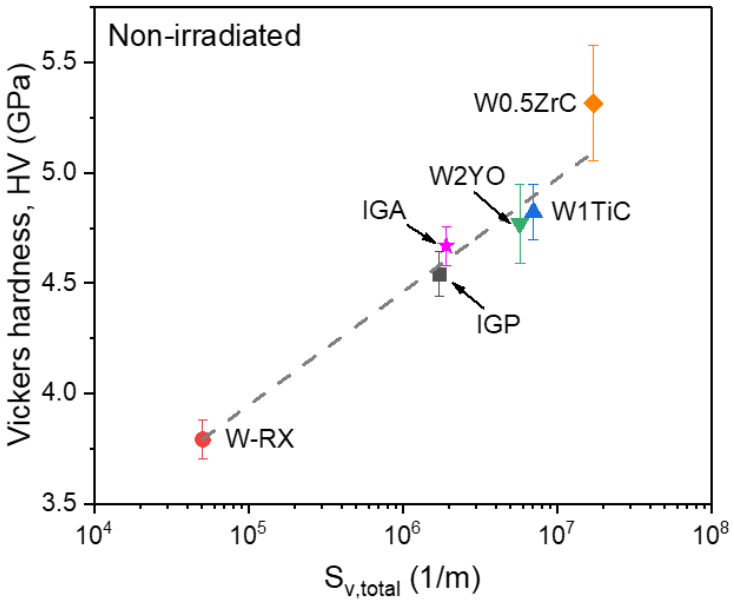

Figure 8.5. Relationship between total boundary surface to volume ratio and Vickers hardness value.

The neutron irradiation hardening and the ratio of irradiation hardening to Vicker hardness of non-irradiated state of the various tungsten grades after irradiation at 600, 1000, and 1200 °C to around 1 dpa are shown in **Figure 8.6**. For the investigated tungsten grades, except for W0.5ZrC, in this work, the irradiation hardening increases with irradiation temperature going from 600

up to 1000 °C. However, for W0.5ZrC, the irradiation hardening at the irradiation temperature of 600 °C is similar to that at 1000 °C. It might be the result of the high sink strength (i.e. high $S_{v,total}$) of the W0.5ZrC grade, which offers a better resistance to irradiation (i.e. lower increase of the hardness) by reducing the accumulation of damage.

As irradiation temperature increases to 1200 °C, the reduction of irradiation hardening effect starts to show up for all tungsten grades except for W1TiC. The reduction of irradiation hardening effect can be the result of the annihilation of irradiation-induced defects and recrystallization. For W1TiC, W2YO, and W-RX, only the annihilation of irradiation-induced defects is expected as these grades must be resistant to the grain growth at 1200 °C. However, it seems that the annihilation of irradiation-induced defects does not happen in W1TiC material, as the hardness keeps on increasing with the irradiation temperature. The absence of a reduction of the irradiation hardening in W1TiC will require further investigation. Differently from the PIM particle reinforced grades and W-RX, IGP and IGA have a high density of LAGB and do not contain strengthening particles. As indicated by Pintsuk, et al. [14] and Tsuchida, et al. [15], both IGP and IGA will be recrystallized after annealing at a temperature of 1200 °C for a long period similar to the irradiation time span applied in this work. Although W0.5ZrC also involved high LAGB density (shown in **Figure 8.4**), the resistance to the recrystallization should be higher than that of the rolled pure tungsten [12]. Therefore, the combined effect of irradiation defect annihilation and temperature-induced recrystallization on the resulting hardness should be more pronounced in the commercial tungsten grades i.e. IGP and IGA.

Other neutron irradiation hardening results from the literature [16-19], for the tungsten materials irradiated in HFIR, and JOYO, are also added in **Figure 8.6**. With a similar dose (~1 dpa), the irradiation hardening resulting from the irradiation in HFIR and JOYO reactors is around two times higher than the one measured after the irradiation in BR2. Two possible reasons can be put forward to explain this difference. Firstly, since the irradiation at HFIR was performed in the flux trap channel, the ratio of thermal to fast neutron flux was very high. In the case of BR2 irradiation, the specimens were placed directly inside the fuel element to reduce thermal to fast ratio as much as possible, and in addition to use thick stainless steel wall to absorb thermal neutrons coming from other fuel elements. As a result, the calculated concentration of the transmuted element (Re and Os) in the HFIR irradiation [16] is higher than the one in BR2. Precipitation from the high concentration of transmuted elements can be responsible for extra hardening, which is the reason why the irradiation hardness of HFIR is higher than the one of BR2 irradiated materials. Secondly, as reported by Hasegawa et al. [16], the

specimens irradiated in JOYO reactor are fabricated from the arc-melted ingot annealed at 1400 °C for 1 hour. Therefore, these specimens are expected to have a large grain size. Since the grain size is larger than those of the specimens studied in this work, more irradiation-induced defects (voids and dislocation loops) are expected to form (due to the effect of the sinking at grain boundaries [20]. However, the concentration of transmuted elements after the irradiation in JOYO reactor should be the lowest since it is a fast reactor. Therefore, the irradiation hardening resulting from the JOYO irradiation is lower compared to the one induced by the irradiation in HFIR reactor.

Given the currently established understanding of the irradiation damage [20, 21], the irradiation hardening effect is expected to reduce with increasing grain boundary density (i.e., reducing grain size) and phase boundary density (i.e., increasing particle density) because both types of these planar defects are believed to act as sinks for the irradiation defects. It is expected that one-dimensionally and three-dimensionally migrating irradiation defects will get absorbed/attracted at these planar defects and therefore will not contribute to the formation of voids and dislocation loops inside the grain interior. The latter defects are the main sources of irradiation hardening in the limit of relative low irradiation doses, while the Re/Os transmutation remains low enough. As shown in **Figure 8.7**, most tungsten grades follow the expected trend, except for the IGP, which has low irradiation hardening although $S_{v,G}$ is relatively small for this material.

The $S_{v,SG}$ is not included in this discussion because regular LAGB have lower sink strength compared to the HAGB. Indeed, as indicated in the literature [22], a large grain boundary density will promote the formation of nano-voids within the grains because of the anisotropy of the diffusion of self-interstitial atom (SIA) and of their clusters, which promotes supersaturation of the 3D-migrating vacancies. Thus, the population of the resulting irradiation-induced defects (voids and dislocation loops) depends not only on irradiation dose and temperature but also on sink strength, which is linked to the boundary (and bulk dislocation) density. As shown in **Figure 8.4** and **8.7**, IGP has a lower $S_{v,G}$ compared to the W1TiC, W2YO, and IGA material. Consequently, one should expect the void density established in the IGP to be lower than that in other tungsten grades. If that is indeed the case, and since the voids have a larger contribution to the hardening compared to the dislocation loops in tungsten [23], the irradiation hardening in the IGP should indeed be lower. Thus, grain refinement, required to achieve high strength and low DBTT in the non-irradiated material, might have a counter-productive effect in terms of the preferential formation of the voids yielding to the irradiation hardness and subsequent embrittlement. Unlike the pure tungsten grades, W1TiC,

W2YO, and W0.5ZrC have strengthening particles that provide phase boundaries as additional sinks. As shown in **Figure 8.7**, these additional sinks have a positive effect on the resistance against irradiation hardening. This might be explained by the different sink strength and sink bias between grain boundary and phase boundary (difference comes the fact that grain boundaries may absorb dislocation loops, while strengthening particles cannot). Clearly, both of the above discussed hypotheses require further investigation by transmission electron microscopy (TEM).

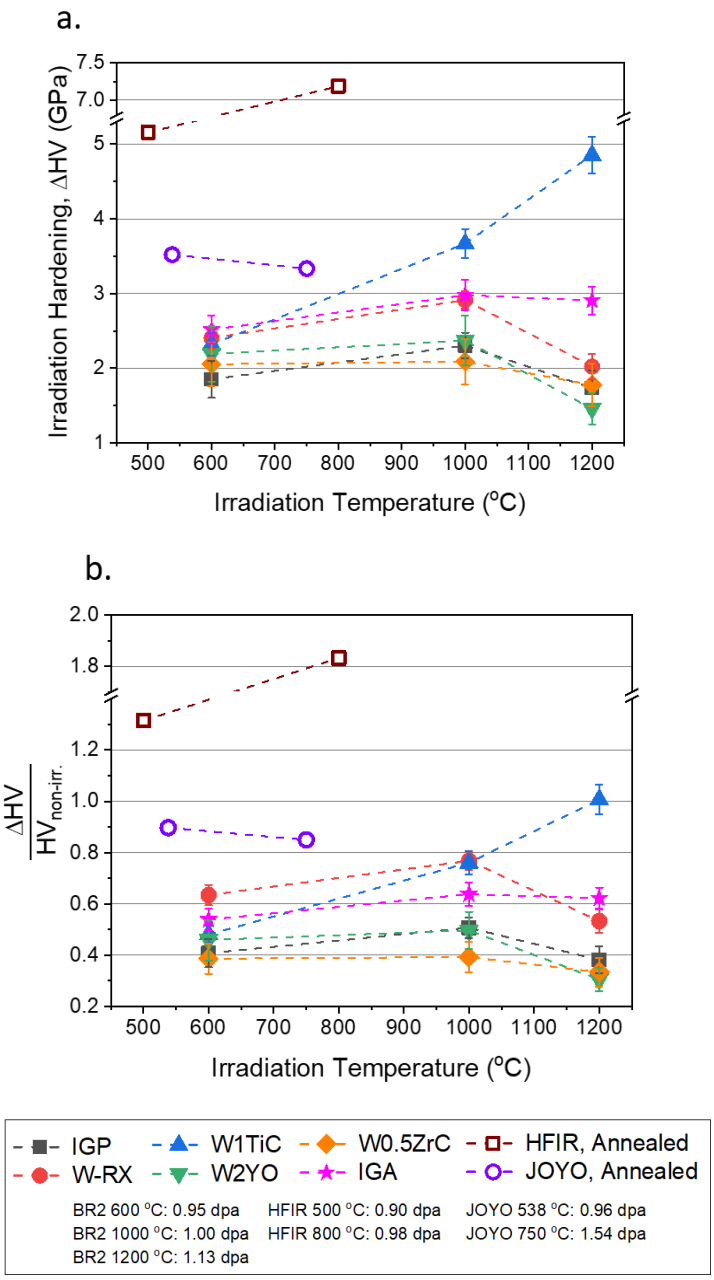

Figure 8.6. (a) Neutron irradiation hardening and (b) ratio of irradiation hardening to Vicker hardness of non-irradiated state as a function of irradiation temperature of various tungsten grades irradiated at different material test reactors and to different doses. The results of the irradiation campaigns at HFIR and JOYO reactors are taken from the literature [16-19].

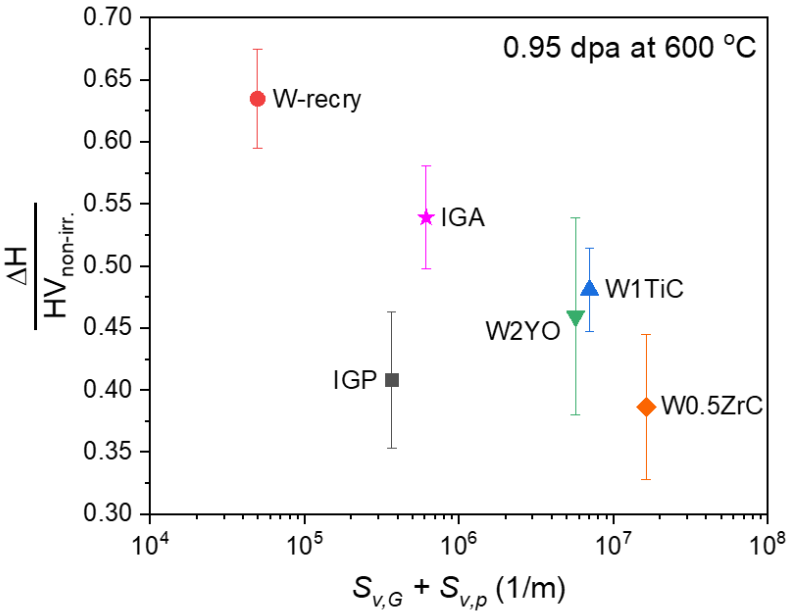

Figure 8.7. Ratio of the irradiation hardening divided by the nominal hardness vs. summed grain boundary and particle surface to volume ratio ($S_{v,G}$ and $S_{v,p}$).

8.2.3. Estimation of irradiation hardening on tensile yield strength

The variation of non-irradiated tensile yield strength as a function of temperature was obtained by fitting the tensile yield strength form our previous work [24, 25] with the **equation 8.11**. This simple fitting is sufficient for capturing the trend of tensile 0.2% yield strength at various temperatures.

$$\sigma_{y,0.2\%}(T) = \sigma_0 + \sigma_A exp(CT) \quad \textbf{(8.11)}$$

where σ_0, σ_A and C are constants; T is the temperature.

As shown in **Figure 8.8**, by shifting the non-irradiated $\sigma_{y,0.2\%}(T)$ with $\Delta\sigma_{y,0.2\%}$, which is calculated using **equation 8.10**, the $\sigma^{irr}_{y,0.2\%}(T)$ after irradiation can be estimated by **equation 8.12**.

$$\sigma^{irr}_{y,0.2\%}(T) = \sigma_{y,0.2\%}(T) + \Delta\sigma_{y,0.2\%} \quad \textbf{(8.12)}$$

Given the new curve of $\sigma^{irr}_{y,0.2\%}(T)$, it should be possible to estimate the shift

of ductile to brittle transition temperature (ΔDBTT) based on the intersection of $\sigma_{y,0.2\%}$ with fracture strength line before and after the irradiation. However, only the curves obtained for the IGP-L after the irradiation cross over the the fracture strength line. From this observation, one may conclude that all irradiated materials are expected to be brittle up to 600°C. However, this is not necessary the case if the fracture strength of the material has changed as a result of the irradiation.

As reported by Garrison, et al. [26], the fracture strength of single crystal tungsten will vary depending on the irradiation conditions and in some cases it increases after the irradiation. Moreover, **Figure 6.11** also show that the fracture strength of W0.5ZrC and ATW increases after the irradiation at ~600 °C to ~1 dpa. The increase yields to about 500 MPa making the fracture strength to be about 1.5 GPa at the test temperature of 600°C. The increase of the fracture strength might be caused by the alternation of the plastic flow evolution due to the presence of irradiation defects. In particular, the presence of the irradiation defects may enhance the homogeneity of the plastic deformation, which otherwise is concentrated around grain boundaries in the non-irradiated material. As a result, the material in the as-irradiated state may experience a higher applied stress prior to the formation and propagation of micro-cracks compared to the non-irradiated material. Hence, the fracture strength indicated in **Figure 8.8** might be underestimated.

Although the results presented in **Figure 8.8** cannot justify the estimation of the ΔDBTT, one can still see that the difference between the estimated yield stress and the reference fracture strength line is the smallest in the case of IGP and W0.5ZrC. This indicates that these two grades should have the smallest DBTT shift i.e. the highest resistance to the irradiation embrittlement.

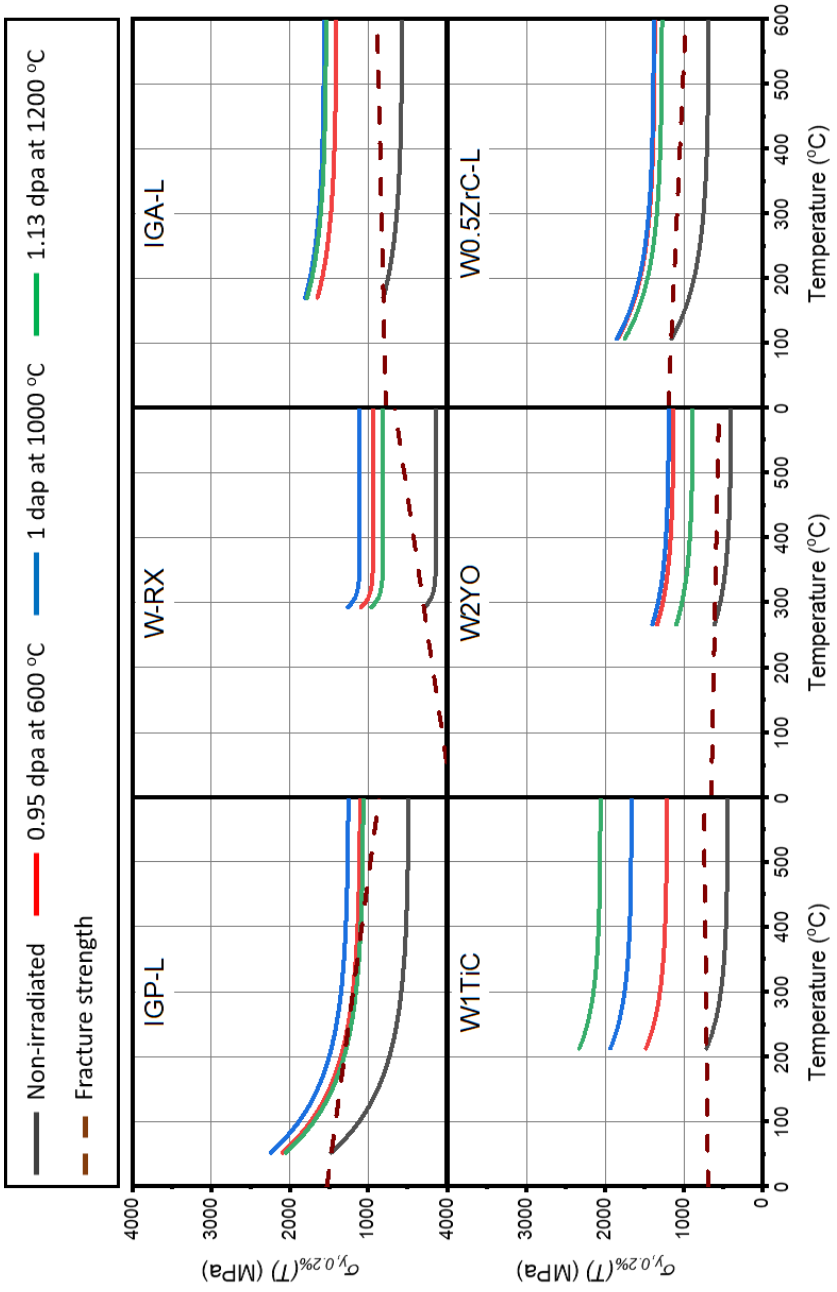

Figure 8.8. Estimation of neutron irradiation effect on $\sigma_{y,0.2\%}(T)$ curve for various tungsten grades. The data of non-irradiated tensile properties are from our previous work [24, 25]. The L behind material code indicates the loading axis is along LD.

8.3. Summary

The irradiation hardening of several tungsten grades irradiated in the BR2 reactor at 600, 1000, and 1200 °C to ~1 dpa is assessed by parametric hardness measurements performed at room temperature. Using the established correlation, the prediction of the yield stress increase resulting from the neutron irradiation is made and compared with the fracture strength of these materials measured in the non-irradiated state. Based on the experimentally measured hardness and its correlation with the yield stress established, the following conclusions can be made:

I. The highest irradiation hardening is reached at 1000 °C in all the tested grades except W1TiC, which shows an abnormal increase of the irradiation-induced hardness at 1200°C. A further microstructural investigation is required for this material to understand the reasons for this unexpected result.

II. Although the increase of the irradiation hardness at 1200 °C is smaller (except for W1TiC, see item above) compared to 600 °C and 1000 °C irradiation, it is far not negligible and actually amounts to about 30 –60% of the reference hardness value. Thus, even high irradiation temperature ($T_m/3$) does not suppress the accumulation of irradiation defects in tungsten.

III. The smallest irradiation induced hardness (i.e. best resistance to irradiation damage) is observed in IGP and W0.5ZrC products at 600 to 1000 °C, which is likely to be explained by a high density of sinks (i.e., the density of LAGB, HAGB, dislocations, and particles in W0.5ZrC). The evaluation of the irradiation hardness at 1200°C requires additional EBSD analysis of the irradiated samples as certain recrystallization may occur during the extended irradiation period (125 days of irradiation).

IV. Following the estimates of 0.2% yield stress based on the correlation with the measured hardness, IGP-L appears to have the best resistance to the irradiation damage. Although the estimated 0.2% yield stress of irradiated material should be quite accurate (the IT test achieves a similar result in Chapter 6 for W0.5ZrC), this estimation should be treated carefully since the fracture strength of the irradiated materials may change as well as the applicability of the proposed correlation function. Further tensile tests are required to substantiate the conclusion and derived correction function.

8.4. Reference

[1] M. Klamkin, Elementary approximations to the area of n-dimensional ellipsoids, The American Mathematical Monthly 78(3) (1971) 280-283.
[2] M. Klamkin, Corrections to “Elementary Approximations to the area of N-Dimensional Ellipsoids” (This Monthly, 78 (1971) 280–283), The American Mathematical Monthly 83(6) (1976) 478-478.
[3] K. Thomsen, Surface area of an ellipsoid. <http://www.numericana.com/answer/ellipsoid.htm#thomsen>, 2004).
[4] K.L. Johnson, Contact mechanics, Cambridge university press1987.
[5] D. Tabor, The hardness of metals, Oxford university press2000.
[6] J. Cahoon, W. Broughton, A. Kutzak, The determination of yield strength from hardness measurements, Metallurgical transactions 2(7) (1971) 1979-1983.
[7] J. Aktaa, C. Petersen, Modeling the constitutive behavior of RAFM steels under irradiation conditions, Journal of Nuclear Materials 417(1-3) (2011) 1123-1126.
[8] C. Yin, D. Terentyev, T. Pardoen, A. Bakaeva, R. Petrov, S. Antusch, M. Rieth, M. Vilemova, J. Matejicek, T. Zhang, Tensile properties of baseline and advanced tungsten grades for fusion applications, Int J Refract Met H 75 (2018) 153-162.
[9] M. Wirtz, J. Linke, T. Loewenhoff, G. Pintsuk, I. Uytdenhouwen, Thermal shock tests to qualify different tungsten grades as plasma facing material, Physica Scripta T167 (2016) 014015.
[10] C. Yin, D. Terentyev, T. Zhang, R.H. Petrov, T. Pardoen, Impact of neutron irradiation on the strength and ductility of pure and ZrC reinforced tungsten grades, Journal of Nuclear Materials 537 (2020).
[11] Z.M. Xie, R. Liu, S. Miao, X.D. Yang, T. Zhang, X.P. Wang, Q.F. Fang, C.S. Liu, G.N. Luo, Y.Y. Lian, X. Liu, Extraordinary high ductility/strength of the interface designed bulk W-ZrC alloy plate at relatively low temperature, Scientific Reports 5 (2015) 1-11.
[12] H. Deng, Z. Xie, Y. Wang, R. Liu, T. Zhang, T. Hao, X. Wang, Q. Fang, C. Liu, Mechanical properties and thermal stability of pure W and W-0.5 wt% ZrC alloy manufactured with the same technology, Materials Science and Engineering: A 715 (2018) 117-125.
[13] S. Antusch, D.E. Armstrong, T.B. Britton, L. Commin, J.S.-L. Gibson, H. Greuner, J. Hoffmann, W. Knabl, G. Pintsuk, M. Rieth, Mechanical and microstructural investigations of tungsten and doped tungsten materials produced via powder injection molding, Nuclear Materials and Energy 3 (2015) 22-31.

[14] G. Pintsuk, S. Antusch, T. Weingaertner, M. Wirtz, Recrystallization and composition dependent thermal fatigue response of different tungsten grades, Int. J. Refract. Met. Hard Mater. 72 (2018) 97-103.
[15] K. Tsuchida, T. Miyazawa, A. Hasegawa, S. Nogami, M. Fukuda, Recrystallization behavior of hot-rolled pure tungsten and its alloy plates during high-temperature annealing, Nuclear Materials and Energy 15 (2018) 158-163.
[16] A. Hasegawa, M. Fukuda, S. Nogami, K. Yabuuchi, Neutron irradiation effects on tungsten materials, Fusion Eng Des 89(7-8) (2014) 1568-1572.
[17] M. Fukuda, K. Yabuuchi, S. Nogami, A. Hasegawa, T. Tanaka, Microstructural development of tungsten and tungsten–rhenium alloys due to neutron irradiation in HFIR, J. Nucl. Mater. 455(1-3) (2014) 460-463.
[18] T. Tanno, M. Fukuda, S. Nogami, A. Hasegawa, Microstructure development in neutron irradiated tungsten alloys, Materials transactions (2011) 1105231402-1105231402.
[19] T. Tanno, A. Hasegawa, J.-C. He, M. Fujiwara, S. Nogami, M. Satou, T. Shishido, K. Abe, Effects of transmutation elements on neutron irradiation hardening of tungsten, Materials Transactions (2007) 0708200165-0708200165.
[20] S. Golubov, B. Singh, H. Trinkaus, Defect accumulation in fcc and bcc metals and alloys under cascade damage conditions–Towards a generalisation of the production bias model, J. Nucl. Mater. 276(1-3) (2000) 78-89.
[21] G.S. Was, Fundamentals of radiation materials science: metals and alloys, springer2016.
[22] N. Castin, A. Bakaev, G. Bonny, A. Sand, L. Malerba, D. Terentyev, On the onset of void swelling in pure tungsten under neutron irradiation: an object kinetic Monte Carlo approach, J. Nucl. Mater. 493 (2017) 280-293.
[23] X. Hu, T. Koyanagi, M. Fukuda, N.K. Kumar, L.L. Snead, B.D. Wirth, Y. Katoh, Irradiation hardening of pure tungsten exposed to neutron irradiation, J Nucl Mater 480 (2016) 235-243.
[24] C. Yin, D. Terentyev, T. Pardoen, A. Bakaeva, R. Petrov, S. Antusch, M. Rieth, M. Vilemova, J. Matejicek, T. Zhang, Tensile properties of baseline and advanced tungsten grades for fusion applications, Int. J. Refract. Met. Hard Mater. 75 (2018) 153-162.
[25] C. Yin, D. Terentyev, T. Zhang, R.H. Petrov, T. Pardoen, Impact of neutron irradiation on the strength and ductility of pure and ZrC reinforced tungsten grades, J. Nucl. Mater. (2020) 152226.
[26] L. Garrison, Y. Katoh, N.K. Kumar, Mechanical properties of single-crystal tungsten irradiated in a mixed spectrum fission reactor, J. Nucl. Mater. 518 (2019) 208-225.

Chapter 9
Anisotropy in the hardness of single crystal tungsten before and after neutron irradiation

9.1. Materials and microindentation measurement

The single crystal tungsten, W(100), used in this study was produced by MaTeck (Germany) in the form of a cylindrical rod of 12 mm diameter. The nominal purity of the material was 99.999%. Disc shaped specimens with about 0.8 mm thickness were cut using electric discharge machining (EDM) and subsequently polished to remove the EDM damage. A mirror-like surface was achieved before the samples were placed in the irradiation rig. After neutron irradiation, optical imaging confirmed that the surface kept its good quality (i.e. no traces of mechanical damage or oxidation on the surface of the sample) after the irradiation.

The micro-hardness tests were performed on W(100) disks of 11 mm diameter and 0.5 mm thickness with surface orientation (001) using a diamond Vickers pyramid indenter. The load was set to 200 gf and both the loading and holding time were 10 seconds each. Two hardness values are presented in this work: the hardness following the ideal projected area, H_{ideal}, and hardness following the true projected area, H_{true}. The ideal projected area, A_{ideal}, is obtained as $d^2/2$, with d the average length of the diagonal left by the indenter, as observed through optical microscopy. The true projected area, A_{true}, accounts for the actual shape of the indent and is computed from optical micrographs via the ImageJ analysis software [1].

An estimate of a pile-up height (or sink-in depth) were calculated from the true shape of the indent, inspired from the work by Kang et al [2]. The depth of the indent, h_ω, is determined as,

$$h_\omega = \frac{d_\omega \cos\omega}{\tan 68^\circ}, \quad \textbf{(9.1)}$$

where d_ω is the distance from the center of the indent to its edge, at a certain angle ω. A schematic representation of indent geometry is given in **Figure 9.1** Following **equation 9.1**, the pile-up height, h_R, is defined as,

$$h_R = h_\omega - h_{min}, \quad \textbf{(9.2)}$$

with $h_{\min}$ being the smallest value of h_ω obtained with varying ω. With this definition, the variation of pile-up height can be estimated around the indent.

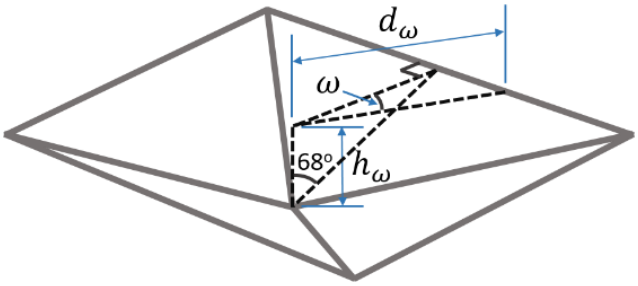

Figure 9.1. Schematic representation of the indent geometry.

9.2. Results and discussion

9.2.1. Anisotropy in single crystal tungsten

The results of the ideal hardness, H_{ideal}, and true hardness, H_{true}, versus rotation angle, θ, are summarized in **Figure 9.2a** and **b**, respectively. The sample was rotated over 180° in steps of 5°, with three independent measurements per θ. The angles for which the indenter diagonal is parallel to specific crystallographic directions are indicated in the plot. The specific crystallographic directions were determined from electron back-scattered diffraction (EBSD) measurements.

Both H_{ideal} and H_{true} oscillate around an average hardness of ~3.7 GPa, with a period of 90°, but are in anti-phase against each other. The minimum and maximum values for H_{ideal} are obtained when the indenter diagonal (wedge) is parallel to a <110> and <100> direction, respectively, while for H_{true} the oposite applies. These trends can be explained by comparing the ideal projected area with the true one, as shown in **Fig. 2**. For an indenter diagonal parallel to a <100> direction, $A_{\mathrm{ideal}} < A_{\mathrm{true}}$, while for an indenter diagonal parallel to a <110> direction, $A_{\mathrm{ideal}} > A_{\mathrm{true}}$. As a consequence, $H_{\mathrm{ideal}} > H_{\mathrm{true}}$ for an indenter diagonal parallel to a <100> direction, while the opposite is true for an indenter diagonal parallel to a <110> direction. The difference between A_{ideal} and A_{true} is thus large enough to change the phase of H_{ideal} such that H_{true} oscillates in anti-phase. The difference in oscillation amplitude (the one for H_{ideal} is smaller than the one for H_{true}) is explained by the same logic.

Clearly, the scatter for H_{ideal} is larger than for H_{true}. The scatter for H_{ideal} is a consequence of inaccuracies in the determination of the indent diagonals, due to the non-ideal shape of the indents (due to non-isotropic plastic deformation), from which A_{ideal} is determined. The values for A_{true}, on the other hand, are computed via the ImageJ analysis software with high accuracy.

As shown in **Figure 9.2b**, H_{true} is well described (correlation factor $R^2 = 0.97$) by the periodic function,

$$H_{true} = H_0 \left[1 + \delta H \, sin\left(2\pi \frac{\theta - \theta_0}{\theta_P}\right)\right]. \qquad \textbf{(9.3)}$$

Here H_0 is the average value of H_{true}, δH is the relative amplitude of the oscillation, θ_0 is a phase shift and $\theta_P = 90°$ is the period of the function. The resulting fit and optimized parameters are shown in **Figure 9.2b** and **Table 9.1**, respectively. The relative amplitude $\delta H = 8\%$ is obtained, meaning that H_{true} can vary by up to 16%, depending on the particular

indenter-sample orientation, solely due to the anisotropy of the plastic slip in single crystal. Hence, it is important to characterize H_0 for a given data set. Thus, if different indenter orientations are not accounted for during the data acquisition, a systematic error of up to 8% could be introduced in the resulting hardness value.

The observed anisotropy in H_{ideal} and H_{true} can be rationalized based on the indenter geometry and single crystal orientation. It is established that the hardness of a material is correlated to its yield strength, σ_y (e.g. via Tabor's relation [3]). In turn, σ_y is related to the critical resolved shear stress, τ_C, i.e., the critical stress to invoke dislocation slip in a specific slip system, via the Schmid factor, m. Thus, for H_{ideal} follows,

$$H_{ideal} \sim \sigma_y = \frac{\tau_C}{m}. \qquad \textbf{(9.4)}$$

In turn, the Schmid factor m is defined as,

$$m = cos\,\phi\, cos\,\lambda, \qquad \textbf{(9.5)}$$

with ϕ being the angle between the applied stress and the slip-plane normal and λ is the angle between the applied stress and slip direction.

For the present set-up, i.e., Vickers pyramid indentation is applied to the (001) plane surface of the single crystal, the Schmid factor m for most common BCC slip systems {110}<111> and {112}<111> for different rotation angles θ was calculated. Hereby, the force applied by the indenter is assumed to transfer into the material via normal stresses perpendicular to the facets of the indenter. In **Figure 9.3a**, values of H_{ideal} obtained from the measurements and **equation 9.4** are plotted as a function of θ. It is noted that maximum obtained absolute value of m was used in **equation 9.4** as the slip system that maximizes $|m|$ generates slip. Given the scatter in the data and the simplicity of the theory, **equation 9.4** well describes the evolution of H_{ideal}. The periodicity of the experimental data is correctly reproduced and the amplitude is in the correct range.

By definition, H_{true} is related to H_{ideal} following,

$$H_{true} = \frac{A_{ideal}}{A_{true}}\, H_{ideal} \sim \frac{A_{ideal}}{A_{true}}\, \frac{1}{m}. \qquad \textbf{(9.6)}$$

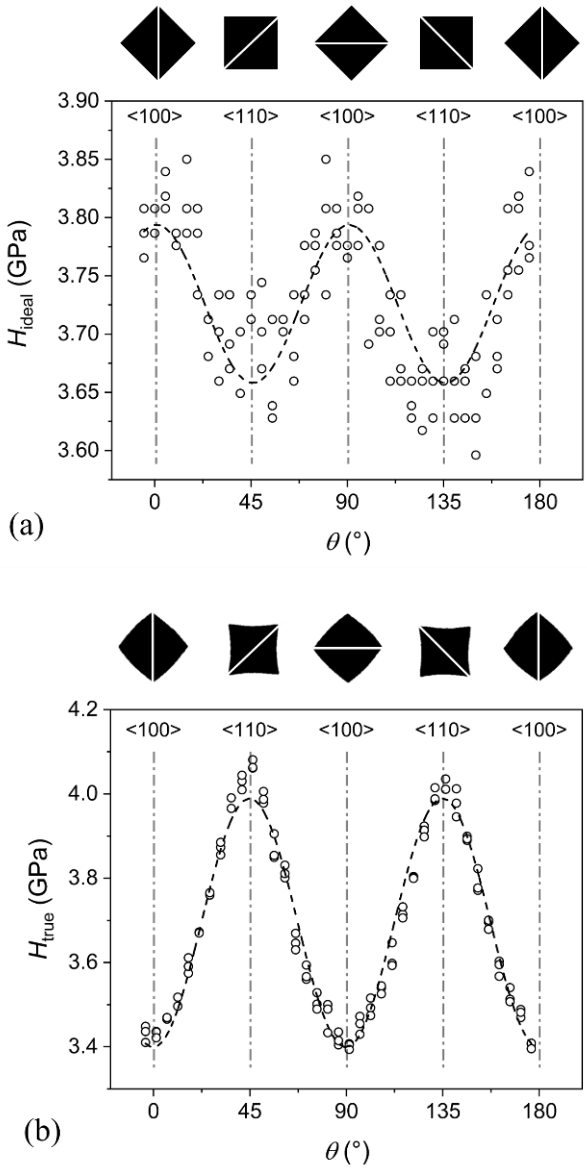

Figure 9.2. Evolution of (a) H_{ideal} and (b) H_{true} with rotation angle θ between indenter diagonal and [100] direction in W(100). Angles for which the indenter diagonal is parallel to specific crystallographic directions are indicated in the graphs. A schematic representation of the indent position is displayed above the graphs. Fitted curves following **equation 9.3** are added to the plots.

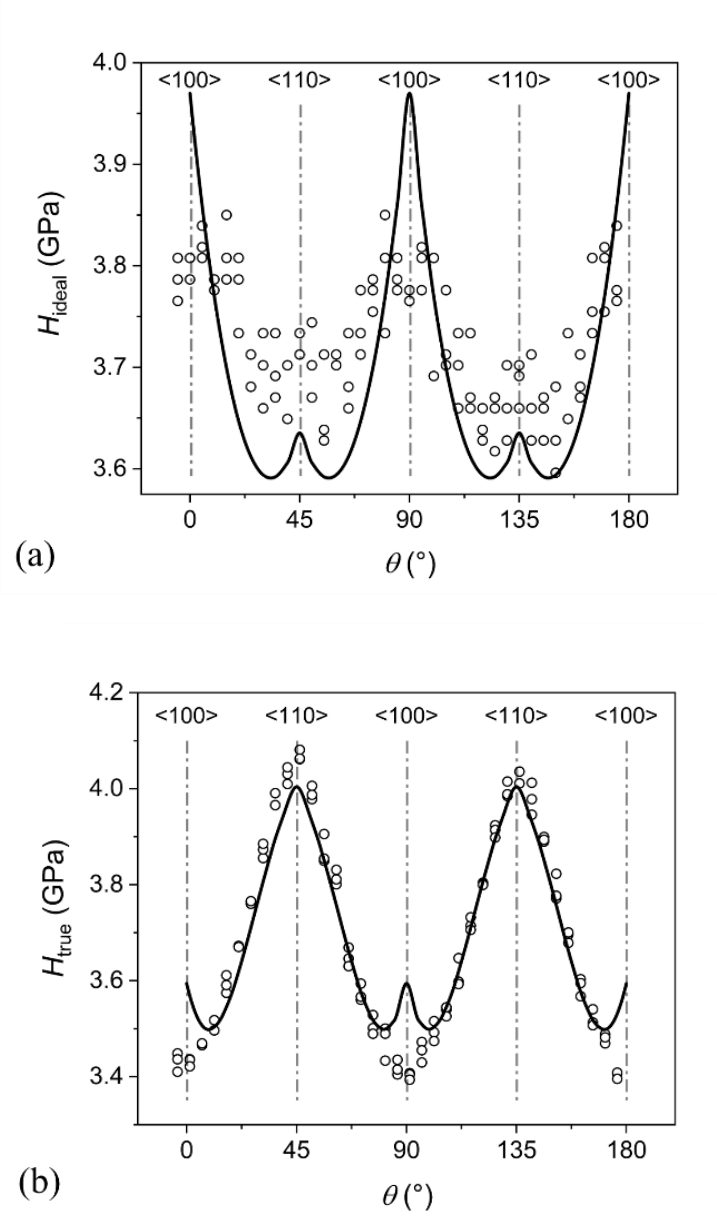

Figure 9.3. Comparison between theory and measured data for (a) H_{ideal} and (b) H_{true}.

In **Figure 9.3b**, the values of H_{true} obtained from the experimental measurements and **equation 9.6** are plotted as a function of θ. The curve obtained using **equation 9.6** is in excellent agreement with the measured

data. Hence, this simple theoretical layout confirms that H_{true} and H_{ideal} are in anti-phase due to the difference true and ideal projected areas ($A_{\mathrm{ideal}}/A_{\mathrm{true}}$). Thus, the observed anisotropy in both H_{ideal} and H_{true} is solely determined by the relative orientation between indenter and single crystal, and in turn being linked with the discreetness of the slip systems available in the BCC lattice.

The discrepancy between A_{ideal} and A_{true} is the consequence of the emergence of pile-ups under the indenter since no sink-in is expected according to the literature [4, 5]. In these studies, it is shown that for W, which has a small hardening rate, pile-up is expected rather than sink-in. Thus, in this work, typical sink-in patterns (e.g. $\theta = 45°$ in **Figure 9.4b**) should merely correspond with the observation of the maximum pile-up at the indenter corner, rather than sink-in at the center of the indenter edge. In **Figure 9.4a**, the pile-up height, h_R, calculated following **equation 9.2** is presented along different crystallographic directions for different orientations of the indenter. The optical micrographs used for these calculations are displayed in **Figure 9.4b**. Clearly, the maximum pile-up height is observed along the <110> directions of the crystal, irrespective of the indenter rotation angle θ. Therefore, at $\theta = 0°$, maximum pile-up is observed at the centre of the indenter edge ($\omega = 0°$), while at $\theta = 45°$, maximum pile-up is observed at the indenter corner ($\omega = 45°$).

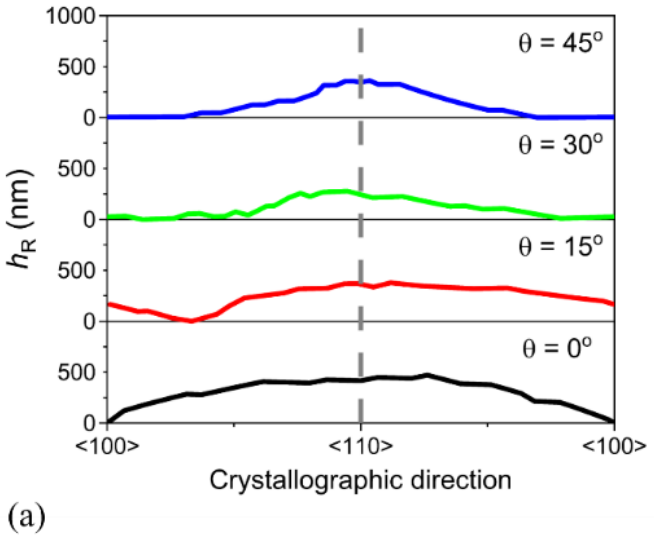

(a)

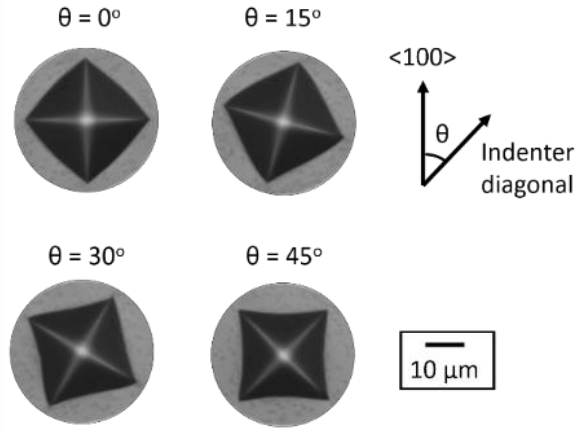

(b)

Figure 9.4. (a) Calculated pile-up height, h_R, along different crystallographic directions for different indenter orientations. (b) Optical micrographs of the corresponding indents.

9.2.2. Effect of neutron irradiation

Based on the detailed analysis of the anisotropy in hardness for unirradiated W(100), H_{true} is determined for the neutron-irradiated samples in the following. To fully characterize H_{true}, measurements were performed at three rotation angles θ, each separated by 30°. For each θ, three independent measurements were performed for statistics. Subsequently, the full curve for H_{true} was obtained by fitting **equation 9.3** to the obtained data points for each sample. The resulting fitted curves for H_{true} and data they are based on are summarized in **Figure 9.5**. For convenience, all relevant fitting parameters are also tabulated in **Table 9.1**.

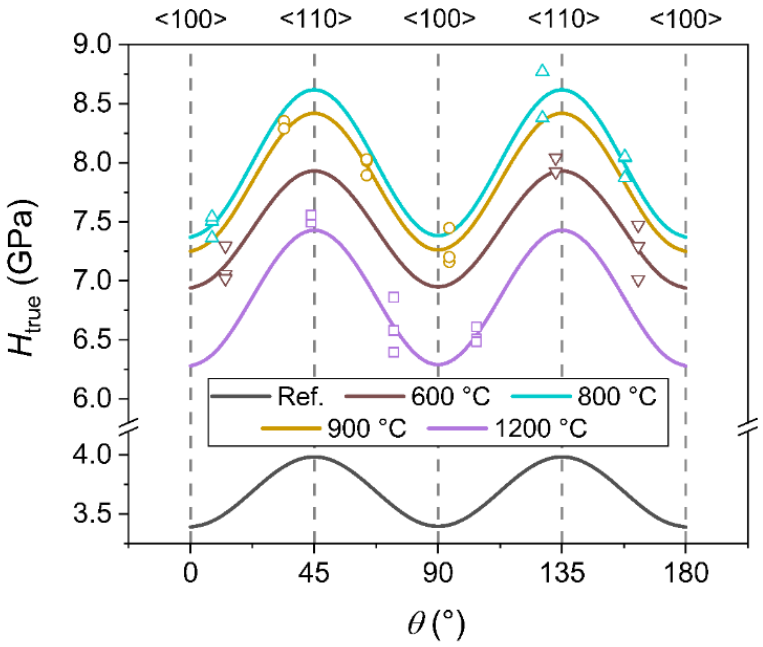

Figure 9.5. Evolution of H_{true} with rotation angle θ for different irradiation temperatures. Angles for which the indenter diagonal is parallel to specific crystallographic directions are indicated in the graph.

Table 9.1. Summary of the fitting parameters characterizing H_{true} via **equation 3**.

Sample	H_0 (GPa)	δH (n.u.)
Ref.	3.69 ± 0.00	0.081 ± 0.003
600 °C	7.44 ± 0.06	0.085 ± 0.011
800 °C	8.00 ± 0.05	0.075 ± 0.009
900 °C	7.84 ± 0.04	0.079 ± 0.006
1200 °C	6.86 ± 0.05	0.085 ± 0.012

The average irradiation hardening, $\Delta H_0 = H_0^{\mathrm{irr}} - H_0^{\mathrm{ref}}$, is shown in **Figure 9.6a**. The maximum radiation hardening is observed at 800 °C, which amounts up to 117% of H_0^{ref}. This maximum is consistent with the reported peak swelling at 800 °C [6]. Recently, a similar trend with irradiation temperature was observed for the same material, irradiated in the same temperature range but only up to 0.12 dpa [7]. In that work, positron annihilation spectroscopy (PAS), object kinetic Monte Carlo (OKMC) [8-10] and a dispersed barrier model were combined to link the radiation-induced microstructure to the observed hardening. The maximum hardness was correlated to a high number density of small voids, while the reduction of irradiation hardening above 800 °C was associated with decreasing a number density of voids (coarsening of small voids into larger ones). The radiation hardening below 800 °C, on the other hand, was associated with the presence of small voids (smaller compared to 800 °C) but with similar number density. Thus, at 1200 °C only a partial recovery of the radiation hardening occurs, while the radiation hardening is still significant, i.e., ~86% of H_0^{ref}.

In **Figure 9.6b** and **Table 9.1**, δH is reported for unirradiated and 1.05 dpa irradiated W samples. Clearly, after the irradiation, δH remains nearly the same compared to the reference value, regardless the irradiation temperature. This implies that the presence of the irradiation defects (at least dislocation loops, voids, and highly likely Re/Os precipitates) does not impose any strong bias in the action/suppression of the slip systems otherwise operating in the non-irradiated material. So that, in the irradiated material, the anisotropy is solely determined by the relative orientation between indenter and single crystal just like in the defect free crystal.

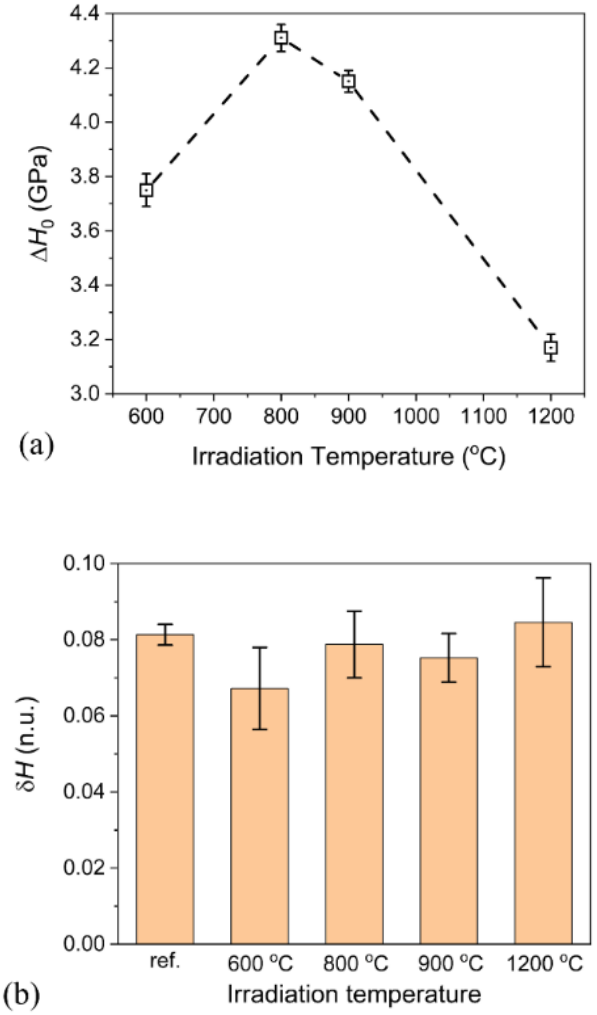

Figure 9.6. (a) Evolution of radiation hardening, $\Delta H_0 = H_0^{\mathrm{irr}} - H_0^{\mathrm{ref}}$, with irradiation temperature. (b) Relative amplitude, δH, obtained for the different samples.

In **Figure 9.7**, the irradiation hardening data (a difference of the hardness measured before and after the irradiation) obtained in the present work is summarized together with available data from the literature obtained for single crystal W after neutron irradiation. The data were obtained from irradiation campaigns executed at the HFIR reactor in the temperature range 80-830 °C with thermal neutron unshielded capsules [11-13]; irradiation

campaigns in the HFIR reactor in the temperature range 580-780 °C using thermal neutron shielded capsules [14]; and irradiation campaigns in the BR2 reactor in the temperature range 600-1200 °C [7]. Clearly, all data (including the data obtained in the present work) fits the same trend described by a typical power law. Thus, no saturation of the hardening is observed at least up to 3 dpa. The scatter in the data due to different radiation temperatures makes it impossible to address the variations in hardness due to different neutron spectra.

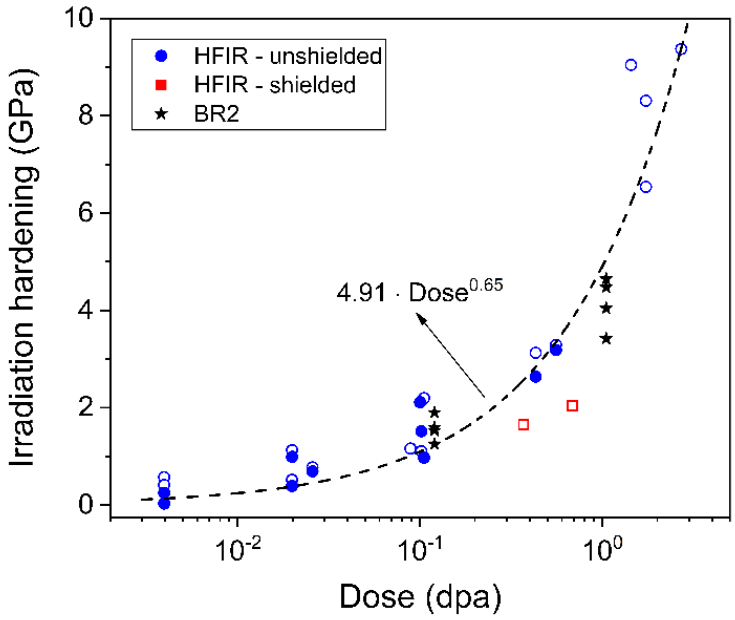

Figure 9.7. Irradiation hardening, expressed as a difference of the hardness measured before and after the irradiation, of single crystal W after neutron irradiation in different reactors under various conditions with accumulated dose. Open symbols represent W(110) while filled symbols represent W(100). References to the data are provided in the text.

9.3. Summary

Based on the results and their discussion, the following conclusions can be formulated.

I. Anisotropy is observed in the hardness of single crystal W(100) with an amplitude up to 8% for both irradiated and unirradiated materials.

II. The true hardness is well described by a sine function with the maximum corresponding to the configuration of the indenter diagonal being parallel to the <110> crystal axis and the minimum – for the indenter diagonal being parallel to the <100> crystal axis.

III. The anisotropy in both irradiated and unirradiated samples is rationalized based on the relative orientation between indenter and a number of available slip systems.

IV. A simple methodology to deduce the mean hardness, H_0, which can be used as an unbiased value to measure the hardness of single crystal W, is proposed here. This method may also prove useful to the case of massive recrystallization in the polycrystalline tungsten, when the grain size becomes large enough to accommodate the strain due to indenter.

V. Neutron irradiation up to 1 dpa causes a strong increase of the hardness (more than a factor of two compared to the reference value). The maximum hardness is attained at 800 °C, which coincides with the temperature of the peak swelling. Only limited recovery of the irradiation-induced hardening is observed after the irradiation at 1200 °C, such that the absolute value of H_0 remains twice as large compared to the reference material. This is a clear proof that even at 1200 °C, neutron irradiation generates considerable density of thermally stable lattice defects (most likely conducted with segregation/precipitation of Re/Os) that are not recovered (annihilated) by thermally activated diffusion processes.

VI. Based on the anisotropy of the hardness, deduced here for reference and neutron irradiated single crystal tungsten, it is recommended to apply an uncertainty of ~8% to the absolute value of the hardness if the exact orientation of the indenter and crystallographic axes of the crystal is not known.

9.4. References

[1] C.A. Schneider, W.S. Rasband, K.W. Eliceiri, NIH Image to ImageJ: 25 years of image analysis, Nature Methods 9(7) (2012) 671-675.
[2] S.K. Kang, J.Y. Kim, C.P. Park, H.U. Kim, D. Kwon, Conventional Vickers and true instrumented indentation hardness determined by instrumented indentation tests, J Mater Res 25(2) (2010) 337-343.
[3] D. Tabor, The Hardness of Metals (1951).
[4] B. Eidel, Crystal plasticity finite-element analysis versus experimental results of pyramidal indentation into (0 0 1) fcc single crystal, Acta Mater. 59(4) (2011) 1761-1771.
[5] W.Z. Yao, J.H. You, Berkovich nanoindentation study of monocrystalline tungsten: a crystal plasticity study of surface pile-up deformation, Philosophical Magazine 97(17) (2017) 1418-1435.
[6] J. Matolich, H. Nahm, J. Moteff, Swelling in neutron irradiated tungsten and tungsten-25 rhenium, Scripta Metallurgica 8 (1974) 837-842.
[7] G. Bonny, M.J. Konstantinovic, A. Bakaeva, C. Yin, N. Castin, K. Mergia, V. Chatzikos, S. Dellis, T. Khvan, A. Bakaev, A. Dubinko, D. Terentyev, Trends in vacancy distribution and hardness of high temperature neutron irradiated single crystal tungsten, Acta Mater. 198 (2020) 1-9.
[8] N. Castin, A. Bakaev, G. Bonny, A.E. Sand, L. Malerba, D. Terentyev, On the onset of void swelling in pure tungsten under neutron irradiation: An object kinetic Monte Carlo approach, Journal of Nuclear Materials 493 (2017) 280-293.
[9] N. Castin, G. Bonny, A. Bakaev, C.J. Ortiz, A.E. Sand, D. Terentyev, Object kinetic Monte Carlo model for neutron and ion irradiation in tungsten: Impact of transmutation and carbon impurities, Journal of Nuclear Materials 500 (2018) 15-25.
[10] N. Castin, A. Dubinko, G. Bonny, A. Bakaev, J. Likonen, A. De Backer, A.E. Sand, K. Heinola, D. Terentyev, The influence of carbon impurities on the formation of loops in tungsten irradiated with self-ions, Journal of Nuclear Materials 527 (2019) 151808.
[11] L.M. Garrison, Y. Katoh, N.A.P.K. Kumar, Mechanical properties of single-crystal tungsten irradiated in a mixed spectrum fission reactor, Journal of Nuclear Materials 518 (2019) 208-225.
[12] M. Fukuda, N.A.P. Kiran Kumar, T. Koyanagi, L.M. Garrison, L.L. Snead, Y. Katoh, A. Hasegawa, Neutron energy spectrum influence on irradiation hardening and microstructural development of tungsten, Journal of Nuclear Materials 479 (2016) 249-254.
[13] X. Hu, T. Koyanagi, M. Fukuda, N.A.P.K. Kumar, L.L. Snead, B.D. Wirth, Y. Katoh, Irradiation hardening of pure tungsten exposed to neutron irradiation, Journal of Nuclear Materials 480 (2016) 235-243.

[14] L.M. Garrison, Y. Katoh, J.W. Geringer, M. Akiyoshi, X. Chen, M. Fukuda, A. Hasegawa, T. Hinoki, X. Hu, T. Koyanagi, E. Lang, M. McAlister, J. McDuffee, T. Miyazawa, C. Parish, E. Proehl, N. Reid, J. Robertson, H. Wang, PHENIX U.S.-Japan Collaboration Investigation of Thermal and Mechanical Properties of Thermal Neutron–Shielded Irradiated Tungsten, Fusion Science and Technology 75(6) (2019) 499-509.

Chapter 10
Summary and Conclusions

The objective of this thesis was to investigate the ductile to brittle transition temperature (DBTT) and the degradation of mechanical properties of tungsten after neutron irradiation. In order to reach these targets, the studies have been performed across three directions: (i) development of miniaturized mechanical testing methods, adapted, or modified in terms of specimen design, loading condition, loading fixtures, and data reduction schemes; (ii) the mechanical tests on non-irradiated tungsten products have been analyzed and interpreted with respect to the microstructure and fracture surfaces as characterized by SEM, EBSD, and EDS; (iii) both procedures were applied to neutron irradiated materials performing tests in hot cells. Twelve different tungsten products, which have been irradiated and tested, are listed in **Table 10.1**.

Table 10.1. Basic information for tested tungsten products

Materials	Composition (by weight)	Grain size (D50, μm)	Manufacturing process
IGP	Pure W	53 – 87	Double hammering
IGA	Pure W	19	Rolling
ATW	Pure W	60	Rolling
W-RX	Pure W	60	IGP annealed 1600 °C/1 hr
FG	Pure W	9	SPS
HDK	W + 60 ppm K	27	Heavily deformed (Rolling)
ALK	W + 30 ppm K	37	Rolling
ALKR	W + 3% Re + 28 ppm K	33	Rolling
W1TiC	W + 1% TiC	6 – 8	PIM
W2YO	W + 2% Y_2O_3	6 – 7	PIM
W0.5ZrC	W + 0.5% ZrC	5 – 7	Rolling + TMT

The main findings and the developments associated with these three directions are summarized hereafter.

10.1. Mechanical testing methods

The developed mechanical testing methods, as shown in the schemes from **Figure 10.1**, can be summarized as follows:

I. The miniaturized three-point bending test can be used as complementary information to determine the DBT transition curve from the fracture toughness test. Since the miniaturized three-point bending specimens are small in volume and exhibit a trivial geometry, a high number of such test specimens can be irradiated in the limited volume available in the high flux positions of material test reactors (and in DONES/IFMIF in the future), the test fixtures can be of rather simple geometry, as well as machining of the rectangular bars from the irradiated broken samples is also possible. As a result, the cost and time to perform the irradiation and post irradiation programs can be reduced. Moreover, homogeneous proton irradiation (for proton energy of tens of MeV) is also possible since the specimen cross-section area is 1 mm^2, which is compatible with the penetration depth of protons for tungsten. Hence, the miniaturized 3PB geometry also enables the application of Fusion Target Station, being under development at SCK CEN within MYRRHA project. The fitting method for the transition curve with a DBTT defined by a flexural strain of 5% has been successfully implemented to identify the DBT transition curves of various tungsten grades. This defined DBTT is also close to the temperature at which the tensile specimen starts to show a small degree of plastic deformation.

II. An estimate of the DBTT region can also be identified by a new test method developed in this study. This is the single specimen interrupted tensile test with the descending test temperature, which captures the lowest temperature at which micro-yielding still takes place. The trend of the yield strength vs. temperature can also be determined by these interrupted tensile tests. It requires finding the stress at half maximum load rate (HMLR). This approach minimizes the number of samples required for the identification of the DBTT region as well as allows one for a significant reduction of the cost and time.

III. Finally, a simple and efficient method was elaborated to extract the hardness of neutron irradiated single crystal, for which the specific crystallographic orientation of the sample is a priori unknown. Indeed, hardness anisotropy in single crystal is well known phenomenon, so that unambiguous determination of the hardness

requires the knowledge of the crystallographic orientation. This study has proposed a parameter H_0, which can be considered as an unbiased hardness value to evaluate single crystal hardness by Vickers indenter. This unbiased hardness method requires at least three hardness tests in different orientations in order to fit the proposed sine function. Based on the obtained results, a recommendation to apply 8% uncertainty for the mean hardness value for both non-irradiated and irradiated samples is drawn, in the case of hardness measurement without indenter rotation or with the unknown crystallographic orientation of the sample.

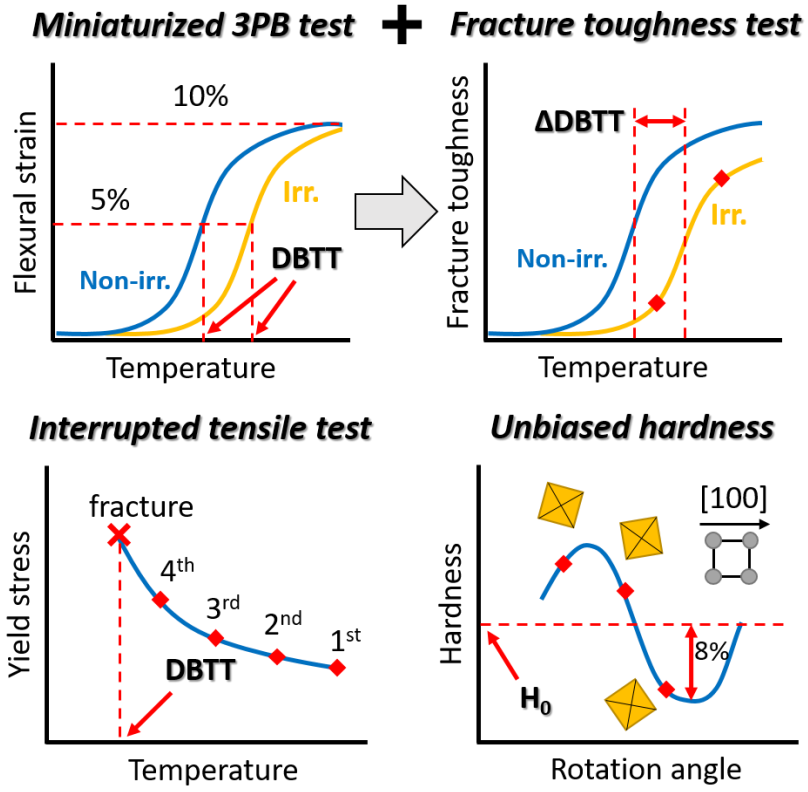

Figure 10.1. Schemes of the developed mechanical testing methods

10.2. Mechanical properties of non-irradiated tungsten alloys

The main results regarding non-irradiated tungsten alloys are shown in **Figure 10.2**. Moreover, the main findings are summarized as follows:

I. For rolled/forged tungsten, the DBTT depends on grain orientation. The lowest DBTT value is found in the longitudinal direction (LD) specimens, which have their elongated grains parallel to the tensile load. The origin of this dependence is related to the crack propagation path, which preferentially takes place along tungsten's grain boundary (weakest link) and which will be deflected to the direction parallel to the fracture plane of LD specimens. If the deflection of the crack is not possible, a transgranular brittle fracture develops. As a result, the LD specimens exhibit a rougher fracture surface and a higher surface coverage by the transgranular brittle fracture mode.

II. Introducing strengthening particles in PIM tungsten (W-1 wt% TiC and W-2 wt% Y_2O_3) appears to have a minor effect on the DBTT compared to the commercial tungsten grades studied here. However, if the particle reinforced tungsten undergoes a thermo-mechanical treatment such as the case of investigated W-0.5 wt% ZrC grade, the DBTT can be further reduced while the strength and ductility are improved compared to the commercial tungsten.

III. Although mechanical treatment like rolling and forging can reduce the DBTT of tungsten alloys, the strain hardening capacity at a high temperature (above 500 ^{o}C) will be reduced. As a result, at 600 ^{o}C, the uniform elongation of rolled/forged tungsten alloys is much smaller than the one without mechanical treatment. For the rolled/forged tungsten alloys, the uniform elongation reaches a plateau as soon as test temperature reaches about 300 ^{o}C above the DBTT. At even higher temperatures, the uniform elongation of rolled/forged tungsten alloys reduces to nearly zero.

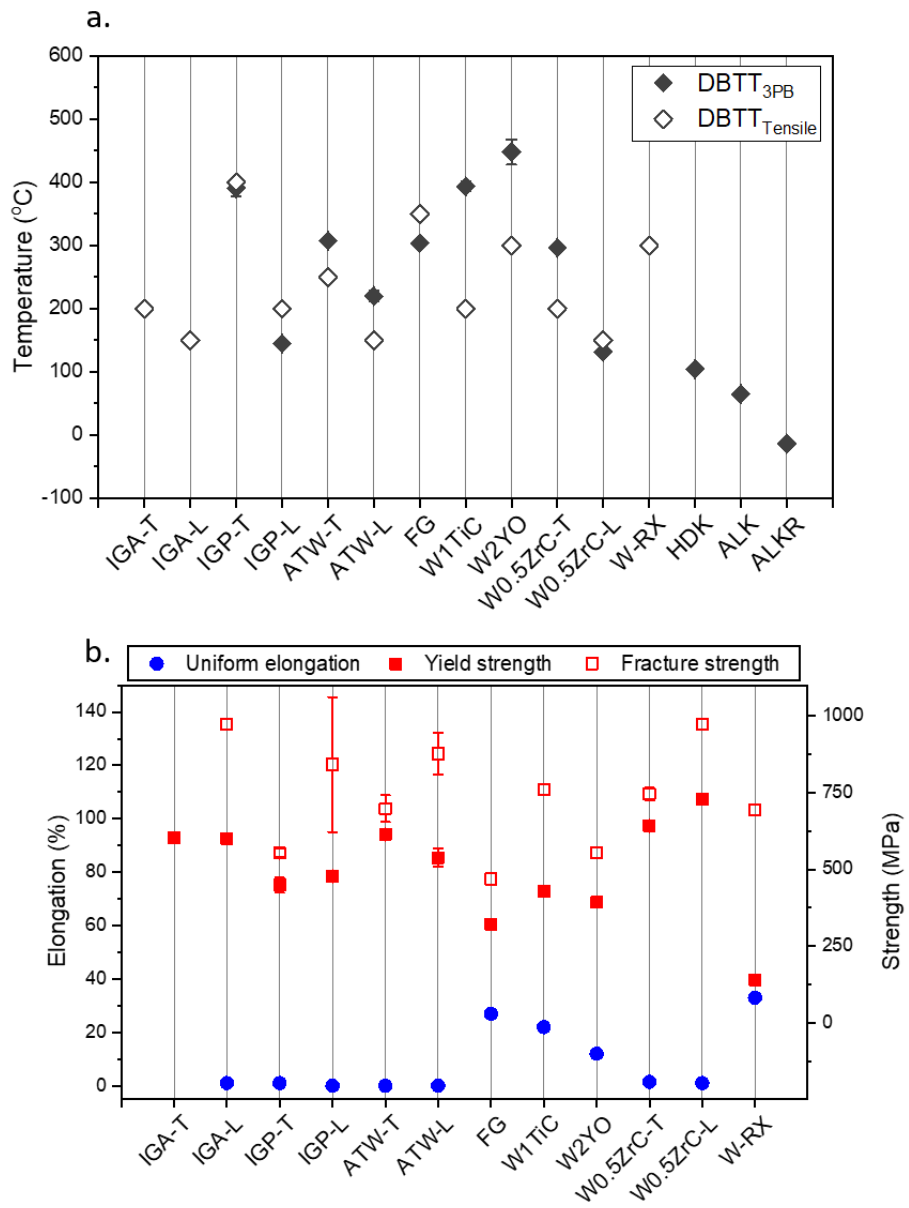

Figure 10.2. Summary of the (a) DBTT and (b) tensile properties of non-irradiated tungsten grades. The yield strength, fracture strength, and uniform elongation are tested at 600 °C. $DBTT_{tensile}$ is defined as the lowest temperature at which tensile specimens show plastic deformation. $DBTT_{3PB}$ is estimated by the three-point bending test.

10.3. Mechanical properties of irradiated tungsten alloys

The main findings regarding the mechanical properties of tungsten alloys after neutron irradiation are summarized in **Figure 10.3** and are listed as follows:

I. The fracture toughness of commercial tungsten grades (IGP and ATW), irradiated at 600 °C, reduces with increasing the irradiation fluence. Apart from the fracture toughness, the fraction of transgranular brittle fracture of the ATW T-L increases after the neutron irradiation, while the intergranular fracture remains dominating in the IGP T-L. The observed phenomenon can be explained by the irradiation-induced defects, which constrain the plastic deformation of grains, and by the grain orientation of ATW T-L, which is perpendicular to the crack propagation plane.

II. The irradiation embrittlement reaches a plateau at the dose above 0.67 dpa for the irradiation temperature of around 600 °C in the case of the ATW T-L. The DBTT shift of the ATW T-L specimens irradiated at 600 °C to 0.67 dpa (evaluated by the fracture toughness test) and the ATW-L specimens irradiated at 610 °C to 1.075 dpa (estimated by the interrupted tensile test) have similar value, which is around 300 °C. Since the irradiation embrittlement results from the irradiation-induced defects mostly formed within the grains (i.e. no strong impact on the structure and chemistry of grain boundaries is expected), the irradiation embrittlement (i.e. DBTT shift) should not depend on grain orientation. As a result, an irradiation dose of around 0.67 dpa might be the plateau threshold of the irradiation embrittlement effect for the ATW grade irradiated at about 600 °C.

III. The neutron irradiation hardening effect estimated from the hardness test shows that the IGP and W-0.5 wt% ZrC grades have the best resistance to the irradiation embrittlement compared to other particle reinforced tungsten grades. The good irradiation resistance of the W-0.5 wt% ZrC material apparently stems from its microstructure composed of fine reinforcing particles (which also rectify the structure of sub-grain boundaries by absorbing oxygen), high dislocation density and small grain size (4.5 μm), which all together creates high sink strength. Although IGA and IGP also have large amount of high and low angle grain boundaries, the anisotropic diffusion properties of the self-interstitial atoms (SIA) will promote the formation of voids in the materials with smaller grains. As a result,

without the presence of the grain-refining particles, the irradiation hardening effect of fine grain grades, like IGA, remains high.

IV. By applying the hardness test on the specimens irradiated at different temperatures, it was observed that the maximum irradiation-induced hardening realizes around 800-900°C, and above this temperature the reduction of the hardening takes place in all types of the tested materials except W-1 wt% TiC. The reduction of the irradiation hardening above ~800°C is very reasonable to expect since the thermally activated diffusion must enhance self-annihilation of irradiation defects, as well as their sinking at the natural material microstructure (dislocations, grain boundaries). The reason for the absence of the hardening reduction in W-1 wt% TiC will require further investigation.

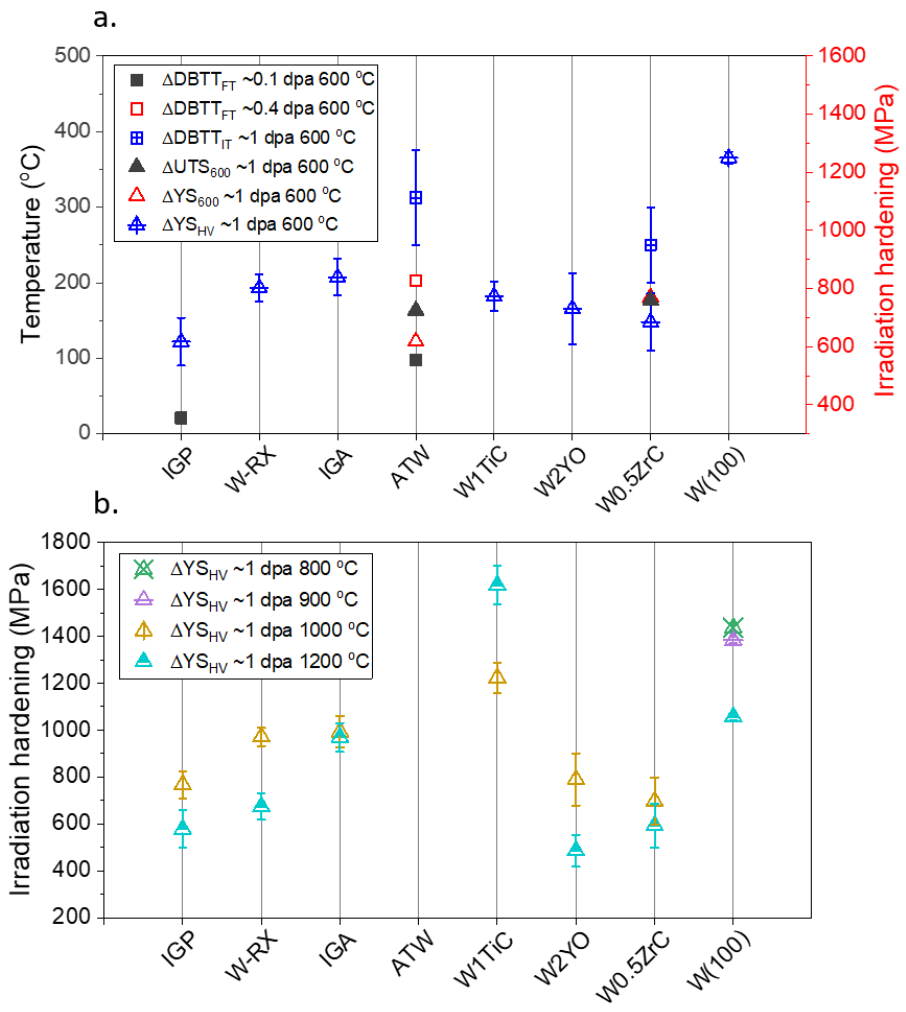

Figure 10.3. Summary of the mechanical properties of tungsten grades irradiated at (a) 600 °C and (b) other temperatures. The doses and temperatures in the legend indicate the irradiation condition. $\Delta\mathrm{DBTT}_{\mathrm{FT}}$ and $\Delta\mathrm{DBTT}_{\mathrm{IT}}$ are the shift of DBTT estimated by the fracture toughness test and the interrupted tensile test, respectively. $\Delta\mathrm{UTS}_{600}$ and $\Delta\mathrm{YS}_{600}$ are the increase of ultimate tensile strength and the increase of 0.2% yield strength measured at ~600 °C. $\Delta\mathrm{YS}_{\mathrm{HV}}$ is estimated from the Vickers hardness.

10.4. Conclusion

In conclusion, the key findings of this work that contribute to the selection of suitable tungsten grade for fusion applications are:

I. Development and validation of new methods for miniaturized bending and tensile specimens to identify DBTT and tensile properties (for details, please refer to **Chapter 4 – 6**);

II. Development of a method coupled with a simple unbiased hardness value H_0 for single crystal specimen, which is tested by Vickers indentation (for details, please refer to **Chapter 9**);

III. Identification of controlling factors of DBTT for rolled/forged tungsten and particle reinforced tungsten based on EBSD analysis and mechanical tests (for details, please refer to **Chapter 3 – 5**);

IV. Assessment of fracture toughness and transition curve of commercial tungsten grades after neutron irradiation at high temperature (for details, please refer to **Chapter 7**);

V. Evaluation of factors controlling the neutron irradiation hardening for tungsten irradiated at 600 ^{o}C with a dose of ~1 dpa (for details, please refer to **Chapter 8**).

10.5. Perspectives

This thesis presents the first results of a large-scale neutron irradiation campaign in BR2 executed for tungsten. Although this thesis has introduced new methods for investigation of mechanical properties and assessed the controlling factors of DBTT in several tungsten grades due to neutron irradiation, a number of questions still require further study and verification. These questions or rather research topics are listed as follows:

I. The applicability of the miniaturized three-point bending for the irradiated tungsten grades needs further confirmation since the method will need to account for the irradiation degradation and thus might require modification.

II. Tensile tests and fracture toughness tests at higher temperatures are needed for some of the studied tungsten grades since the DBTT is higher than 600 °C, which is the highest test temperature available in the hot lab used for this thesis.

III. Since most of the mechanical testing standards involving irradiation are designed for the steels, the codes and standards for high DBTT metal, like tungsten, require more experimental and simulation results for the validation and standardization of testing procedures.

IV. The microstructural investigations of the evolution of irradiation induced defects by transmission electron microscopy (TEM) and positron annihilation spectroscopy (PAS) are necessary in order to verify the proposed here relationship between irradiation hardening and microstructural properties.

V. The microstructural assessment of the texture evolution and effect of irradiation on (potential) recrystallization of the tungsten grades irradiated at high temperature is needed. Thus, EBSD and TEM analysis is of interest for the heavily deformed plate (with high potential for recrystallization), commercially pure rolled tungsten, fine-grain structured tungsten and PIM W-TiC, which showed abnormal increase of the hardness after the irradiation at 1200 °C .